USING SUCTION FOR LAMINAR FLOW CONTROL IN HYPERSONIC QUIET WIND TUNNELS: A FEASIBILITY STUDY

A Thesis

Submitted to the Faculty

of

Purdue University

by

Phillip P. Portoni

In Partial Fulfillment of the

Requirements for the Degree

of

Masters of Science in Aeronautics and Astronautics

December 2019

Purdue University

West Lafayette, Indiana

THE PURDUE UNIVERSITY GRADUATE SCHOOL
STATEMENT OF THESIS APPROVAL

Dr. Steven Schneider, Chair

School of Aeronautics and Astronautics

Dr. Gregory Blaisdell

School of Aeronautics and Astronautics

Dr. Jonathan Poggie

School of Aeronautics and Astronautics

Approved by:

Dr. Gregory Blaisdell

Head of the Graduate Program

To an interesting and (hopefully) financially stable career.

ACKNOWLEDGMENTS

First and foremost, a thanks is required for Dr. Steven Schneider. Without his feedback and direction, this project would have never happened. Thanks are deserved by my committee members Dr. Gregory Blaisdell and Jonathan Poggie. Funding for this project was provided by the Office of Naval Research under Grant N00014-16-1-2500.

Thanks need to be given to the machinists Robin Snodgrass, Jim Younts, and Jerry Hahn. Without their help in the design and production of the suction system, this project would be but blocks of aluminum and steel. Thanks to Calspan and CAV-AT for the production of the suction inserts.

To the BAM6QT lab group during my time here: Dr. Brandon Chynoweth, Josh Edelman, Greg McKiernan, Drew Turbeville, Katie Gray, Mark Wason, Varun Viswanathan, Liz Benitez, Carson Lay, and Chris Yam. You all helped out in so many different ways, and as such, thank you.

TABLE OF CONTENTS

Page

LIST OF TABLES viii

LIST OF FIGURES x

SYMBOLS xviii

ABBREVIATIONS xxi

ABSTRACT xxiii

1 INTRODUCTION AND BACKGROUND 1
- 1.1 Hypersonic Laminar-Turbulent Transition 1
- 1.2 Hypersonic Boundary-Layer Instabilities 3
  - 1.2.1 Tollmien-Schlichting Waves or Second-mode 3
  - 1.2.2 Görtler Instability 4
- 1.3 Suction-Type Laminar Flow Control 5
- 1.4 Quiet Wind Tunnels 7
- 1.5 Computational Work on the Suction Geometry 9

2 FACILITY, MODEL, AND INSTRUMENTATION 17
- 2.1 Boeing/AFOSR Mach-6 Quiet Tunnel 17
  - 2.1.1 Determining Test Conditions 18
  - 2.1.2 Nozzle-Wall Boundary-Layer Separation and Unstart 20
- 2.2 Cone-Flare Model 21
  - 2.2.1 Preliminary Work With Inverse-Flare Geometry 25
  - 2.2.2 Suction Sections 26
- 2.3 Instrumentation and Data Reduction 38
  - 2.3.1 Oscilloscopes 38
  - 2.3.2 PCB132A31 Piezotronics Pressure Sensors 39
  - 2.3.3 Kulite Pressure Transducers 40
  - 2.3.4 Probe Traversing System 41
  - 2.3.5 Schmidt-Boelter Heat Transfer Gauges 48
  - 2.3.6 Temperature-Sensitive Paint 48
  - 2.3.7 Oil-Flow Visualization 51
  - 2.3.8 Focused Laser Differential Interferometry 52

3 SUCTION SYSTEM DESIGN 54
- 3.1 Sonic Suction 54
  - 3.1.1 Surface Conditions 54

Page

3.2 Suction System Design . . . 55
3.2.1 Throughput and Conductance . . . 57
3.2.2 Plumbing Hardware . . . 58
3.3 Predicting the Plenum Pressure . . . 62
3.3.1 Results from the Prediction Code . . . 65
3.3.2 Comparison of Code to Measured Plenum Pressure . . . 71

4 RESULTS AND DISCUSSION . . . 74
4.1 Early Experiments . . . 74
4.1.1 Inverse Flare Geometry . . . 74
4.1.2 Vortex imaging with different lenses using TSP . . . 75
4.1.3 Oil-Flow Visualization on the Flare . . . 79
4.1.4 Leaking Suction System . . . 83
4.2 Baseline Results with Smooth Plenum Insert . . . 84
4.2.1 Surface Pressure Fluctuations . . . 84
4.2.2 Surface Heat Transfer . . . 92
4.2.3 Pitot Probe Measurements . . . 96
4.3 Suction Measurements I . . . 107
4.3.1 Sonic Suction Through Perforated Skin . . . 107
4.3.2 Surface Pressure Fluctuations . . . 111
4.3.3 Surface Heat Transfer . . . 118
4.3.4 Pitot-Probe Measurements . . . 123
4.4 Suction Measurements II . . . 141
4.4.1 Surface Pressure Fluctuations . . . 141
4.4.2 Surface Heat Transfer . . . 146
4.4.3 Pitot-Probe Measurements . . . 151
4.4.4 FLDI Measurements . . . 156

5 SUMMARY OF RESULTS . . . 159
5.1 Future Work . . . 160

REFERENCES . . . 162

A LOG OF RUN CONDITIONS . . . 166
A.1 Inverse Flare Entry . . . 166
A.2 Smooth Insert Entry I . . . 166
A.3 Low Max-Quiet Entry . . . 167
A.4 Oil-Flow Entry . . . 167
A.5 Unsuccessful Suction System Entry . . . 167
A.6 Smooth Insert Entry: Successful . . . 168
A.7 Suction Insert Entry I: Successful . . . 169
A.8 Suction Insert Entry II: Successful . . . 170

B MODEL DRAWINGS . . . 173

Page

C PLENUM PRESSURE PREDICTION CODE 188

D TRAVERSE POSITIONING PROGRAM 204

E INSTALLING THE SUCTION SYSTEM 208
E.1 Install Sequence 208
E.2 29A-Flange 209
E.3 Steel Plug and Tunnel-Flange 210
E.4 Pipe Insert 213
E.5 Sting 214
E.6 Pipe, Solenoid Valve, and Hose 214
E.7 Sealing and Leak Testing 218

F VACUUM SENSOR CALIBRATIONS 219

LIST OF TABLES

Table		Page
2.1	Surface-sensor locations in the suction model.	23
2.2	Hole patterns of the suction sections with CAV-AT-measured Percent Open Area (POA).	28
2.3	Measured physical characteristics of suction sections	33
2.4	Measured porosity along Suction Section 5. Measurements were made approximately every 2.8 mm	34
3.1	Solutions from Taylor-Maccoll analysis for a 7° half-angle cone in Mach 6 flow.	55
3.2	Surface values for Mach 6 flow on a 7° half-angle cone with $P_0 = 155$ psia.	55
3.3	Iterations of the suction system	59
3.4	Conductance of suction-pipe segments in the Rev.2 design with $\bar{p} = 3.14$ Torr. Colors correspond to Figure 3.2	61
4.1	RMS values for PSDs in Figure 4.11	88
4.2	Peak second-mode frequency and RMS pressure fluctuations from suction runs with Re_∞ between 10.8×10^6 and 11.1×10^6.	112
4.3	Run conditions and peak frequencies for Figure 4.34. Pitot probe is 26.9 cm axially from nosetip. Run SS1.8	113
4.4	Run conditions and peak frequencies for Figure 4.35. Pitot probe is 28.9 cm axially from nosetip. Run SS1.11, 14	116
4.5	Run conditions and peak frequencies for Figure 4.36. Pitot probe is 34.8 cm axially from nosetip. Run SS1.18, 21	116
4.6	Run conditions and peak frequencies for Figure 4.37.	118
4.7	Comparison of the smooth and suction pitot noise levels for runs with $p_{0,i}$ = 155 psia	137
4.8	Peak frequency and RMS pressure fluctuations at different axial locations, $Re_\infty = 10.3 \times 10^6$ m^{-1}	143
4.9	Peak frequency and RMS pressure fluctuations for the PSDs shown in Figure 4.59.	144

Table Page

4.10 Peak frequency and RMS pressure fluctuations for the PSDs shown in Figure 4.60. 146

4.11 Peak frequency and RMS pressure fluctuations for the PSDs shown in Figure 4.61 148

4.12 RMS of optical-path fluctuations measured at $x = 26.9$ cm with FLDI . 156

4.13 RMS of optical-path fluctuations measured at $x = 31.5$ cm with FLDI . 157

F.1 Comparison of Ceravac 100 torr vacuum sensor against a Ceravac 1000 torr vacuum sensor 219

F.2 Comparison of Ceravac 100 torr vacuum sensor against a Ceravac 1 torr vacuum sensor 220

F.3 Calibration of low pressure sensor with serial number 51 222

F.4 Calibration of low pressure sensor with serial number 49 222

LIST OF FIGURES

Figure Page

1.1 Heat shield of the Apollo 12 reentry capsule. The pitting that is circled can develop from local regions of higher heat transfer during reentry or from spalling of heat shield flows. Picture taken by the present author at the Virginia Air and Space Center, Hampton, VA. 2

1.2 Depiction of idealized T-S growth and boundary layer transition on a flat plate at zero incidence. Redrawn from reference [6] 4

1.3 Shadowgraph of cone traveling Mach 4.3 down ballistics range. Illustrates the contrast in noise radiated from laminar and turbulent boundary layers. Used with permission from Reference [15]. 7

1.4 Geometric parameters varied in designing the suction geometry. 10

1.5 Surface pressure distribution on the suction geometry with Re = 12.13×10^6 m^{-1}. Redrawn from [19]. 11

1.6 Mach number contours on the suction geometry with Re = 12.13×10^6 m^{-1}. Redrawn from [19]. 12

1.7 Mack mode N-factors along the flare of the suction geometry for $Re_\infty = 12.13 \times 10^6$. Redrawn from Li et al. [19]. 13

1.8 Comparison of Mack mode and most amplified secondary instability. Redrawn from Figure 13 of [20]. 15

2.1 Boeing/AFOSR Mach 6 Quiet Tunnel schematic 17

2.2 Uncalibrated voltage trace from the nozzle-wall pressure transducer for a quiet run with initial stagnation pressure of 155 psia. 19

2.3 Nozzle-wall boundary-layer separation shown in nozzle-wall static pressure and hot-film traces for a suction-enabled run with $p_{0,i} = 155$ psia. Run SS1.17 20

2.4 Diagram of the cone-flare geometry with the smooth blank for the suction insert installed. 21

2.5 Picture of the sharp nosetip taken with a digital camera on a microscope. Radius determined , $r = 76\mu m$ (0.003 in.) 22

2.6 Cross section of the suction geometry. 24

Figure Page

2.7 Approximate location of the pressure transducer measuring the plenum pressure. 24

2.8 2-ft, 1-1/4-in. pipe passing through tunnel wall 25

2.9 Diagram of the inverse-flare cone geometry. 26

2.10 Drawing of suction section plenum (blue) with fit-rings (gray) and the suction skin (red) provided by Calspan 27

2.11 Images of the four perforation patterns captured with a Zygo ZeGage optical profiler. The scale shown with Suction Section 5 is valid for all four images. 29

2.12 Suction section mounted for measurements with the Zygo ZeGage Optical Profiler 30

2.13 Three stages of how pores were counted for calculating porosity of the suction sections. Shown is Suction Section 2. 32

2.14 Approximate locations where porosity is measured along the Suction Section 5. The measurements were made approximately every 2.8 mm. 33

2.15 Comparison of the surface roughness of Suction Sections 3 and 2. SS.3 exhibits roughness of up to 1 mil peak-to-valley, while SS.2 shows no noticeable roughness. 36

2.16 Damages to perforated skin of Suction Section 5. Arrows point to regions of cracking along the rays. Photo provided by Calspan. 37

2.17 Protective shield for use in load testing the welds on the perforated skins. Installed in the cup is Suction Section 1. 38

2.18 Frequency band used for RMS pressure-fluctuation calculations. 40

2.19 Traverse motor and rail positioner mounted on top of the BAM6QT. . . . 43

2.20 Kulite probe mount used to measure pressure fluctuations in the freestream above the model. 44

2.21 Depiction of locations above the model where data was captured by the pitot probe. 46

2.22 Close-up of the traversed positions 46

2.23 Pitot probe in tunnel above the model. Probe located 26.9 cm from nosetip. 47

2.24 The suction model painted with temperature-sensitive paint (yellow region). 49

2.25 Example calibration of TSP plotted against the Schmidt-Boelter gauge measurements during a run. 50

Figure Page

2.26 Linear calibration of TSP temperature change to heat transfer. 51

2.27 The oil applied to the suction model before a run. 52

2.28 Illustration of FLDI setup with beam separation enlarged for clarity. Used with permission from Liz Benitez [35]. 53

3.1 Streamwise mass-flux profile in the boundary layer of a 7° half-angle cone at 0° angle of attack located at axial position 0.258 meters (10.16 inches) from the nosetip. Calculated via STABL mean-flow solver with freestream conditions $p_0 = 170$ psia and $T_0 = 433$K. 56

3.2 Schematic of the Rev.2 suction-system assembly. Refer to Table 3.4 for sizes of each section. 60

3.3 Static pressure at the upstream end of the 6-inch line for a run with $p_{0,i} =$ 155 psia. 62

3.4 Schematic of suction system during the startup of the plenum-pressure prediction analysis. 64

3.5 Results from plenum-pressure analysis code for Suction Section 1 with the suction system depicted in Figure 3.2. 67

3.6 Results from plenum-pressure analysis code for a 5%-porosity suction section paired with the suction system depicted in Figure 3.2. 68

3.7 Results from plenum-pressure analysis code for a 5%-porosity suction section with the 2-inch hose in the suction system. 69

3.8 Pressure ratio between plenum and surface plotted from 0.05 to 3.5 seconds. Results from plenum-pressure analysis code with time-varying freestream pressure with a 3.5%-porosity suction section and the constructed suction system. 70

3.9 Plenum-pressure trace from a run with $p_{0,i} = 155$ psia and $T_{0,i} = 424$ K. Measured with a pressure transducer inside the plenum. Run SS1.7 72

3.10 Comparison between different models used in predicting the plenum pressure. Run SS1.7 73

3.11 Schematic of simplified, sonic-orifice model of the suction system. 73

4.1 Hot-film trace for bleeds-open runs with the inverse flare model. Run INF.3 75

4.2 Temperature change with the smooth blank insert. Freestream unit Reynolds number in images is $8.30 \times 10^6\,\mathrm{m}^{-1}$. Run SJF.11 76

4.3 Heat transfer measurement with a 105-mm focal-length lens. $Re_\infty =$ $8.27{\times}10^6$ m^{-1}. Run SSF.8 78

Figure Page

4.4 Oil-flow visualization of suction model with the smooth blank insert. Freestream Reynolds in images is 11.0×10^6 m^{-1}. Run OIF.4 80

4.5 Image intensity of oil-flow visualization along vertical slices at $x = 0.526$ m for a range of Reynolds numbers. Runs OIF 3, 4 81

4.6 Image intensity of oil-flow visualization along vertical slices at $Re_\infty = 11.1 \times 10^6$ m^{-1}. Run OIF.4 82

4.7 Comparison of the static pressure in the model plenum with the leaking suction system on and off. $p_{0,i} = 28.9$ psia for both. Run SAF.12-13 83

4.8 PSDs of PCB1, PCB2, and PCB3 before model alignment. $Re_\infty = 10.3 \times 10^6$ m^{-1}. Run Smooth.1 85

4.9 PSDs of PCB1, PCB2, and PCB3 after model alignment. $Re_\infty = 10.3 \times 10^6$ m^{-1}. Run Smooth.3 86

4.10 PSDs of PCB5 ($x = 47.5$ cm) with decreasing Reynolds number. Run Smooth.3, 4, 5 87

4.11 PSDs of surface pressure fluctuations at $x = 45.0$ cm and $x = 47.5$ cm. $Re_\infty = 11.3 \times 10^6$ m^{-1}. Run Smooth.3 89

4.12 PSDs of surface-pressure fluctuations at $x = 47.5$ cm showing repeatability of results. $Re_\infty = 10.8 \times 10^6$. Run Smooth.2, 3 90

4.13 PSDs of surface-pressure fluctuations at $x = 47.5$ cm for runs with and without the pitot probe. $Re_\infty = 11.3 \times 10^6$ m^{-1}, $h = 25$ mm. Run Smooth.3, 8, 14, 20 91

4.14 To-scale depiction of the Mach line from the pitot probe impinging on the top of the model. The pitot probe is located at $h = 25$ mm and $x = 26.9$. $Re_\infty = 11.3 \times 10^6$ m^{-1}. Run Smooth.8 92

4.15 Surface heat transfer with the smooth insert with $Re_\infty = 11.3 \times 10^6$ m^{-1}. The pitot probe is located at $h = 25$ mm, $x = 26.9$ cm. Run Smooth.8 . . 93

4.16 Surface heat transfer with the smooth insert with $Re_\infty = 8.77 \times 10^6$ m^{-1}. The pitot probe is located at $h = 20$ mm and $x = 28.9$ cm. Run Smooth.10 94

4.17 Depiction of region where heat transfer was spanwise averaged for Figure 4.18. Run Smooth.10 94

4.18 Heat transfer averaged along a narrow spanwise slice below the main sensor array for different Reynold's numbers. Also plotted is Li et al.'s mean flow heat transfer [19]. Run Smooth.8 and Smooth.10 95

Figure Page

4.19 Normalized mean pitot pressures above the model 26.9 cm axially from the nosetip. Runs Smooth.6-11 97

4.20 Mach lines from Li et al. computations overlaid with the pitot-probe measurement locations 97

4.21 Mean pitot pressures above the model 28.9 cm axially from the nosetip. Runs Smooth.12-17 98

4.22 Mean pitot pressures above the model 34.8 cm axially from the nosetip. Runs Smooth.18-23 99

4.23 PSD of pitot fluctuations measured 26.9 cm from the nosetip at $Re_\infty = 11.3\times10^6$ and $Re_\infty = 9.87\times10^6$. 101

4.24 PSDs of pitot fluctuations measured at $h = 25$ mm for three axial positions. $Re_\infty = 11.3\times10^6$. Run Smooth.8, 14, 20 102

4.25 Noise level measured in each vertical position above the model 26.9 cm axially from the nosetip. Runs Smooth.6-11 103

4.26 Noise levels measured in each vertical position above the model 28.9 cm axially from the nosetip. Runs Smooth.12-17 104

4.27 Noise levels measured in each vertical position above the model 34.8 cm axially from the nosetip. Runs Smooth.18-23 105

4.28 Noise levels measured at $x = 34.8$ cm, omitting the high values measured at $h = 1$ and 3 mm with $p_{0,i} = 155$ psia. Runs Smooth.18-23 106

4.29 Pressure inside the suction plenum from a run with $p_{0,i} = 155$ psia. Run SS1.6 108

4.30 Running average of plenum pressure for a run with $p_{0,i} = 155$ psia with error bars. Run SS1.6 109

4.31 Pressure inside the suction plenum for a run with $p_{0,i} = 135$ psia. Run SS1.14 110

4.32 PSDs of surface-pressure fluctuations at $x = 52.6$ cm. $Re_\infty = 10.7 \times 10^6$ m^{-1}. Run SS1.8, 9, 18 112

4.33 PSDs of surface-pressure fluctuations for aligned 0° angle of attack (Refer to Section 4.4) and nominal 0°. $x = 52.6$ cm and $Re_\infty = 10.8 \times 10^6$ m^{-1}. Runs SS1.11 and SS2.10 113

4.34 PSDs of surface pressure fluctuations at $x = 52.6$ cm at decreasing Reynolds numbers. Pitot probe is 26.9 cm from nosetip and 25 mm above model. Run SS1.8 114

Figure Page

4.35 PSDs of surface pressure fluctuations at $x = 52.6$ cm at decreasing Reynolds numbers. Pitot probe is 28.9 cm from nosetip and 25 mm above model. Run SS1.11, 14 115

4.36 PSDs of surface pressure fluctuations at $x = 52.6$ cm at decreasing Reynolds numbers. Pitot probe is 34.8 cm from nosetip and 25 mm above model. Run SS1.18, 21 117

4.37 PSDs of surface pressure fluctuations at $x = 52.6$ cm with both the baseline and suction measurements. Re_m around 11.2×10^6 m^{-1}. Runs Smooth.3, SS1.8 118

4.38 Heat transfer on suction model at $Re_\infty = 11.0 \times 10^6$ m $^{-1}$. Run SS1.8 . . 119

4.39 Heat transfer on suction model at $Re_\infty = 9.9 \times 10^6$ m^{-1}. Run SS1.14 . . 120

4.40 Depiction of the slice used when calculating heat transfer as a function of axial location in Figure 4.41. 121

4.41 Axial change in mean heat transfer from a narrow spanwise slice about spanwise reference of 0 m. 122

4.42 Comparison of axial change in heat transfer with both smooth and suction measurements. Runs Smooth.8, SS1.8 123

4.43 Time trace and PSD of example case of apparent model boundary layer interaction with pitot probe. 125

4.44 Normalized, mean pitot pressures measured above the model 26.9 cm axially from the nosetip in runs with suction on. Run SS1.6:8 126

4.45 Mach lines from Li et al. computations overlaid with the pitot-probe measurement locations. From left to right, the vertical lines are located at $x = 26.9$, 28.9, and 34.8 cm. 127

4.46 Normalized, mean pitot pressures measured above the model 28.9 cm axially from the nosetip in runs with suction on. Run SS1.9:14 128

4.47 Normalized, mean pitot pressures measured above the model 34.8 cm axially from the nosetip in runs with suction on. Run SS1.16:21 129

4.48 PSDs of three pitot probe measurements behind the suction section, 26.9 cm from nosetip. Run SS1.6-8 130

4.49 PSDs of pitot probe measurements above the flare at $x = 34.8$ cm. Run SS1.16:18 131

4.50 PSDs of three pitot probe measurements at $h = 25$ mm. Re_∞ between 11.0×10^6 and 11.3×10^6 m^{-1}. Run SS1.8, 11, 18 132

Figure Page

4.51 Noise levels measured above the model 26.9 cm from model nosetip. $p_{0,i}$ = 155 psia. Run SS1.6-8 133

4.52 Noise levels measured above the model 28.9 cm from model nosetip. Run SS1.9-14 134

4.53 Noise levels measured above the model 34.8 cm from the model nosetip. Run SS1.16-21 135

4.54 Comparison of suction and smooth noise levels above the model 26.9 cm from the model nosetip. 138

4.55 Comparison of suction and smooth noise levels above the model 28.9 cm from the model nosetip. 139

4.56 Comparison of suction and smooth noise levels above the model 34.8 cm from the model nosetip. 140

4.57 PSD of PCB1, PCB2, and PCB3. $Re_\infty = 10.3\times10^6$ m^{-1}. Run SS2.8 . . . 142

4.58 PSD of 4 sensors axially spaced by 2.54 cm at $Re_\infty = 10.3 \times 10^6$ m^{-1}. Run SS2.10 143

4.59 PSDs measured at $x = 50.0$ cm for four suction-enabled runs with $Re_\infty = 11.0 \times 10^6$. Run SS2.8-10, 13 144

4.60 PSDs of surface pressure fluctuations measured at $x = 45.1$ cm at decreasing Reynolds number. Run SS2.10, 12 145

4.61 PSD of PCB13 while suction disabled. Run SS2.15 147

4.62 Heat transfer on the suction model at $Re_\infty = 11.0 \times 10^6$ m^{-1} with the probe not in the flow. Run SS2.10 149

4.63 Axial change in mean heat transfer from a narrow slice at spanwise reference of 0.01 m, depicted in Figure 4.64. Also shown are Li et al.'s predicted heat transfer at $Re_\infty = 12.1 \times 10^6$ m^{-1} [19] Run SS2.10 149

4.64 Depiction of the streamwise slice used to determine axial change in heat transfer in Figure 4.63. Run SS2.10 150

4.65 Mean pitot pressure with respect to vertical position measured at $x = 31.5$ cm with $p_{0,i}$ = 155 and 135 psia. Run SS2.18-23 152

4.66 PSDs of pitot probe measurements 31.5 cm from nosetip. 154

4.67 Noise levels measured above the model 31.5 cm from the model nosetip. Run SS2.18-23 155

4.68 PSD from FLDI measurements at $x = 26.9$ cm. Run SS2.36-39 157

Figure Page

4.69 PSD from FLDI measurements at $x = 31.5$ cm with suction enabled. Run SS2.40-48 158

E.1 29A-flange connecting to 6-in aluminum pipe plumbed through the wall between 29A and 29B 209

E.2 6-inch, stainless steel plug typically installed in the side of the BAM6QT just downstream of the sting support. 211

E.3 Flange with 2-in. NPT adapter 212

E.4 The hole in the pipe insert observed thorough the hole created when the stainless steel plug is removed. 213

E.5 2-ft, 1-1/4-in. pipe mating with sting inside BAM6QT 215

E.6 2-ft, 1-1/4-in. pipe passing through tunnel wall 216

E.7 2-in hose connection to solenoid valve 217

F.1 Picture of 29A-flange set up to calibrate ETL-79-HA-DC-190-5A Kulite pressure transducers. 221

SYMBOLS

A	area
$A_{orifice}$	area of porous region of suction section
C	conductance
c_p	specific heat at constant pressure
f	frequency
G_θ	Görtler number
h	height of traverse probe
h_w	enthalpy at model wall
H_0	total enthalpy
I_{dark}	intensity of "dark" images
I_{off}	intensity of "off" images
I_{on}	intensity of "on" images
k	thermal conductivity
K	Gladstone-Dale constant
k_v	viscous coefficient for conductance
l	length variable
L	paint thickness
L_{int}	integration length in processing FLDI
M	Mach number
$\dot{m}$	mass flow rate
n	azimuthal wavenumber
p	pressure
$\dot{q}$	heat flux
Q	throughput
r	radius of curvature

R_θ	Reynolds number based on momentum thickness
Re	Reynolds number per unit length
s_p	plenum pressure sample standard deviation
St	Stanton number
t	time
T	temperature
u	velocity
U_p	uncertainty in plenum pressure
V	volume
$\bar{V}$	voltage
x	axial distance from nosetip
z	pipe-axial coordinate
γ	ratio of specific heats
ΔT	temperature change
ν	dynamic viscosity
θ	momentum thickness
λ	laser wavelength
ρ	density
ϕ'	phase change
$\Delta\phi_i$	baseline phase shift
$\Delta\Phi$	optical-path fluctuations

Subscripts

0	stagnation condition
edge	boundary-layer edge condition
i	initial condition
mean	mean value
peak	peak
pipe	suction system pipe condition

$plenum$	suction system plenum condition
pr	photoreceiver
ref	reference value
$surf$	model surface condition
$tank$	suction system vacuum tank condition
∞	freestream condition

ABBREVIATIONS

AAE	Aeronautical and Astronautical Engineering
AFOSR	Air Force Office of Scientific Research
ASPE	American Society of Plumbing Engineers
BAM6QT	Boeing/AFOSR Mach-6 Quiet Tunnel
CAV-AT	CAV-Advanced Technologies
CFD	Computational Fluid Dynamics
cfm	cubic-feet per minute
DNS	Direct Numerical Simulation
FLDI	Focused Laser Differential Interferometry
INF.N	Run reference for inverse flare entry
IR	Infrared
LFC	Laminar Flow Control
NASA	National Aeronautics and Space Administration
NPT	National Pipe Taper
OIF.N	Run reference for oil-flow visualization entry
POA	Percent Open Area
PSD	Power Spectral Density
Rev.N	Reference for suction system iteration
RMS	Root Mean Square
SAF.N	Run reference for unsuccessful suction entry before redesigning the suction system
SB	Schmidt-Boelter Heat Transfer Gauge
SJF.N	Run reference for unsuccessful smooth insert entry
Smooth.N	Run reference for successful entry with the smooth plenum blank
SN	Serial number

SS	Suction Section
SS.N	Suction Section N
SS1.N	Run reference for first successful entry with suction enabled
SS2.N	Run reference for second successful entry with suction enabled
SSF.N	Run reference for unsuccessful suction entry with the final version of the suction system
T-S	Tollmien-Schlichting
TSP	Temperature Sensitive Paint

ABSTRACT

Portoni, Phillip P. M.S.A.A., Purdue University, December 2019. Using Suction for Laminar Flow Control in Hypersonic Quiet Wind Tunnels: A Feasibility Study. Major Professor: Steven P. Schneider.

To reduce the risk of using suction in a hypersonic quiet-tunnel nozzle design, this project tested micro-perforated suction sections to remove the boundary layer on an axisymmetric model in the Boeing/AFOSR Mach-6 Quiet Tunnel. The model was a cone-flare geometry tested at 0° angle of attack. The turn from the 7° half-angle cone to the flare was designed to prevent flow separation. The flare was designed to amplify the Görtler instability.

Five suction sections were designed with different perforation patterns and porosities. Four were successfully manufactured, but only the first of the four sections has been tested so far. The first suction section has pores drilled along straight lines with a nominal 5% porosity.

Measurements were made with temperature-sensitive paint and oil-flow visualization on a non-perforated blank to measure the baseline development of Görtler vortices on the flare. Although the signal-to-noise ratio of the measurement techniques were insufficient to measure the vortices, it was confirmed that the boundary layer is laminar for the entire model. Measurements with suction also did not show the Görtler vortices.

Surface pressure fluctuations were measured on the flare. Apparent second-mode waves were detected. The suction measurements showed a slight increase in second-mode peak frequency over the baseline results, as expected.

Concerns had been raised about acoustic noise that might be radiated from the suction section. Thus, fluctuations above the suction section were measured using a pitot probe and using focused-laser differential interferometry. The measurements

during suction showed no noticeable increase in fluctuations compared to the baseline results.

1. INTRODUCTION AND BACKGROUND

1.1 Hypersonic Laminar-Turbulent Transition

In the design of hypersonic vehicles, accurate prediction of boundary-layer transition is often critical. The intensity and types of disturbances in the boundary layer greatly affect the aerodynamics and heating on the vehicle. A laminar boundary layer is smooth and has minimal fluctuations. Instabilities from disturbances such as acoustic waves, surface roughness, or shock waves can be amplified in the viscous regime. These can cause the boundary layer to transition into turbulence. Turbulent boundary layers can have heating exceeding three times laminar conditions as shown by Bertin et al. on the Shuttle Orbiter [1]. Shown in Figure 1.1 is the ablative heat shield of the Apollo 12 reentry capsule on display at the Langley Air and Space Museum. During reentry the Mach number was high, and the capsule's boundary layer was turbulent yielding extremely high heating. For reusable and controlled-descent vehicles the thermal protection design requires accurate knowledge of the boundary-layer state.

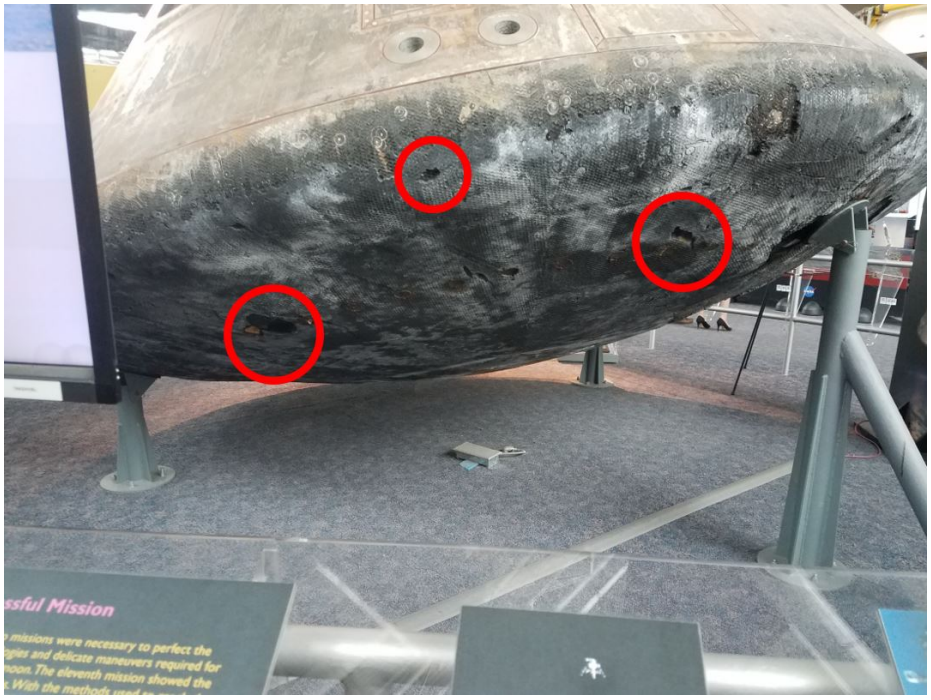

Figure 1.1. Heat shield of the Apollo 12 reentry capsule. The pitting that is circled can develop from local regions of higher heat transfer during reentry or from spalling of heat shield flows. Picture taken by the present author at the Virginia Air and Space Center, Hampton, VA.

In order to predict the boundary-layer state during flight conditions, combinations of empirical correlations, wind tunnel experiments, and computer simulations are used. The e^N method is a semi-empirical relationship, developed in 1956 [2], which uses linear stability theory to predict transition based on the most amplified boundary-layer disturbance. There are several limitations to this correlation, as it does not take into account roughness, freestream noise, non-linear growth, or vibrations. Experimental tests on models are completed to determine flow physics, but a single wind tunnel cannot simulate all aspects of flight. For example, quiet wind tunnels are used to replicate flight-like freestream noise levels to study transition but have low Reynolds numbers when compared to conventional tunnels. Other tunnels can be useful for studying non-equilibrium chemistry and high-enthalpy flow with

other limitations. Computational methods are used to predict flow fields and boundary layer interactions. However, in order to validate these computer simulations they have to be compared with experimental results.

1.2 Hypersonic Boundary-Layer Instabilities

1.2.1 Tollmien-Schlichting Waves or Second-mode

Tollmien-Schlichting (T-S) and second-mode waves develop due to viscous interactions with perturbations on the wall. This results in a disturbance reflecting between the wall and the Mach line in the boundary layer which forms a resonance with the least damped mode [3]. For high Mach number flow, the oblique, three-dimensional aspects of the instability can dominate transition. This was shown experimentally by Demetriades [4] in 1958, with theoretical solutions computed by Brown [5]. Both studies used a flat-plate geometry at Mach 5. Figure 1.2 shows the idealized growth of T-S waves on a flat plate. Initially, the boundary-layer is smooth up to some critical Reynolds number. Beyond which, fairly uniform, parallel T-S waves begin to develop and grow, seen in Regions 2 and 3. Further downstream, the disturbance starts to break down and becomes increasingly random. This is considered transitional, Region 4. By Region 5, vortices start shedding from the waves and turbulent spots can be seen in the boundary layer. Eventually, the boundary layer is very random and is considered turbulent. As the waves propagate downstream, they grow and begin to breakdown causing transition, depicted in Region 4.

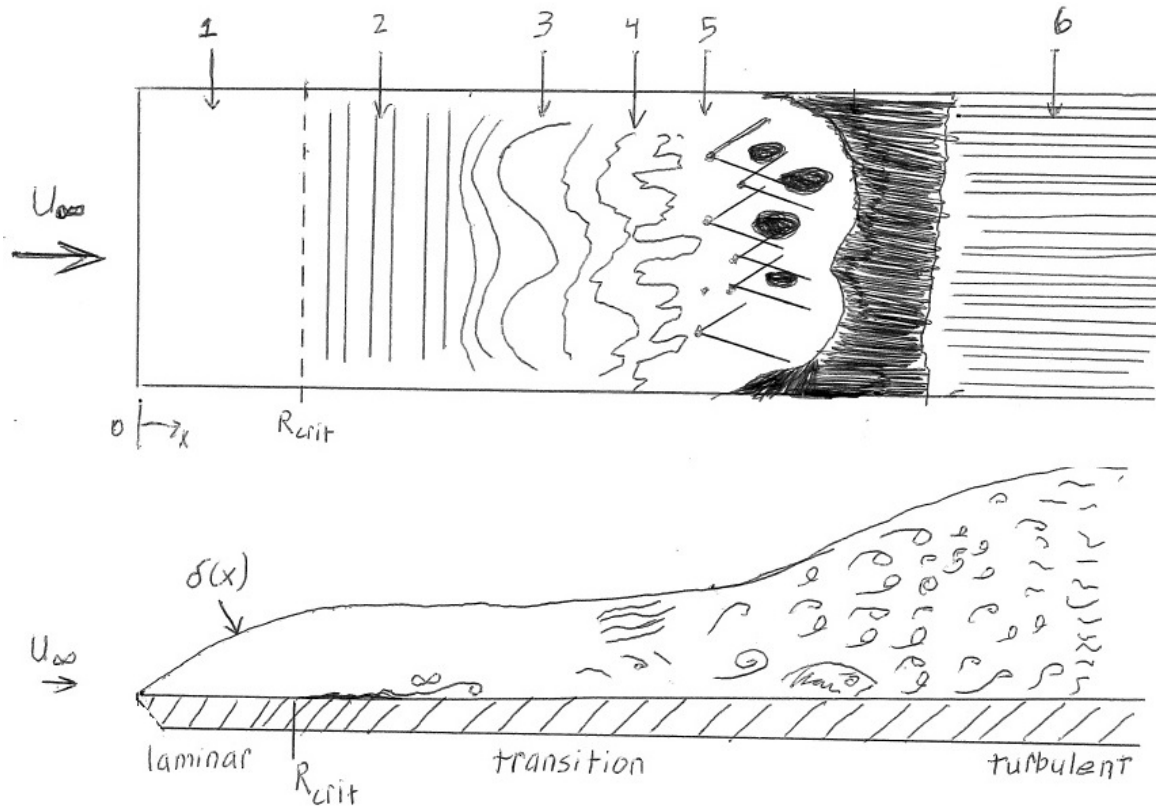

Figure 1.2. Depiction of idealized T-S growth and boundary layer transition on a flat plate at zero incidence. Redrawn from reference [6]

1.2.2 Görtler Instability

In laminar flow over a concave, curved surface, a velocity difference between the outer and inner regions of the boundary layer occurs due to centrifugal forces. The resulting pressure variation develops into the Görtler instability, manifesting as paired, counter-rotating, stationary, streamwise vortices. In his 1940 publication, Görtler calculated the neutral stability and growth rate of these instabilities and vortices [7]. His solutions to the differential equations were built from Taylor's work on the stability of flow between concentric rotating cylinders. There were several limiting assumptions in his work. These include constant boundary layer thickness, constant

wall curvature, and constant freestream velocities. It is also assumed the vortices grow exponentially with time. In 1955, Smith refined the Görtler instability problem by modeling the vortex as a function of distance [8]. His results removed the previously mentioned restrictions of Görtler's original work. The stability of a Görtler vortex can be reported in terms of the nondimensional Görtler number defined by

$$G_\theta = R_\theta \sqrt{\theta / r} \tag{1.1}$$

where R_θ is the Reynolds number based on the momentum thickness, θ, and r is the local radius of curvature.

Generally, a large Görtler number implies a less-stable vortex [9]. If the Görtler vortices become sufficiently large, they could break down leading to boundary-layer transition. Referring back to the Görtler number defined in Equation **??**, the obvious methods to reduce the strength of the Görtler instability are to reduce the Reynolds number, reduce the momentum thickness, or increase the radius of curvature. Reducing the Reynolds number is not desired when designing a wind tunnel. In order to increase the radius of curvature, the nozzle-expansion length would need to be increased which is beyond the scope of this literature review. The focus of the current work is to reduce the momentum thickness by suction of the boundary layer without causing it to transition. This process is a subfield of laminar flow control as described in Section 1.3.

1.3 Suction-Type Laminar Flow Control

Laminar flow control (LFC) has been a topic of research since the 1930s. LFC is any technique used to maintain a laminar boundary layer. Two broad categories of LFC are active flow control using suction and passive flow control using methods such as geometry shaping. The applications are not limited to the development of quiet wind tunnels, as controlling transition on aircraft wings was a driving factor in the development of LFC.

Active LFC often requires the use of a vacuum system to remove portions of the boundary layer. Exhaustive descriptions of active LFC's progress and history are presented by Joslin and Braslow, references [10] and [11] respectively. Presented here are a few noteworthy achievements in wind-tunnel experiments using suction.

In 1939, active LFC using slots was researched by National Advisory Committee for Aeronautics in subsonic wind tunnels. These studies reportedly led to successful flight tests in the early 40's [12].

In supersonic wind tunnel tests at Mach 2.5, 3.0, and 3.5, Pate measured laminar flow on a body-of-revolution with suction slots [13]. There were 150 spanwise slots on the model with widths varying from 0.0040 to 0.0080 in. With suction on, a laminar boundary layer was maintained for the full length of the model (77.8 in.) in Mach 3.0 flow.

Pfenninger performed a series of simulations with suction in an attempt to analytically reduce the freestream noise in both rectangular and axisymmetric nozzles [14]. The two-dimensional tunnel design considered had a freestream Mach number of 4.6, and for the axisymmetric design the Mach number was varied from 3 to 9. The test-section unit Reynolds numbers were around 26.2×10^6 m^{-1} with a length factor based on the nozzle-exit diameter. To simulate area suction, he used closely spaced, small diameter electron-beam drilled holes, but non-uniformities in the suction induced streamwise vorticity which was then amplified by the Görtler instability. Longitudinal and highly swept slots reduced the induced mean flow disturbances but require higher suction rates and also induced a crossflow velocity in the boundary layer. Flush, spanwise to moderately swept slots were shown to prevent streamwise vorticity. However, they generated weak shocks which radiated into the freestream and caused early transition on models. He also showed that cooling the nozzle wall increases the growth rate of the Görtler vortices.

1.4 Quiet Wind Tunnels

Conventional hypersonic facilities have freestream noise levels that are orders of magnitude higher than flight conditions, which are typically 0.5-1% of the mean [15]. These fluctuations impact the growth of boundary-layer instabilities and can lead to inaccurate transition predictions. Quiet wind tunnels have freestream noise levels less than 0.05% [15]. Tunnel noise levels are often measured as the ratio between the RMS pitot-pressure fluctuations and the mean pitot pressure. In order to reduce freestream fluctuations, the boundary layer on the nozzle wall needs to remain laminar. A comparison of the noise radiated into the freestream from laminar versus turbulent boundary layers is shown in Figure 1.3. The shadowgraph is of a cone traveling at Mach 4.3 in a ballistics range. The bottom half of the cone has a turbulent boundary layer, and substantial noise can be seen radiating into the freestream. The upper surface is partially laminar with some turbulent spots. In the laminar regions, the radiated noise is significantly reduced.

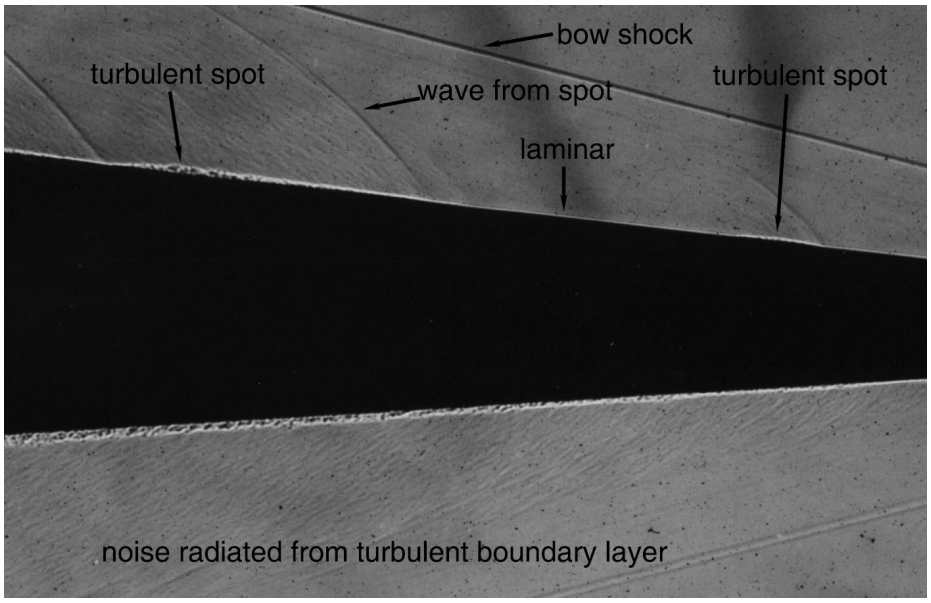

Figure 1.3. Shadowgraph of cone traveling Mach 4.3 down ballistics range. Illustrates the contrast in noise radiated from laminar and turbulent boundary layers. Used with permission from Reference [15].

The design of hypersonic quiet facilities is far from trivial and has been a topic of interest since the 1960s. Typically, wind-tunnel nozzles use either a rectangular (two-dimensional) or axisymmetric cross-sections. Two-dimensional rapid-expansion nozzles were initially thought to be superior to axisymmetric for testing models at large angles of attack and for testing swept wings [16]. However, rectangular nozzles are more sensitive to corner-flow and spanwise pressure gradients, leading to crossflow velocities. The azimuthal uniformity in axisymmetric tunnels can simplify testing conical and cylindrical models. Regardless of geometry, several factors will contribute to transition on the nozzle wall. A few instabilities of note include Görtler vorticity on concave regions, surface-roughness-induced disturbances, and Tollmien-Schlichting waves.

In a 1981 study, Beckwith and Holley experimentally evaluated the Görtler instability impact on nozzle-wall transition using two axisymmetric Mach 5 nozzles [17]. The Reynolds numbers at the nozzle exit ranged from 6.0×10^6 to 25×10^6, using the nozzle-exit diameter for the length scale. One nozzle used a rapid expansion contour with bleed slots in the throat, and the other used a conventional design with a gradual expansion. Bleed slots remove the boundary layer at the end of the contraction and allow a new laminar boundary layer to develop on the highly polished nozzle. The tests controlled the boundary-layer transition location by varying the Reynolds number. When the tunnels transitioned in the concave wall region, the local Görtler number ranged from 5.3 to 6.0. Calculations from linear stability theory on equivalent flat-plate geometries yielded Görtler amplification N-factors from 4 to 15 at transition.

In 1988 Beckwith, Chen, and Malik reviewed the progress on quiet-tunnel development [18]. Tests to determine the maximum allowable roughness height were completed in Mach 3.0 and 3.5 low-disturbance tunnels with the efforts towards designing a Mach 6.0, hypersonic quiet tunnel. By polishing the nozzle, the supersonic tests maintained quiet flow up to 4.7 in. from the throat for a unit-Reynolds number of 2.0×10^6 in.$^{-1}$. Their results suggest that for a Mach 6, low-noise tunnel with

freestream unit Reynolds number of 5.1 $\times 10^5$ in^{-1} the maximum allowable local roughness height is 30 μin in the throat. Additional tests studying nozzle contour showed transition Görtler numbers ranging from 6 to 10 in Mach 3.0, 3.5, and 5.0 tunnels. In order to reduce the Görtler instability, they advised utilizing a long-expansion nozzle contour.

1.5 Computational Work on the Suction Geometry

The present project was performed as part of a collaborative effort involving multiple institutions. Cone-flare geometries to amplify the Görtler instability were computed using STABL2D as part of AAE 624 coursework by members of the BAM6QT lab group. Computations on the Görtler instability were performed by Fei Li and Meelan Choudhari of NASA Langley, who also determined the final model geometry. The final geometry is detailed in Section 2.2. Charles Hollander of the University of Minnesota simulated suction in a Direct Numerical Study (DNS) with the final geometry.

Görtler Instability and Its Control via Surface Suction Over an Axisymmetric Cone at Mach 6

Li et al. performed analyses of the Görtler instability on cones with a concave flare at the aft end [19]. Flow conditions correspond to the maximum quiet condition of the BAM6QT. This is presently a freestream unit Reynolds number of 12.1×10^6 m^{-1}. They performed a parametric study of 13 geometries to maximize the peak Görtler N-factor while preventing flow separation where the model transitions into the flare. The geometric variables checked were the cone half-angle, turn radius, flare radius, axial location of turn, and model length. These parameters are depicted in Figure 1.4.

The mean-flow characteristics for these geometries were computed using NASA Langley VULCAN code. The chosen geometry for the present experiment, Case 9 of

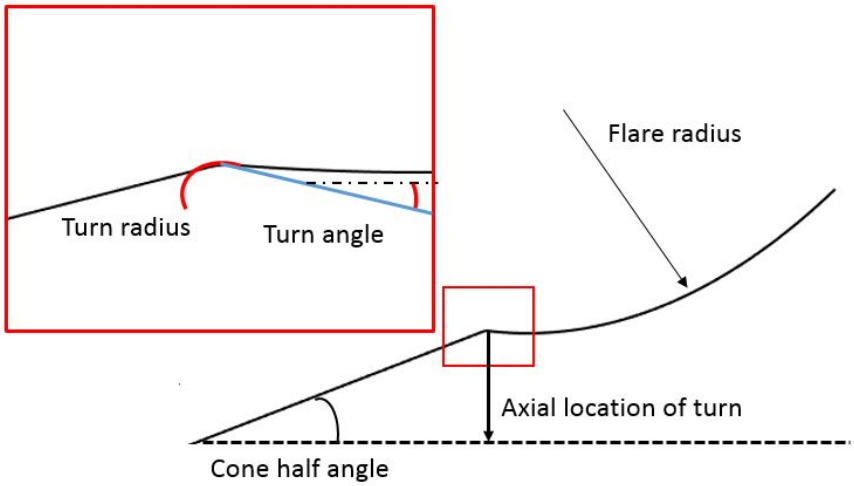

Figure 1.4. Geometric parameters varied in designing the suction geometry.

Table 1 in Reference [19], is detailed in Section 2.2 of this thesis. Figures 1.5 show the model-surface pressure and heat flux from the mean-flow calculations. When the flow expands around the turn at X = 0.293 m, a large drop in pressure and heat transfer is expected. Beyond X = 0.55 m, the compression from the concave flare would result in a shock forming on the model. This led to limiting the length of the experimental model to 0.54 m.

Figure 1.6 shows the Mach number contours for the suction geometry. Above the 7° cone portion, the Mach number is between 5.0 and 5.5 and is fairly constant between the boundary layer and bow shock. Downstream of the turn at X = 0.293 m, the expansion causes the Mach number to increase. Beyond X = 0.55 m, the Mach number near the model surface drops to less than 5.0 due to the shock. The most amplified Mack mode on the flare has an N-factor of 5.6 with a peak frequency of 120 kHz.

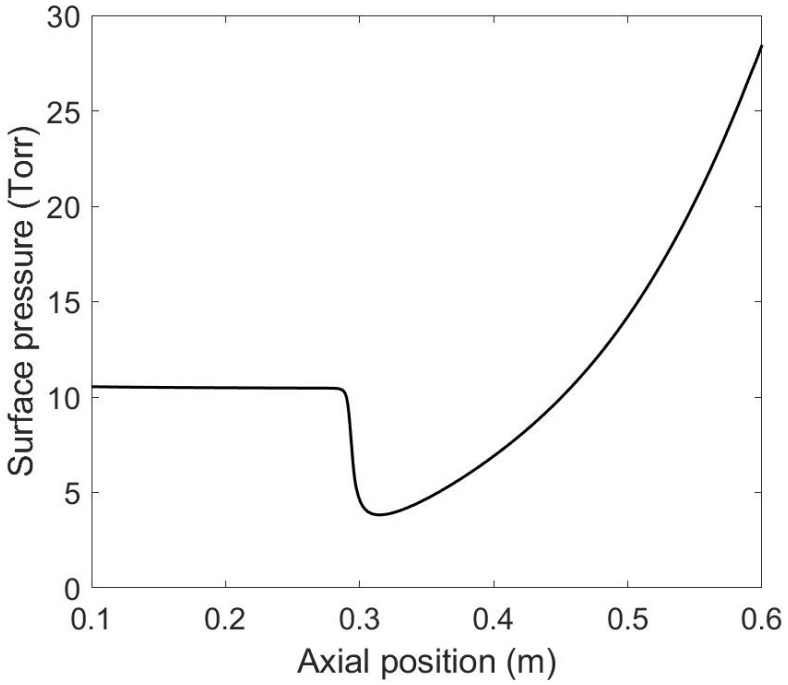

Figure 1.5. Surface pressure distribution on the suction geometry with $\mathrm{Re} = 12.13 \times 10^6$ m^{-1}. Redrawn from [19].

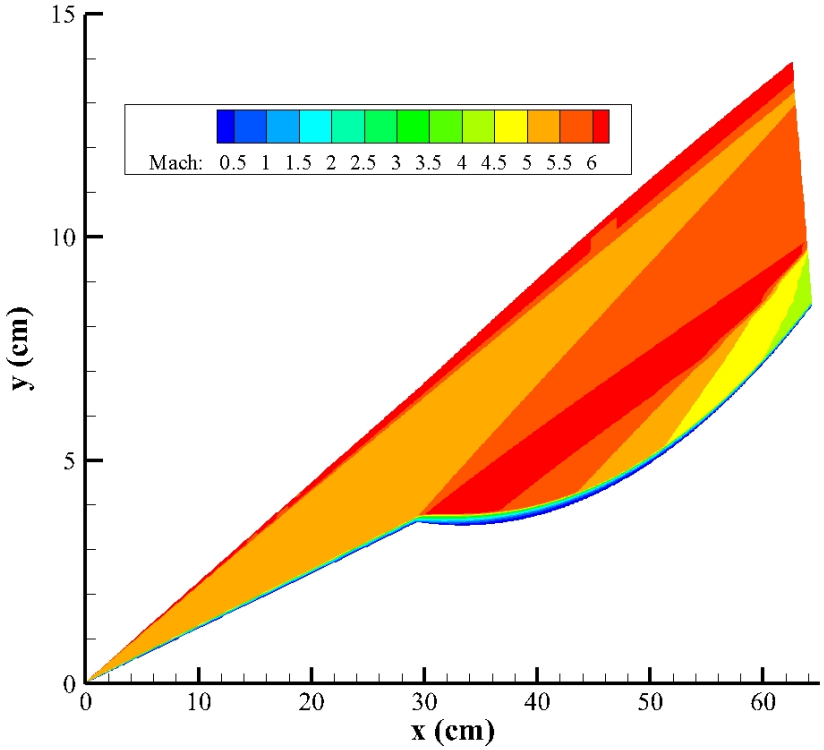

Figure 1.6. Mach number contours on the suction geometry with Re = 12.13×10^6 m^{-1}. Redrawn from [19].

From a stability analysis on the suction geometry, a peak Görtler N-factor of nearly 8 was calculated at the end of the model with an azimuthal wavenumber of 130. The waves have a broad band of azimuthal wavenumbers from 125 to 145 with N-factors greater than 7. The peak Görtler number has a peak of approximately 20 at 0.41 m from the model nosetip. The Mack mode instabilities along the flare were calculated for select frequencies, shown in Figure 1.7. The most-amplified frequency is 120 kHz and has a peak N-factor of 5.5 for $X > 0.47$ m.

The computational study used a roughness array to simulate suction-induced disturbances with an azimuthal wavenumber of 100. The resulting computations showed that both moving the roughnesses farther upstream and increasing their height increase the amplitude of Görlter vortices as they evolve downstream. This suggests the suction should be closer to the flare to reduce seeding the Görtler instability.

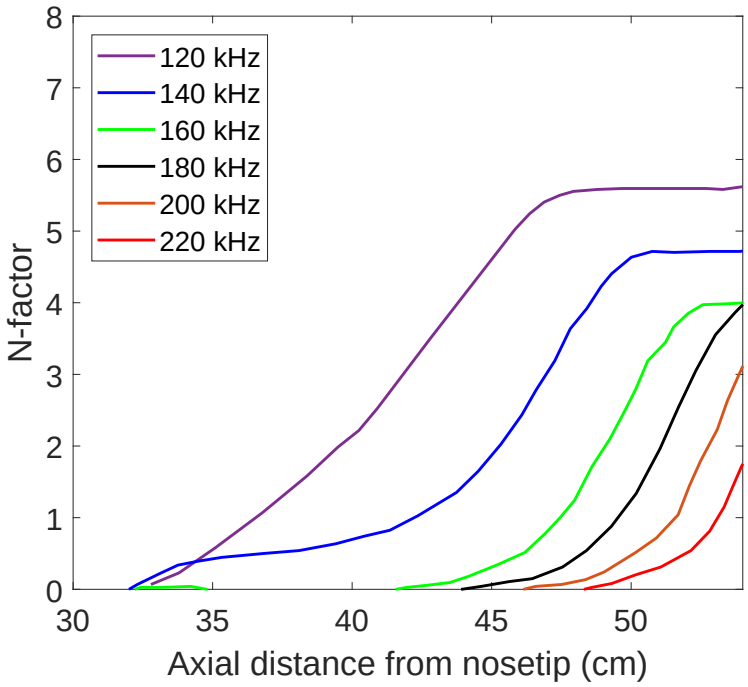

Figure 1.7. Mack mode N-factors along the flare of the suction geometry for $Re_\infty = 12.13 \times 10^6$. Redrawn from Li et al. [19].

Nonlinear Görtler vortices and Their Secondary Instability in a Hypersonic Boundary Layer

Li et al. continued analyses of the Görtler instability on the suction geometry with emphasis on the secondary instabilities [20]. Using DNS, they calculated the secondary instability growth rates for three roughness heights. Similar to their previous work, the flow conditions correspond to a BAM6QT unit Reynolds number of 12.13×10^6 m^{-1}. The equivalent tunnel conditions would be $p_0 = 160$ psia and $T_\infty = 51.92$ K. Their calculations showed that the most amplified, secondary instability of the Görtler is likely a modulated Mack mode (second mode) instability. Specifically for a roughness height of 0.05 mm, the instability has a peak frequency of 130 kHz at an axial location 0.35 m from the model nosetip. Figure 1.8 shows a comparison of the Mack mode and the most amplified secondary instability, called S1 mode, for these conditions.

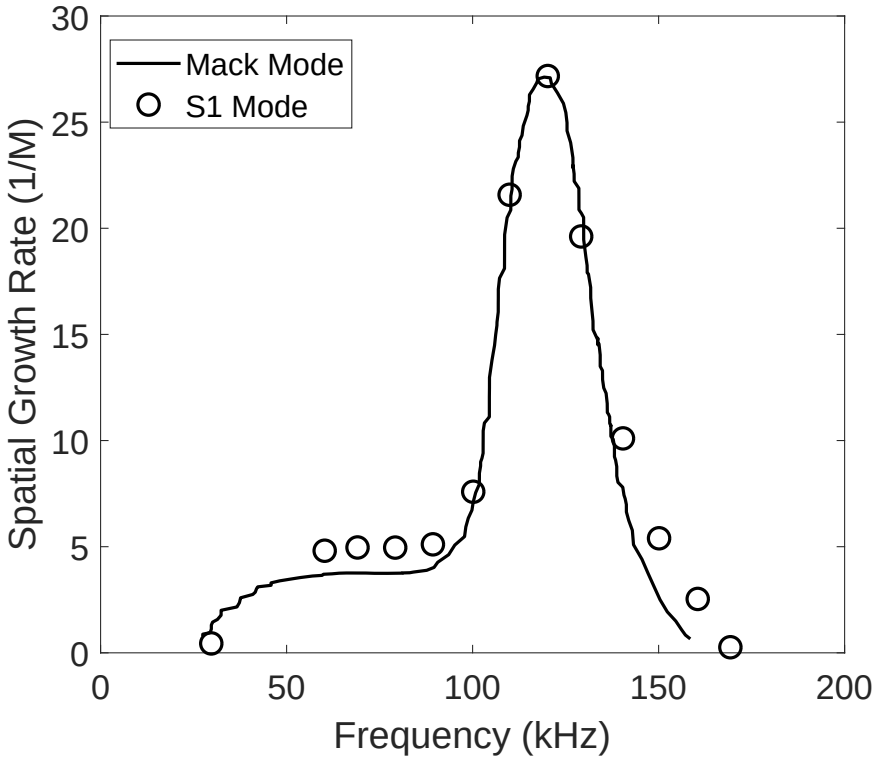

Figure 1.8. Comparison of Mack mode and most amplified secondary instability. Redrawn from Figure 13 of [20].

Response of a Mach 6 Cone-Flare Geometry to Steady Vortical Disturbances: Effect of Steady Suction

Hollender et al. used DNS to calculate the effect of suction on reducing the growth of the Görtler instability for the cone-flare geometry [21]. The base flow used in the calculations was Mach 6 with a unit Reynolds number of 9.0×10^6 m^{-1}. This corresponds to BAM6QT conditions with $T_\infty = 52.6$ K and $p_0 = 122$ psia.

Suction was simulated using a fixed mass flow rate of 0.5 g/s and assumed uniform suction with no wall roughness. The mass flow rate was based on the preliminary design of the suction system which assumed a removal of 50% of the boundary layer on a 7° half-angle cone over the region of suction. The boundary layer was calculated in STABL2D by Josh Edelman. Suction was applied in two regions, one on the cone at $x = 0.2$ m to simulate the experiments in this thesis and the other on the flare with $x = 0.28$ m to simulate suction on curved nozzle.

The calculations showed that suction on the 7° cone portion of the model did not significantly affect the boundary-layer thickness near end of the flare. The Görtler number similarly had an insignificant reduction. However, suction on the flare had a larger impact.

The DNS showed that disturbances were amplified in the regions of suction due to compressing the instability in a thinner boundary layer. The recompression shock at the end of the suction region further amplified the disturbance. However, downstream of the suction, the growth rate of the disturbance is suppressed although not significantly.

2. FACILITY, MODEL, AND INSTRUMENTATION

2.1 Boeing/AFOSR Mach-6 Quiet Tunnel

The Boeing/AFOSR Mach-6 Quiet Tunnel (BAM6QT) is a Mach-6 wind tunnel with low freestream noise. It is a Ludwieg tube design, featuring a long driver tube, an axisymmetric converging-diverging nozzle, and a vacuum tank. A schematic of the BAM6QT is shown below in Figure 2.1.

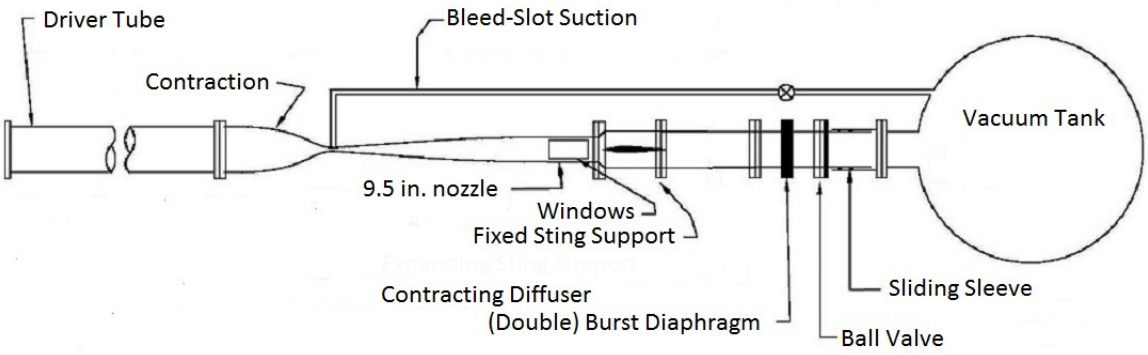

Figure 2.1. Boeing/AFOSR Mach 6 Quiet Tunnel schematic

For each run, the region upstream of the diaphragms is pressurized while the downstream portion is under vacuum. The gap between burst disks is maintained at half the upstream pressure. After the tunnel is filled to the desired pressure, operators wait 10 minutes for temperature gradients and disturbances to settle out. The diaphragm gap is then opened to vacuum, and the diaphragms burst. This leads to an expansion wave propagating upstream into the driver tube. As the wave passes through the throat, Mach 6 flow begins. The expansion continues to the upstream end of the driver tube before reflecting back towards the throat. When this happens,

the stagnation pressure drops by 1-2%, and the wave reflects back up the driver tube. This wave propagation cycles with a period of approximately 200 ms, but between reflections, the flow is quasi-static. The tunnel typically remains started with quiet flow for 3 to 4 seconds.

The BAM6QT maintains a laminar boundary layer on the nozzle wall to minimize noise radiating into the core flow. The throat and diverging sections of the nozzle are polished to a mirror finish to reduce roughness-induced disturbances. In order to minimize the growth of the Görtler instability, the nozzle has a long radius of curvature which slowly expands the flow. Bleed slots in the contraction are used to remove the boundary layer just before the throat, allowing for a new laminar boundary layer to develop on the polished nozzle wall. Currently, the maximum freestream unit Reynolds number for quiet flow is 11.4×10^6 m^{-1} which corresponds to an initial stagnation pressure of approximately 155 psia. A typical initial stagnation temperature is 430 K. At this Reynolds number, the freestream noise levels are on the order of 0.01% [22] and [23]. Alternatively, the tunnel can be operated with bleed slots closed. In this configuration, the flow has freestream fluctuations up to 3% of the mean pitot pressure and a reduction in Mach number to 5.8.

2.1.1 Determining Test Conditions

Prior to a run, the initial total temperature, $T_{0,i}$ is measured from a thermocouple in the driver tube. The total pressure, p_0 is measured both before and during a run using a Kulite XTEL-190-500A pressure transducer in the contraction section. The total temperature during a run is calculated using the isentropic relation,

$$T_0 = T_{0,i} \left(\frac{p_0}{p_{0,i}} \right)^{\frac{\gamma-1}{\gamma}} \tag{2.1}$$

where γ is the ratio of specific heats.

The static temperature, T, and pressure, p, during a run are also calculated via isentropic relations. The viscosity, μ, is calculated using Sutherland's law. With these, the freestream unit Reynolds number, Re, can be calculated using

$$Re = \frac{pM}{\mu}\sqrt{\frac{\gamma}{RT}}. \tag{2.2}$$

In order to determine if the boundary layer is laminar, a Dantec model 55R45 single-element hot film is installed on the nozzle wall. The hot film output is proportional to the shear stress, and when the boundary layer is turbulent, higher voltages are measured. A second method used to monitor the boundary layer is a Kulite ETL-79-HA-DC-190-5A pressure transducer installed near the hot film [24]. The sensor measures the wall static pressure. Voltage spikes are visible when turbulent bursts occur on the nozzle wall. Figure 2.2 shows a sample Kulite trace from a max quiet run.

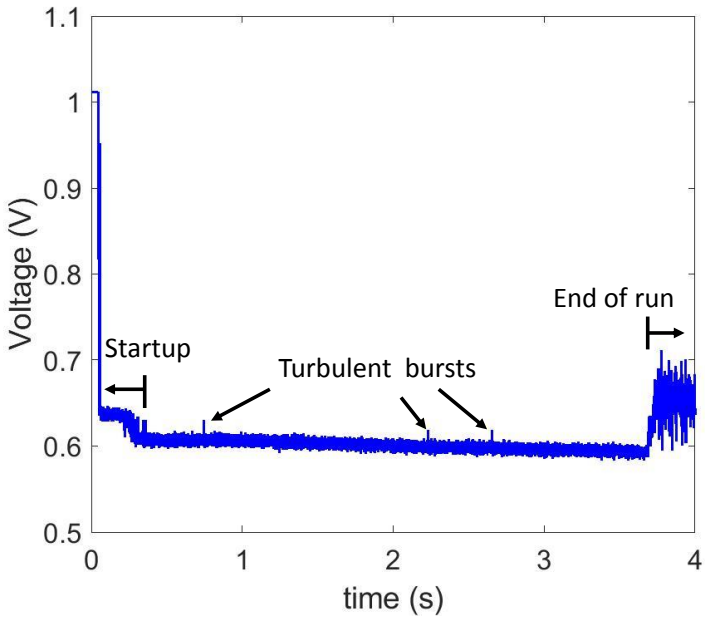

Figure 2.2. Uncalibrated voltage trace from the nozzle-wall pressure transducer for a quiet run with initial stagnation pressure of 155 psia.

2.1.2 Nozzle-Wall Boundary-Layer Separation and Unstart

It is often important to operate the tunnel with the largest feasible model. However, this is limited by the ability to start the tunnel. The BAM6QT has been known to have difficulty maintaining quiet flow with large models. Matt Borg measured 2 seconds of separated nozzle-wall boundary layer in the middle of runs while testing the HIFiRE-5 geometry in the BAM6QT [25]. With the suction model and suction enabled, examples of the nozzle-wall static pressure and hot-film traces are shown in Figure 2.3. The initial stagnation pressure was nominally 155 psia. The nozzle-wall boundary layer separates around 1.68 seconds and reattaches at 2.15 seconds.

During the period of separation, the measured model-surface pressure fluctuations, surface heat transfer, and pitot fluctuations are much higher. Data captured during the separated time are not used.

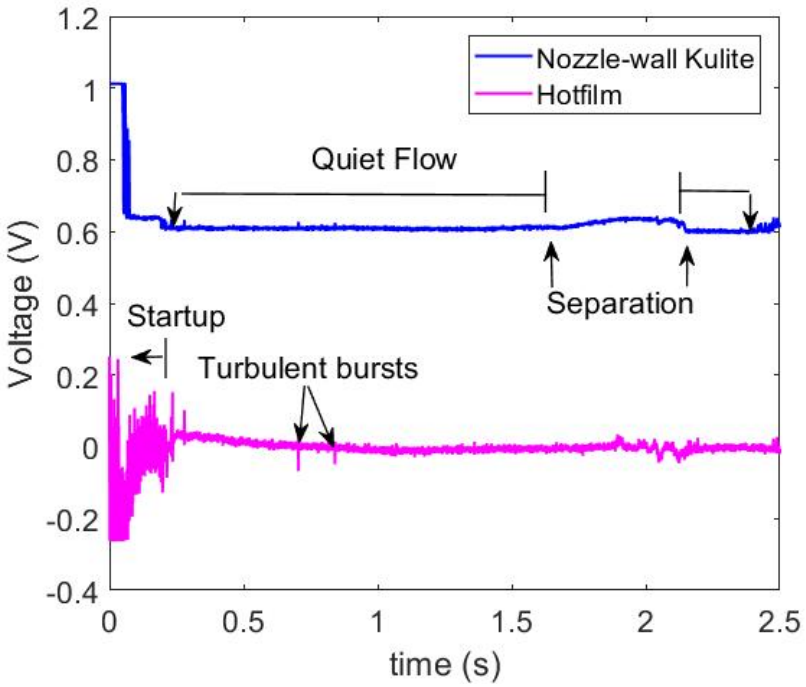

Figure 2.3. Nozzle-wall boundary-layer separation shown in nozzle-wall static pressure and hot-film traces for a suction-enabled run with $p_{0,i} = 155$ psia. Run SS1.17

2.2 Cone-Flare Model

The geometry for the suction project was designed in a group effort by Dr. Fei Li and Dr. Meelan Choudhari of NASA Langley and Purdue. For simplicity, the model is referred to as the suction model. The model design consists of a nominally sharp nosetip followed by a 7° half-angle cone. As shown in Figure 2.5, the actual nosetip radius is approximately 76μm. The nosetip image was taken with a digital camera on a microscope, and the radius was calculated in Matlab. The aft end of the model is a flare with a radius of curvature of 1.0 m. The turn radius from the cone to the flare is 3.0 cm with an initial turn angle of 2° to prevent separation. The flare extends until the model base diameter reaches 11.4 cm. A simple diagram of the model with the original sensor locations numbered is depicted in Figure 2.4. More detailed drawings of the model are available in Appendix B.

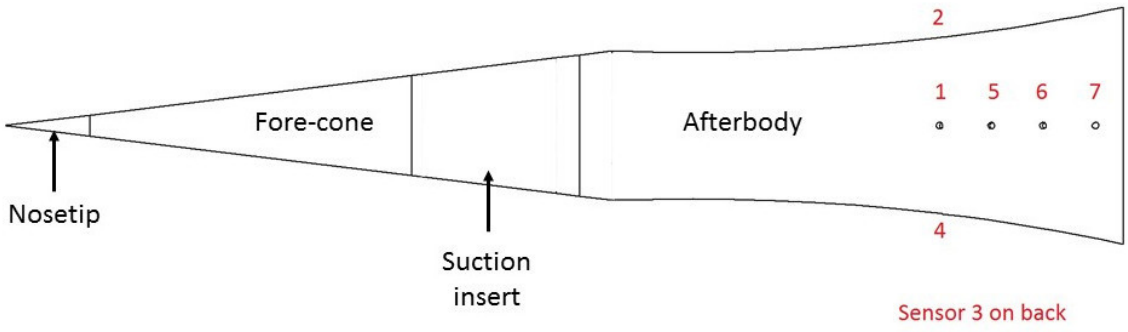

Figure 2.4. Diagram of the cone-flare geometry with the smooth blank for the suction insert installed.

In order to install the suction section, the model is assembled in four pieces. The 17-4PH H900 stainless steel nosetip threads into the fore-cone. The fore-cone is made of Al 6061-T6511 and assembles with the suction section and smooth blank inserts. The smooth, blank insert is also made from Al 6061-T6511. The Al 6061-T6511 after-body consists of the turn and flare.

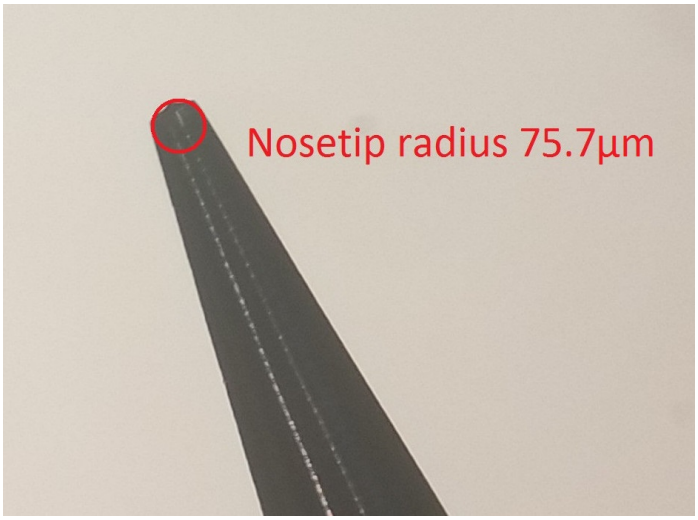

Figure 2.5. Picture of the sharp nosetip taken with a digital camera on a microscope. Radius determined , $r = 76\mu m$ (0.003 in.)

Initially, seven 1/8-inch (0.318 cm) sensor ports were drilled in the flared portion of the model. The hole locations and the installed sensor types are provided in Table 2.1. Four ports are equally spaced around the azimuth located 45.0 cm axially from the nosetip. For an axisymmetric cone at 0° angle of attack, the frequency of the peak second-mode disturbance should be identical around the azimuth. The frequency can be measured via PCB132A31 pressure transducers installed in the four ports evenly spaced around the azimuth. With the adjustable adapter, a full turn of a screw corresponds to a change of 0.11°.

The three additional sensor ports are located 2.54 cm apart axially along the same azimuthal position as sensor number 1. These four in-line sensors are referred to as the main sensor array. Sensor port 6 is used for the Schmidt-Boelter heat transfer gauge (SB). The SB gauge is used to calibrate temperature-sensitive-paint measurements to heat transfer. The remaining ports are used for PCB132A31 sensors to track the growth of the second-mode disturbances along the flare. The model afterbody and baseplate were modified to allow for 7 additional sensors in March 2019. In Table

2.1, these sensor locations are separated from the initial design by a double line. Descriptions of each sensor are available in Section 2.3.

Table 2.1. Surface-sensor locations in the suction model.

Sensor-port Number	**Axial Location (cm)**	Azimuthal Position	**Sensor Type**
1	45.0	0°	PCB132A31
2	45.0	90°	PCB132A31
3	45.0	180°	PCB132A31
4	45.0	270°	PCB132A31
5	47.5	0°	PCB132A31
6	50.1	0°	Schmidt-Boelter
7	52.6	0°	PCB132A31
11	45.0	10°	PCB132A31
12	47.5	10°	PCB132A31
13	50.1	10°	PCB132A31
14	52.6	10°	PCB132A31
15	52.6	90°	PCB132A31
16	52.6	180°	PCB132A31
17	52.6	270°	PCB132A31

The interior of the model is hollow to allow for the suction airflow, as shown in Figure 2.6. A detailed cross-section view is available in Appendix B. The narrower portion has a diameter of 2.25 inch and expands to 3 inches at the aft end. A Kulite ETL-79-HA-DC-190-5A pressure transducer is sealed inside to measure the static pressure in the suction plenum during runs. The sensor is located as shown in Figure 2.7. The sensor is taped to the inside wall of the model to prevent it from shifting during runs.

The base of the model has a detachable plate to access the interior for assembly. The baseplate is Al6061-T6511 and has three 1/4-inch NPT holes that allow sensor wires sealed with Conax Technology compression seal fittings to exit the model. Also, a 10-32 hole in the baseplate allows an additional ETL-79-HA-DC-190-5A sensor to measure the internal pressure of the model during runs. The baseplate has a 7-inch

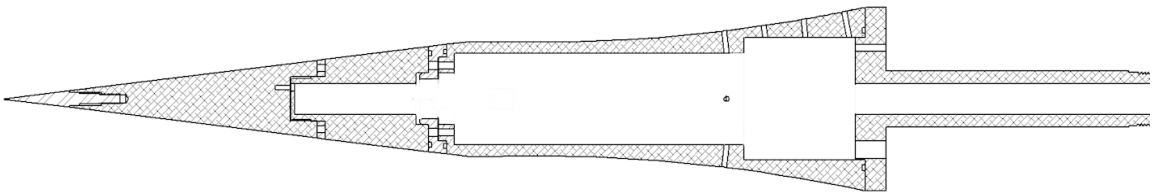

Figure 2.6. Cross section of the suction geometry.

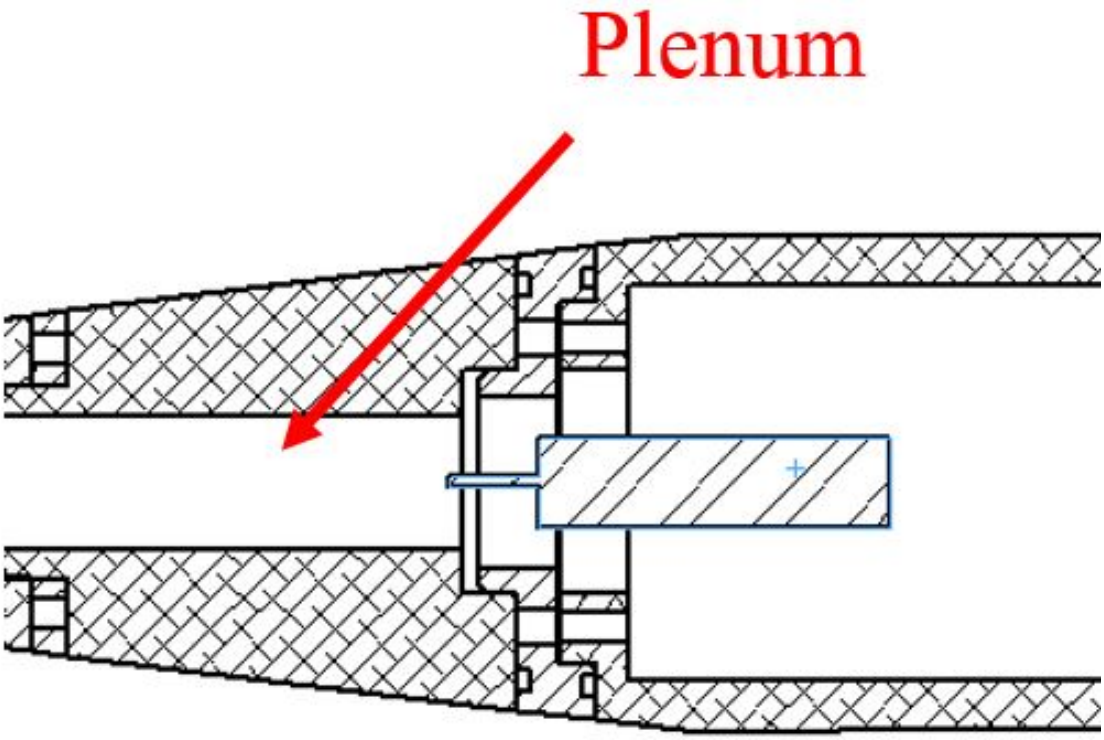

Figure 2.7. Approximate location of the pressure transducer measuring the plenum pressure.

extension that screws into the fine angle-of-attack adapter. A 3/4-inch bore through the extension allows for suction.

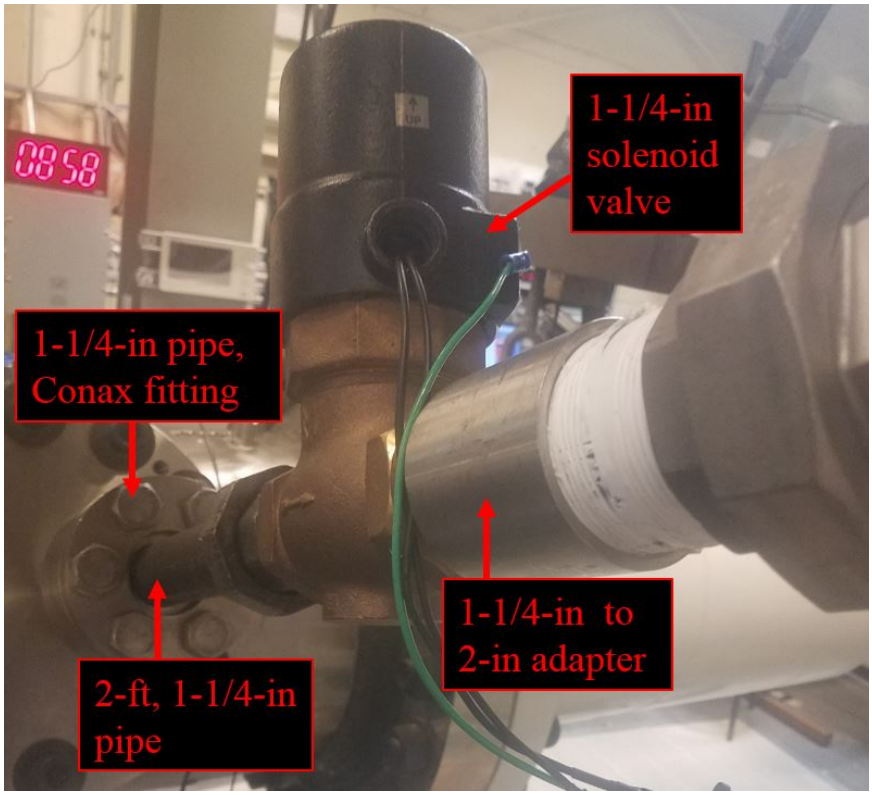

Figure 2.8. 2-ft, 1-1/4-in. pipe passing through tunnel wall

A custom fine angle-of-attack adapter was machined from 4140H alloy steel with a 1-inch bore to allow air flow. Four 3/8-24 screws around the azimuth are used to adjust the model. This adapter mates with a hollow, 17-4PH H900 stainless steel sting which connects to a system of 1-1/4-inch pipes which exits the tunnel. Due to a slight misalignment in one entry, the joint where 1-1/4-inch pipe mates with the sting was sealed with RTV. This pipe system is sealed to the outside tunnel wall via a Conax fitting before assembling with a solenoid valve as shown in Figure 2.8.

2.2.1 Preliminary Work With Inverse-Flare Geometry

An earlier iteration of the suction model featured a 7° half-angle cone that merges into an inverse flare, as shown in Figure 2.9. STABL computations were performed on the geometry and experiments were performed by Viswanathan and Wason [26].

It was shown that the Mach-6 nozzle-wall boundary layer was separated during quiet runs. Additional experiments were performed with the model, but the tunnel never successfully started.

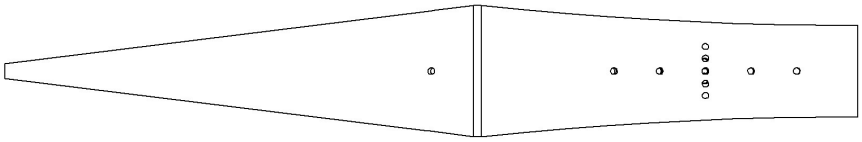

Figure 2.9. Diagram of the inverse-flare cone geometry.

2.2.2 Suction Sections

Five suction sections were designed for this project. Each test article consists of a titanium plenum onto which a perforated skin is electron-beam welded. Beneath the suction skins is a chamber of throttling holes meant to reduce mean-suction irregularities. The plenum design, machining, and assembly was completed by Calspan. The concept design is shown in Figure 2.10. The perforated, titanium skins were laser-drilled by CAV Advanced-Technologies, Consett, United Kingdom (CAV-AT) with hole patterns designed in a joint effort between Dr. Steve Schneider, Dr. Meelan Choudhari, and Mark Romero of CAV-AT. The skins were then rolled and electron-beam welded to the plenum by Calspan and its contractors.

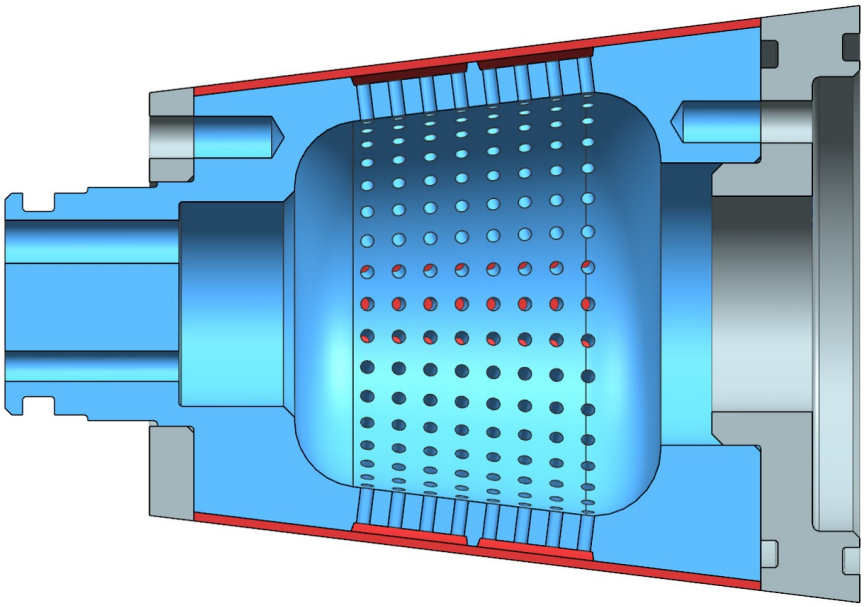

Figure 2.10. Drawing of suction section plenum (blue) with fit-rings (gray) and the suction skin (red) provided by Calspan

The five hole patterns are described in Table 2.2 with images of each in Figure 2.11. The laser-drilled pores of each suction section are nominally 50 micron. For SS.1 the pores were drilled along densely-packed, straight lines. SS.1 would establish a base for suction measurements with the laser-drilled micro-perforations. SS.2 was designed to be a higher porosity version of the first pattern. The higher porosity may remove more of the boundary layer and further suppress instabilities. Removing more of the boundary layer may also increase the strength of acoustic disturbances radiated into the flow, though. The pores of the SS.3 were drilled along densely packed arcs that span the cone circumference. As the optimum pore layout is unknown, a controlled layout is useful to compare with SS.2. The pores from SS.4 were drilled along rays from the cone vertex with 1.5° spacing. This was designed to seed the Görtler instability with an azimuthal wavenumber of 120, but the piece was damaged during production, as described later in this section. SS.5 was designed to taper the porosity near the leading and trailing edge. The porosity at the edges would be 20% of the peak porosity in the center. As the sudden change in boundary-layer thickness

Table 2.2. Hole patterns of the suction sections with CAV-AT-measured Percent Open Area (POA).

Suction Section	**Hole configuration**	**POA**	**Reference figure**
SS.1	straight lines	3.5%	Figure 2.11(a)
SS.2	straight lines	8.04%	Figure 2.11(b)
SS.3	azimuthal arcs	8.36%	Figure 2.11(c)
SS.4	rays from vertex	2.03%	no figure available
SS.5	Tapered-porosity, azimuthal arcs	6.06%	Figure 2.11(d)

at the edges of suction could create strong Mach waves, tapering the porosity there might weaken the radiated waves. The pores were drilled along azimuthal arcs similar to the third layout.

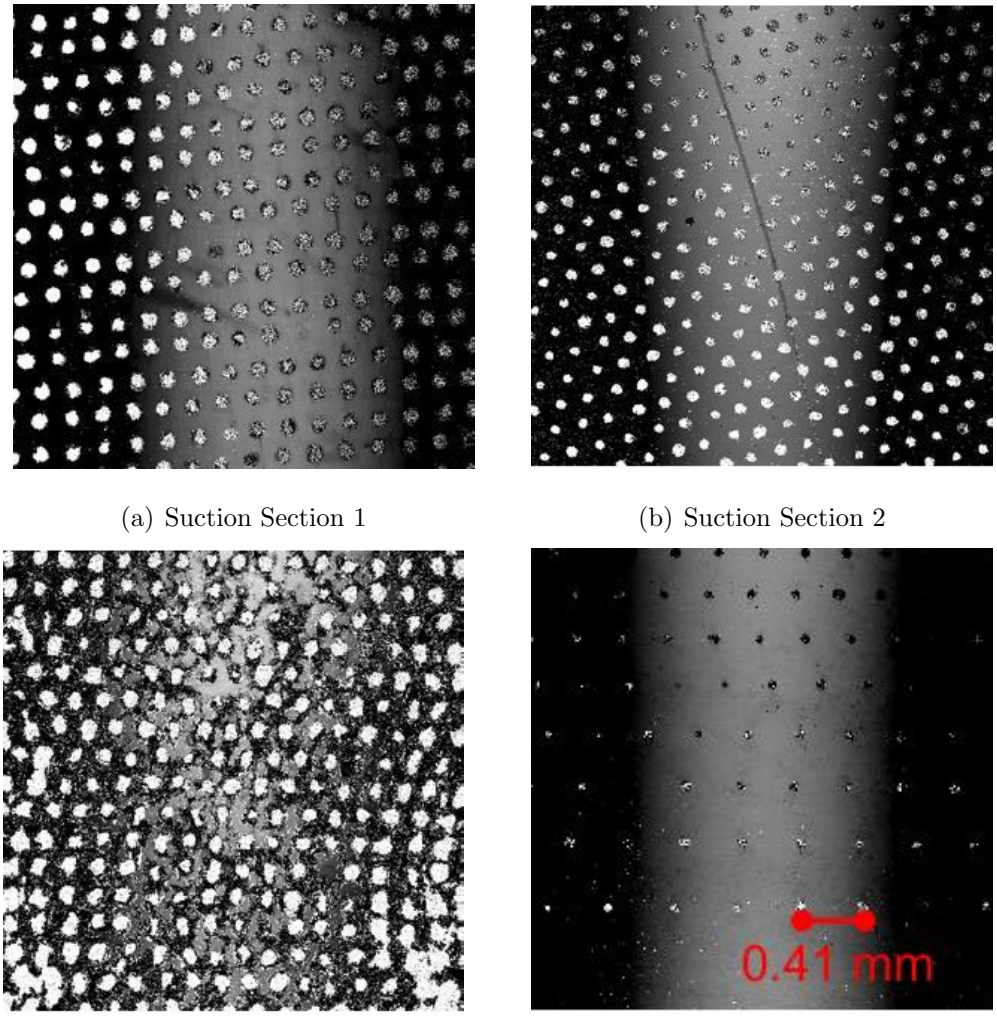

(a) Suction Section 1

(b) Suction Section 2

(c) Suction Section 3

(d) Suction Section 5

Figure 2.11. Images of the four perforation patterns captured with a Zygo ZeGage optical profiler. The scale shown with Suction Section 5 is valid for all four images.

2.2.2.1 Measuring Porosity of Suction Sections with Zygo

The suction sections were mounted with the surface perpendicular to a Zygo ZeGage Optical Profiler, as shown in Figure 2.12. Depth-map images were captured with magnifications of 2.75X and 10X. The 2.75X lens measures a 3.0 mm $\times$ 3.0 mm region, and the 10X measures a 830 μm $\times$ 830 μm section. Each suction section was imaged in three locations on the surface. The imaged locations were chosen arbitrarily in different axial and azimuthal positions. The 10X lens was used to make more accurate measurements of pore diameter, and the 2.75X lens was used for porosity approximations.

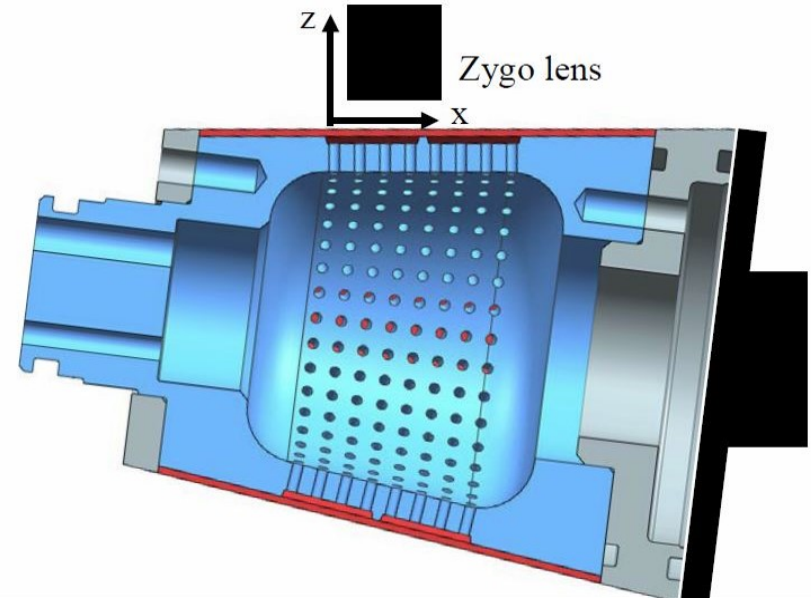

Figure 2.12. Suction section mounted for measurements with the Zygo ZeGage Optical Profiler

The depth-map images are processed in Matlab to allow for feature recognition. The image is post-processed with the following steps to count the number of the pores in the images:

- The background noise is removed from the image.
- The image is binarized with a 50% threshold.

- Using Matlab's Circular Hough Transform, most pores in an image can be recognized.

As some pores were missed or interpreted as two or more, the image's pore count was updated after manually reviewing the processed image. Figure 2.13 shows a sample image of the porous skin at different stages of image processing. An output of the Circular Hough Transform is the circle radii. The pore diameter for each suction section is calculated as the mean of the circle radii for an image taken with the 10X lens.

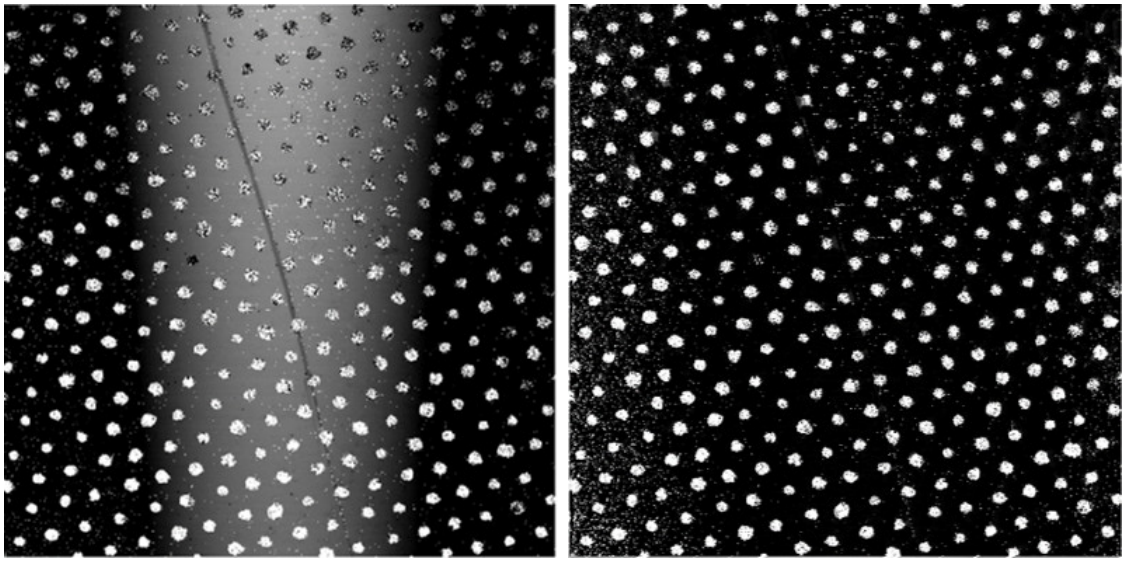

(a) Raw image

(b) Background removed

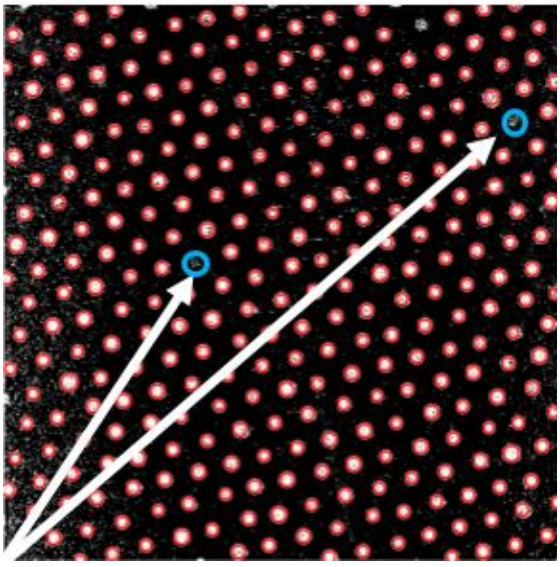

(c) Fully processed, unrecognized pores called out

Figure 2.13. Three stages of how pores were counted for calculating porosity of the suction sections. Shown is Suction Section 2.

The resulting measured porosities are provided in Table 2.3.

Table 2.3. Measured physical characteristics of suction sections

Suction Section	Mean pore diameter (μm)	Std. Deviation of diameter	Calculated Porosity (%)
SS.1	85.9	9.22	12.0%
SS.2	63.2	2.66	11.1%
SS.3	84.5	10.6	16.5%
SS.5	61.0	2.79	12.9% (at center)

As the porosity of Suction Section 5 tapers at the beginning and end, nine images were taken from the leading edge of pores to the peak porosity along a single ray from the cone vertex. The last row of holes in each image captured was the first row of holes in the following position as shown in Figure 2.14. The measurements were made approximately every 2.8 mm. Table 2.4 lists the measured porosity in each of these nine images.

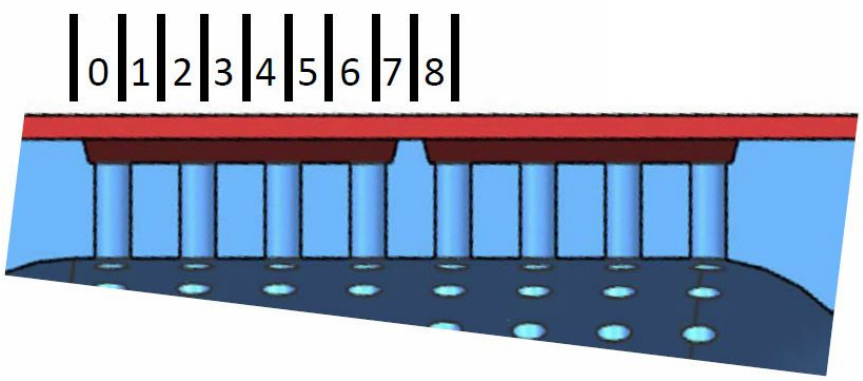

Figure 2.14. Approximate locations where porosity is measured along the Suction Section 5. The measurements were made approximately every 2.8 mm.

Table 2.4. Measured porosity along Suction Section 5. Measurements were made approximately every 2.8 mm

Position along taper	**Porosity (%)**
0 (front)	3.25
1	7.94
2	12.59
3	12.73
4	12.83
5	12.91
6	12.95
7	12.87
8	10.96

Roughness with Suction Section 3 Perforated Skin

Shown in Figure 2.15(a), the surface profile for Suction Section 3 shows substantial roughness between the pores. For comparison, Figure 2.15(b) depicts the surface profile of Suction Section 2 also measured with the 10X Zygo lens. Suction Section 3 has peak-to-valley height differences of up to 1 mil between pores while Suction Section 2 is nominally smooth. As the roughness significantly increased the background noise, pore recognition was difficult, and the porosity of Suction Section 3 may not be accurate.

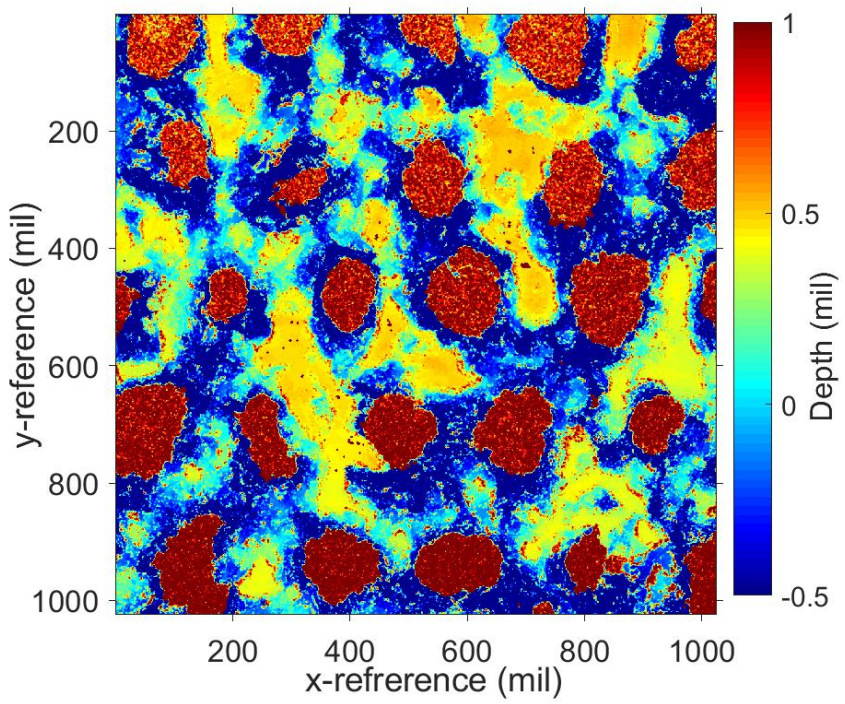

(a) Suction Section 3, significant surface roughness

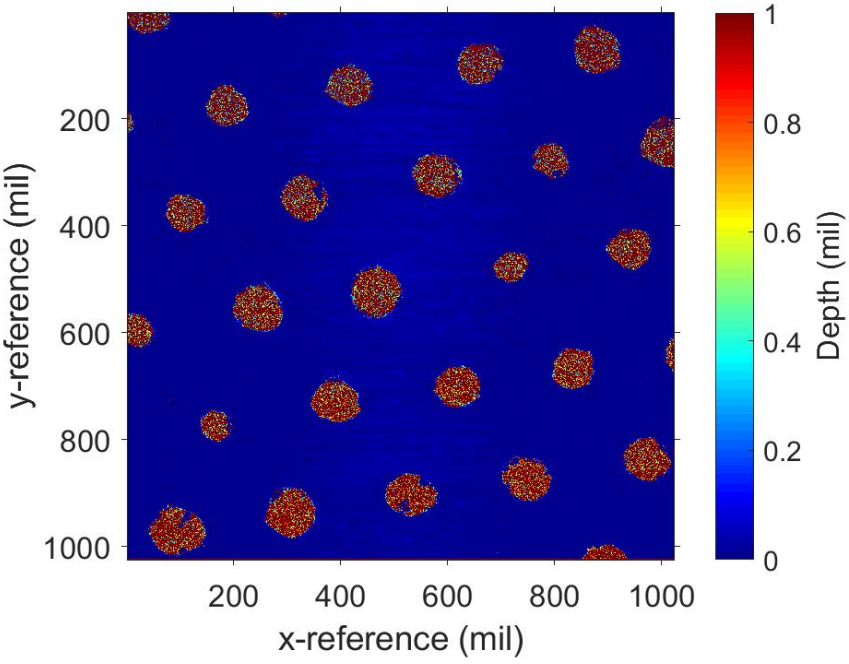

(b) Suction Section 2, no noticeable roughness

Figure 2.15. Comparison of the surface roughness of Suction Sections 3 and 2. SS.3 exhibits roughness of up to 1 mil peak-to-valley, while SS.2 shows no noticeable roughness.

Damage to the Suction Section 4 During Production

During the rolling process to shape Suction Section 4 into a 7° half-angle cone, the skin was split along the rays of perforations. This is shown in Figure 2.16. This was believed to result from the closely packed holes being drilled along radial rays creating lines of weakness. During rolling, the skin was stretched along the lines and led to cracks developing along the lines of holes. Should this section be remade in the future, an alternative design may be required.

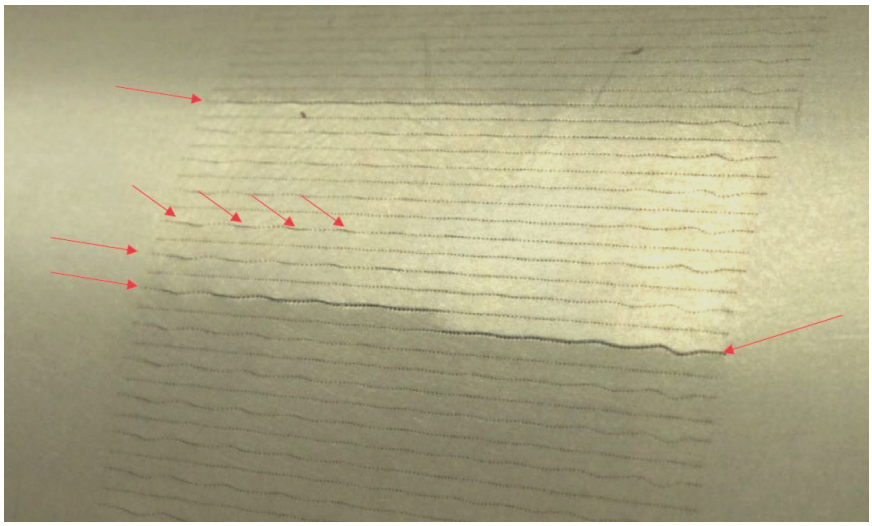

Figure 2.16. Damages to perforated skin of Suction Section 5. Arrows point to regions of cracking along the rays. Photo provided by Calspan.

Load Testing the Suction Sections

Before testing with the model, Suction Section 1 was load tested in the BAM6QT to ensure the weld on the perforated skin would not break during runs. The test was implemented by mounting the suction section in an aluminum cup that directly connected to the sting. The sting was installed so that the cup was facing the downstream direction in the tunnel. The elbow adapter was attached to the upstream end

of the sting to prevent it from slipping. The tunnel was run at 160 psia. Should the perforated skin rupture during the test, the cup would protect the tunnel from damage. A picture of the cup is shown in Figure 2.17 with Suction Section 1 installed.

No damage was found while inspecting the suction section after the test. Suction Sections 2, 3, and 5 have not been tested.

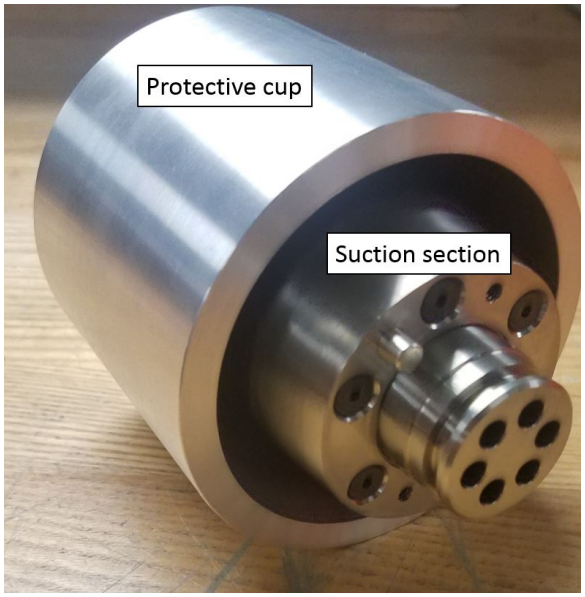

Figure 2.17. Protective shield for use in load testing the welds on the perforated skins. Installed in the cup is Suction Section 1.

2.3 Instrumentation and Data Reduction

2.3.1 Oscilloscopes

Data collected in these experiments were recorded using a combination of Tektronix DPO7054, DPO7014, and DPO3014 oscilloscopes. The scopes sampled all signals at a minimum of 2 MHz. The oscilloscopes were set to Hi-Res mode which both improves the vertical resolution by sampling at the maximum rate, and digitally averages acting as an anti-aliasing filter.

2.3.2 PCB132A31 Piezotronics Pressure Sensors

The PCB132A31 fast pressure transducer, subsequently referred to as a PCB, is manufactured by PCB Piezotronics Inc. It is used in the BAM6QT to measure high-frequency pressure fluctuations in the boundary layer. The sensor contains a piezoceramic sensing element in a stainless-steel housing sealed with epoxy. The sensors are 0.125 inches in diameter and 0.3 inches long. The newer model of this sensor, the PCB132B38, was not used in this project.

If the steel housing is in contact with the aluminum model, electrical noise can be introduced to the output signal. Nail polish is used to both create an electrically insulating layer between the sensor and model and to adhere the sensor to the model. Due to the vacuum inside the model, a layer of room-temperature-vulcanizing silicone is used to prevent the sensor from being pulled into the model.

The outputs of the PCBs are AC-coupled and sampled between 2 and 5 MHz. The PCB voltage signals are converted to pressure using the factory calibrations. The frequency response of PCBs are not well understood, and multi-point calibrations are being pursued at Purdue University [27].

The fluctuations are normalized with the model-wall pressure. The wall pressure was calculated as part of Li et al.'s computations on this geometry with NASA Vulcan [19]. When processing the signal from PCBs, a power spectral density (PSD) is used to describe the averaged power of the measured fluctuations. The PSDs are calculated using Welch's method with a Hamming window over a duration of 0.05 seconds, a frequency resolution of 2 kHz, and a 50% overlap between segments.

When calculating the magnitude of the second-mode instability, the root-mean-square (RMS) amplitude of the pressure fluctuations was calculated by taking the square root of the integrated PSD for a range of frequencies. Unless otherwise noted, the frequency range used for these RMS calculations was 70 to 180 kHz. Shown in Figure 2.18 is the frequency band used for RMS pressure-fluctuation calculations, between the dashed lines. The PSD shown is from a PCB located at $x = 47.5$ cm with

$Re = 11.3\times10^6$ m^{-1} with the smooth insert. The lower limit was chosen as non-second mode pressure fluctuations were measured from 0 to 60 kHz, and it was desired to isolate the second-mode peak. The upper limit was picked to cut off the harmonic of the second mode.

The peak frequency of the second mode was chosen to be the apparent center of the peak in the PSD. A more consistent approach to determining the peak was not achieved.

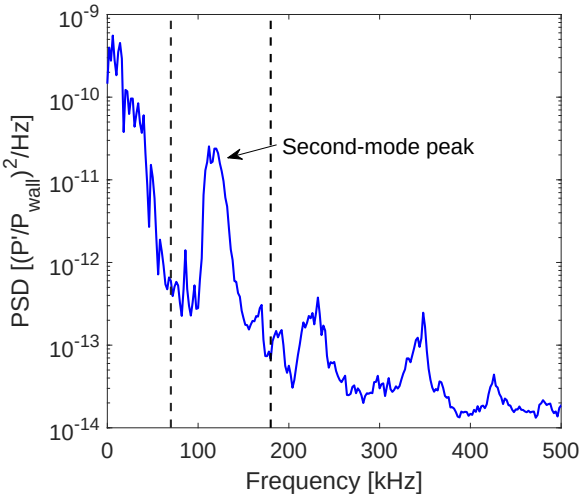

Figure 2.18. Frequency band used for RMS pressure-fluctuation calculations.

2.3.3 Kulite Pressure Transducers

Three different models of Kulite pressure transducers were used.

A Kulite XTEL-190-500A is permanently installed in the contraction section of the BAM6QT to measure the stagnation pressure during runs. The sensor functions up to 500 psia and has an operating range from -55°C to 273°C [28]. The contraction Kulite is DC coupled, and the sensor is calibrated with each entry. The output is converted to mean pressure from this calibration.

A Kulite XCE-062-15A, ultra-miniature pressure transducer is used in the traverse probe to measure acoustic radiation above the suction section. The traverse probe is

described in Section 2.3.4. The diaphragm has a protective screen over it, called a B-screen, consisting of a circle of eight holes with a diameter of 0.15 mm. The sensor operates up to 15 psia and in a temperature range from −55°C to 273°C [29]. The sensor has a outer diameter of 0.066 in. The sensor is used to measure both the mean pitot pressure and the pitot fluctuations.

The XTEL and XCE voltage signals pass through a custom-built conditioning box to power the sensors and apply a gain to the signal. The box outputs the DC-coupled signal amplified with a gain of 100. The sensors are calibrated according to this output with each entry. The DC-coupled output is used to calculate the mean pitot pressure. For use with small fluctuations expected during quiet runs, the box outputs the high-pass filtered signal amplified with a gain of 10,000. The high-pass filter is set at 840 Hz.

Two Kulite ETL-79-HA-DC-190-5A sensors are installed in the suction model to measure the internal static pressure during runs. This sensor is mechanically stopped at 5 psia and has a quoted accuracy of ±0.005 psia in a temperature range from −55°C to 273°C [30]. The sensor has a response time of 3.5×10^{-5} seconds [31]. These sensors are calibrated using a Ceravac 101N 100-Torr vacuum pressure gauge before each entry. The outputs are DC-coupled and sampled at 2 MHz. The uncertainty of the plenum pressure at a specified time is calculated using

$$U_p^2 = s_p^2 + accuracy^2. \tag{2.3}$$

The variable U_p is the magnitude of the uncertainty, *accuracy* is the quoted sensor accuracy, and s_p is the sample standard deviation of the plenum pressure measured within an arbitrarily chosen ±0.05 seconds of the specified time.

2.3.4 Probe Traversing System

The traverse system moves a probe through the freestream above the model. A Kulite XCE-062-15A, B-screen pressure transducer is installed in the probe to measure pressure fluctuations in the flow. It is important to note that the fluctuations

measured by the transducer have to pass through a bow shock on the front of the probe. The traverse uses an Aerotech model BMS280 motor to move the probe along a Parker rail-positioner. The motor can move the probe in increments of 0.5 μm and is accurate to 20 μm [23]. The maximum speed is 0.241 $\frac{\text{m}}{\text{s}}$. The motor is controlled via an Aerotech-A3200 power supply and the Aerotech motion-composing software. A script used to cycle the probe position during runs is provided in Appendix D. The axial location of the probe is set via a ball screw and ruler. The ruler has a precision of 0.5 mm. The axial position is set by visually aligning the pitot probe with the fit ring on the plenum insert. A labeled picture of the traverse system is shown in Figure 2.19.

The traverse is mounted on the tunnel above a 12.5-inch slot in the last section of the nozzle. This slot allows for tunnel-axial-location adjustments to be made between runs. The slot is sealed by compressing a brass bar around O-rings on the three probe struts.

The probe struts are clamped into the rail-positioner. As shown in Figure 2.20, the rods are attached to a brass double wedge. The pressure transducer is mounted in a strut that is angled 7° below the horizontal. The sensor-mount diameter is 0.125 in. and has a rounded face. When processing the fluctuations, the signal is normalized by the mean pitot pressure before computing the PSD. Similar to the PCBs, the PSD is calculated using Welch's method with a Hamming window over a duration of 0.05 seconds and a 50% overlap between segments. However, the frequency resolution used is instead 1 kHz. When calculating the RMS amplitude of the pressure fluctuations, the frequency band ranges from 0 to 100 kHz. This frequency range was chosen as a peak appeared in some measurements between 50 and 100 kHz. Pitot measurements in the freestream and above a cone made by Gray were processed from 0 to 50 kHz [23].

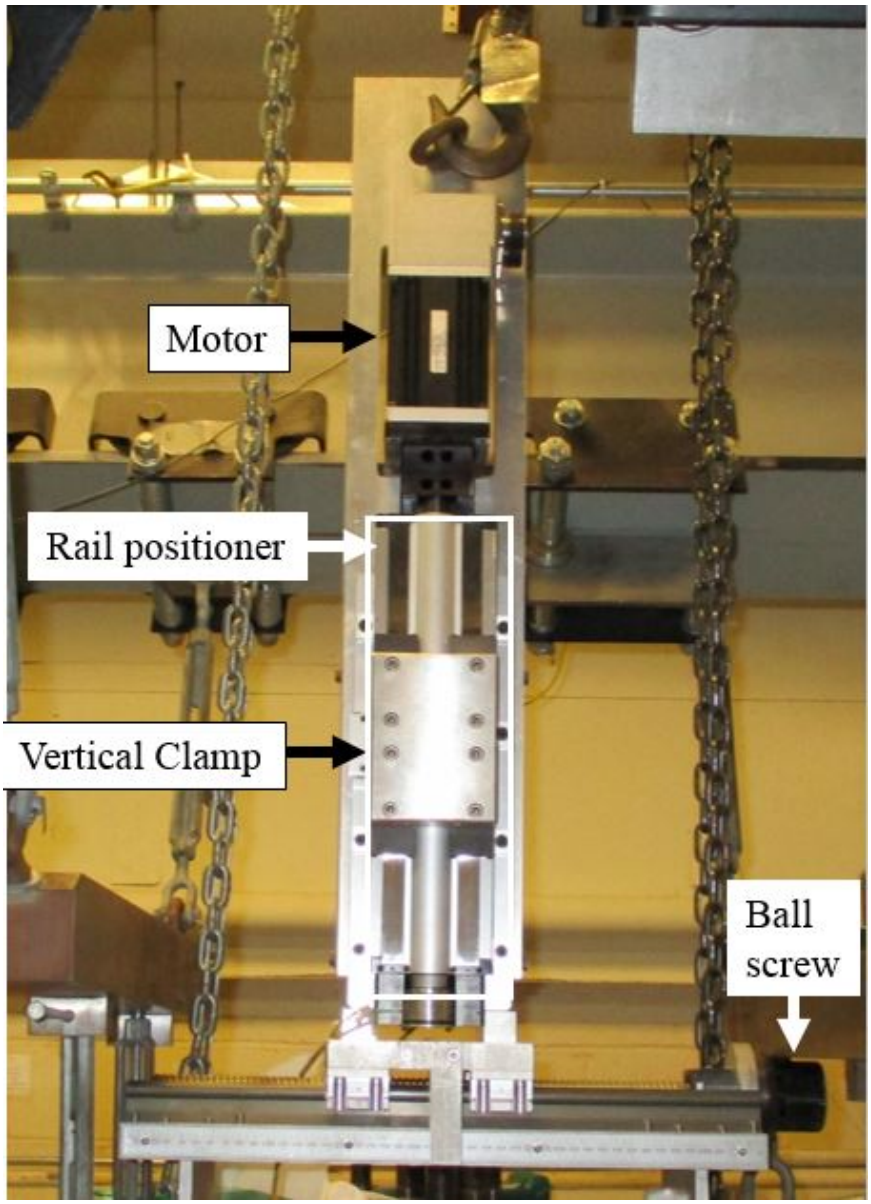

Figure 2.19. Traverse motor and rail positioner mounted on top of the BAM6QT.

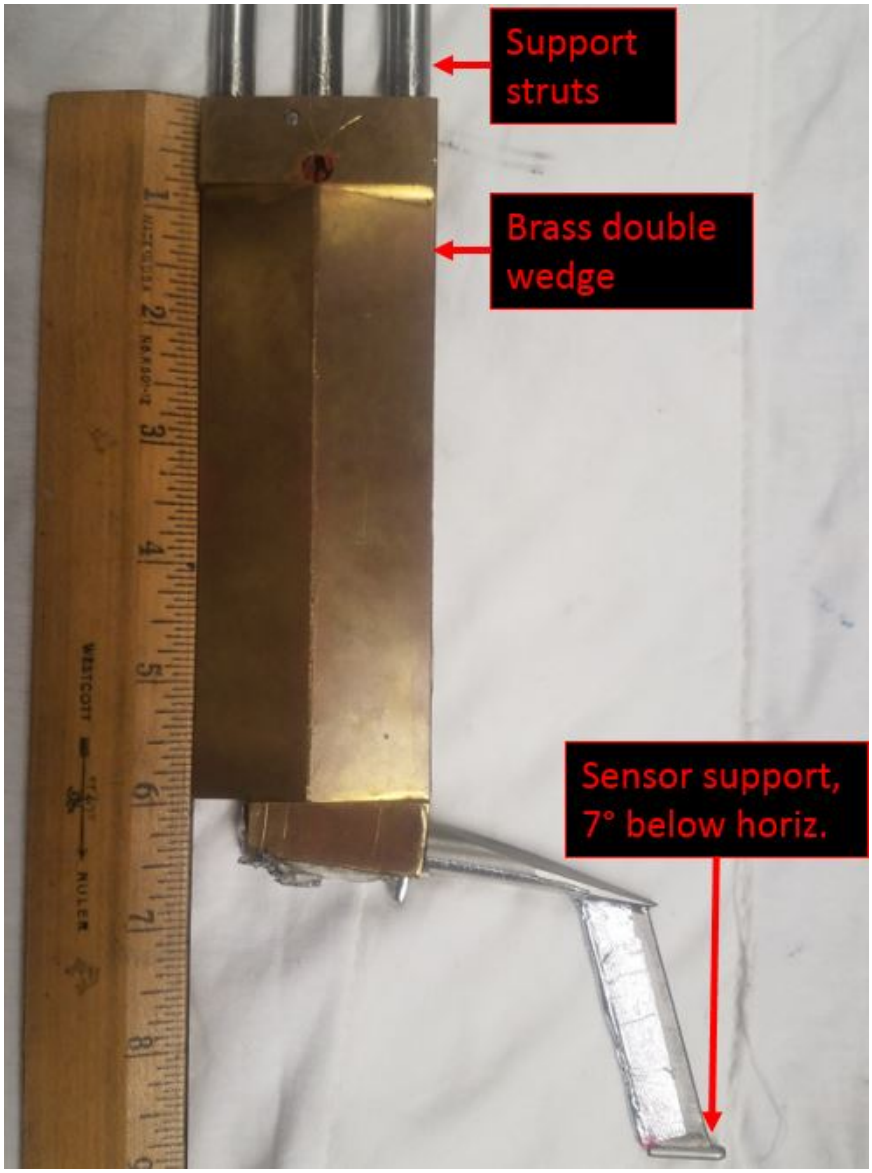

Figure 2.20. Kulite probe mount used to measure pressure fluctuations in the freestream above the model.

Traverse Sweep Locations

Measurements were made in four different axial locations relative to the model nosetip and nine positions above the model in each axial location. The axial locations were 26.9, 28.9, 31.5, and 34.8 cm from the nosetip. The positions were chosen to make measurements immediately downstream of the suction section (26.9 cm) and at semi-regular intervals with increasing downstream position. The vertical positions were nominally 1, 3, 5, 10, 15, 20, 25, 30, and 35 mm above the surface. The 1 mm position was set by lowering the traverse until the probe visually touched the model surface. The probe centerline is 1.6 mm from the outer edge. The remaining vertical positions were controlled by the traverse motor. Figure 2.21 depicts the nominal, streamwise probe locations where measurements were made. Figure 2.22 shows the vertical positions. The depicted angle of the oblique shock was calculated via Taylor-Maccoll. The Mach lines from the start and end of the suction were calculated by Li et al. based on the full mean flow. Figure 2.23 shows a picture of the pitot probe in the tunnel above the model.

The current method of determining the probe position makes it easy to introduce error into the vertical position measurements. It was found that in early entries a set screw was missing from the probe support. When the probe was lowered to touch the model to set the zero position, it could deflect. Additionally, the zero position was set for each axial location.

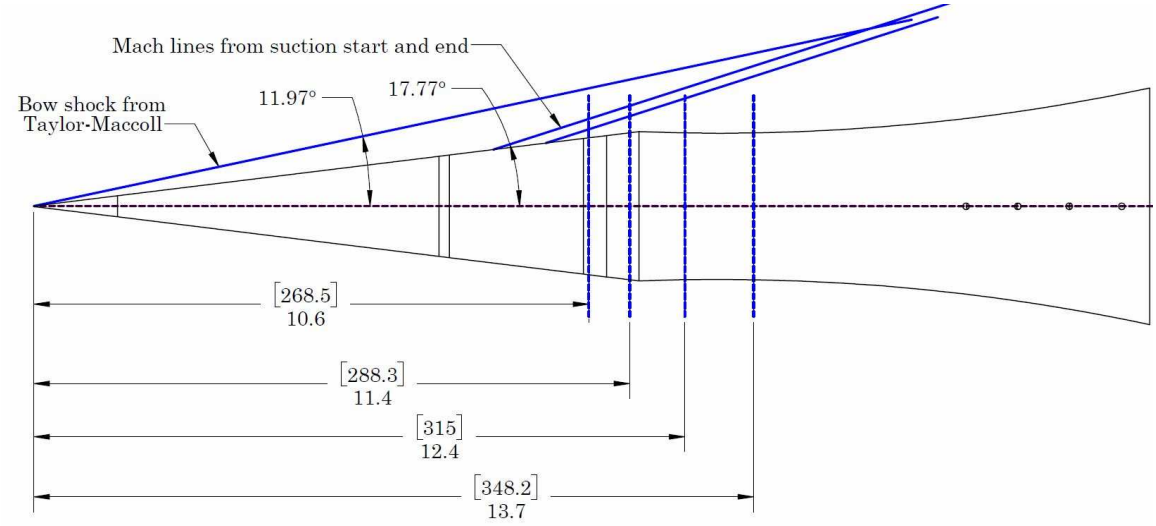

Figure 2.21. Depiction of locations above the model where data was captured by the pitot probe.

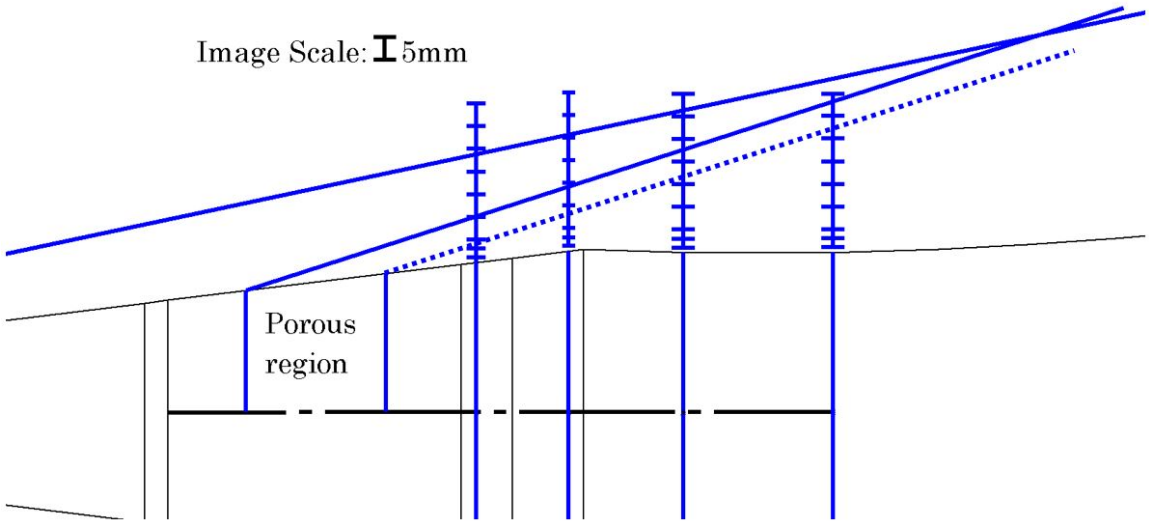

Figure 2.22. Close-up of the traversed positions

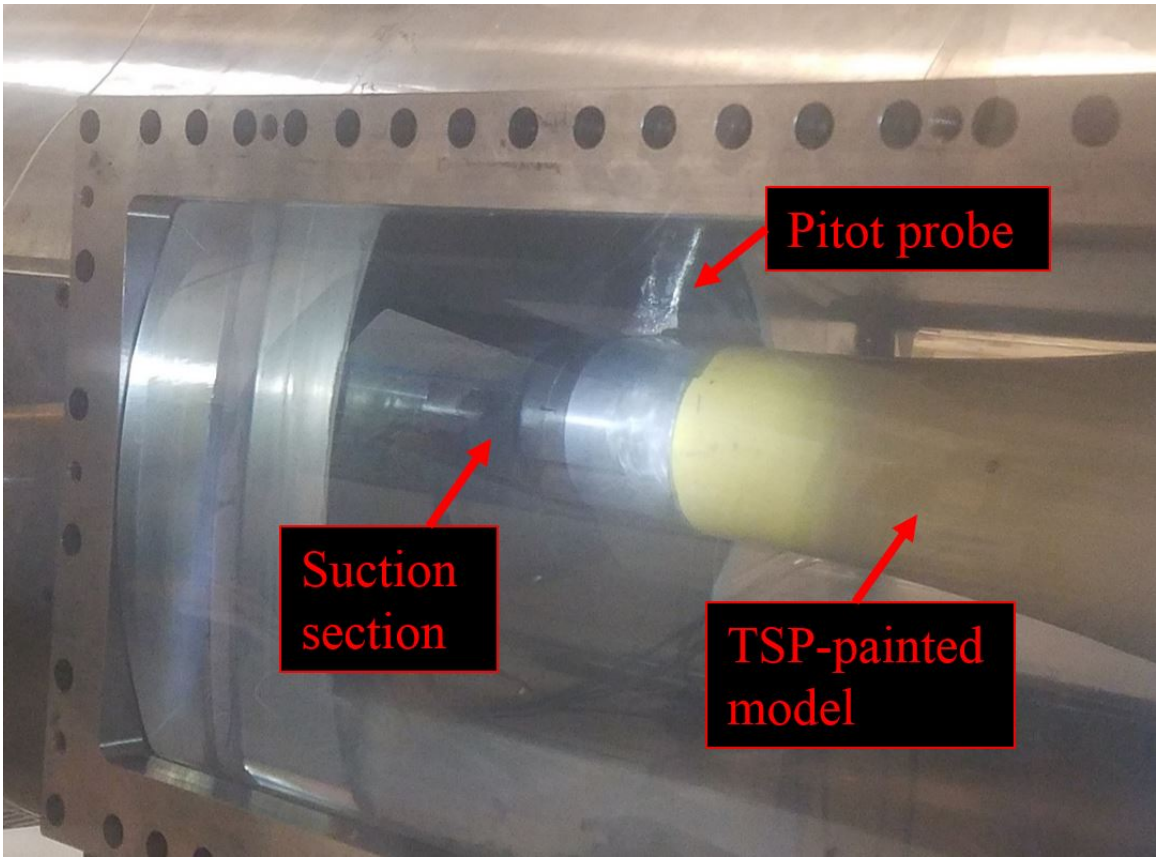

Figure 2.23. Pitot probe in tunnel above the model. Probe located 26.9 cm from nosetip.

2.3.5 Schmidt-Boelter Heat Transfer Gauges

A Medtherm Corporation model 8-1-0.25-48-20835TBS Schmidt-Boelter (SB) gauge was used to measure the local heat transfer on the model surface. This is used to calibrate the temperature-sensitive paint to global heat transfer. An SB sensor uses a stack of thermocouples, called a thermopile, housed in a copper shell. The shell is coated in a conductive, black epoxy to maximize absorption. The sensor diameter is 0.125 inches. The sensor uses T-type thermocouples, and the factory calibration is used to convert to heat transfer. The heat transfer data was low-pass filtered at 30 Hz and amplified with a gain of 100 using a Stanford Research Systems SR560 Low-Noise Preamplifier.

The surface thermocouple was connected to a cold-junction compensator, and the output was measured with an Agilent 34401A digital multimeter. This value was used to calculate the model surface temperature before a run. The pre-run surface temperature is used to calculate the temperature change from temperature-sensitive paint.

2.3.6 Temperature-Sensitive Paint

Temperature-sensitive paint (TSP) was used to measure global heat transfer on the model. The paint uses a polymer coating doped with the luminescent molecule Tris(2,22-bipyridine)dichlororuthenium(II) Hexahydrate (Ru(bpy)) dissolved in ethanol. The polymer coating is AmTech AM-500-4 clearcoat activated with AM-570-12 medium hardener. The model is coated with an insulating layer of white paint before the mixture is applied to the model with a spray gun. A picture of a painted model is shown in Figure 2.24.

TSP measures the temperature change through a process known as thermal quenching. The luminophore molecules are excited with a pair of blue LED arrays with a wavelength of 465 nm. When the molecule returns to the ground state, the photon released is of a longer wavelength. The temperature of the molecule is inversely pro-

portional to the intensity of the light emitted. This light is captured with an ISSI PSP-CCD-M 14-bit camera with a 550-nm long-pass filter and either a 24 mm or 105 mm lens. For an exhaustive explanation of the theory, application, and processing of TSP refer to Reference [32].

Figure 2.24. The suction model painted with temperature-sensitive paint (yellow region).

During a run, 75 images are taken at 15 Hz. Before running, 15 "dark" and 15 "off" images are taken. Dark images are taken with the LED lights off and no flow, and the off images are take with the blue LEDs turned on and still no flow.

As elaborated in Sullivan et al. [32], the TSP calibration for the temperature change was found using a linear fit to the luminescence properties of Ru(bpy). The resulting equation is

$$\Delta T = (362 - T_{ref}) \left(1 - \frac{I_{on} - I_{dark}}{I_{off} - I_{dark}}\right) \tag{2.4}$$

where T_{ref} is the surface temperature measured by the SB thermocouple. The calibration is good for temperatures ranging 15°C to 60°C.

To calibrate the temperature change, the heat transfer measured by the SB gauge is compared to a nearby TSP-calibration patch. This simplification assumes 1-D, wall-normal heat transfer, and that the temperature profile is linear across the insulating layer. Additionally, it is assumed that the model temperature is spatially uniform and temporally constant throughout a run. Presented in Figures 2.25 and 2.26 are an example of the Schmidt-Boelter trace with the resulting TSP calibration. From the linear regression, r-squared values are typically greater than 0.9. Per Sullivan

et al. [32], the heat transfer from the linear calibration can be considered accurate within 20% for a straight cone at 0° angle of attack. For more complex models, such as a flared surface, the TSP data-reduction method is less accurate.

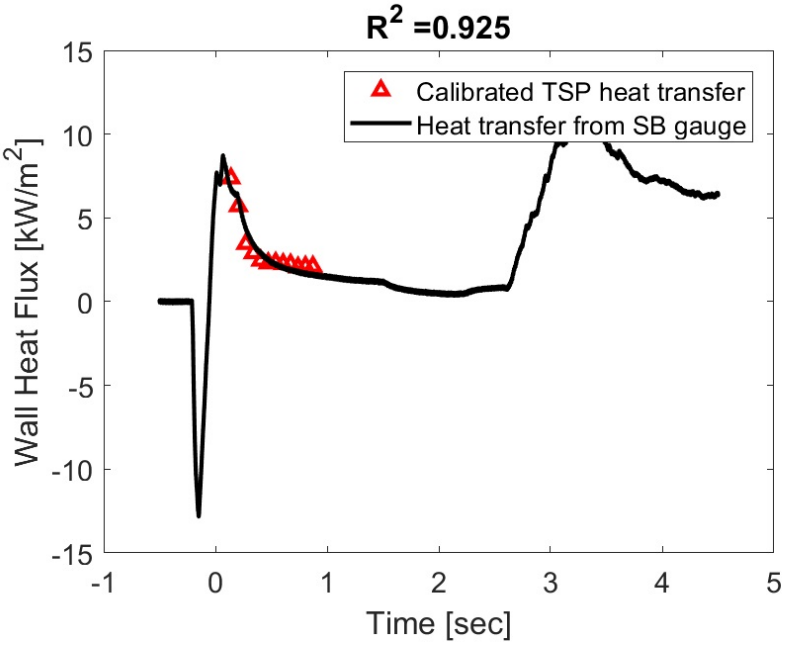

Figure 2.25. Example calibration of TSP plotted against the Schmidt-Boelter gauge measurements during a run.

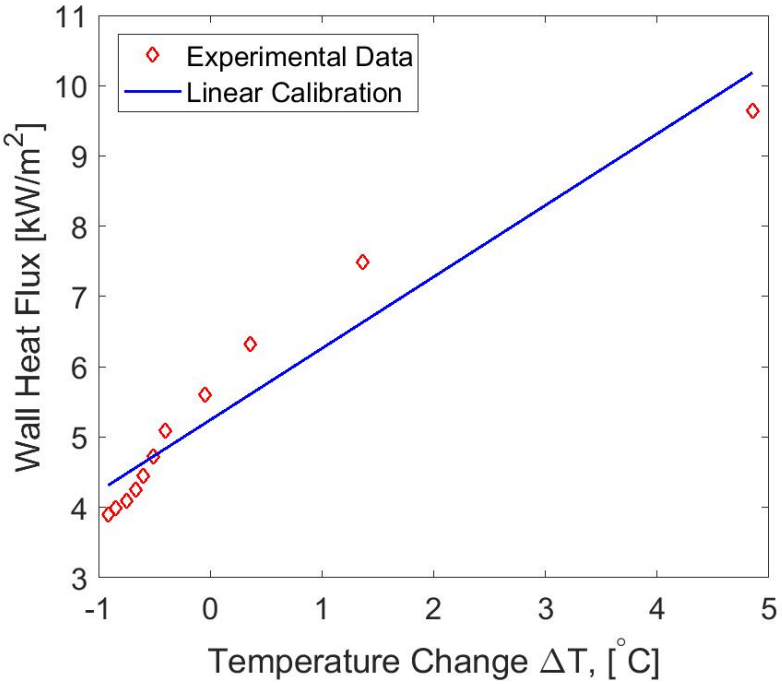

Figure 2.26. Linear calibration of TSP temperature change to heat transfer.

2.3.7 Oil-Flow Visualization

Oil flow was used to visualize Görtler vortices on the model flare without suction. A film of oil on a surface will be influenced by shear stress, gravity, pressure gradients, and surface tension. Quantitative measurements of these variables using oil flow were not pursued in this thesis.

In order to improve signal-to-noise ratio, a coat of black spray paint was used as a background layer for the oil. The oil used was a mixture of 50 mL Dow Corning 200 Fluid (350 centiStokes) to 30 mL DayGlo Aurora Pink powder. Oil was applied to the flare and any excess was allowed to drip off before closing the tunnel, shown in Figure 2.27. The oil was illuminated with the two blue LED arrays, and images were captured using the ISSI PSP-CCD-M 14-bit camera and a 24 mm lens. An alternative method using azimuthal lines of oil was attempted, but the resulting signal intensity was too low to process the images.

The oil-flow images were processed similarly to the TSP. The intensity ratio of the light was processed via

$$\Delta I = \left(\frac{I_{on} - I_{dark}}{I_{off} - I_{dark}} \right). \tag{2.5}$$

During a run, regions with more oil yields a higher intensity ratio, so an qualitative measurement of surface shear stress can be visualized. No method of converting intensity to shear stress was pursued.

Figure 2.27. The oil applied to the suction model before a run.

2.3.8 Focused Laser Differential Interferometry

A focused laser differential interferometer, FLDI, is a relatively non-intrusive method of measuring density fluctuations in compressible flow. FLDI is very briefly described here, and for more detailed explanations, refer to sources such as Parziale [33]. A change in the density of a gas causes a change in the index of refraction.

The FLDI setup used in this research was recently designed and constructed by E. Benitez [34]. The FLDI setup is illustrated in Figure 2.28. The laser used is linearly

polarized with a wavelength of 633 nm. A polarizer located before the pair of 3.00 mm photodiode allows the beams to interfere on the sensor. This FLDI should measure instabilities up to 7.3 MHz.

The FLDI has an optical path length of 65 mm. This was determined by Benitez by traversing a jet through the FLDI at various distances from the focus until the RMS of the fluctuations was $\frac{1}{e}$ [35].

From the interference pattern the phase change can be measured via

$$\phi' = \cos^{-1}\left(\frac{\bar{V}_{pr} - \bar{V}_{i,2}}{\bar{V}_{i,1}}\right) + \Delta\phi_i \tag{2.6}$$

where $\bar{V}_{pr}$ is the voltage from the photoreceiver, and $\bar{V}_{i,1}$ and $\bar{V}_{i,2}$ are the peak amplitudes measured while traversing a full interference curve. $\Delta\phi_i$ is the baseline phase shift. With the phase change, optical-path fluctuations can be calculated via

$$\Delta\Phi = \frac{\lambda}{2\pi} * \phi' \tag{2.7}$$

Equation 2.7. where λ is the wavelength of the laser.

Presently, no method of accounting for the nonuniform sensitivity across the optical path length is available. As such, the optical-path fluctuations were not converted to density change.

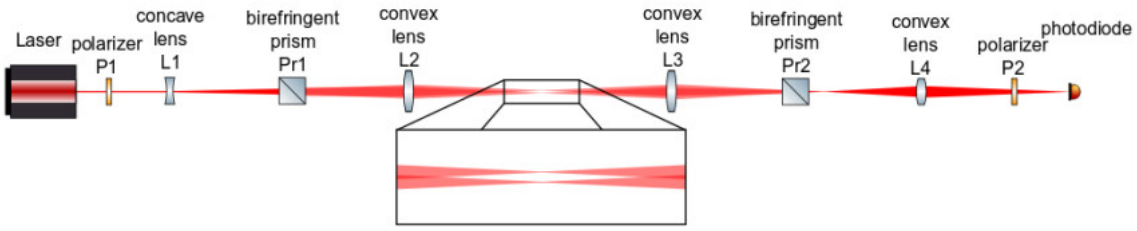

Figure 2.28. Illustration of FLDI setup with beam separation enlarged for clarity. Used with permission from Liz Benitez [35].

3. SUCTION SYSTEM DESIGN

3.1 Sonic Suction

In order to both limit disturbances transmitted from the suction into the freestream and to predict how much mass is being removed, the flow through the suction skin must be sonic. The pressure ratio to choke flow in a duct of varying area can be calculated via

$$\frac{p_{plenum}}{p_{surface}} < \left(\frac{2}{\gamma+1}\right)^{\gamma/\gamma-1} = 0.528. \tag{3.1}$$

as detailed in [36]. The equation assumes isentropic flow. To achieve sonic flow, the pressure ratio between the plenum, p_{plenum}, and the surface, $p_{surface}$, needs to be less than 0.528. As the surface pressure on the sharp cone is a function of the freestream conditions, the required minimum plenum pressure can be obtained easily using the Taylor-Maccoll solutions.

3.1.1 Surface Conditions

The boundary-layer edge flow conditions can be calculated with the Taylor-Maccoll solution for Mach 6 flow past a 7° half-angle cone at 0° angle of attack. A Fortran code modified from Reference [37] was used to calculate the Taylor-Maccoll solutions. The solutions for the edge conditions from the code are provided in Table 3.1 .

The pressure across the boundary layer is assumed to be constant. Surface temperatures near 300 K are typically measured by thermocouples installed in the model. Since the model temperature during a run is much higher than the edge temperature, the density across the boundary layer must also change to account for the temperature gradient. The surface density can be calculated with

$$\rho_{surf} = \rho_{edge}\frac{T_{surf}}{T_{edge}}. \tag{3.2}$$

Table 3.1. Solutions from Taylor-Maccoll analysis for a 7° half-angle cone in Mach 6 flow.

$\frac{p_{edge}}{p_0}$	1.245×10^{-3}
$\frac{T_{edge}}{T_\infty}$	1.217
$\frac{\rho_{edge}}{\rho_\infty}$	1.615

The results from applying a Taylor-Maccoll analysis and Equation 3.2 to a 7° half-angle cone in Mach 6 flow with a $p_0 = 155$ psia and $T_0 = 433$ K are presented in Table 3.2. The model surface temperature, T_{surf}, is assumed constant during a run at 300 K. These results are used to calculate the mass flow rate into the suction section in Section 3.3.

Table 3.2. Surface values for Mach 6 flow on a 7° half-angle cone with $P_0 = 155$ psia.

p_{surf}	10 Torr
T_{surf}	300 K
ρ_{surf}	$0.0156 \frac{\text{kg}}{\text{m}^3}$

3.2 Suction System Design

As initially a mass flow rate was needed to proceed with designing the suction system, an assumption was made that at least 10% of the boundary-layer mass flow would be removed during a run. The 10% was chosen because the maximum porosity of the suction section was planned to be less than 10%. The boundary-layer mass-flux profile for a 7° half-angle cone at $x = 0.258$ m is shown in Figure 3.1. This was calculated by Joshua Edelman with the mean-flow solver in STABL at freestream conditions of $p_0 = 170$ psia and $T_0 = 433$ K. Integrating the profile around the

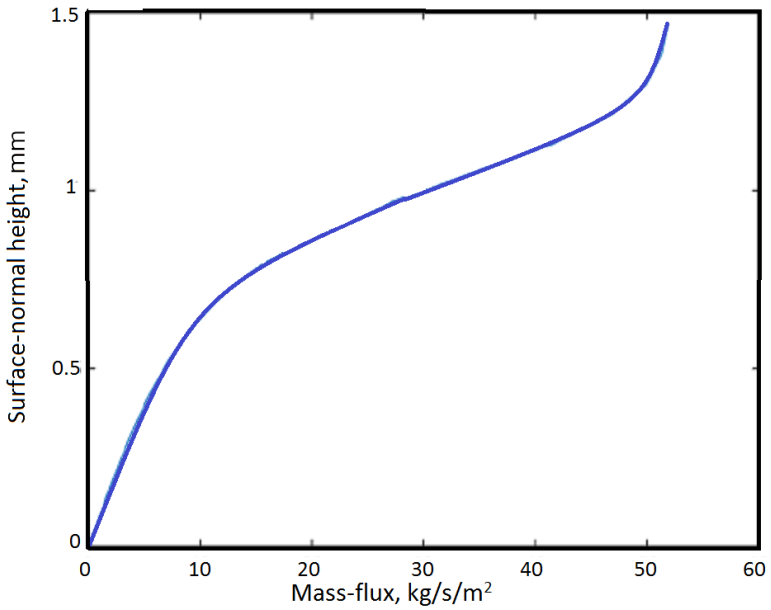

Figure 3.1. Streamwise mass-flux profile in the boundary layer of a 7° half-angle cone at 0° angle of attack located at axial position 0.258 meters (10.16 inches) from the nosetip. Calculated via STABL mean-flow solver with freestream conditions $p_0 = 170$ psia and $T_0 = 433$K.

circumference yields a total mass flow rate of 0.0061 $\frac{\text{kg}}{\text{s}}$. The desired mass flow rate, $\dot{m}$, into the plenum is at least 0.61×10^{-3} $\frac{\text{kg}}{\text{s}}$.

Assuming ideal gas law with constant temperature and constant volume, the rate of pressure rise in the plenum can found using

$$\frac{dp_{plenum}}{dt} = \frac{R_{air} T_{surf}}{V_{plenum}} (\dot{m}_{in} - \dot{m}_{out}). \tag{3.3}$$

R_{air} is the gas constant for dry air, 287.058 $\frac{\text{J}}{\text{kg}\cdot\text{K}}$. The volume of the suction-section plenum is approximately 0.055 L.

For a steady-state solution, the outgoing flow rate has to equal the incoming flow rate. Additionally, the pressure in the plenum needs to be low enough to maintain choked suction. Using a standard vacuum analysis, elaborated in Section 3.2.1, the throughput of the vacuum system required to support the outgoing flow rate to maintain the low pressure in the plenum can be determined. From this, the required

throughput of the suction system is 393.9 $\frac{\text{Torr}\cdot\text{L}}{\text{s}}$. Using this, the minimum conductance of the pipes in the suction system can be determined, and the design of the suction system could proceed.

3.2.1 Throughput and Conductance

A summary of throughput and conductance analysis of a vacuum system follows. For further elaboration refer to Roth, reference [38]. The approach considers the amount of air flowing between parts of a vacuum system, referred to as throughput, Q. Throughput in a circular pipe can be calculated with the Hagen-Poiseuille equation,

$$Q = (p_1 - p_2) \cdot C \tag{3.4}$$

where p_1 and p_2 are the pressures at the upstream and downstream ends of the pipe, respectively. The Hagen-Poiseuille equation assumes the fluid is incompressible, fully-developed, and laminar, and it assumes the no-slip condition on the pipe walls. The typical unit of throughput is $\text{Torr} \cdot \frac{\text{L}}{\text{s}}$. The conductance of the connecting pipes, C, is given by Equation 3.5 with units of volume flow rate, typically $\frac{\text{L}}{\text{s}}$. The conductance,

$$C = k_v \bar{p} \frac{d^4}{l}, \tag{3.5}$$

is valid in the viscous vacuum regime defined as $\bar{p} \cdot d > 0.5$ Torr $\cdot$ cm, per Appendix A.5 of [38]. To determine minimum diameter size, a plenum pressure of 4 Torr and a vacuum-tank pressure of 0 Torr is assumed. With this, the minimum diameter to maintain the viscous flow regime is 0.25 cm.

The variable $\bar{p}$ is the mean pressure between the source and vacuum tank, d is the diameter of the pipe in cm, l is the length of the pipe in cm, and k_v is a viscous factor. The variable k_v can be calculated via

$$k_v = \frac{\pi}{128\mu}. \tag{3.6}$$

Similar to circuits, for multiple pipes in series the total conductance can be given by

$$\frac{1}{C_{tot}} = \frac{1}{C_1} + \frac{1}{C_2} + \frac{1}{C_3} + ... \tag{3.7}$$

where C_i is the conductance of each pipe segment. Lastly, the rate of change of pressure in the source is calculated via

$$\frac{dp}{dt} = \frac{Q}{V} \tag{3.8}$$

where V is the volume of the source.

3.2.2 Plumbing Hardware

After the preliminary estimate of the required conductance was computed, an iterative process of designing the suction system began. Factors considered were vacuum tank volume, pipe diameters and lengths, and how the plumbing would interface with the tunnel. Table 3.3 provides a reference for the different iterations suction-system design. A schematic of the final suction system, Rev.2, is shown in Figure 3.2. The process for installing the suction-system hardware with labeled pictures is provided in Appendix E. Note that the pipe sizes are nominal.

Three options were considered for the vacuum tank. The large 3500 cubic foot tank used as the vacuum source for the BAM6QT was deemed unsuitable early on since the pressure inside rises too quickly at the beginning of a run. In Rev.0, a 35 cubic foot tank that would be kept downstairs from the tunnel was considered because it would minimize hose lengths. However, evacuating the high-pressure air inside the model before a run would raise the tank pressure such that suction would be impractical. The option used in current experiments is a 500 cubic-foot tank typically used with a small supersonic tunnel. A 12-inch wafer valve was installed between the supersonic tunnel and the vacuum tank to reduce leaks. A 6-inch, schedule-10, aluminum pipe was installed to allow high-conductance access to the vacuum tank from the BAM6QT test area. The conductance of the 6-inch pipe is approximately 37,000 $\frac{\mathrm{L}}{\mathrm{s}}$. This is much higher than the rest of the system, as shown in Table 3.4, and has a negligible impact on the total conductance of the system.

For the piping between the sting and the 6-inch aluminum pipe, a 1-inch pipe was initially considered, but it was unable to achieve the required conductance. A

Table 3.3. Iterations of the suction system

Reference key	Size of Vacuum tank	Brief Description
Rev.0	35 cu. ft.	Unconstructed design which used a 35 cu. ft. vacuum tank
Rev.1	500 cu. ft.	Initially constructed design which allowed 1-in. pipe to run upstream between the inside-tunnel wall and the pipe insert. 1-1/4-in. hose connects to the 6-in. pipe to the vacuum tank
Rev.2	500 cu. ft.	Design shown in Figure 3.2, 1-1/4-inch pipe passes through a hole in the pipe insert and out of the tunnel, 1-1/4-in. hose connects to the 6-in. pipe to the vacuum tank
Rev.2b	500 cu. ft.	Same design as Rev.2 except 2-in. hose is used to connect to the 6-in. pipe.

1-1/4-inch pipe was chosen because its conductance per mean pressure, $\frac{C}{\bar{p}}$, is about 57% higher than a 1-inch pipe of equivalent length. Note that the inner diameter of 1-1/4-inch pipe is actually 1.38 inches.

An early method, Rev. 1, of running the pipes out of the BAM6QT used 1-inch pipe coming out of the model baseplate. The pipe would then run upstream between the inside-tunnel wall and the pipe insert. It would screw into an NPT-tapped hole inside the tunnel, and 1-1/4-inch hose would run from outside the tunnel to the vacuum tank. This idea was rejected after a BAM6QT entry, both due to

interference between the pipe-insert rail supports and the elbow joints, and due to an inability to seal the elbow joints inside the tunnel.

The next design, Rev. 2, removed air from the model via a rigid pipe attached to the hollow sting. A schematic of this assembly is shown in Figure 3.2. The pipe turns via a 1-to-1-1/4 elbow adapter, and the 1-1/4-inch pipe passes through a hole in the pipe insert and out of the tunnel. The equivalent length for a short-radius elbow is 30 $\frac{L}{D}$. The relations for equivalent length of joints and valves are available in Fox et al. [39]. Per the ASPE standards for vacuum systems, reference [40], these non-vacuum equivalent lengths are also valid for vacuum systems. The outside of the pipe passing through the tunnel wall is sealed with a Conax pressure fitting. A solenoid control valve is mounted on the end of the 1-1/4-inch pipe, and downstream of the valve is flexible 1-1/4-inch hose. The conductance of each section is presented in Table 3.4.

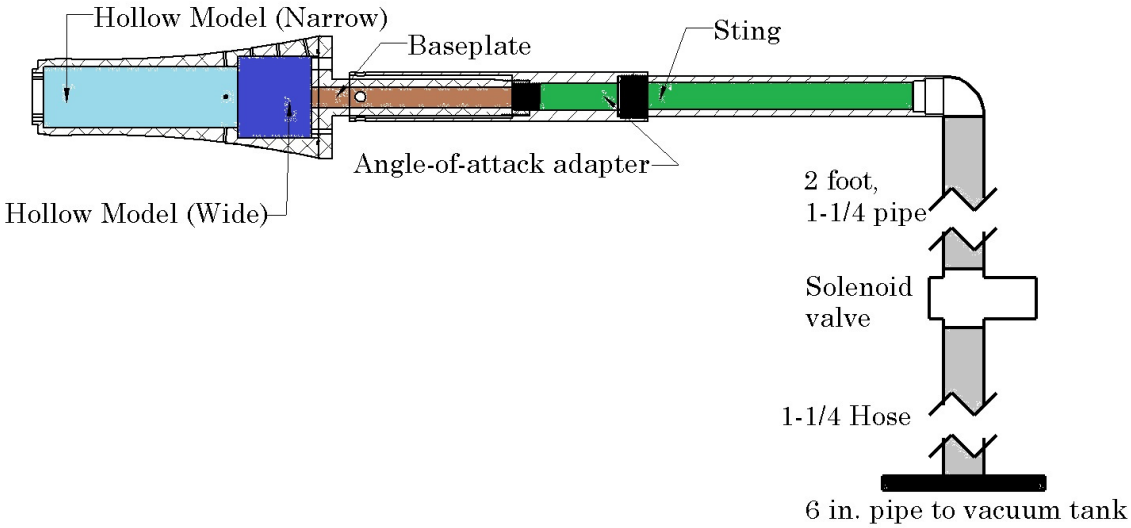

Figure 3.2. Schematic of the Rev.2 suction-system assembly. Refer to Table 3.4 for sizes of each section.

Table 3.4. Conductance of suction-pipe segments in the Rev.2 design with $\bar{p} = 3.14$ Torr. Colors correspond to Figure 3.2

Location	**Inner Diameter (in (cm))**	**Length (in (cm)**	**Conductance ($\frac{L}{s}$)**
Hollow Model (narrow) (light blue)	2.25 (5.71)	7.2 (18.3)	3.36×10^4
Hollow Model (wide) (dark blue)	3.0 (7.62)	3.0 (7.62)	2.53×10^5
Model Baseplate (brown)	0.75 (1.91)	7.3 (18.5)	407.6
AoA adapter and Sting (green)	1.0 (2.54)	11.5 (29.2)	814.3
short-radius, 1-1/4-in. 90° elbow (white)	1.05 (2.67)	41.4 (105)	820.4
1-1/4-in. pipe (gray)	1.38 (3.51)	12 (366)	235.9
1-1/4-in. hose (gray)	1.38 (3.51)	120 (366)	235.9
6 inch pipe to vacuum tank (black)	6 (15.24)	183 (465)	6.6×10^5
		Total Conductance	109.0

In an effort to improve the conductance in February 2019, design Rev.2b uses a 10-ft. long, 2-in. hose was acquired to replace the 10-ft. long, 1-1/4-in. hose. The inner diameter of 2-inch hose is 2.07 in. (5.26 cm). With the conditions from Table 3.4, the new hose has a conductance of 1424.6 $\frac{L}{s}$, and the total conductance increases to 157.7 $\frac{L}{s}$.

Solenoid Valve and Vacuum-Tank Pressure Sensor

A solenoid valve is used to control when suction begins during the run. The valve is a Magnatrol model 33A55. It is closed by default, has a nominally 1-1/4-inch full-port flow, and allows pressure differentials ranging from 0 to 300 psia. The valve is mounted outside the tunnel to the 2-ft. long, 1-1/4-in. pipe. The solenoid valve is controlled via a solid-state relay. When the tunnel diaphragms burst at the start of a run, the pressure drop in the tunnel is measured by a Kulite pressure transducer. The voltage drop from the pressure transducer is detected by a Tektronix oscilloscope which outputs a trigger-signal to the relay. The relay switches, and power is delivered to the solenoid opening the valve. There is a measured delay of 0.02 seconds from the scope trigger signal to the solenoid actuation.

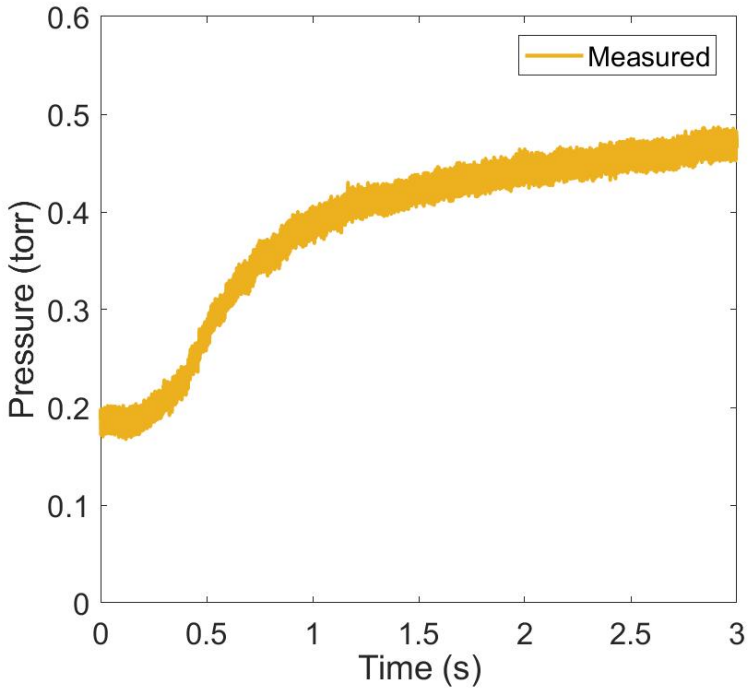

Figure 3.3. Static pressure at the upstream end of the 6-inch line for a run with $p_{0,i} = 155$ psia.

The static pressure in the 6-inch line during a run is measured using a Leybold Ceravac CTR 101 N100 vacuum pressure sensor. The sensor is located on the flange at the upstream end of the 6-inch line near the suction side. The sensor has a measurement range form 0.01 to 100 Torr and a sensitivity of 0.01 Torr. The uncertainty in the sensor is listed as 0.12% of full scale (0.12 Torr) with temperature effects $\pm 0.0025 \frac{\%}{^\circ\text{C}}$. The sensor is internally regulated to 45°C. An example pressure trace measured by the sensor during a run with $p_{0,i} = 155$ psia is plotted in Figure 3.3. The solenoid is opened at 0 seconds.

3.3 Predicting the Plenum Pressure

Before and after constructing the plumbing system, a method to predict the plenum pressure during a run was desired. The full Matlab script is provided in

Appendix C. The code models the mass flow in to and out of the plenum to predict the plenum pressure. As of the time of publishing this thesis, the code has not been properly validated. Due to limitations on time, improvements to the code have been left as future work.

Unless otherwise specified, the freestream conditions for the analysis assume steady Mach 6 flow with $p_0 = 155$ psia and $T_0 = 430$ K. Referring to Table 3.2, $p_{surf} = 10$ Torr, $\rho_{surf} = 15.6\ \frac{\text{g}}{\text{m}^3}$, and $T_{surf} = 300$ K. Varying ρ_{surf} and T_{surf} by $\pm 10\%$ yielded negligible effects on the results.

Predicting the plenum pressure before suction began using a physics-based model was difficult. The time-marching method described here was chosen for the final iteration of the code. Before suction begins, the flow in the system upstream of the solenoid valve can be modeled as a pipe with uniform initial pressure, $p_{0,i}$. Refer to the schematic in Figure 3.4 for a visualization of the pipes considered for this model. At the start of a run the plenum pressure is high, and air would blow from the model into the freestream through the perforated skin because the nozzle freestream pressure is already falling. However, the mass flow from blowing should be negligible compared to the air being removed by the suction system and is omitted from this part of the analysis. As such, before suction begins the system was modeled as a capped pipe at the plenum. The plenum is located at $z = 0$, where z is a pipe-axial coordinate. The solenoid valve opens to a constant-pressure vacuum tank at $t = 0$, with the valve located at $z = l$. Note that the 1-1/4 in. hose is omitted from this part of the analysis.

Livesey presented a similar model for unsteady, molecular flow in pipes that are long relative to their diameter [41]. The model is analogous to one-dimensional heat conduction in an infinite slab of width l. With this, the pressure in a pipe, $p_{pipe}(t, z)$ can thus be modeled via

$$p_{pipe}(t,z) - p_{tank} = \frac{4}{\pi}(p_{0,i} - p_{tank}) \sum_{n=0}^{\infty} \frac{-1^n}{(2n+1)} exp\left(-(2n+1)^2 \frac{\pi^2}{4} \frac{C}{V} t\right) cos\left((2n+1)\frac{\pi}{2}\frac{z}{l}\right). \tag{3.9}$$

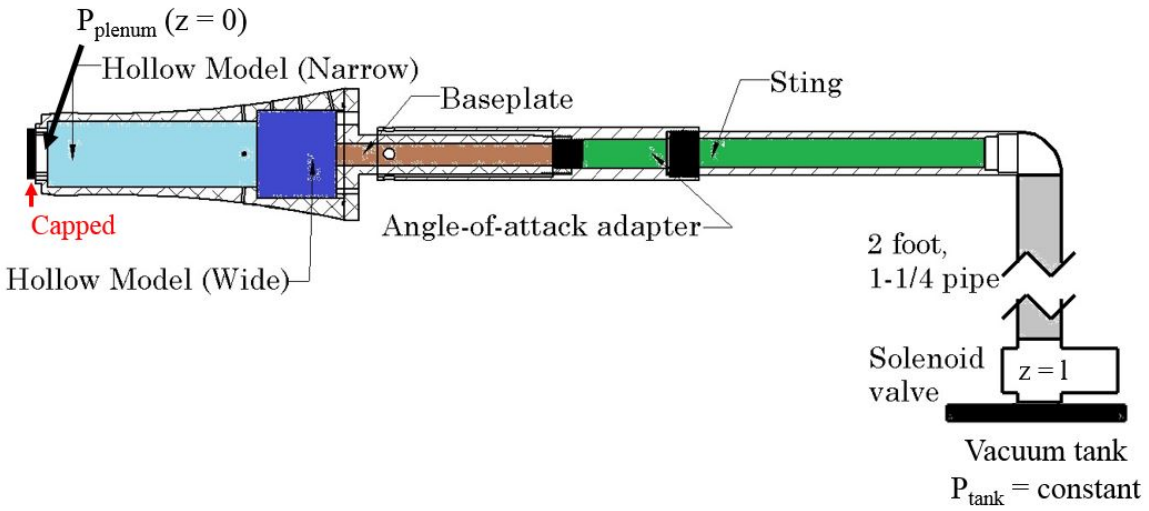

Figure 3.4. Schematic of suction system during the startup of the plenum-pressure prediction analysis.

The equivalent pipe being the region from the plenum to the solenoid valve shown in Figure 3.4. As the diameter of the pipes vary, the conductance of the equivalent pipe is approximated by Equation 3.7. However, this may introduce additional error to the analysis. Simplifying this as the first term of the summation and evaluating in the plenum, $z = 0$. This gives

$$p_{plenum}(t) - p_{tank} = \frac{4}{\pi}(p_{0,i} - p_{tank})exp\left(-\frac{\pi^2}{4}\frac{C}{V}t\right). \tag{3.10}$$

Livesey commented that this is a good approximation for times greater than 0.3 times the time constant for the first term in Equation 3.9. Once the pressure in the plenum is low enough for suction to occur, the method of calculating the pressure in the plenum is changed. The schematic shown in Figure 3.2 is representative of the suction system for the remainder of the calculations. The mass flow rate out of the

plenum is approximated via the throughput equations, Equations 3.4 and 3.7. The incoming flow is calculated with

$$\dot{m}_{in,subsonic} = C_d A_{orifice} \sqrt{2 \cdot p_{surf} \rho_{surf} \left(\frac{\gamma}{\gamma - 1}\right) \left[\left(\frac{p_{plenum}}{p_{surf}}\right)^{\frac{2}{\gamma}} - \left(\frac{p_{plenum}}{p_{surf}}\right)^{\frac{\gamma+1}{\gamma}}\right]} \tag{3.11}$$

for subsonic flow and

$$\dot{m}_{in,sonic} = C_d A_{orifice} \sqrt{2 \cdot p_{surf} \rho_{surf} \left(\frac{2}{\gamma + 1}\right)^{\frac{\gamma+1}{\gamma-1}}} \tag{3.12}$$

for choked flow. The equations for discharge rate of adiabatic, frictionless, compressible flow through an orifice, Equations 3.11 and 3.12, are available in Reference [42]. C_d is a discharge coefficient, and $A_{orifice}$ is the area of a hole. A low value for the discharge coefficient used was 0.6, for margin.

The total porous area of the suction section can be approximated as the product of the porosity and surface area of the suction section. For Suction Section 1, the surface area is about 4.48×10^{-3} m^2 and the porosity was nominally 3.5% yielding $A_{orifice} = 1.6 \times 10^{-4}$ m^2.

The pressure in the vacuum tank is initially 0.2 Torr, and the tank temperature is assumed constant at 300 K. Per the vacuum-pump manual [43], the pump removes air at 400 cubic-feet per minute (cfm) in the range of 1 to 10 Torr. Using ideal gas law to approximate the density of air, the mass flow rate out of the tank is as follows, $\dot{m}_{out} = 5.04 \times 10^{-4}$ $\frac{\text{kg}}{\text{s}}$.

3.3.1 Results from the Prediction Code

The outputs from analyzing the Rev.2 design with the Suction Section 1, 3.5% porosity, are presented in Figure 3.5. The throughput from plenum to vacuum tank is shown in Figure 3.5(a), and the pressure ratio between the plenum and surface is shown in Figure 3.5(b). The model begins sucking in the freestream air at 0.04 seconds and the pressure ratio reaches 0.528, the sonic-suction minimum, at 0.08 seconds. The throughput reaches a steady state at 0.11 seconds during which the

pressure ratio is 0.493. The mean total conductance from 0.1 to 0.3 seconds is 104.8 $\frac{L}{s}$.

The results show that when the Rev.2 design is used with a nominally 5% porosity suction section, the nominal porosity of Suction Section 2, there is very little margin. Figure 3.6(a) shows the system throughput and indicates the suction begins at 0.046 seconds. Figure 3.6(b) shows the pressure ratio between the plenum and surface is around 0.514, barely satisfying the sonic-suction minimum. The increased porosity results in more flow being sucked into the plenum from the boundary layer. The mean total conductance from 0.1 to 0.3 seconds is 90.53 $\frac{\mathrm{L}}{\mathrm{s}}$. This is less than the minimum conductance from the preliminary analysis, but it appears to work.

In order to account for the increase in surface-flow removal, the diameter of some pipes could be increased. As seen in Table 3.4, the section with lowest conductance in the Rev. 2 suction system is the 1-1/4 pipe. The Rev.2b design replaces the 10-foot hose from the solenoid to the 6-inch line with 2-inch hose, and the length of 1-1/4-inch pipe is reduced to 2 feet. For a 5%-porosity suction section, the resulting mean total conductance from 0.1 to 0.3 seconds increases to 150.1 $\frac{\mathrm{L}}{\mathrm{s}}$. As shown in Figure 3.7(b), sonic suction is again achieved beginning at 0.07 seconds, but with a steady-state pressure ratio of 0.487.

The code was adjusted to model the freestream total pressure as a linear decrease with time from 155 psia at $t = 0$ s to 123 psia at $t = 3.5$ s, simulating the tunnel flow. Figure 3.8 shows that the decrease in surface pressure removes the steady-state effect from the earlier analysis. The resulting pressure ratio shows sonic flow up to 2.9 seconds with subsonic suction afterwards.

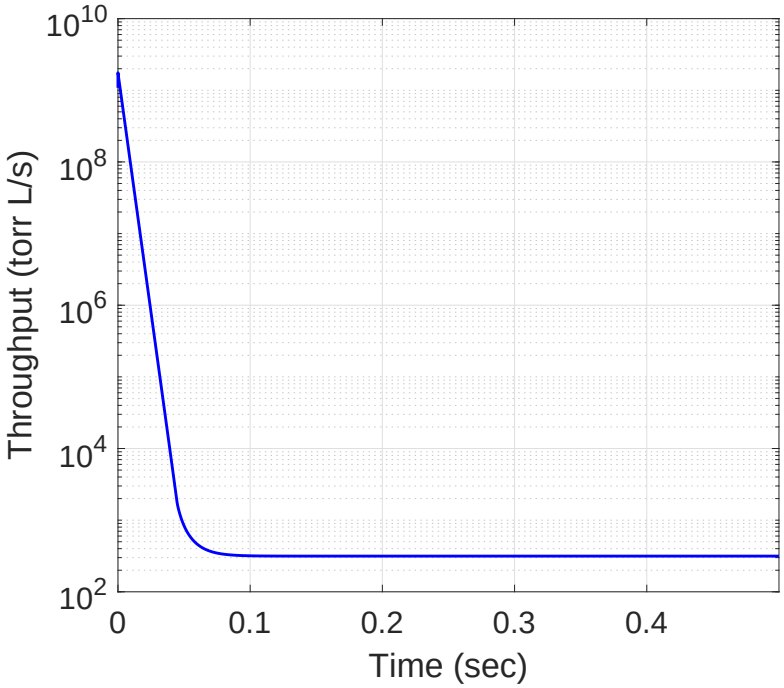

(a) Throughput from plenum to vacuum tank

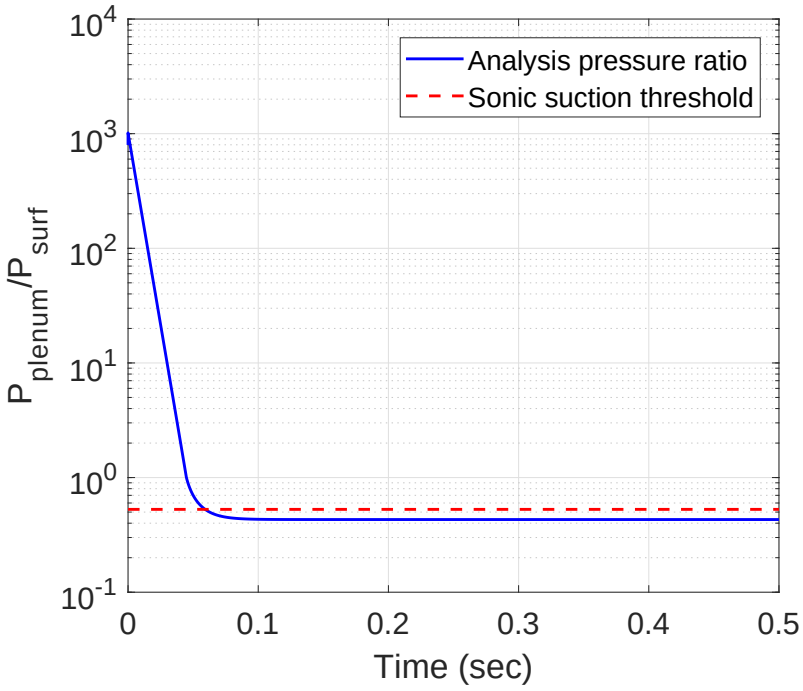

(b) Pressure ratio between plenum and surface

Figure 3.5. Results from plenum-pressure analysis code for Suction Section 1 with the suction system depicted in Figure 3.2.

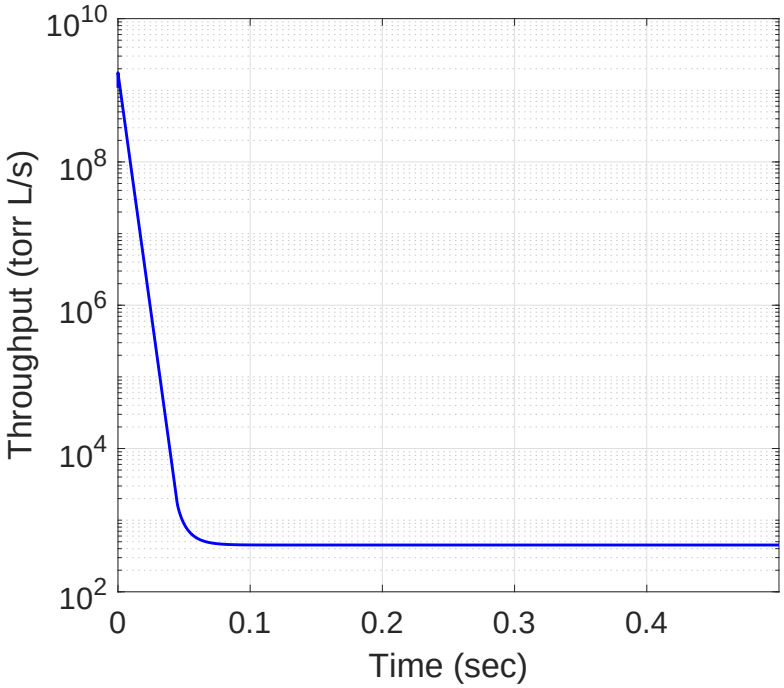

(a) Throughput from plenum to vacuum tank

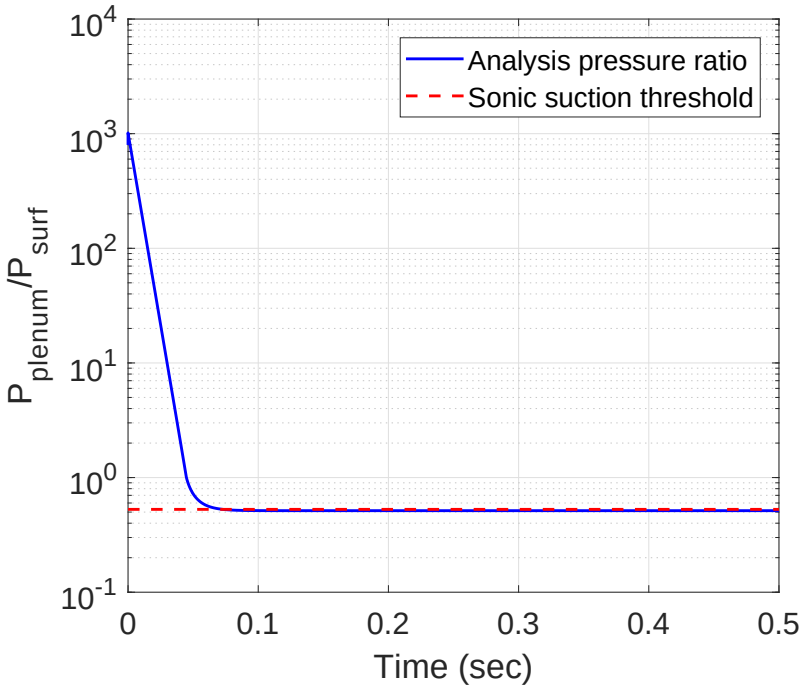

(b) Pressure ratio between plenum and surface

Figure 3.6. Results from plenum-pressure analysis code for a 5%-porosity suction section paired with the suction system depicted in Figure 3.2.

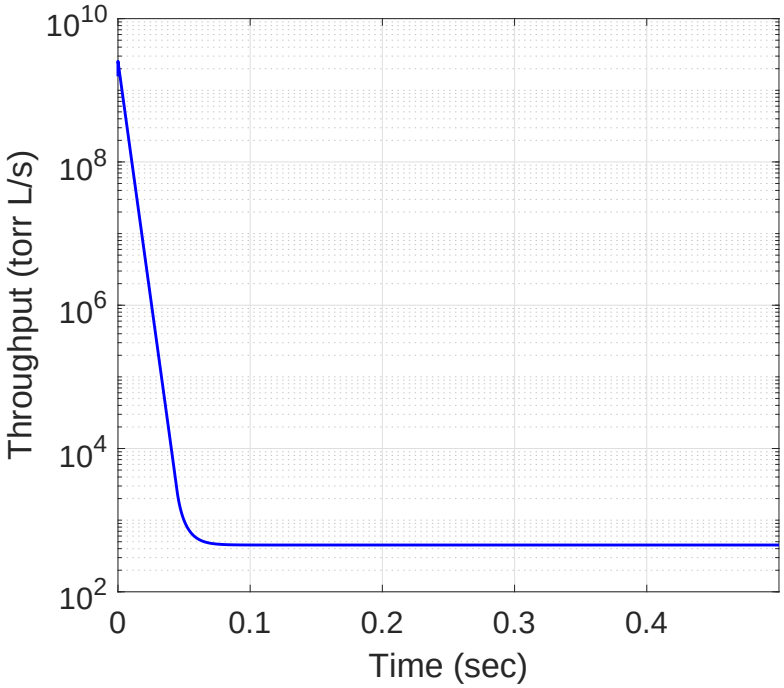

(a) Throughput from plenum to vacuum tank

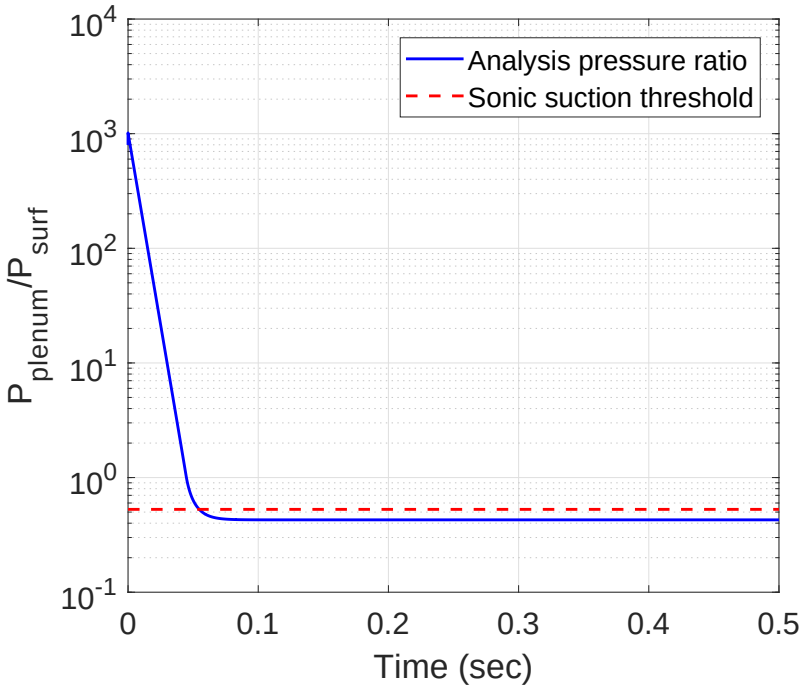

(b) Pressure ratio between plenum and surface

Figure 3.7. Results from plenum-pressure analysis code for a 5%-porosity suction section with the 2-inch hose in the suction system.

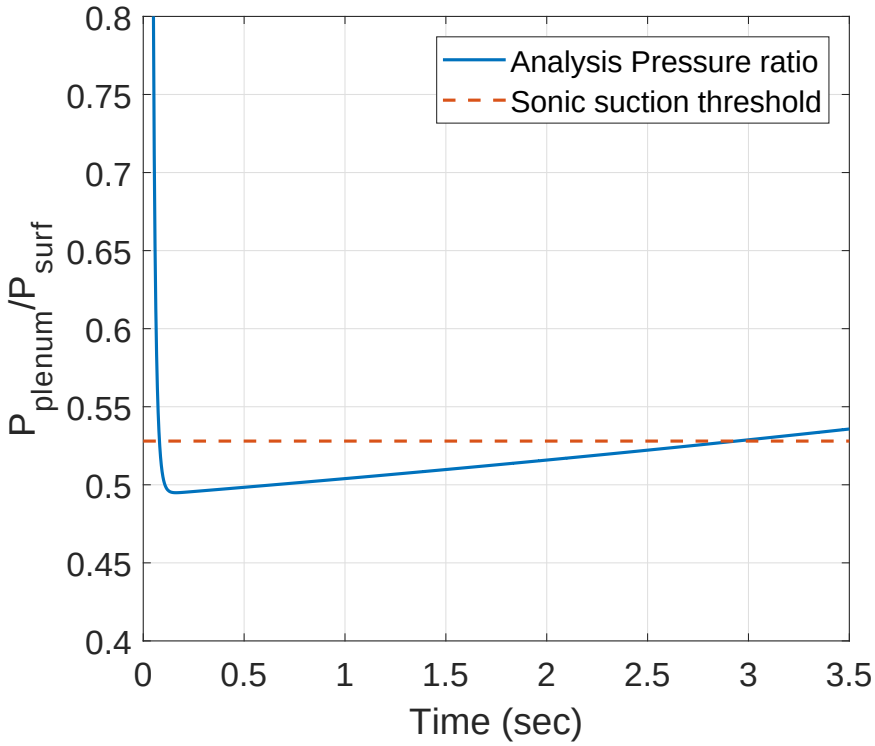

Figure 3.8. Pressure ratio between plenum and surface plotted from 0.05 to 3.5 seconds. Results from plenum-pressure analysis code with time-varying freestream pressure with a 3.5%-porosity suction section and the constructed suction system.

3.3.2 Comparison of Code to Measured Plenum Pressure

Ideally, the code should align with the experimentally measured conditions despite the many computational approximations. Figure 3.9 shows the measured model-suction-plenum pressure from a run with $p_{0,i} = 155$ psia and $T_{0,i} = 424$ K. The experiment used Suction Section 1 which has a porosity of 3.5%. The static pressure on the tunnel nozzle wall from the run is also shown, but the signal was cut off on the oscilloscope above 30 Torr. As the plenum-pressure transducer is mechanically stopped above 5 psia, the plenum pressure from 155 psia to 5 psia is not available. The plenum pressure reached 5 psia at 0.011 seconds. Note that in this run, the diaphragms break at -0.16 seconds, but the oscilloscopes do not send the trigger signal to the solenoid valve until 0 seconds. An inflection point at 0.17 seconds appears to coincide with the beginning of quiet flow. This could be attributed to the freestream pressure decrease when the Mach number rises from 5.8 to 6.0. An alternative explanation for the inflection is that the pressure inside the plenum is around 37 Torr. At this plenum pressure, the mass flow blowing out of the plenum into the freestream may no longer be negligible.

Multiple models for predicting the mass flow rate out of the pipes and calculating the plenum pressure are compared with the plenum pressure measured during a suction-enabled run in Figure 3.10. The experimental measurement was made during a run with nominally $p_{0,i} = 155$ psia with Suction Section 1. The model labeled sonic orifice in the figure was a very simplified of the system used to approximate a lower limit. This model approximated the plenum and pipes as a tank with an equivalent volume to the Rev.2 design of the suction system. The initial pressure inside the tank was 155 psia and an 1-1/4 hole in the side opens to perfect vacuum at $t = 0$ s. A schematic of this model is shown in Figure 3.11. The outgoing mass flow rate was calculated via Equation 3.12 for small time steps, and the internal pressure was iteratively updated. As expected, the sonic-orifice model under-approximates the time to remove air from the plenum. If the throughput equations are used for the initial,

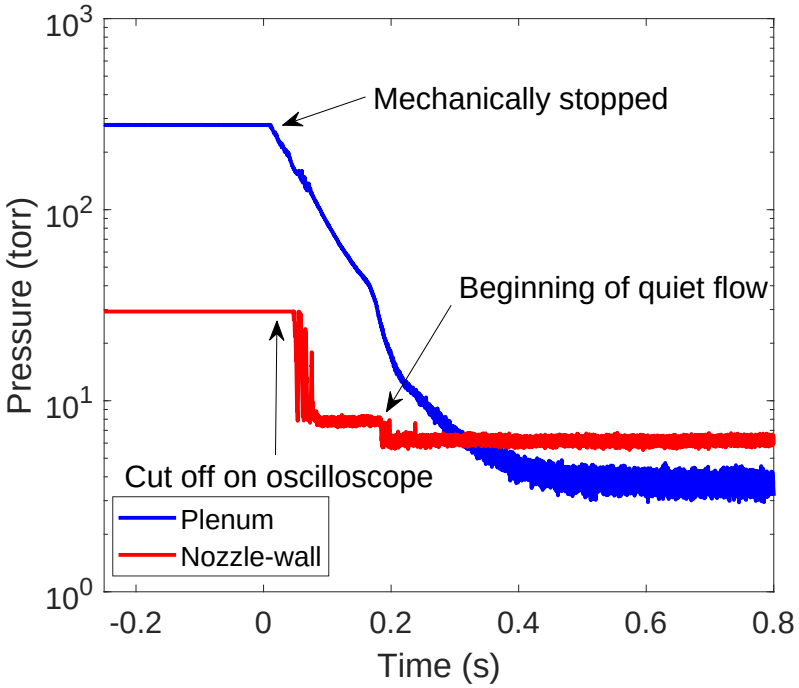

Figure 3.9. Plenum-pressure trace from a run with $p_{0,i} = 155$ psia and $T_{0,i} = 424$ K. Measured with a pressure transducer inside the plenum. Run SS1.7

high-pressure flow (labeled Throughput), the air is shown to be removed faster than sonic orifice model. This is likely due to errors introduced by the incompressible and laminar-flow assumptions in the Hagen-Poiseuille equation used in the model. The model described in Section 3.3.1 (labeled Livesey model) uses the model presented by Livesey for the pre-suction flow. The result was closer to the experimentally-measured result, but still underestimated the time measured to empty the plenum.

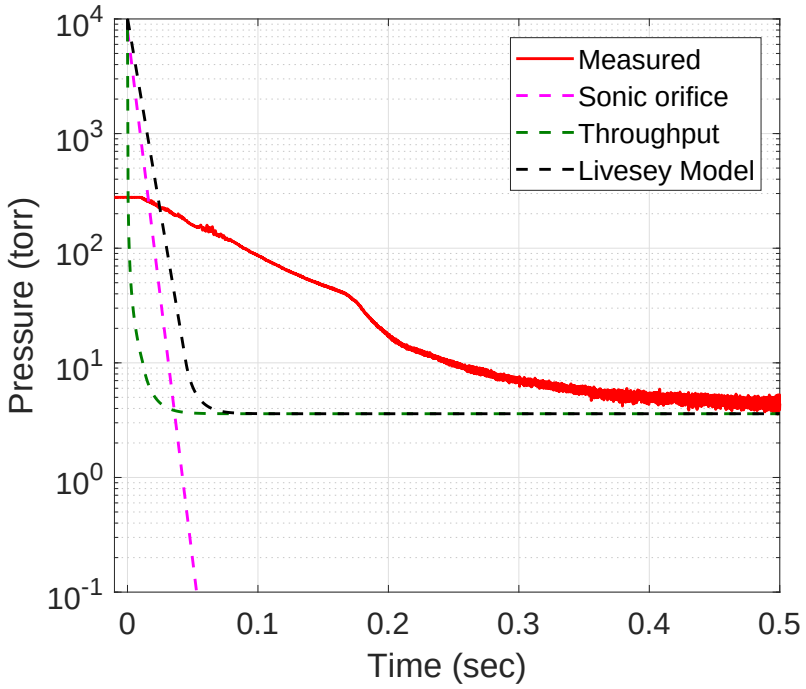

Figure 3.10. Comparison between different models used in predicting the plenum pressure. Run SS1.7

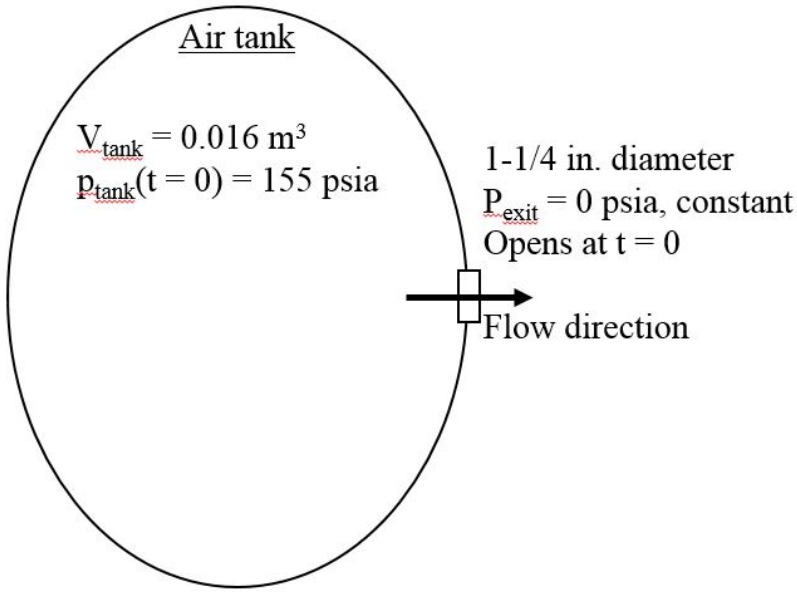

Figure 3.11. Schematic of simplified, sonic-orifice model of the suction system.

4. RESULTS AND DISCUSSION

4.1 Early Experiments

Early experiments in this project were met with a number of complications. The measurements from these tests are not representative of the final results, but the issues motivating incremental improvements are presented here for reference.

4.1.1 Inverse Flare Geometry

Tests with the inverse flare geometry, the precursor to the suction model as described in Section 2.2.1, apparently caused the nozzle-wall boundary layer to separate during runs. The separation is indicated by a prolonged increase in voltage on the nozzle-wall hot-film trace as shown in Figure 4.1. When the flow separates, the tunnel is considered unstarted, the freestream Mach number is unknown, and the flow is uncharacterized. The resulting data from the runs are unused. All quiet runs with the inverse flare geometry seemed to cause the nozzle-wall boundary layer to separate.

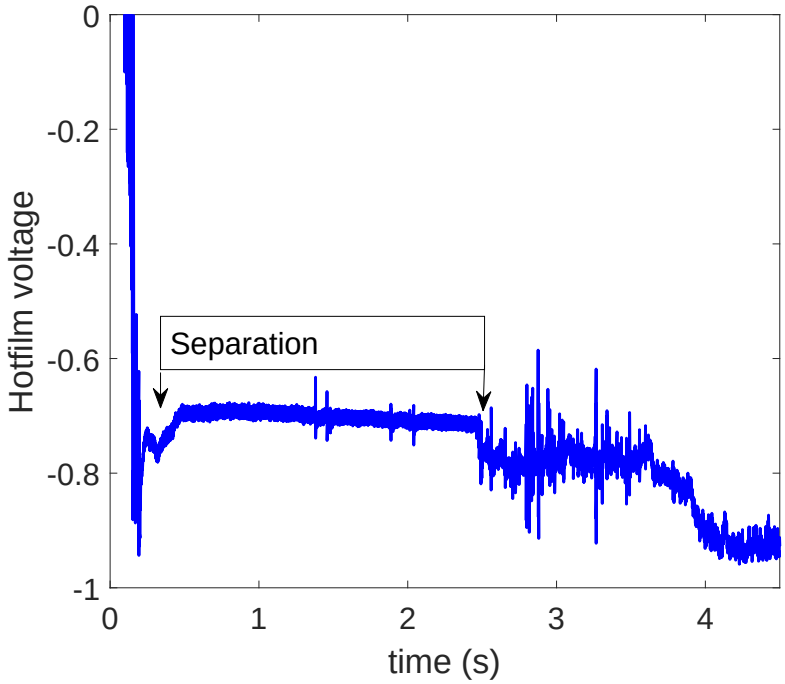

Figure 4.1. Hot-film trace for bleeds-open runs with the inverse flare model. Run INF.3

4.1.2 Vortex imaging with different lenses using TSP

As the diameter of the Görtler vortices was unknown in early entries, images of the suction model for TSP and oil-flow visualization were captured through a lens with a focal length of 24 mm. Li et al.'s work, Reference [19], calculates that the Görtler vortices would have a width of 2 mm. For pictures captured with the 24 mm lens, the resolution on the model is about 7.3 $\frac{\text{pixels}}{\text{mm}}$. Figure 4.2 shows the temperature change on the model surface with a close-up of the aft region. The data were collected under quiet flow at a freestream unit Reynolds number of 8.30×10^6 m^{-1}. The SB-gauge was not functioning during the TSP-image shown. No noticeable streamwise vortices are visible in the flowfield. If the TSP had higher signal-to-noise ratio or the Görtler vortices were stronger, then the vortices might be measurable.

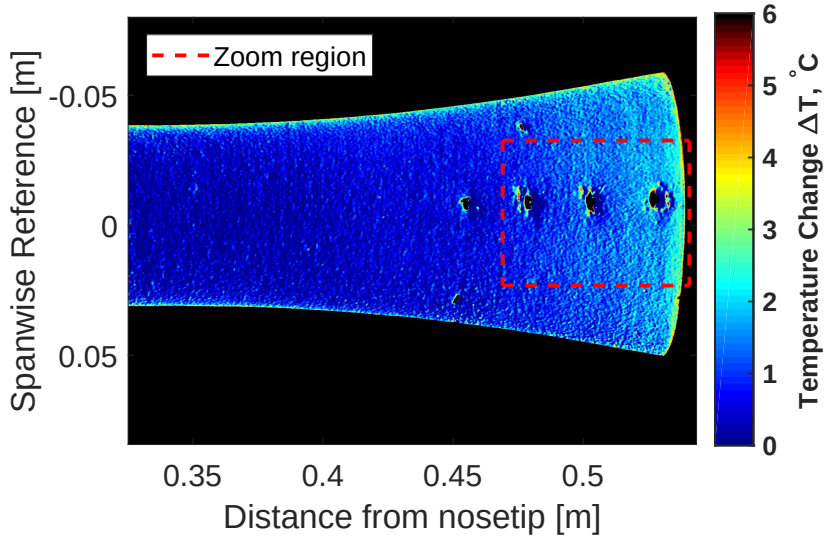

(a) Full image

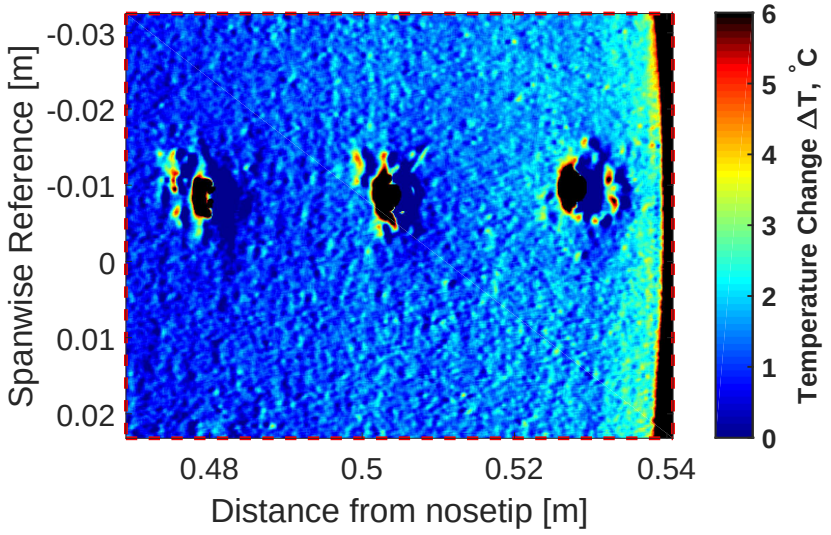

(b) Close up of model aft

Figure 4.2. Temperature change with the smooth blank insert. Freestream unit Reynolds number in images is $8.30 \times 10^6\,\mathrm{m}^{-1}$. Run SJF.11

Figure 4.3 shows the heat transfer measured on the model while using the 105 mm lens with unit Reynolds number 8.27×10^6 m^{-1}. This lens provided an approximate resolution of 19 $\frac{\text{pixels}}{\text{mm}}$. The heat transfer does not change significantly with streamwise

position. In the streamwise direction, vortices are not apparent. Figure 4.3(b) shows a spanwise slice along an axial position 0.532 m from the nosetip. The decrease in heat transfer around spanwise reference = 0 m is the sensor port. Assuming the vortices exist, they did not appear to cause a measurable change in the heat transfer at this Reynolds number.

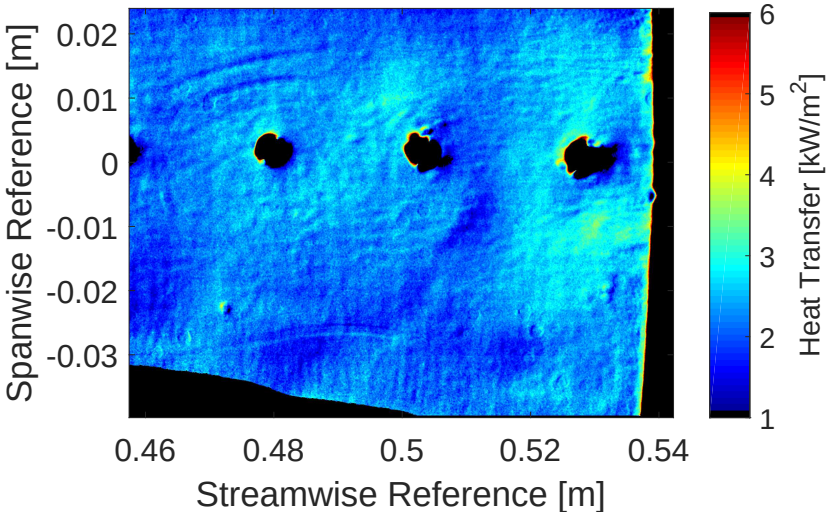

(a) Heat transfer with 105 mm lens

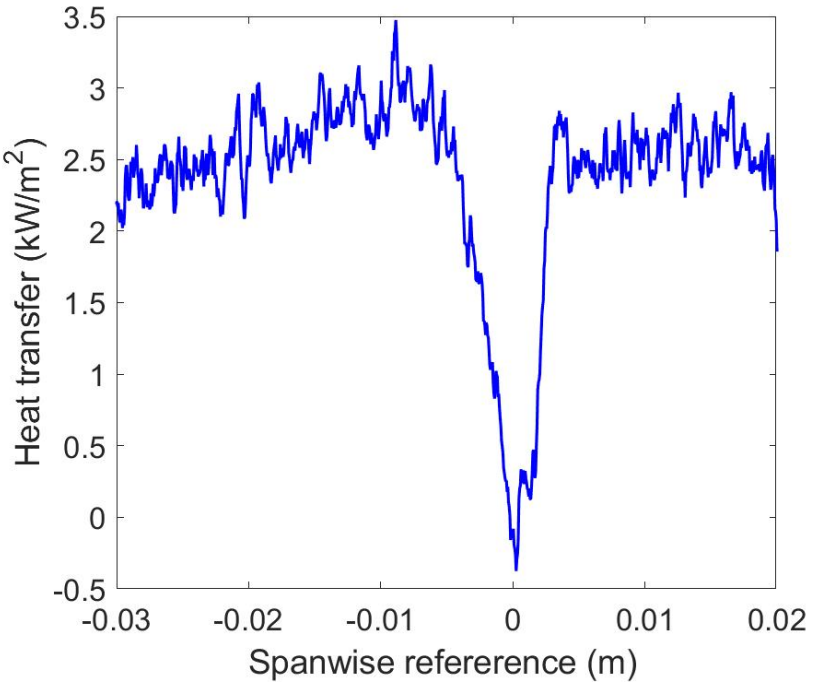

(b) Spanwise slice along axial position 0.532 m

Figure 4.3. Heat transfer measurement with a 105-mm focal-length lens. $Re_\infty = 8.27{\times}10^6$ m^{-1}. Run SSF.8

4.1.3 Oil-Flow Visualization on the Flare

Oil-flow visualization was attempted with the model as described in Section 2.3.7. An example of the resulting intensity image is shown in Figure 4.4(a) at $Re_\infty = 11.0 \times 10^6$ m^{-1}. The image shows a slight oscillating, spanwise pattern, but it is unclear due to the low signal-to-noise ratio. The region of bright intensity on the bottom is where the oil gathered due to gravity during the tunnel-filling process. A spanwise slice of the intensity image was taken at an axial location of 0.526 m (20.71 in.) from the nosetip, shown in Figure 4.4(b). The slice shows the oscillating pattern with a spanwise, peak-to-peak period of about 4.6 mm with relative intensity change of around 0.1. These peaks occur with an approximate azimuthal wavenumber of 100.

Figure 4.5 shows slices of the oil-flow intensity ratio at $x = 0.52$ m for a range of Reynolds numbers. The wavenumber of the peaks in intensity increase from 78 at $Re_\infty = 9.7 \times 10^6$ m^{-1} to 101 at 11.3×10^6 m^{-1}. Figure 4.6 shows slice of the oil-flow intensity ratio at $Re_\infty = 11.1 \times 10^6$ m^{-1} for a range of axial locations. The wavenumber of the peaks increase from 53 at $x = 0.4$ m to 100 at $x = 0.52$ m.

From Li et al. [19], the most amplified wavenumber for the Görtler instability should be 130 with $Re_\infty = 12.3 \times 10^6$ along the length of the flare. It remains unclear if these oscillations are Görtler vortices, but it seems that they might be.

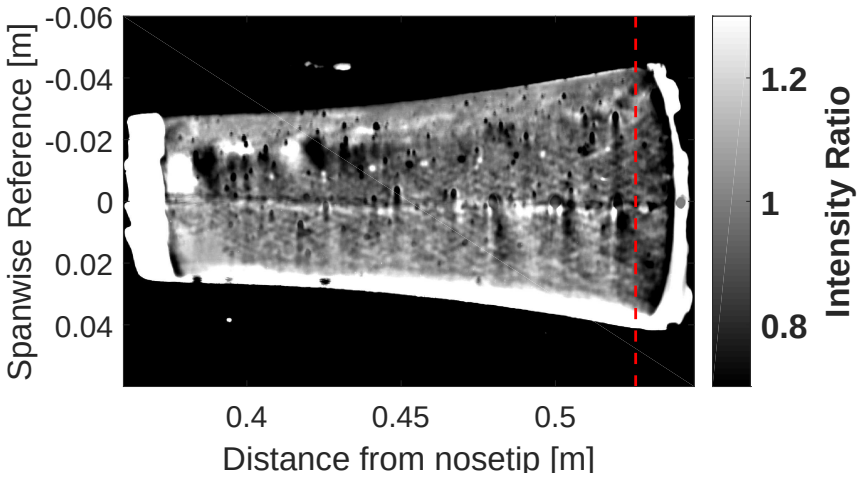

(a) Oil-Flow visualization

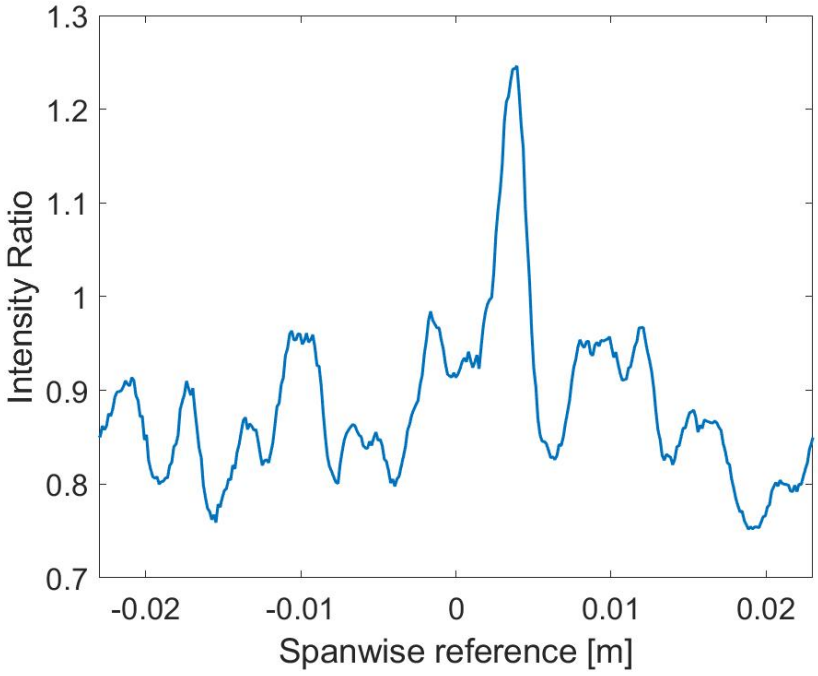

(b) Image intensitiy along vertical slice axially 0.526 m (20.71 in.) from nosetip

Figure 4.4. Oil-flow visualization of suction model with the smooth blank insert. Freestream Reynolds in images is $11.0 \times 10^6\,\mathrm{m}^{-1}$. Run OIF.4

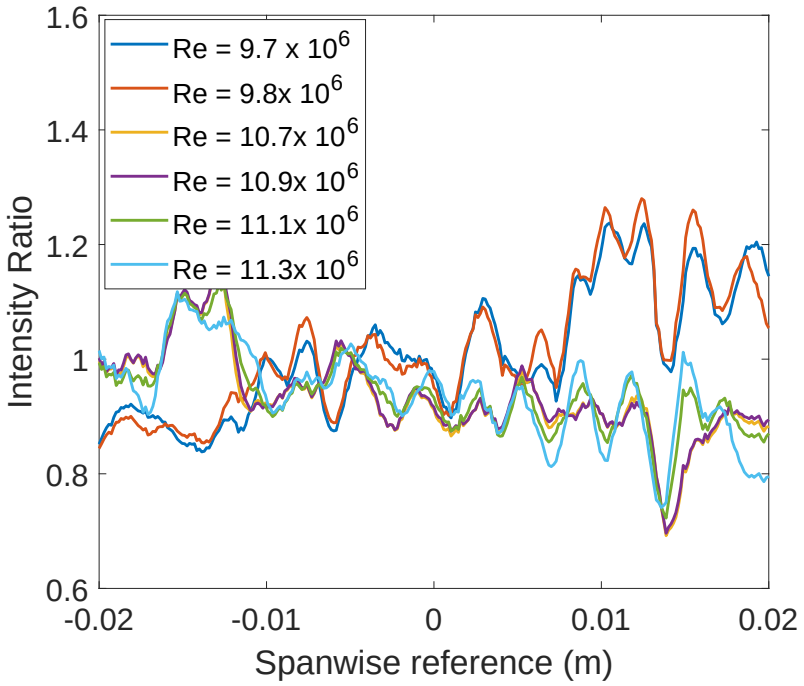

Figure 4.5. Image intensity of oil-flow visualization along vertical slices at $x = 0.526$ m for a range of Reynolds numbers. Runs OIF 3, 4

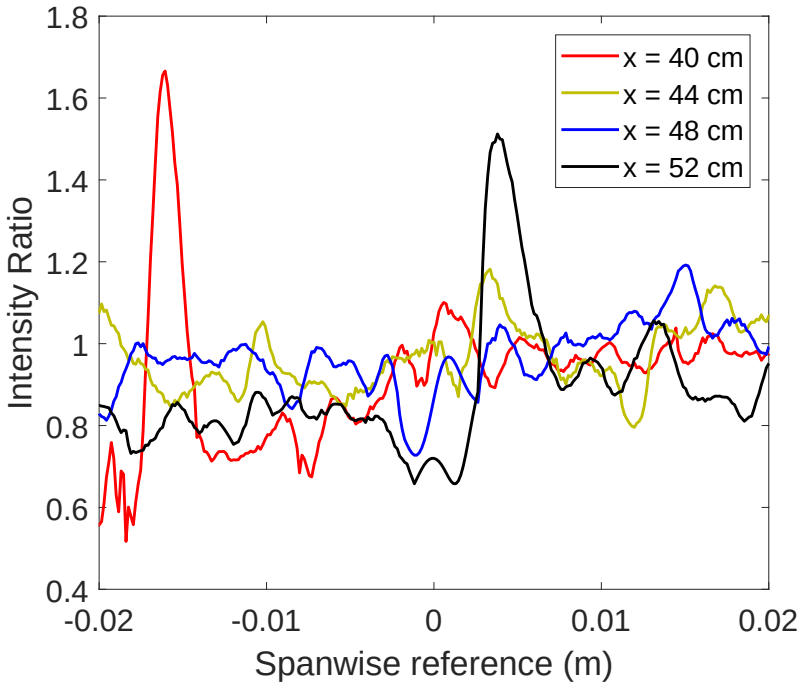

Figure 4.6. Image intensity of oil-flow visualization along vertical slices at $Re_\infty = 11.1 \times 10^6$ m^{-1}. Run OIF.4

4.1.4 Leaking Suction System

The first iteration of the suction-system piping leaked due to design flaws. These leaks resulted in an internal-model pressure too high for sonic suction. However, the test showed that the suction system could remove air from the model during a run. A comparison of the pressure in the model plenum for runs with and without suction enabled is shown in Figure 4.7. Both runs were made in quiet flow with an initial stagnation pressure of 28.9 psia, and the surface-static pressure of 1.87 Torr. At the time of this entry, the BAM6QT maximum quiet pressure was 28 psia, and no higher Reynolds number measurements were made.

After this entry, the suction-system design was revised. The revision is detailed in Section 3.2.2.

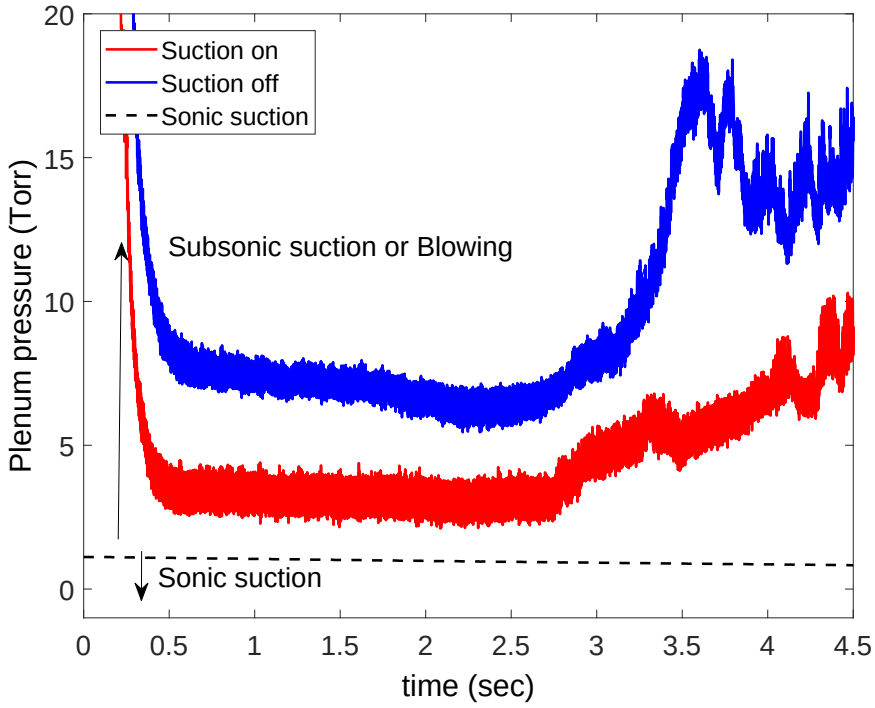

Figure 4.7. Comparison of the static pressure in the model plenum with the leaking suction system on and off. $p_{0,i} = 28.9$ psia for both. Run SAF.12-13

4.2 Baseline Results with Smooth Plenum Insert

Presented here are measurements with the smooth insert in place of the suction section. These measurements establish the baseline to compare with the suction measurements. The runs presented in this section use the reference number Smooth.N as logged in Section A.6 of Appendix A. All measurements were made under quiet flow.

4.2.1 Surface Pressure Fluctuations

Zeroing Angle of Attack

For a model at 0° angle of attack, the peak frequency of the second-mode instability should be uniform around the azimuth at any given streamwise location. Using this principle, small adjustments were made to the angle of attack of the model until the peak second mode was approximately identical.

The PSDs of the pressure fluctuations measured before adjustments to the angle-of-attack are shown in Figure 4.8. The pressure fluctuations were measured with three PCBs on the flare at 0°, 90°, and 180° around the model azimuth, PCB1, PCB2, and PCB3, respectively. These sensors are located at $x = 45.0$ cm, where x is the axial distance from the model nosetip. The wire for PCB4 at 270° broke during installation and was unusable for zeroing the angle of attack. A second-mode instability peak was measured at 106 kHz on PCB3. No peak seemed to be measured on PCB1 or PCB2 which may have been attributed to lee-side, forward transition. A full, clockwise turn of the alignment screws at 0° and 90° was applied. A corresponding, counter turn was applied at 180° and 360°. A full turn of an alignment screw corresponds to an approximate 0.11° change in the model angle of attack.

After the adjustment, the PSDs of the pressure fluctuations are as shown in Figure 4.9. The peak frequency measured by each sensor was measured within 3 kHz of 110 kHz. Similarly, Turbeville and Chynoweth reported peak-frequency alignment within

4 and 2 kHz, references [44] and [45] respectively. Harmonics of the three peaks are seen around 220 kHz.

The peak frequency from PCB3 apparently shifted 4 kHz for a 0.11° change in angle of attack. As the peak frequencies around the azimuth are within 3 kHz of each other, the model angle of attack is assumed to be within ±0.08° of 0°.

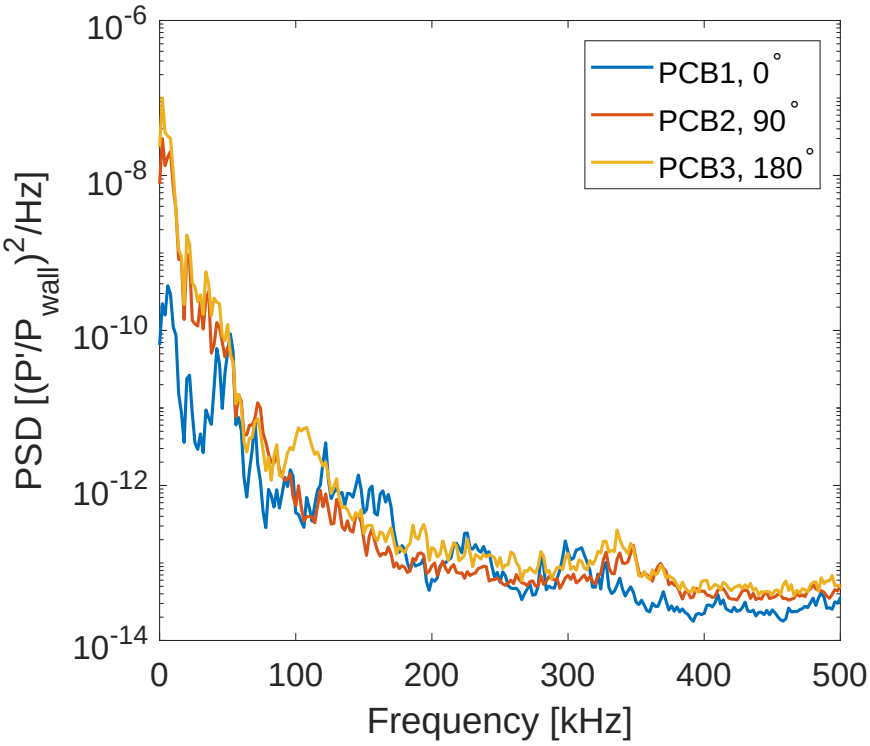

Figure 4.8. PSDs of PCB1, PCB2, and PCB3 before model alignment. $Re_\infty = 10.3 \times 10^6$ m^{-1}. Run Smooth.1

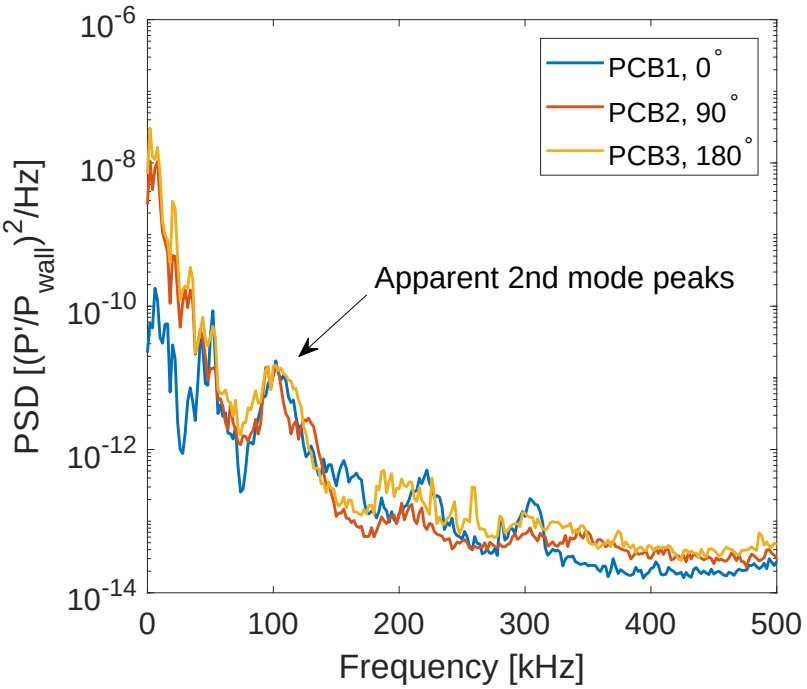

Figure 4.9. PSDs of PCB1, PCB2, and PCB3 after model alignment. $Re_\infty = 10.3 \times 10^6$ m^{-1}. Run Smooth.3

Second-mode Instability

With decreasing Reynolds number, the peak frequency of the second-mode instability appears to decrease slightly as shown in Figure 4.10. This would be expected as the boundary-layer thickness is typically thicker with decreasing Reynolds number. The measurements were made at $x = 47.5$ cm. The peak frequency decreases from around 118 kHz at $Re_\infty = 11.3 \times 10^6$ m^{-1} to 114 kHz at $Re_\infty = 9.82 \times 10^6$ m^{-1} At $Re_\infty = 8.38 \times 10^6$ m^{-1}, the peak of the second mode is difficult to distinguish. As described in Section 2.3.2, frequencies were chosen at the apparent center of the peak in the PSD.

A common indicator of boundary layer transition is an increase in broadband noise. No broadband spectral filling is observed indicating the boundary layer is laminar.

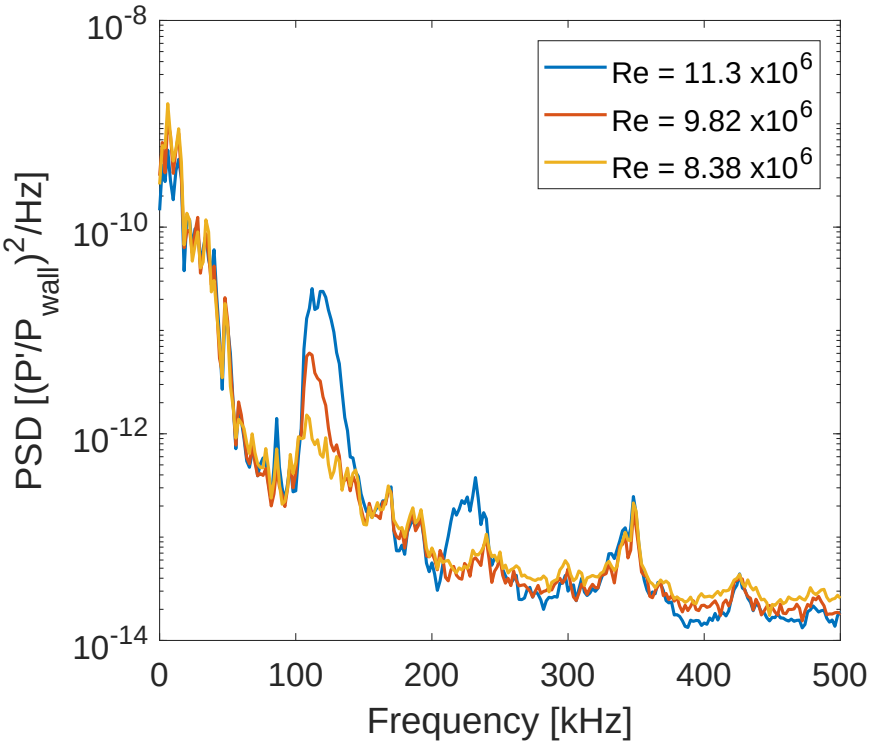

Figure 4.10. PSDs of PCB5 (x = 47.5 cm) with decreasing Reynolds number. Run Smooth.3, 4, 5

Per Li et al. [19], the most-amplified second mode should not grow significantly downstream of x = 46.0 cm. This is reflected in the PSD of PCB1 (x = 45.0 cm) and PCB5 (x = 47.5 cm) in Figure 4.11. For the data shown, the freestream unit Reynolds number is 11.3×10^6 m^{-1}. The peak frequency increased from 116 kHz at x = 45.0 cm to 118 kHz at x = 47.5 cm. As the wire for the sensor at x = 52.6 cm broke during the entry, no further downstream measurements are available. The measurement at x = 47.5 cm measured a 40% increase in RMS fluctuations, as listed in Table 4.1.

To check the repeatability of the results, two runs with similar conditions were made in one entry. The PSDs of the surface-pressure fluctuations at x = 47.5 cm for the two runs are shown in Figure 4.12. For both signals, Re_∞= 10.8×10^6 m^{-1}. The peak frequency of both occur at f = 110 kHz and RMS pressure fluctuations are

Table 4.1. RMS values for PSDs in Figure 4.11

axial position, x **(cm)**	f_{peak} **(kHz)**	$\frac{p'_{RMS}}{p_{wall}} * 100\%$
$x = 45.0$	116	0.0486%
$x = 47.5$	118	0.0678%

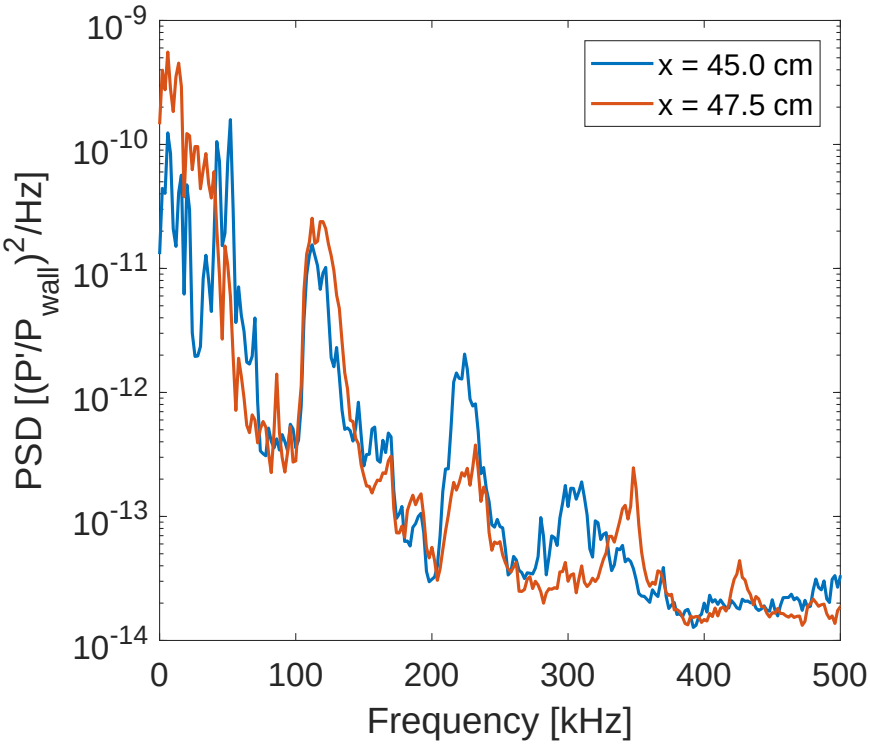

Figure 4.11. PSDs of surface pressure fluctuations at $x = 45.0$ cm and $x = 47.5$ cm. $Re_\infty = 11.3 \times 10^6$ m^{-1}. Run Smooth.3

within $\pm 0.001\%$ of 0.120%. A harmonic was measured in the run labeled Smooth.2 but not Smooth.3.

When the pitot probe is installed in the tunnel, the wake significantly changes the measured surface-pressure fluctuations as shown in Figure 4.13. The PSDs are from the surface-pressure fluctuations at $x = 47.5$ cm with $Re_\infty = 11.3 \times 10^6$ m^{-1}. The probe height, h, is 25 mm above the model in the relevant runs. With the probe in the flow, the model surface is disturbed by the wake, the second-mode peak becomes indistinguishable, and a small broadband spectral increase is measured.

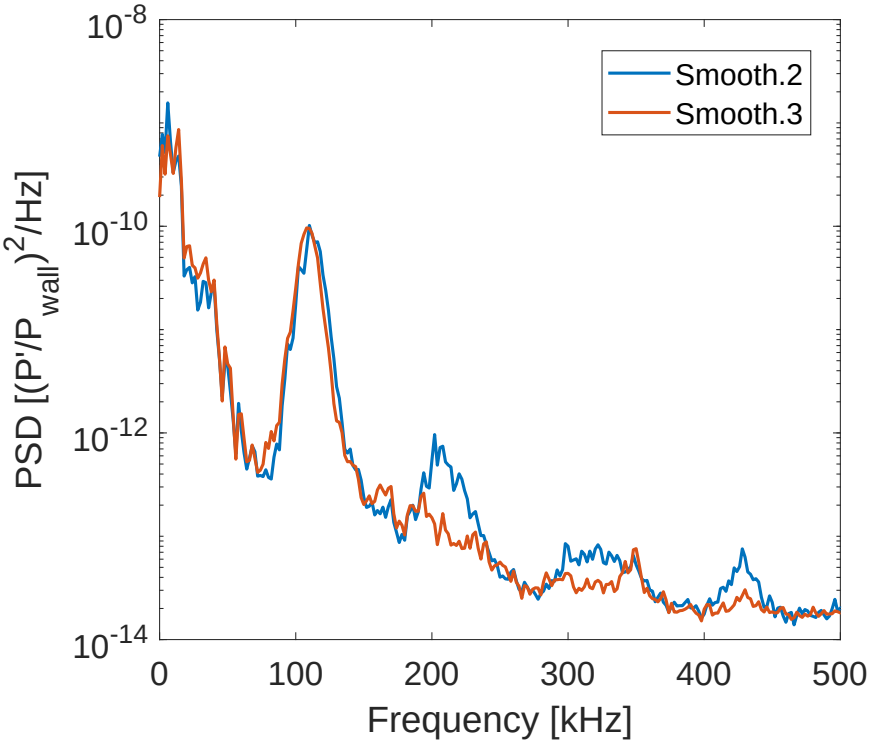

Figure 4.12. PSDs of surface-pressure fluctuations at $x = 47.5$ cm showing repeatability of results. $Re_\infty = 10.8 \times 10^6$. Run Smooth.2, 3

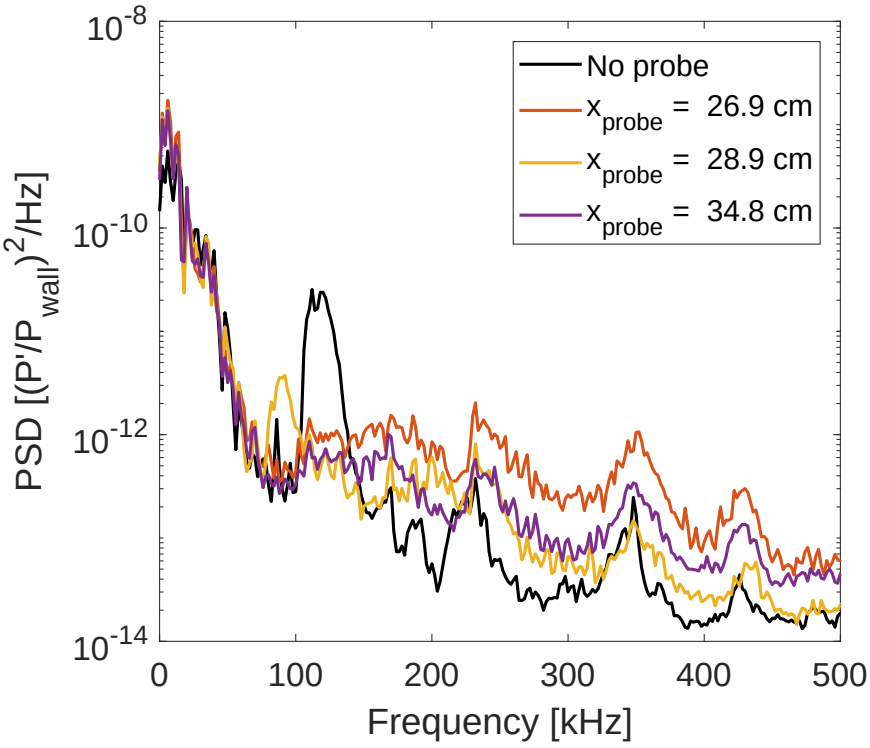

Figure 4.13. PSDs of surface-pressure fluctuations at $x = 47.5$ cm for runs with and without the pitot probe. $Re_\infty = 11.3\times10^6$ m^{-1}, $h = 25$ mm. Run Smooth.3, 8, 14, 20

4.2.2 Surface Heat Transfer

The Schmidt-Boelter gauge was not functioning during the runs without the pitot probe in the tunnel. The heat transfer measurements shown below have the probe in the flow. However, the wake of the probe affects the surface heat transfer as shown in Figure 4.14. The probe is drawn to scale in the flow above the model at $x = 26.9$ cm and $h = 25$ mm. The Mach line, at Mach 6.0, from the probe impinges on the model near where an increase in heating is measured.

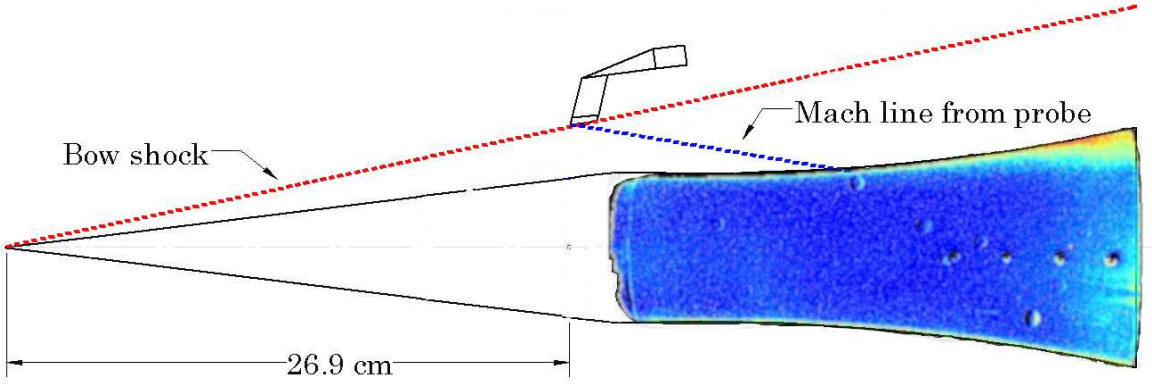

Figure 4.14. To-scale depiction of the Mach line from the pitot probe impinging on the top of the model. The pitot probe is located at $h =$ 25 mm and $x = 26.9$. $Re_\infty = 11.3 \times 10^6$ m^{-1}. Run Smooth.8

Figure 4.15 shows the surface heat transfer on the model at $Re_\infty = 11.3 \times 10^6$ m^{-1}. The pitot probe is located at $h = 25$ mm and $x = 26.9$ cm. The freestream conditions were $p_0 = 149$ psia and $T_0 = 425$ K. The high heating on the top of the model is again from the wake of the probe. The higher heating below the main sensor array are likely due to the chip in the upstream edge of the paint.

Figure 4.16 shows the surface heat transfer on the suction model at $Re_\infty = 8.77 \times 10^6$ m^{-1}. The pitot probe is located at $h = 20$ mm and $x = 28.9$ cm. The freestream conditions were $p_0 = 103$ psia and $T_0 = 397$ K. Again, the high heating on the top of

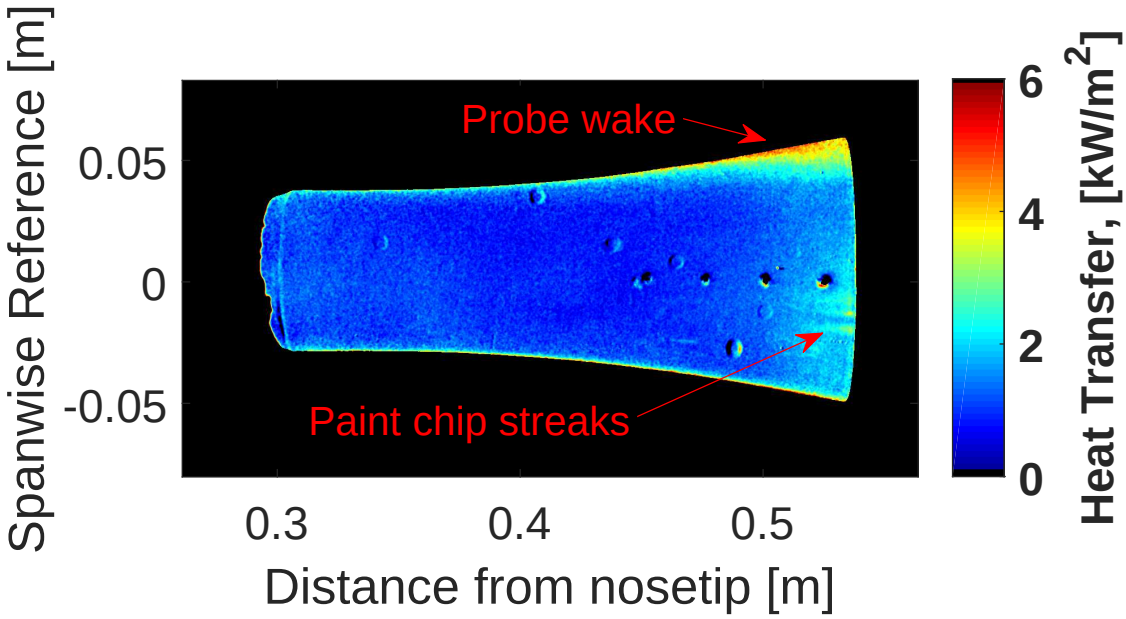

Figure 4.15. Surface heat transfer with the smooth insert with Re_∞ = 11.3×10^6 m^{-1}. The pitot probe is located at h = 25 mm, x = 26.9 cm. Run Smooth.8

the model is from the wake of the probe. The probe wake shows an influence on the aft end of the model that spreads azimuthally.

The heat transfer of two runs is averaged along a narrow axial slice at a spanwise reference of -0.01 as depicted in Figure 4.17. Shown in Figure 4.18, there is a decrease in heat transfer upstream of x = 0.45 m in either case, but higher heating is measured with higher Reynolds number. Downstream of x = 0.45 m, the heat transfer increase begins to increase rapidly. Li et al.'s heat transfer calculation with Re_∞ = 12.13 ×10^6 m^{-1} is also shown in the figure for comparison. From both Li et al.'s and Hollender et al. mean flow calculations [19] and [21], the heat transfer on the flare is predicted to steadily increase with axial distance from nosetip. The disagreement with computations is likely a limitation of the accuracy of TSP.

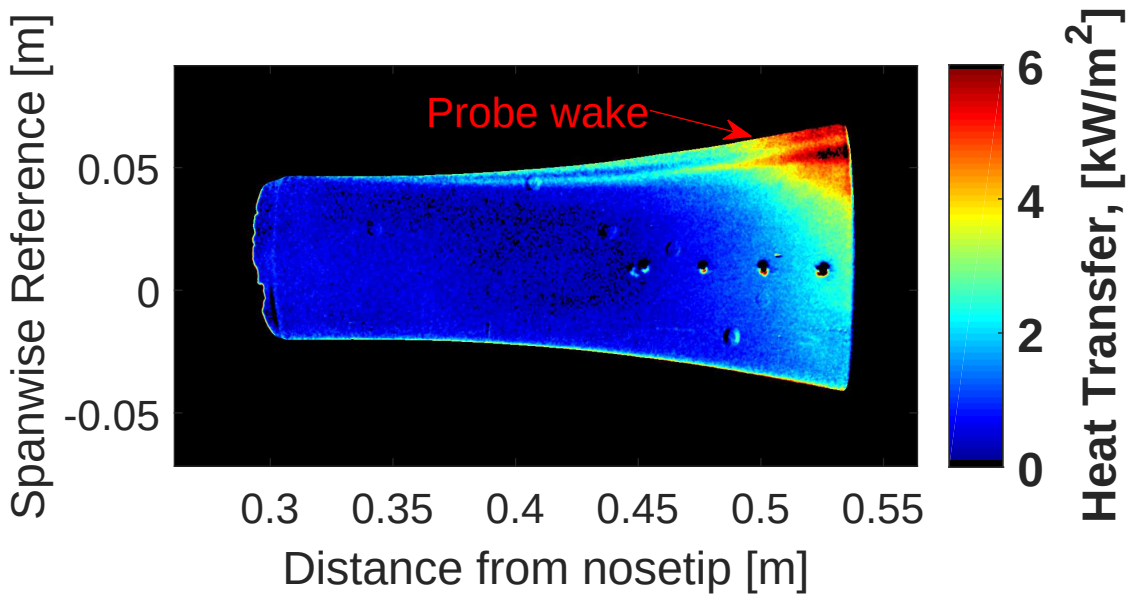

Figure 4.16. Surface heat transfer with the smooth insert with Re_∞ = 8.77×10^6 m^{-1}. The pitot probe is located at h = 20 mm and x = 28.9 cm. Run Smooth.10

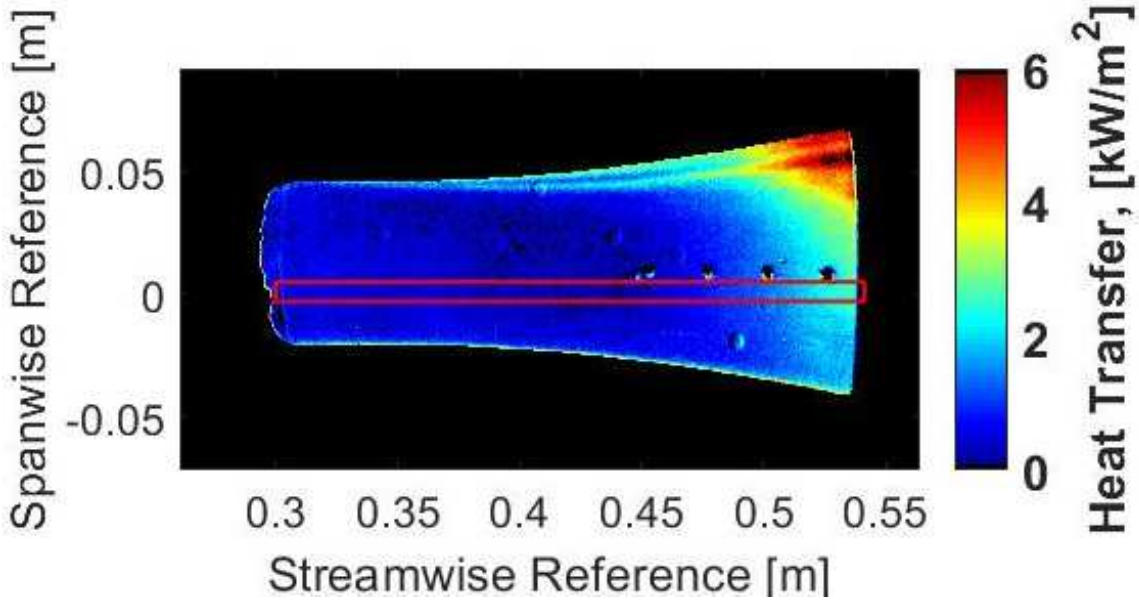

Figure 4.17. Depiction of region where heat transfer was spanwise averaged for Figure 4.18. Run Smooth.10

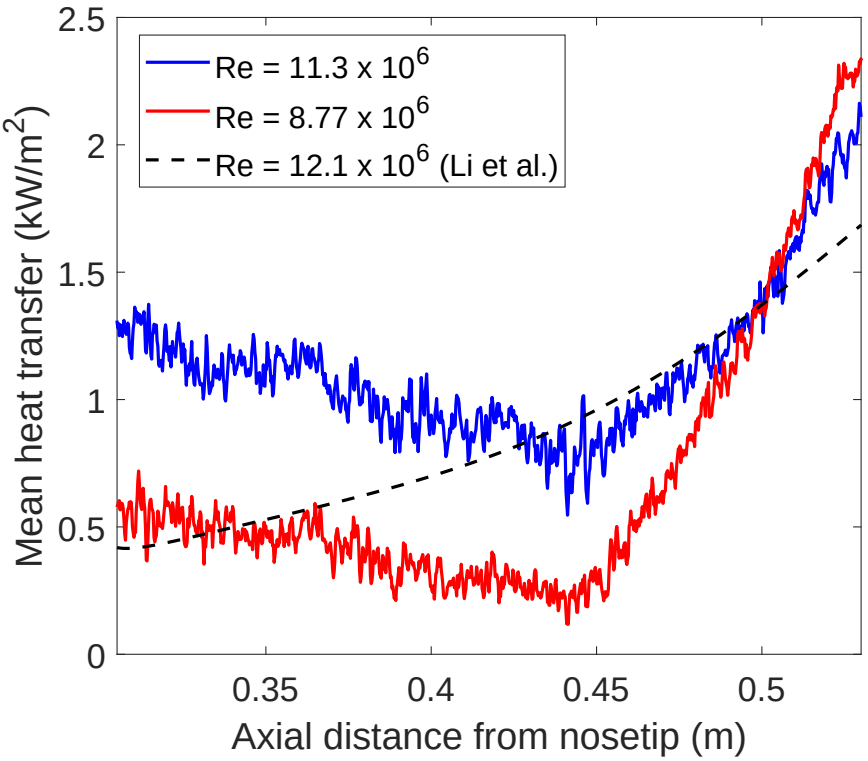

Figure 4.18. Heat transfer averaged along a narrow spanwise slice below the main sensor array for different Reynold's numbers. Also plotted is Li et al.'s mean flow heat transfer [19]. Run Smooth.8 and Smooth.10

4.2.3 Pitot Probe Measurements

As discussed in Section 2.3.4, the pitot probe traverses the flow near the model surface. The probe measures the mean pitot pressure and the pressure fluctuations near the model and in the freestream above the model. A set screw was found to be missing from the probe mount which could have allowed the probe to deflect up to 0.5 cm in the vertical direction. The deflection could occur both when setting the zero position and during runs. As such, all reported vertical positions with the smooth plenum are nominal. Low-pressure no-flow noise measurements were not made for the probe sensor during the entry.

Mean Pitot Pressure

The normalized mean pitot pressures measured 26.9 cm axially from the nosetip are shown in Figure 4.19. The drop in pressure, as seen between $h = 10$ and 15 mm with $p_{0,i} = 155$ psia, occurs when the pitot probe crosses the model bow shock. In the $p_{0,i} = 155$ psia case, the probe crosses the shock between 10 and 15 mm above the model. This is closer to the model than the expected 24.0 mm from the Taylor-Maccoll solution. Also plotted are the expected heights of Mach waves from the beginning and end of suction. The error in vertical position is likely an effect of the probe wiggling when setting the zero position. In the 135 psia case, the probe crosses the shock 30 to 35 mm above the model. Figure 4.20 shows the locations where the pitot probe measurements were nominally made, overlaid with the Mach contours from the Langley computations.

Similar normalized mean pitot pressure plots for the pitot probe positioned at $x =$ 28.9 and 34.8 cm are shown in Figures 4.21 and 4.22, respectively. From the Taylor-Maccoll solution, the shock height at $x = 25.8$ cm is 25.8 mm, and for $x = 34.8$ cm is at 31.0 mm. For the measurements 34.8 cm from the model nosetip, the expansion from the model turn decreased the measured mean pitot pressure. In most cases, the

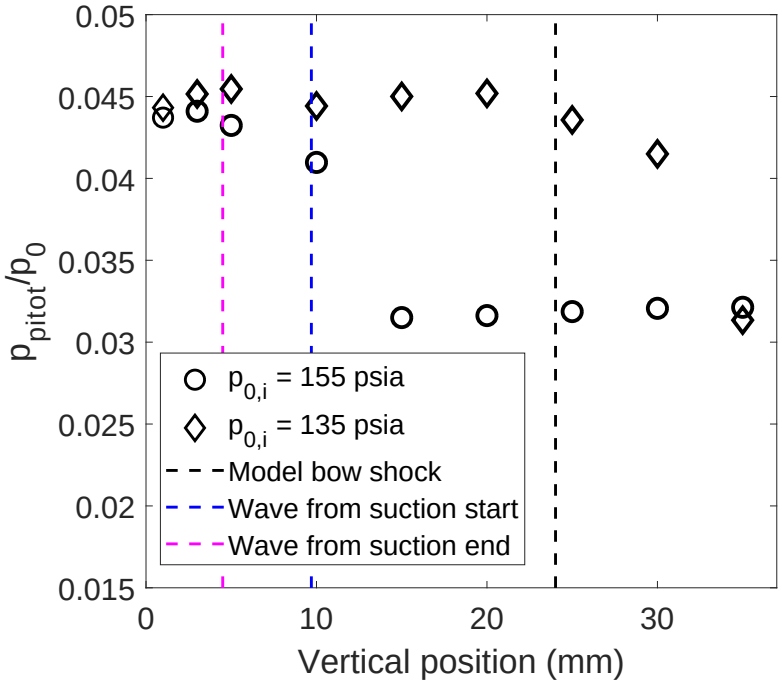

Figure 4.19. Normalized mean pitot pressures above the model 26.9 cm axially from the nosetip. Runs Smooth.6-11

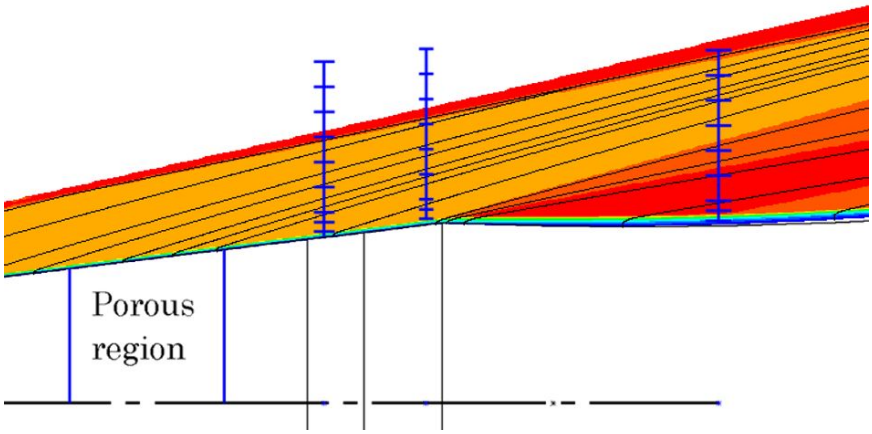

Figure 4.20. Mach lines from Li et al. computations overlaid with the pitot-probe measurement locations

pitot measures a sudden change across a shock. However, quantitative comparisons are not possible due to the uncertainty in the pitot location.

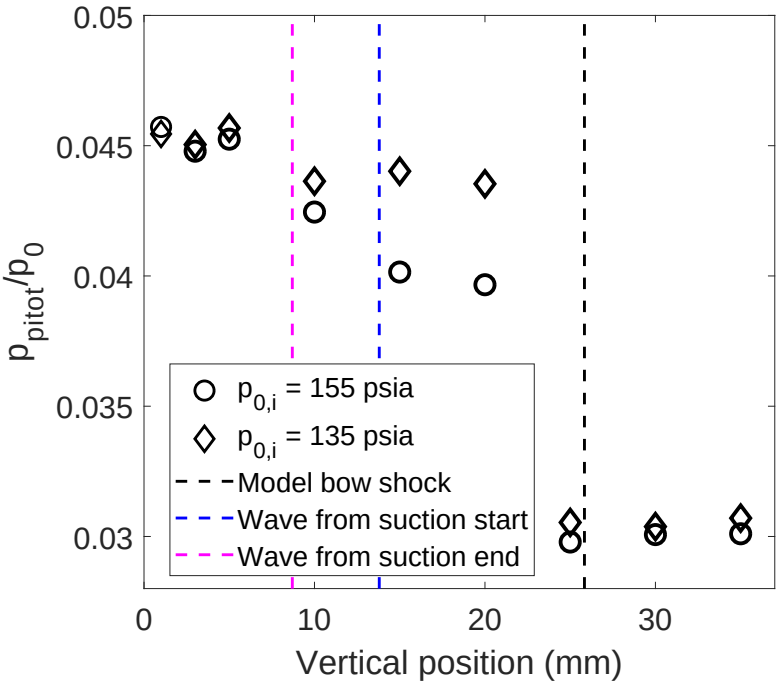

Figure 4.21. Mean pitot pressures above the model 28.9 cm axially from the nosetip. Runs Smooth.12-17

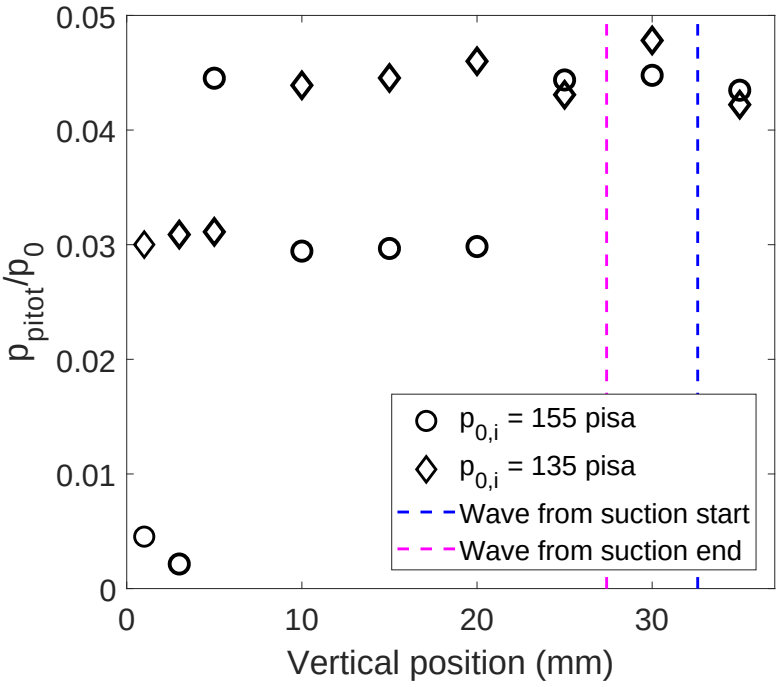

Figure 4.22. Mean pitot pressures above the model 34.8 cm axially from the nosetip. Runs Smooth.18-23

Frequency Content

Figure 4.23 shows the PSDs for the pitot fluctuations normalized by the mean pitot pressure, measured 26.9 cm axially from the nosetip, for vertical positions at 1, 10, and 25 mm. In Figure 4.23(a), $Re_\infty = 11.3\times10^6$ m^{-1}. Similarly Figure 4.23(b) is at $Re_\infty = 9.87\times10^6$ m^{-1}. A broad increase in power is measured centered around 57 kHz in both conditions. The spectral content does not appear to change significantly for the different vertical positions or Reynolds numbers. As unstopped, electronic noise levels were not measured during this entry, it is difficult to distinguish individual peaks from noise.

Figure 4.24 shows the PSDs for the pitot fluctuations measured at $h = 25$ mm, for axial positions of 26.9, 28.9, and 34.8 cm. The Reynolds number is 11.3×10^6 m^{-1} for all three PSDs. A broad increase in spectral content is measured around 57 kHz. There is not a significant, apparent change in the spectral content for the different axial positions.

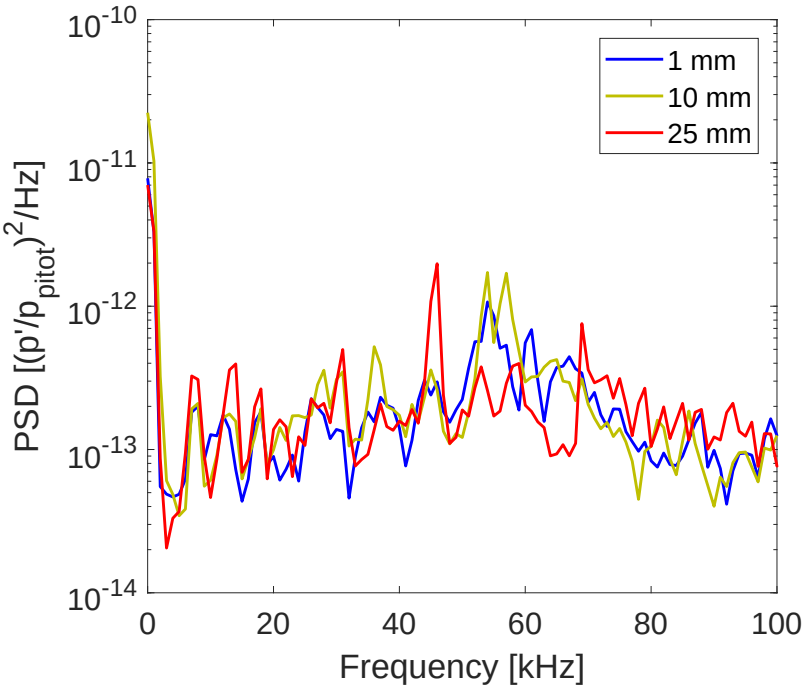

(a) $p_{0,i} = 155$ psia. Run Smooth.6:8

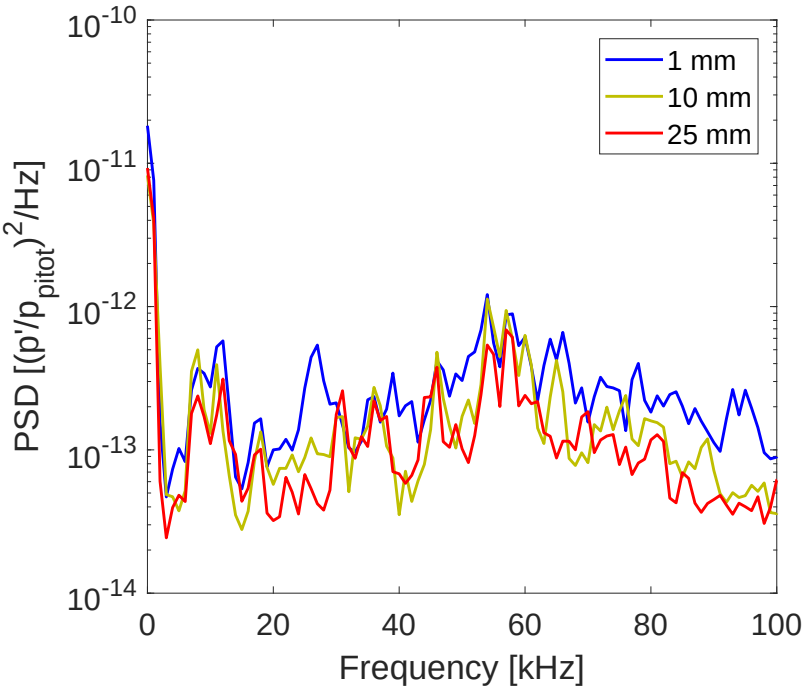

(b) $p_{0,i} = 135$ psia. Run Smooth.9:11

Figure 4.23. PSD of pitot fluctuations measured 26.9 cm from the nosetip at $Re_\infty = 11.3\times10^6$ and $Re_\infty = 9.87\times10^6$.

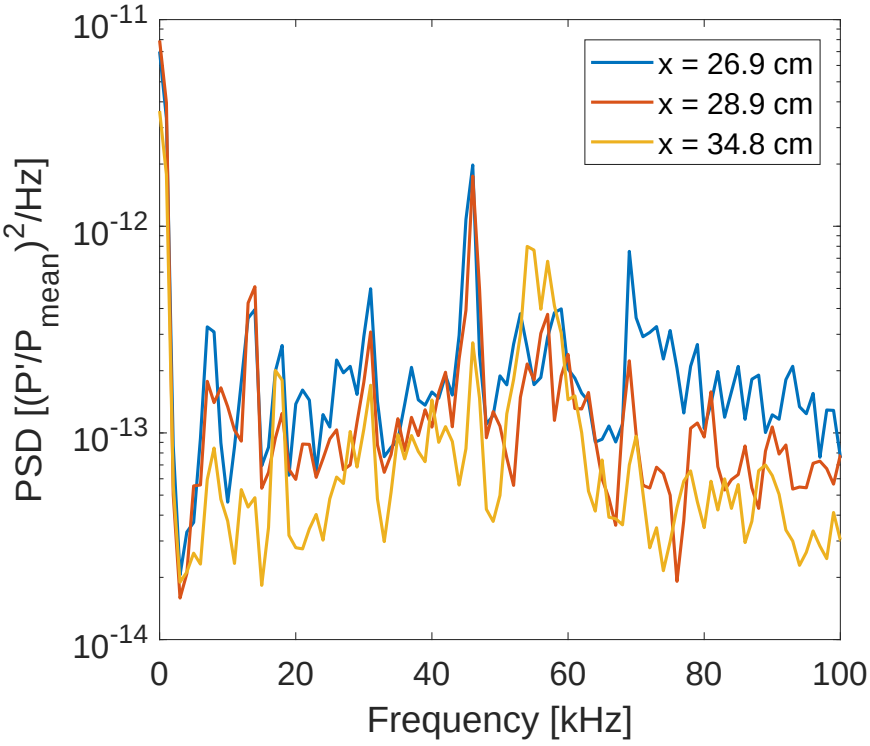

Figure 4.24. PSDs of pitot fluctuations measured at $h = 25$ mm for three axial positions. $Re_\infty = 11.3\times10^6$. Run Smooth.8, 14, 20

Noise Levels

The PSDs of the normalized pitot fluctuations were integrated from 0 to 100 kHz to obtain the magnitude of RMS pressure fluctuations. Figure 4.25 shows the noise levels measured 26.9 cm axially from the nosetip for $p_{0,i}$ = 155 psia and 135 psia runs. The measured noise levels are all within ±0.005% of 0.011% which is an order of magnitude less than the quiet flow threshold of 0.1%. The scatter in the signal may be an effect of the probe wiggle. Noise levels are comparable inside and outside the model bow shock. Also shown are the expected heights of the Mach waves from the locations corresponding to the leading and trailing edges of the porous region, but note that there is no suction with the blank.

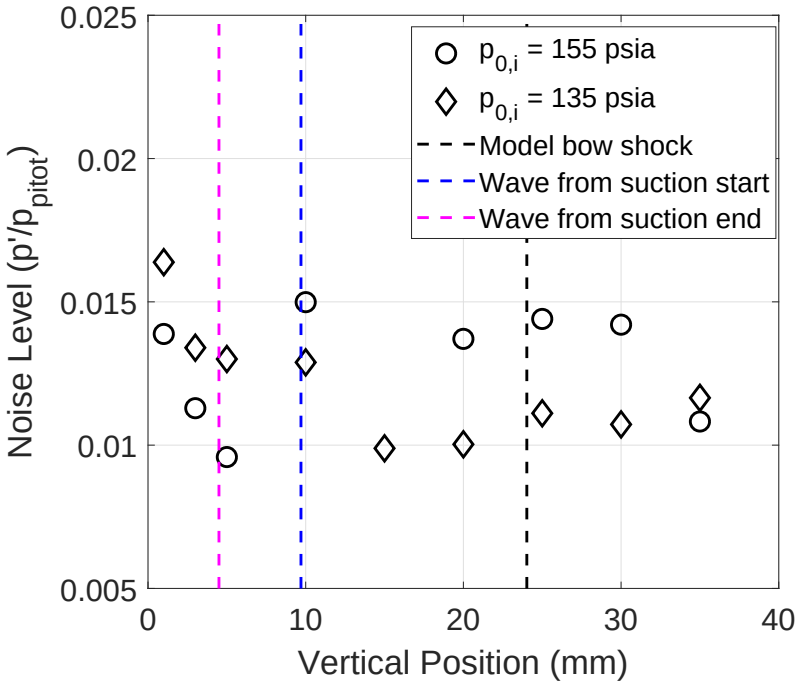

Figure 4.25. Noise level measured in each vertical position above the model 26.9 cm axially from the nosetip. Runs Smooth.6-11

Noise level measurements at 28.9 cm from the nosetip are presented in Figure 4.26. For measurements 28.9 cm from the nosetip, noise levels are similar to the 26.8 cm

measurements and are in the quiet regime. The noise levels are all within ±0.002% of 0.009%. In Gray's measurements of noise levels above a 7° cone at 0° angle of attack, she similarly measured 0.009% at $h = 19$ mm [23].

Noise level measurements at 34.8 cm from the model nosetip are shown in Figure 4.27. The inconsistency between the $p_{0,i} = 155$ psia and the $p_{0,i} = 135$ psia measurements is likely due to the probe wiggle affecting the zero position of the probe. Omitting the high values near the model surface, $h = 1$ and 3 mm with $p_{0,i} = 155$ psia, the noise levels are within ±0.002% of 0.009%. This is shown in Figure 4.28.

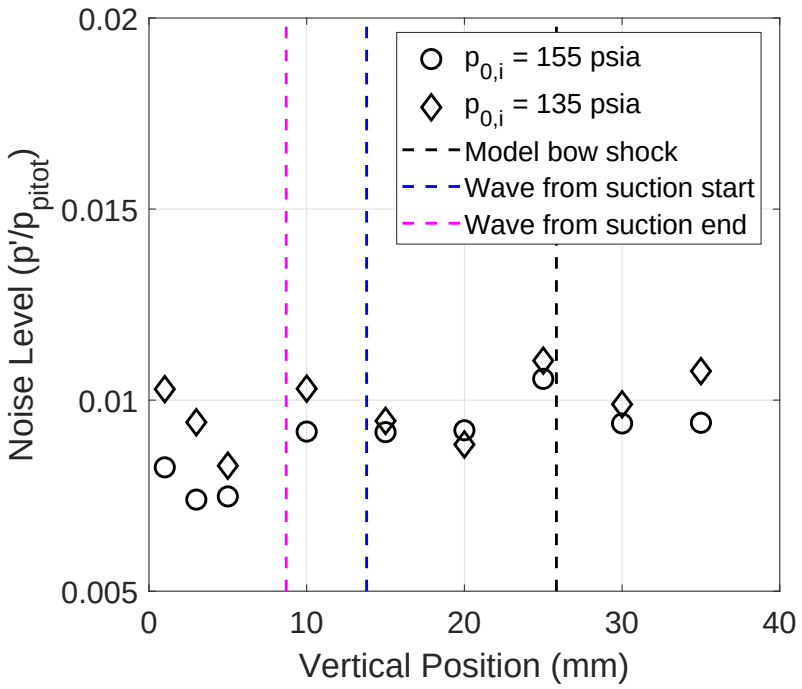

Figure 4.26. Noise levels measured in each vertical position above the model 28.9 cm axially from the nosetip. Runs Smooth.12-17

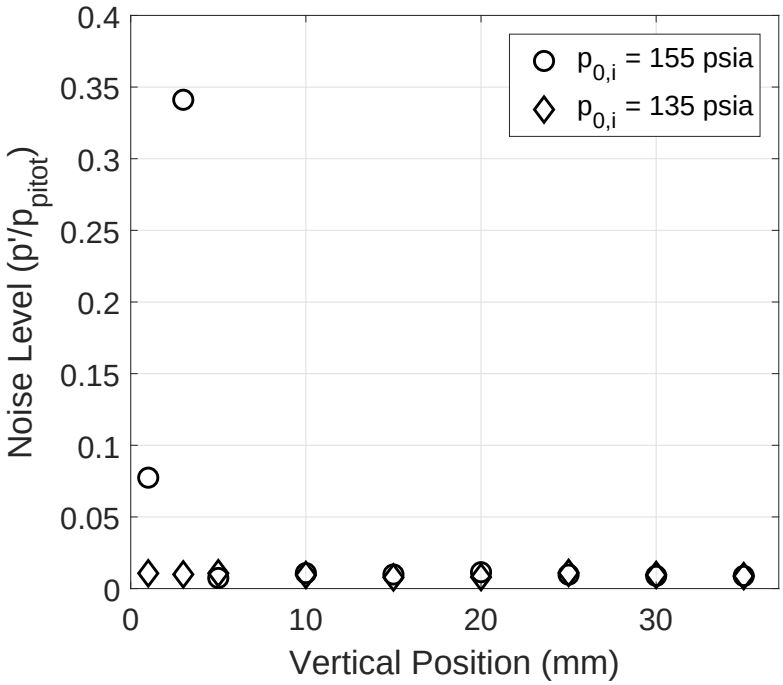

Figure 4.27. Noise levels measured in each vertical position above the model 34.8 cm axially from the nosetip. Runs Smooth.18-23

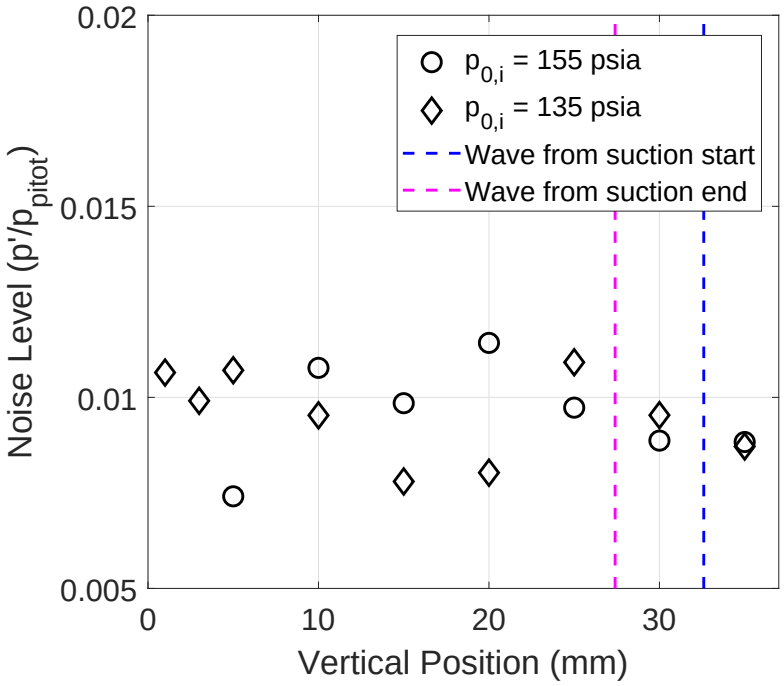

Figure 4.28. Noise levels measured at $x = 34.8$ cm, omitting the high values measured at $h = 1$ and 3 mm with $p_{0,i} = 155$ psia. Runs Smooth.18-23

4.3 Suction Measurements I

The measurements from the first entry using Suction Section 1 are presented here. The pitot probe was in the tunnel for all runs. Due to a mis-design of the location of the alignment hole on the model, the weld on the suction skin was aligned with the main sensor array. Measurements without the weld effects and without the probe are presented in Section 4.4. The runs presented use the reference format Suction Section Entry 1, abbreviated to SS1.N, and are logged in Appendix A.7.

4.3.1 Sonic Suction Through Perforated Skin

The flow through the perforated skin needs to be choked to more accurately predict mass flow and minimize fluctuations radiated from suction. Figure 4.29 shows the static pressure inside the model plenum for a run with $p_{0,i}$ = 155 psia. After 0.35 seconds, the pressure inside the plenum is lower than the pressure required to choke the suction flow through the orifices. The mean pressure in the plenum from 0.5 to 2.0 seconds was 3.45 Torr, and the pressure remains low enough for choked suction until the end of quiet flow at 2.3 seconds. The difference between the measured plenum pressure and the required plenum pressure to maintain sonic flow was around 1 Torr during the run. The pressure in the 6-inch pipe leading to the suction-system vacuum tank increased from 0.36 Torr to 0.38 Torr during the run. The nozzle-wall boundary layer did not appear to separate during runs with $p_{0,i}$ = 155 psia.

Figure 4.30 shows a running average of the plenum pressure from Figure 4.29 with error bars. The running average was calculated with a 0.01 s window. The error bars are placed at discrete times every 0.25 seconds. The sensor has a quoted accuracy of $\pm$0.26 Torr. Including the uncertainty, the plenum pressure is still less than the pressure required for sonic suction.

Figure 4.31 shows the static pressure inside the model plenum for a run with $p_{0,i}$ = 135 psia. After 0.43 seconds, the plenum pressure is low enough to choke the flow. Again, the pressure remains low enough for choked suction until the end of quiet flow

with a margin of about 0.8 Torr. The pressure in the vacuum line increased from 0.21 Torr to 0.24 Torr during the run. The plenum pressure does not appear to be affected by the nozzle-wall boundary-layer separation measured from 1.1 to 2.2 seconds, but the pitot and surface data are influenced. The nozzle-wall boundary layer separated and reattached during most runs with $p_{0,i}$ = 135 psia. The initial time and duration of separation varied between runs. These examples are representative of the plenum pressures measured for runs in this entry.

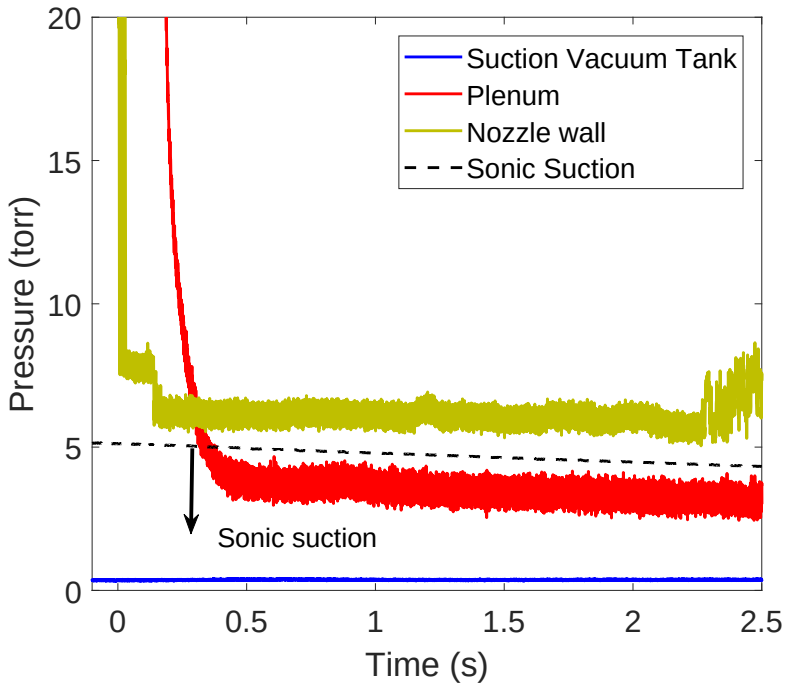

Figure 4.29. Pressure inside the suction plenum from a run with $p_{0,i}$ = 155 psia. Run SS1.6

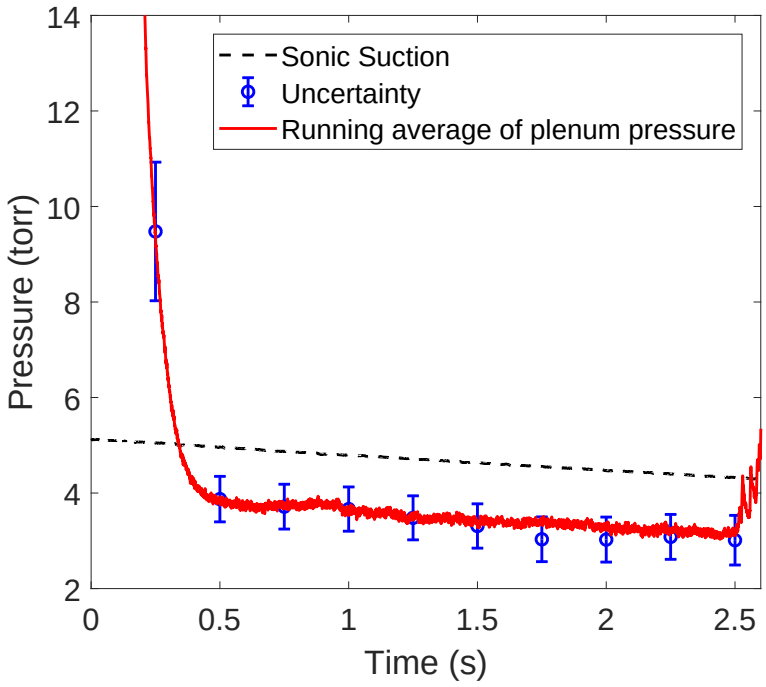

Figure 4.30. Running average of plenum pressure for a run with $p_{0,i}$ = 155 psia with error bars. Run SS1.6

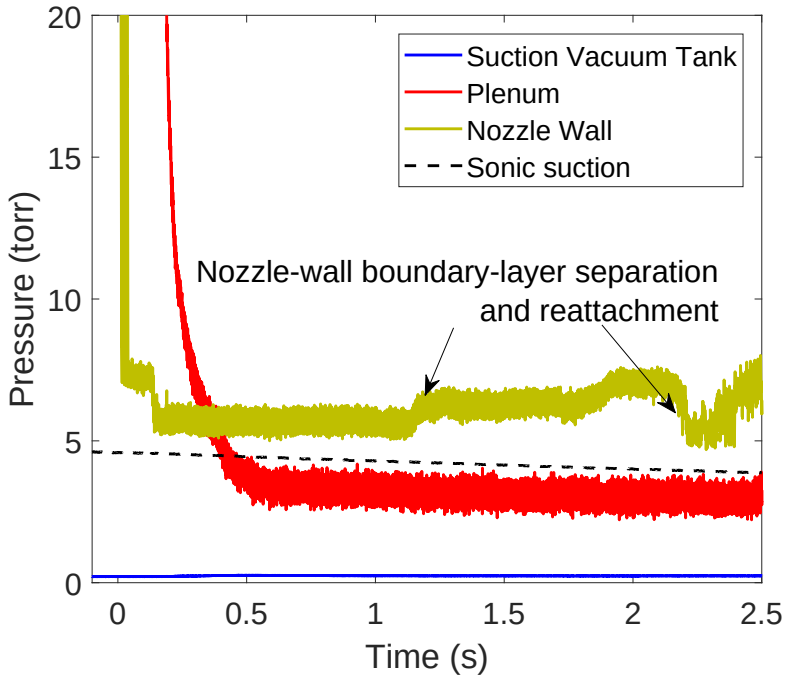

Figure 4.31. Pressure inside the suction plenum for a run with $p_{0,i} =$ 135 psia. Run SS1.14

4.3.2 Surface Pressure Fluctuations

In this entry, several PCB wires broke during installation, including three of the sensors around the azimuth, and the sensor at 47.5 cm from the nosetip. As a result, the model is only nominally at 0° angle of attack. The model was adjusted to be close to 0° by setting a digital protractor on the 7° cone. The model angle was adjusted so that the digital protractor read 7.0°.

Figure 4.32 shows the PSDs measured 52.6 cm from the model nosetip from three different suction runs with $Re_\infty = 10.8 \times 10^6$ m^{-1}. Note the sensor is downstream of the pitot probe. The run conditions are listed alongside the measured second-mode peak frequency and normalized RMS pressure fluctuations in Table 4.2. The peak frequency varies from 98 to 124 kHz. The RMS pressure fluctuations, calculated over the frequency range 70 to 180 kHz, similarly vary from 0.0239% to 1.77%. The inconsistency is likely an effect of the pitot-probe wake.

Detailed in Section 4.4, the peak frequency of the second mode was measured with the model carefully aligned to 0°. A comparison of PSD of the surface-pressure fluctuations for the carefully-aligned case and the nominally 0° angle of attack is shown in Figure 4.33. Both measurements were made at $x = 52.6$ cm with $Re_\infty = 10.8 \times 10^6$ m^{-1}. The pitot probe was not in the tunnel for the carefully aligned case, and the peak frequency is 134 kHz. For the nominally 0° case with the probe at $x = 28.9$ cm and $h = 25$ mm, the peak frequency is 112 kHz. Although it has been shown that the pitot probe influences the peak frequency of the second mode, the lower-frequency peak could also be because the sensor was slightly leeward.

Figure 4.34 shows the PSDs measured at $x = 52.6$ cm at decreasing Reynolds numbers. The pitot probe is fixed at 26.9 cm axially from the nosetip and 25 mm above the model surface. The run conditions and peak frequencies are listed in Table 4.3. In Figure 4.34, the pitot probe is 26.9 cm axially from the nosetip. From unit Reynolds number 11.1×10^6 to 10.8×10^6 m^{-1} the peak frequency decreases from 118 kHz to 110 kHz, and the RMS pressure fluctuations increase from 4.18% to 6.98%.

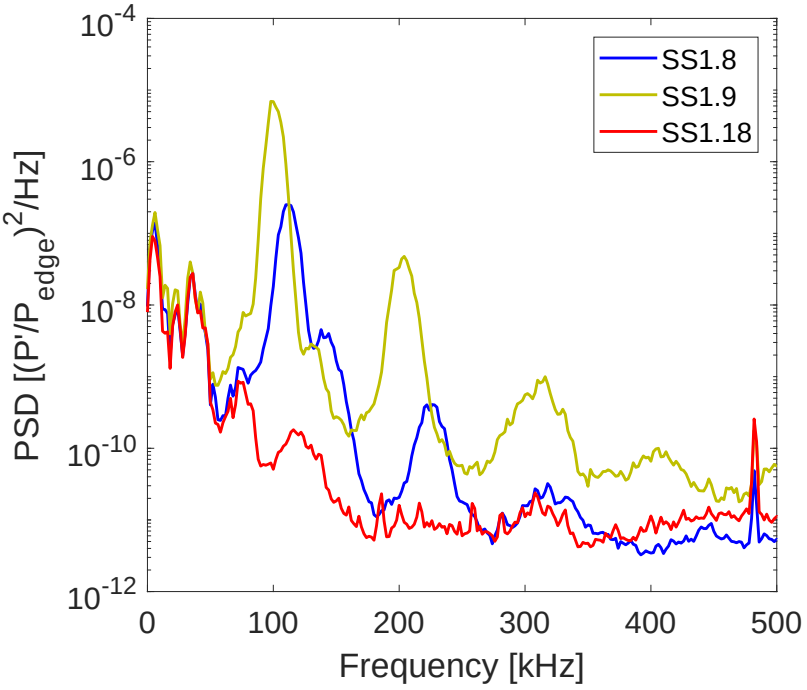

Figure 4.32. PSDs of surface-pressure fluctuations at $x = 52.6$ cm. $Re_\infty = 10.7 \times 10^6$ m^{-1}. Run SS1.8, 9, 18

Table 4.2. Peak second-mode frequency and RMS pressure fluctuations from suction runs with Re_∞ between 10.8×10^6 and 11.1×10^6.

Run reference	Re_∞ **(m^{-1})**	x_{probe} **(cm)**	h_{probe} **(mm)**	f_{peak} **(kHz)**	$\frac{p'_{RMS}}{p_{edge}} \times 100\%$
SS1.6	10.8×10^6	26.9	1	104	0.342%
SS1.7	10.9×10^6	26.9	10	102	0.157%
SS1.8	10.9×10^6	26.9	25	112	0.386%
SS1.9	10.8×10^6	28.9	1	98	1.77%
SS1.10	11.1×10^6	28.9	10	124	0.0628%
SS1.11	11.1×10^6	28.9	25	112	1.18%
SS1.16	10.9×10^6	34.8	1	122	0.0641%
SS1.17	10.9×10^6	34.8	10	112	0.767%
SS1.18	10.8×10^6	34.8	25	118	0.0239%

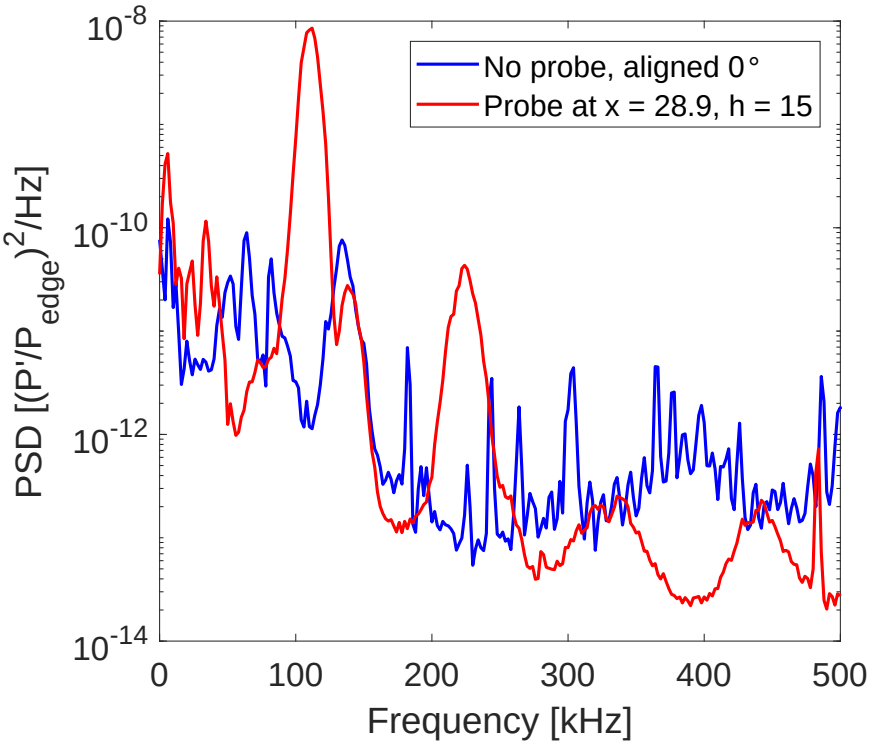

Figure 4.33. PSDs of surface-pressure fluctuations for aligned 0° angle of attack (Refer to Section 4.4) and nominal 0°. $x = 52.6$ cm and $Re_\infty = 10.8 \times 10^6$ m^{-1}. Runs SS1.11 and SS2.10

Table 4.3. Run conditions and peak frequencies for Figure 4.34. Pitot probe is 26.9 cm axially from nosetip. Run SS1.8

$\mathbf{Re_m}$ $\mathbf{(m^{-1})}$	f_{peak} **(kHz)**	$\frac{p'_{RMS}}{p_{edge}} \times 100\%$
11.1×10^6	118	0.268%
11.0×10^6	116	0.386%
10.8×10^6	110	0.448%

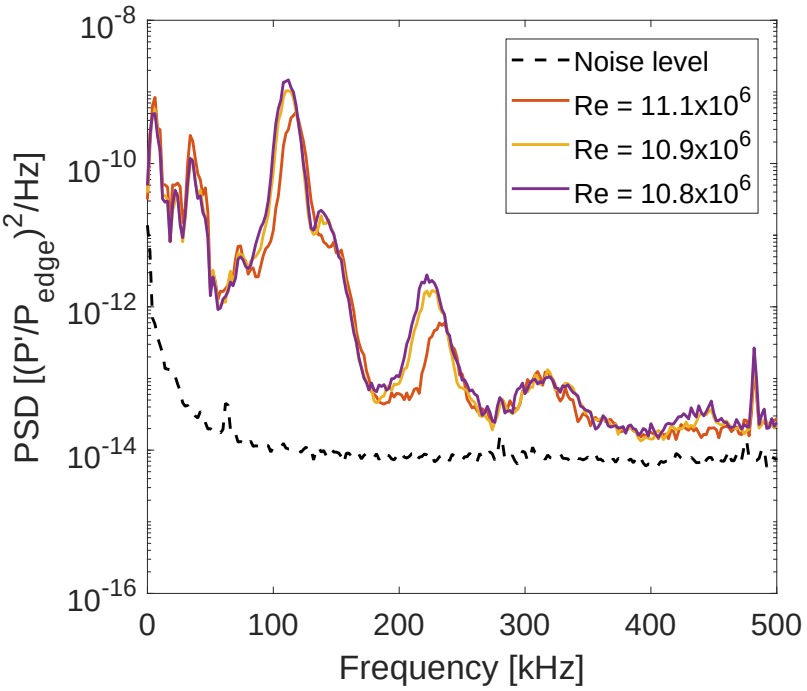

Figure 4.34. PSDs of surface pressure fluctuations at $x = 52.6$ cm at decreasing Reynolds numbers. Pitot probe is 26.9 cm from nosetip and 25 mm above model. Run SS1.8

In Figure 4.35, the pitot probe is 28.9 cm from the nosetip and 25 mm above the model. It is unclear why the peak frequency shifts from 116 to 108 kHz in the higher Reynolds number run, Run SS1.11, but remains at 112 kHz for the lower Reynolds number run, Run SS1.14. The RMS pressure fluctuations are lower for the lower Reynolds number run as shown in Table 4.4.

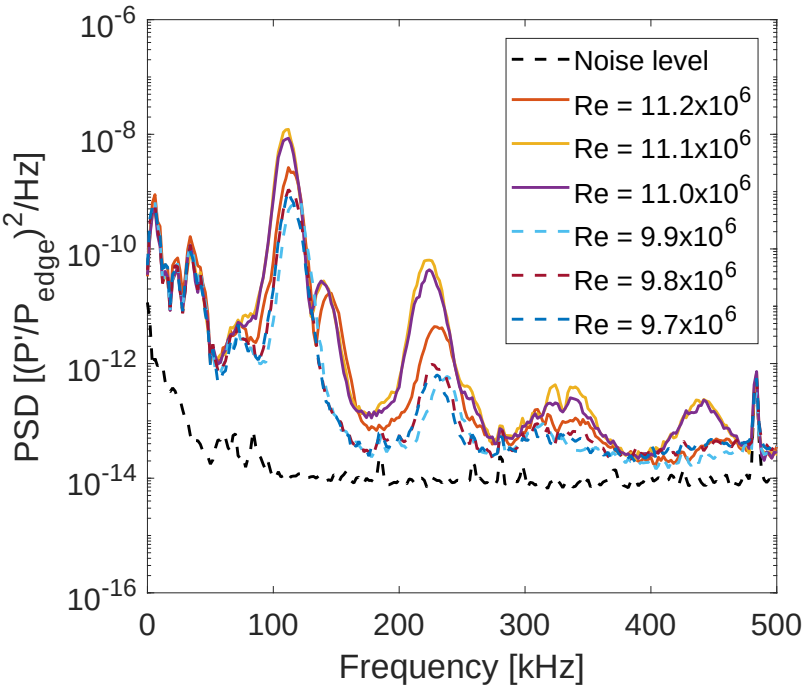

Figure 4.35. PSDs of surface pressure fluctuations at $x = 52.6$ cm at decreasing Reynolds numbers. Pitot probe is 28.9 cm from nosetip and 25 mm above model. Run SS1.11, 14

Table 4.4. Run conditions and peak frequencies for Figure 4.35. Pitot probe is 28.9 cm axially from nosetip. Run SS1.11, 14

Run reference	$\mathbf{Re_m}$ **(m^{-1})**	f_{peak} **(kHz)**	$\frac{p'_{RMS}}{p_{edge}} \times 100\%$
SS1.11	11.2×10^6	116	0.562%
SS1.11	11.1×10^6	110	1.18%
SS1.11	11.0×10^6	108	1.03%
SS1.14	9.9×10^6	112	0.305%
SS1.14	9.8×10^6	112	0.366%
SS1.14	9.7×10^6	112	0.324%

In Figure 4.36, the pitot probe is 34.8 cm from the nosetip and 25 mm above the model. The peak frequencies shift from 120 to 112 kHz at decreasing Reynolds numbers. Shown in Table 4.5, the RMS pressure fluctuations are an order of magnitude lower than the previous cases.

Table 4.5. Run conditions and peak frequencies for Figure 4.36. Pitot probe is 34.8 cm axially from nosetip. Run SS1.18, 21

Run reference	$\mathbf{Re_m}$ **(m^{-1})**	f_{peak} **(kHz)**	$\frac{p'_{RMS}}{p_{edge}} \times 100\%$
SS1.18	11.0×10^6	120	0.0228%
SS1.18	10.8×10^6	120	0.0239%
SS1.18	10.7×10^6	118	0.0240%
SS1.21	9.80×10^6	112	0.0208%
SS1.21	9.70×10^6	112	0.0217%
SS1.21	9.60×10^6	112	0.0204%

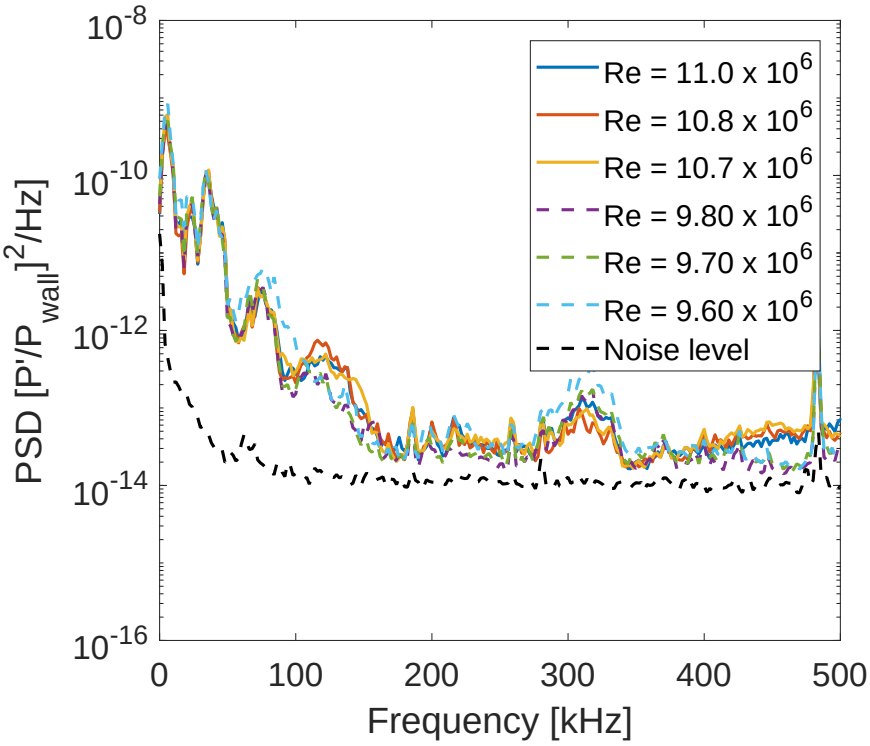

Figure 4.36. PSDs of surface pressure fluctuations at $x = 52.6$ cm at decreasing Reynolds numbers. Pitot probe is 34.8 cm from nosetip and 25 mm above model. Run SS1.18, 21

Comparison to smooth plenum measurements

The PSDs of both a smooth and a suction measurement at $x = 52.6$ cm is shown in Figure 4.37. Table 4.6 lists the flow condition, peak frequency, and RMS amplitudes for the two measurements. The peak frequency increased from 112 to 122 kHz when suction was enabled. This was expected as the boundary layer should be thinner with suction enabled. The RMS amplitude increased from 0.049% to 0.056%. The suction apparently did not introduce large unsteadiness.

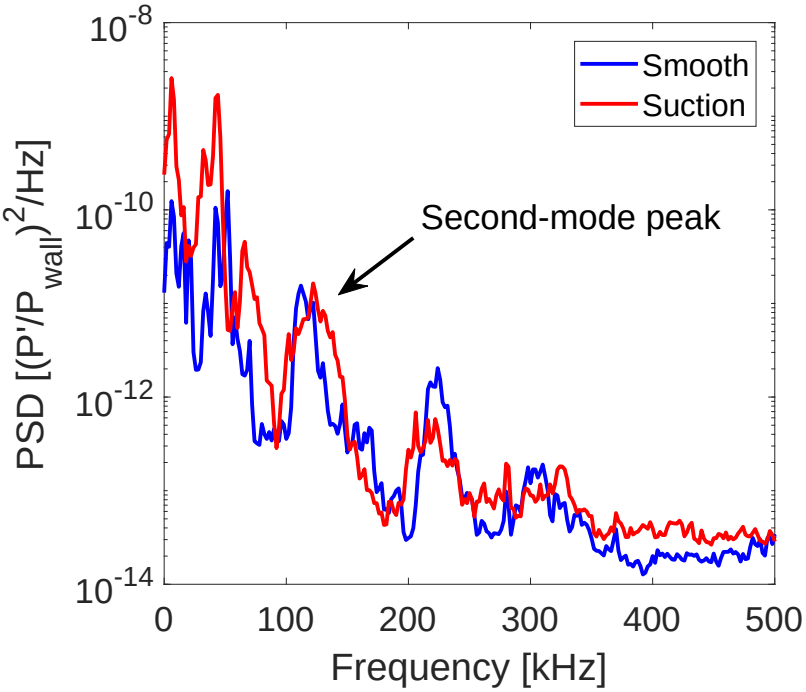

Figure 4.37. PSDs of surface pressure fluctuations at $x = 52.6$ cm with both the baseline and suction measurements. Re_m around 11.2×10^6 m^{-1}. Runs Smooth.3, SS1.8

Table 4.6. Run conditions and peak frequencies for Figure 4.37.

Condition	$\mathbf{Re_m}$ **(m^{-1})**	f_{peak} (kHz)	$\frac{p'_{RMS}}{p_{edge}} \times 100\%$
Smooth	11.3×10^6	112	0.049%
Suction	11.1×10^6	122	0.056%

4.3.3 Surface Heat Transfer

Figure 4.38 shows the surface heat transfer at $Re_\infty = 11.0 \times 10^6$ m^{-1} for a suction-enabled run. The freestream conditions were $p_0 = 146$ psia and $T_0 = 425$ K. The pitot probe is located 25 mm above the model, 26.9 cm axially from the nosetip. The high heating on the top of the model is from the wake of the probe. The streaks of high heating near the main sensor array are likely due to the weld on the suction skin

which was mistakenly aligned with the sensors. Additional streaks are seen below the sensor array, but the cause of these is unknown.

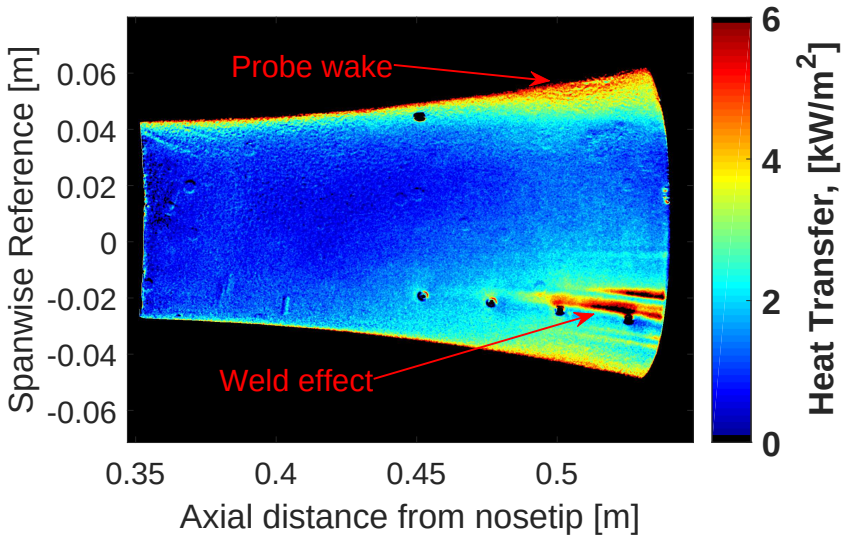

Figure 4.38. Heat transfer on suction model at $Re_\infty = 11.0 \times 10^6$ m $^{-1}$. Run SS1.8

Figure 4.39 shows the surface heat transfer on the suction model at $Re_\infty = 9.9 \times 10^6$ m^{-1}. The freestream conditions were $p_0 = 129$ psia and $T_0 = 423$ K. The pitot probe is located 25 mm above the model, and 28.9 cm axially from the nosetip. Again, the higher heating on the top of the model is due to the wake of the probe, and the high heating near the sensors is likely due to the weld.

A streamwise slice of the heat transfer was taken from Figures 4.38 and 4.39 at spanwise reference 0 m as depicted in Figure 4.40. The heat transfer along the slices are shown in Figure 4.41. The heat transfer starts to increase beyond 0.42 m in both cases, and the magnitudes are similar. The measured heat transfer is slightly higher than the mean-flow prediction from Li et al. As the heat transfer reduced from TSP is typically considered accurate with ±20%, the agreement is fair. It is unclear if

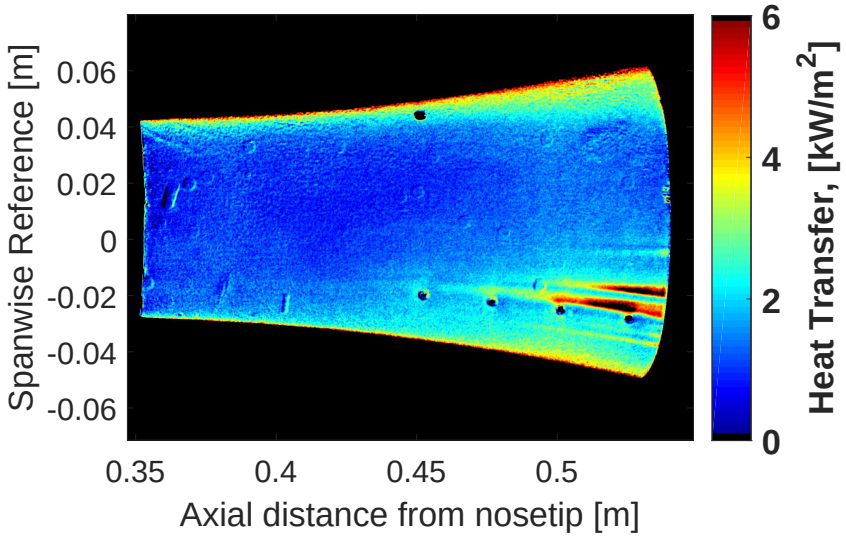

Figure 4.39. Heat transfer on suction model at $Re_\infty = 9.9 \times 10^6$ m^{-1}. Run SS1.14

the heat transfer behavior seen upstream of 0.42 m is real or an effect of the low signal-to-noise ratio of TSP.

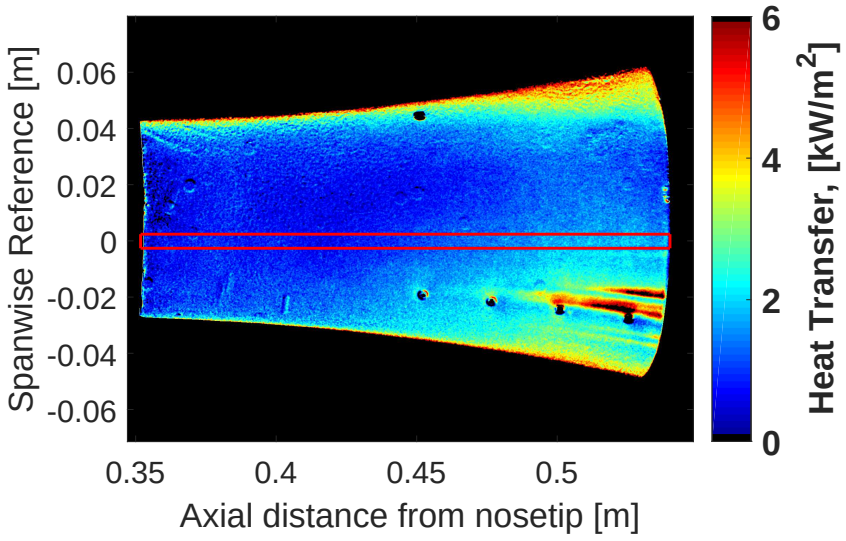

Figure 4.40. Depiction of the slice used when calculating heat transfer as a function of axial location in Figure 4.41.

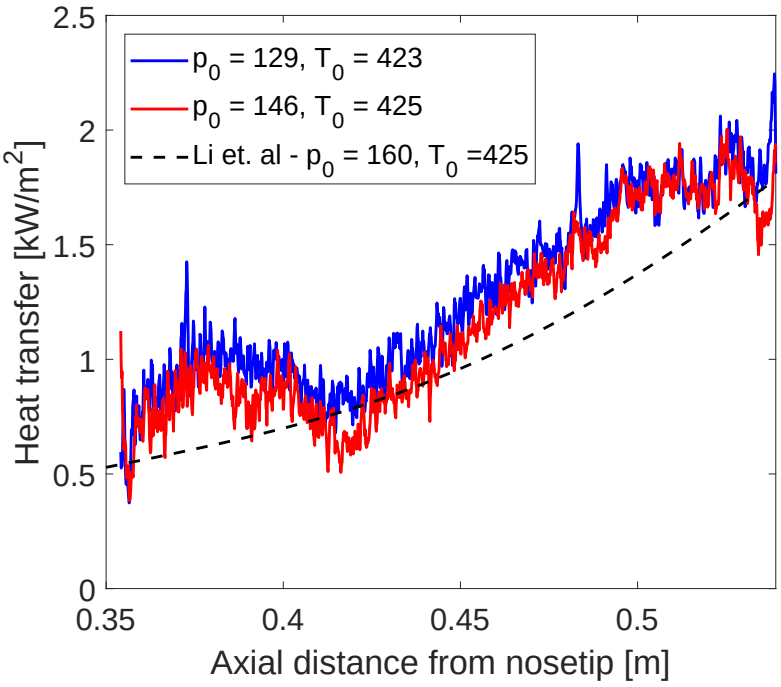

Figure 4.41. Axial change in mean heat transfer from a narrow spanwise slice about spanwise reference of 0 m.

Comparison to smooth plenum measurements

The change in heat transfer to the axial slice as measured with the smooth and suction inserts is shown in Figure 4.42. The Reynolds numbers of the two measurements are similar around $Re_m = 11.1 \times 10^6$ m^{-1}. The heat transfer similarly decreases from $x = 0.35$ m to around $x = 0.43$ m with both cases. Further downstream, the heat transfer increases. Both measurements show fair agreement with computations.

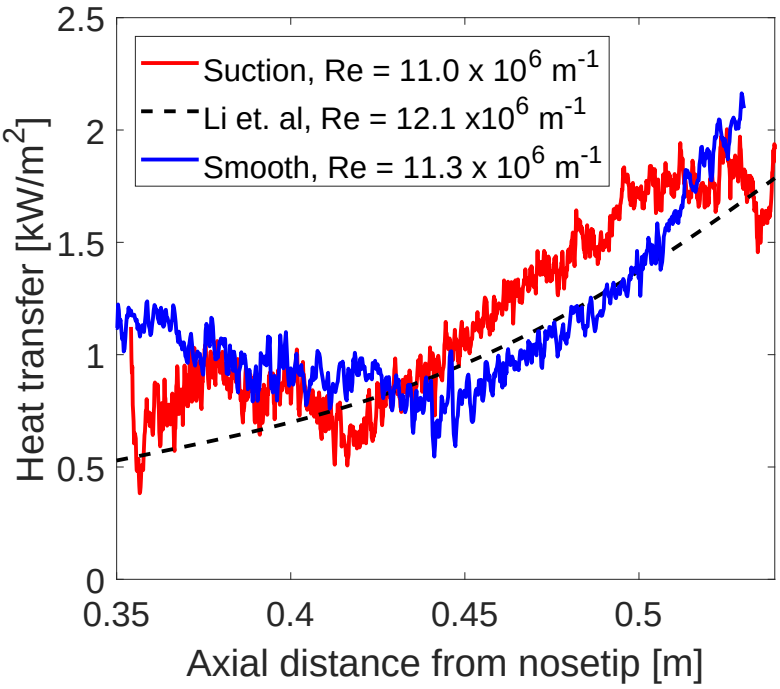

Figure 4.42. Comparison of axial change in heat transfer with both smooth and suction measurements. Runs Smooth.8, SS1.8

4.3.4 Pitot-Probe Measurements

The pitot probe was traversed above the model downstream of the suction section during runs with $p_{0,i} = 155$ and 135 psia. As with the baseline measurements, the set screw was loose for this entry, and vertical positions are only nominal. Electronic noise levels were not measured for this entry.

Apparent Model Boundary-Layer Interaction with Pitot Probe

When the pitot probe was in the position nominally 1 mm above the model surface, some mean pitot pressure measurements show substantial fluctuations. This may have been due to an interaction between the bow shock from the pitot probe and the model boundary layer. Morkovin showed that pitot probe measurements with a pitot diameter comparable to the wall-normal distance can experience local separation and backflow [46].

An example of the measured fluctuation is shown in Figure 4.43(a). The pitot probe is 26.9 cm axially from the model nosetip and measures the flow 1, 3, and 5 mm above the model surface. The run was made with $p_{0,i} = 155$ psia. The power of the measured fluctuations in the 1 mm position is larger than those in the 3 mm position by about 3 orders of magnitude.

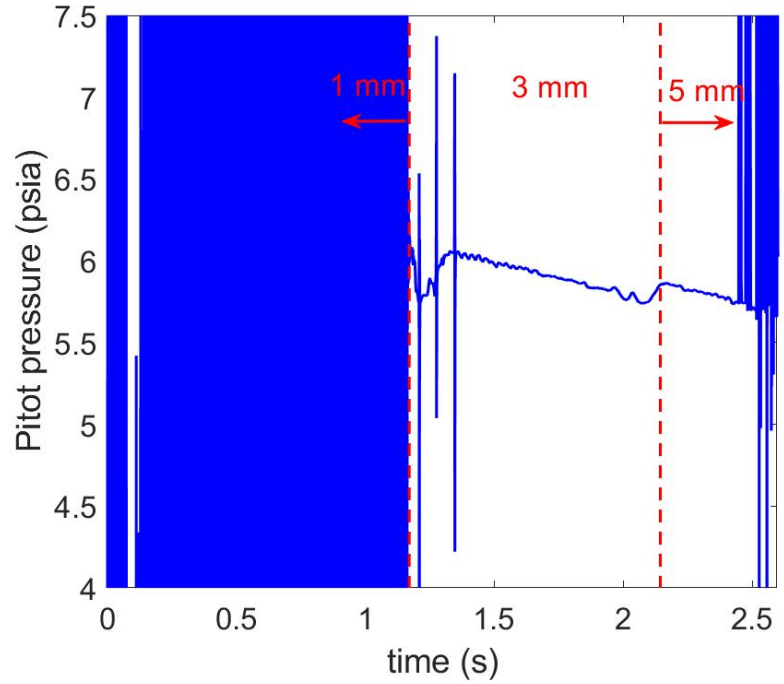

(a) Time trace

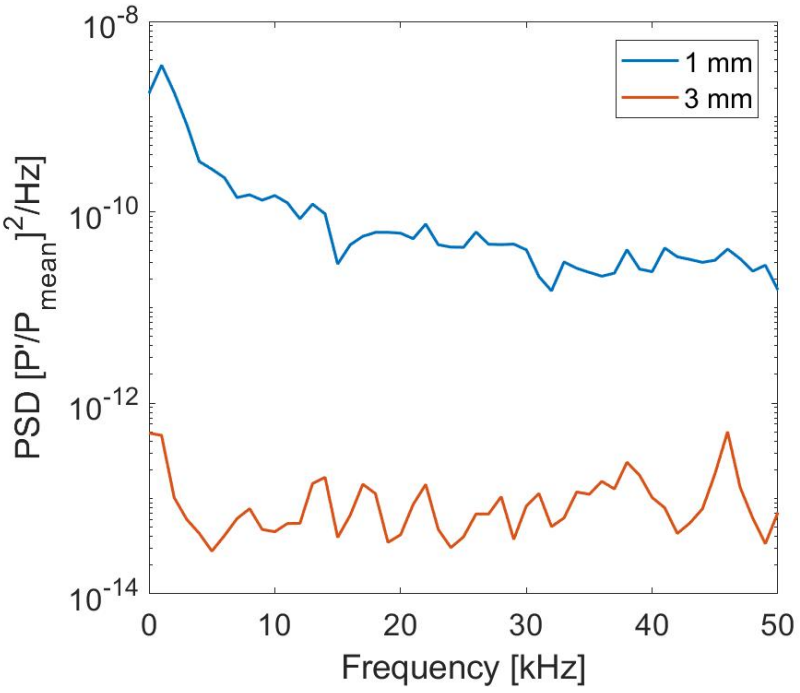

(b) PSD

Figure 4.43. Time trace and PSD of example case of apparent model boundary layer interaction with pitot probe.

Mean Pitot Pressure

Figure 4.44 shows the normalized, mean pitot pressures above the cone measured 26.9 cm axially from the nosetip. Measurements 1 mm above the model surface were influenced by the probe-boundary layer interaction and have been omitted. The pressure decrease due to crossing the bow shock is measured between the 20 and 25 mm position. The vertical position aligns with the Taylor-Maccoll calculation of 24 mm. Repeated in Figure 4.45 are the nominal locations where pitot measurements were made overlaid with the Mach contours from the Langley computations.

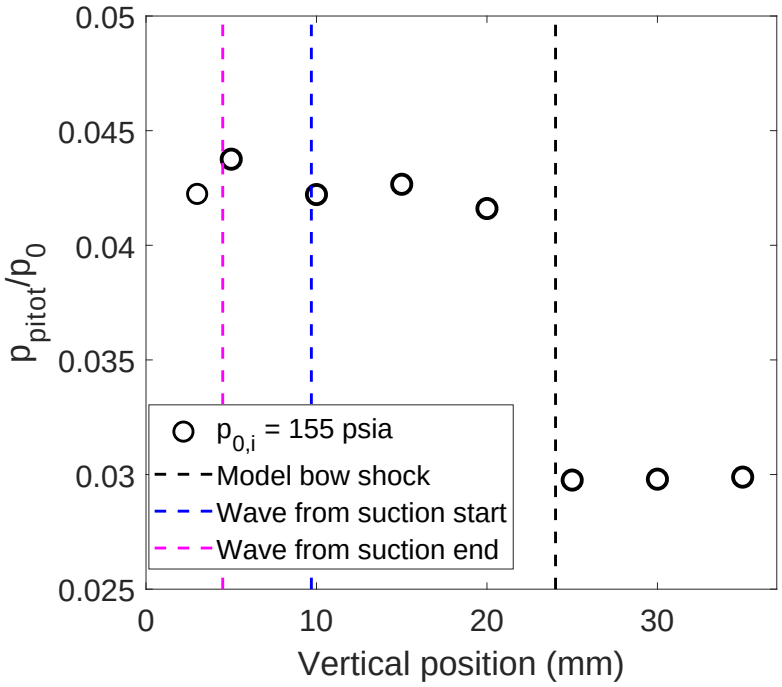

Figure 4.44. Normalized, mean pitot pressures measured above the model 26.9 cm axially from the nosetip in runs with suction on. Run SS1.6:8

Figure 4.46 shows the normalized, mean pitot pressures measured 28.9 cm axially from the nosetip. The measurement 1 mm above the model surface with $p_{0,i} = 155$ psia was influenced by the probe-boundary layer interaction and has been omitted. The probe crossed the model shock between 20 and 25 mm, but the Taylor-Maccoll

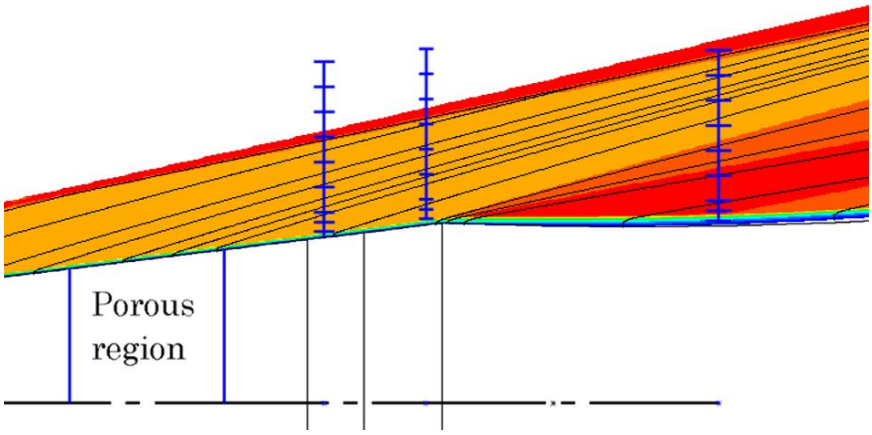

Figure 4.45. Mach lines from Li et al. computations overlaid with the pitot-probe measurement locations. From left to right, the vertical lines are located at $x = 26.9$, 28.9, and 34.8 cm.

calculation puts the bow shock at $h = 25.8$ mm. For the measurements with $p_{0,i} =$ 135 psia, the tunnel did not start while the probe traversed from 1 to 5 mm position. The probe crossed the bow shock between the 30 and 35 mm positions which is 10 mm higher than the expected position. The loose pitot probe likely deflected when setting the zero position, causing the significant error in vertical position.

Figure 4.47 shows the normalized, mean pitot pressures measured 34.8 cm axially from the nosetip. Due to the expansion downstream of the turn, the mean pressure is expected to be lower near the model surface. This is shown by the measurement 1 mm above the model with in the case with $p_{0,i} = 155$ psia. As expected, the pitot probe does not appear to cross the bow shock for these measurements. There did not appear to be a probe boundary-layer interaction in these measurements. This could be due to the probe deflection affecting the determined height. The nozzle-wall boundary layer was separated for most of the measurements with $p_{0,i} = 135$ psia. Two measurements were successfully made at $h = 25$ and 35 mm.

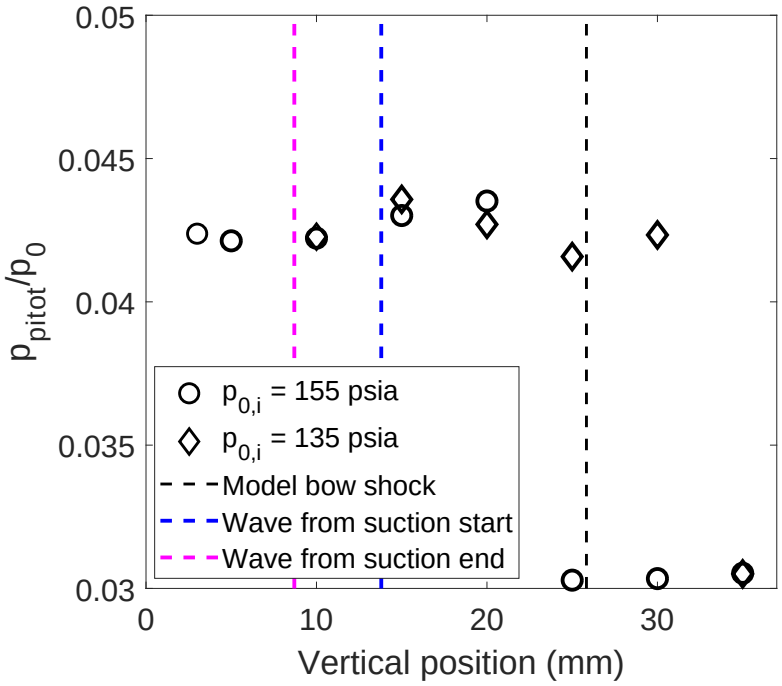

Figure 4.46. Normalized, mean pitot pressures measured above the model 28.9 cm axially from the nosetip in runs with suction on. Run SS1.9:14

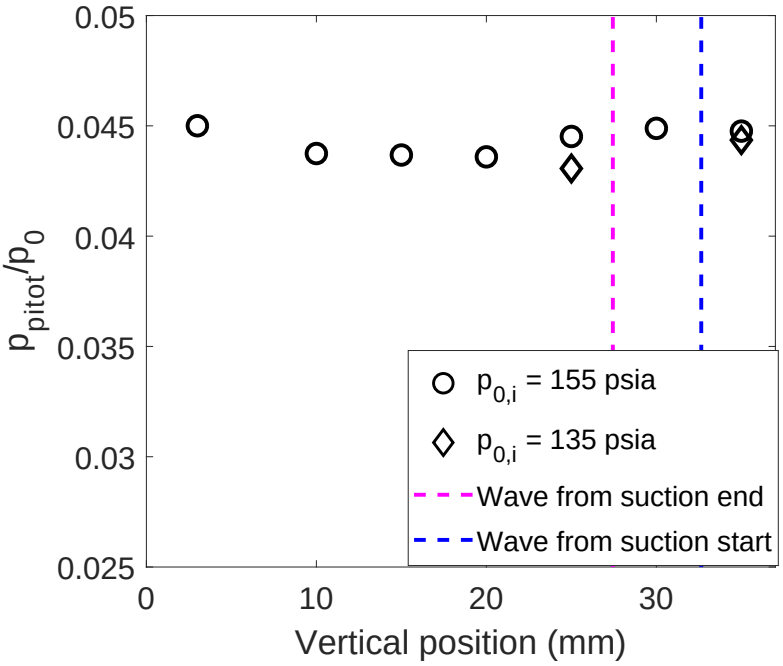

Figure 4.47. Normalized, mean pitot pressures measured above the model 34.8 cm axially from the nosetip in runs with suction on. Run SS1.16:21

Frequency Content

Figure 4.48 shows three PSDs for measurements made 26.9 cm from the nosetip at $Re_\infty = 10.7 \times 10^6$ m^{-1}. In the 3 mm position, there are two peaks measured at 5 and 59 kHz. Additional peaks may exist but are difficult to distinguish from noise. From these PSDs, distinct frequency phenomena are difficult to distinguish based on probe height. The measurements made 28.9 cm from the nosetip similarly do not have distinct-frequency peaks.

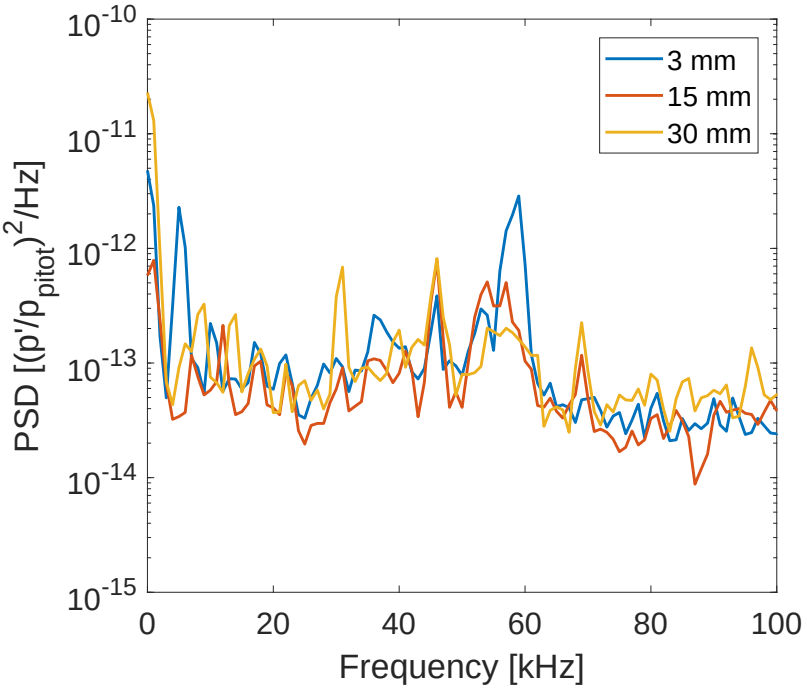

Figure 4.48. PSDs of three pitot probe measurements behind the suction section, 26.9 cm from nosetip. Run SS1.6-8

Figure 4.49 shows PSD measurements made 34.8 cm from the nosetip. The measurements made from $h = 1$ to 20 mm show a peak between 55 and 58 kHz. The peak is not measured starting at 25 mm above the model surface. The cause of the peak is unclear.

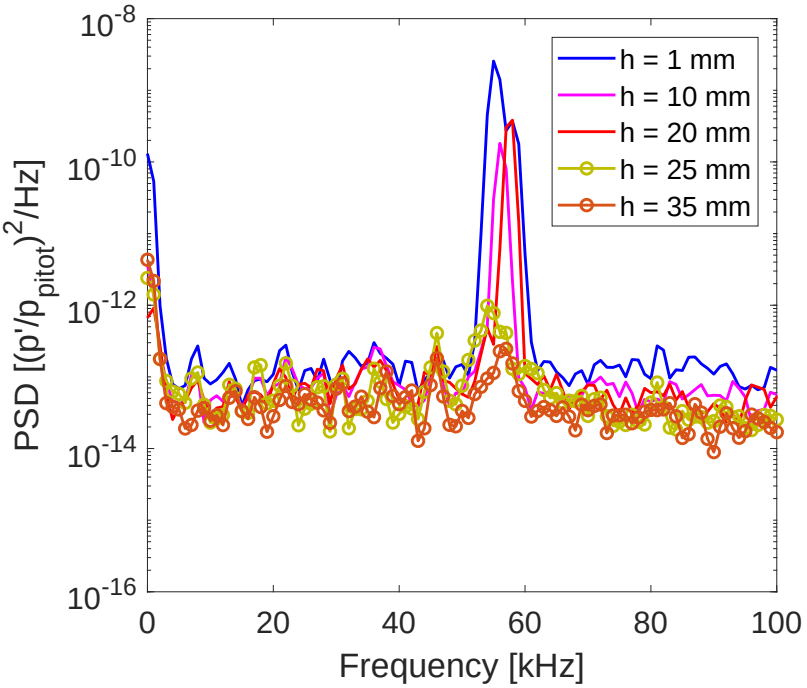

Figure 4.49. PSDs of pitot probe measurements above the flare at x = 34.8 cm. Run SS1.16:18

Figure 4.50 shows three PSDs for measurements made at x = 26.9, 28.9, and 34.8 cm with the probe 25 mm above the model. The Reynolds numbers are between 11.0×10^6 and 11.3×10^6 m^{-1}. A common peak is observed at 46 and 57 kHz in each. Without the electronic noise level, it is difficult to distinguish additional peaks. However, the measurements appear close to the noise floor.

Noise Levels

The RMS pressure fluctuations were calculated by integrating the PSD over a frequency range of 0 to 100 kHz, as described in Section 2.3.3. The model bow shock height and the height of the Mach waves were obtained from the Langley computations [19].

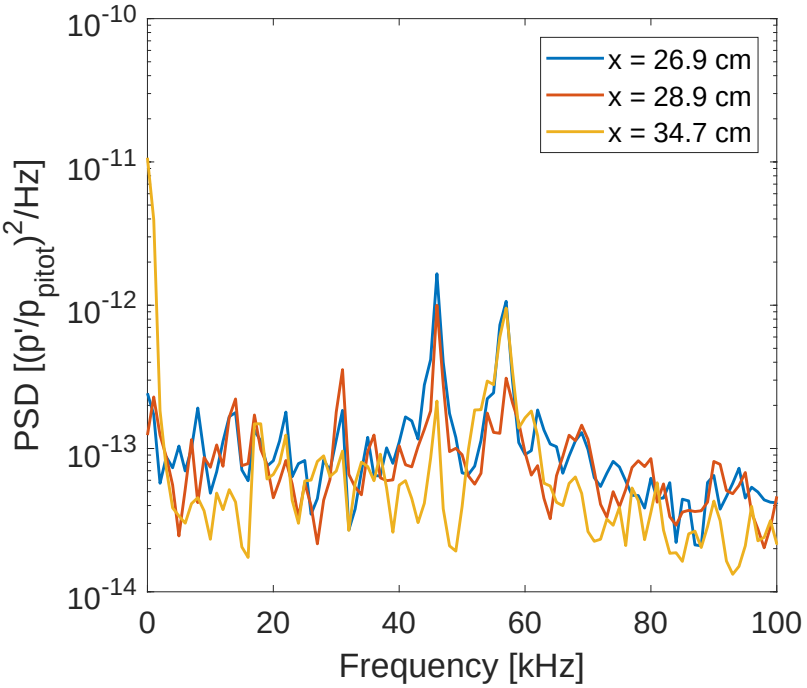

Figure 4.50. PSDs of three pitot probe measurements at $h = 25$ mm. Re_∞ between 11.0×10^6 and 11.3×10^6 m^{-1}. Run SS1.8, 11, 18

Figure 4.51 shows the noise levels measured above the model 26.9 cm axially from the model nosetip. The initial stagnation pressure was nominally 155 psia for each run. The noise levels vary from just under 0.008 to 0.014%.

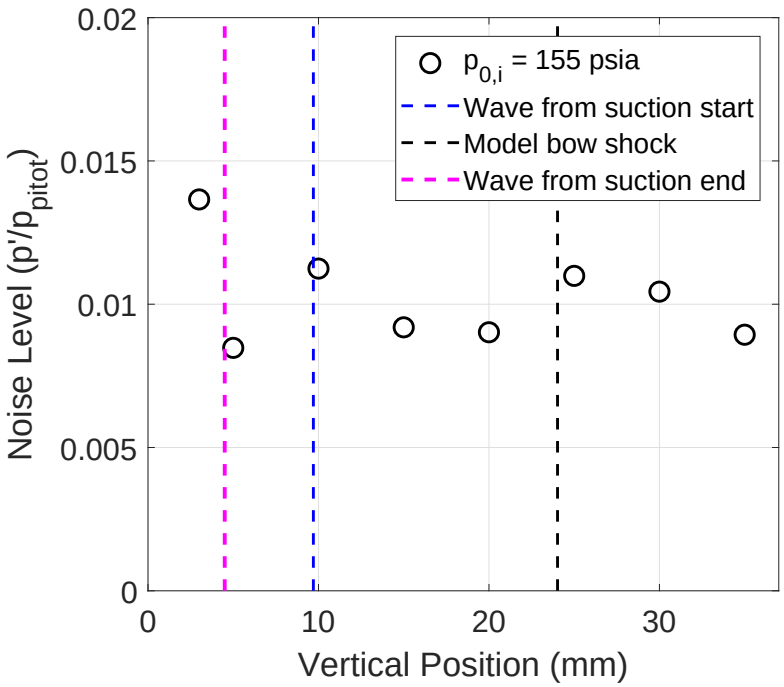

Figure 4.51. Noise levels measured above the model 26.9 cm from model nosetip. $p_{0,i}$ = 155 psia. Run SS1.6-8

Figure 4.52 shows the noise levels measured 28.9 cm from the nosetip. For heights less than 30 mm, the noise levels measured range from 0.008 to 0.011%. Higher noise levels are measured at h = 35 mm with values of 0.015 and 0.019% for runs with $p_{0,i}$ = 155 and 135 psia, respectively.

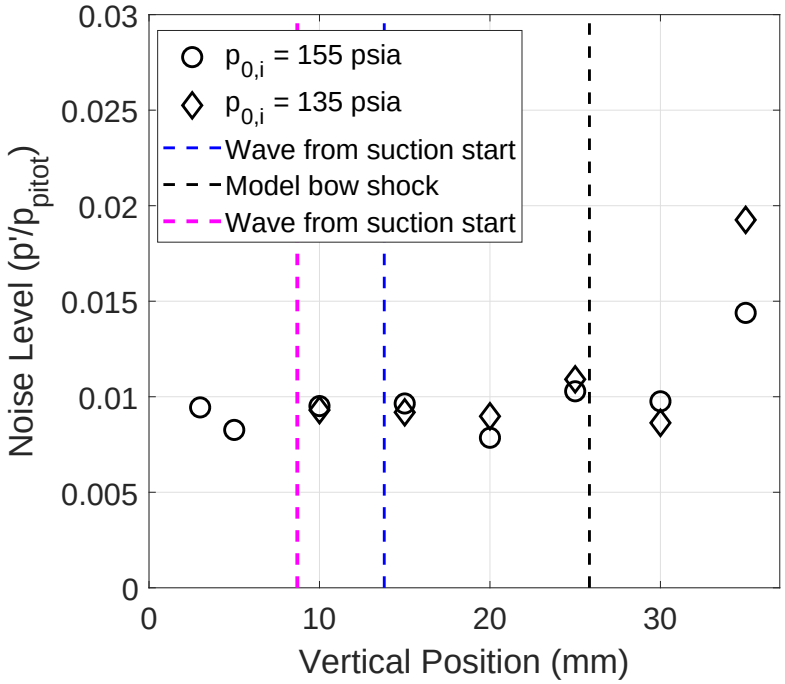

Figure 4.52. Noise levels measured above the model 28.9 cm from model nosetip. Run SS1.9-14

Figure 4.53 shows the noise levels measured 34.8 cm from the nosetip. The noise levels are significantly higher for heights less than 20 mm. This is due to the 57 kHz fluctuation shown in Figure 4.49. At higher vertical positions, the measured noise level is around 0.01%. In all of these data, there are no indications of any higher noise being radiated from the suction section.

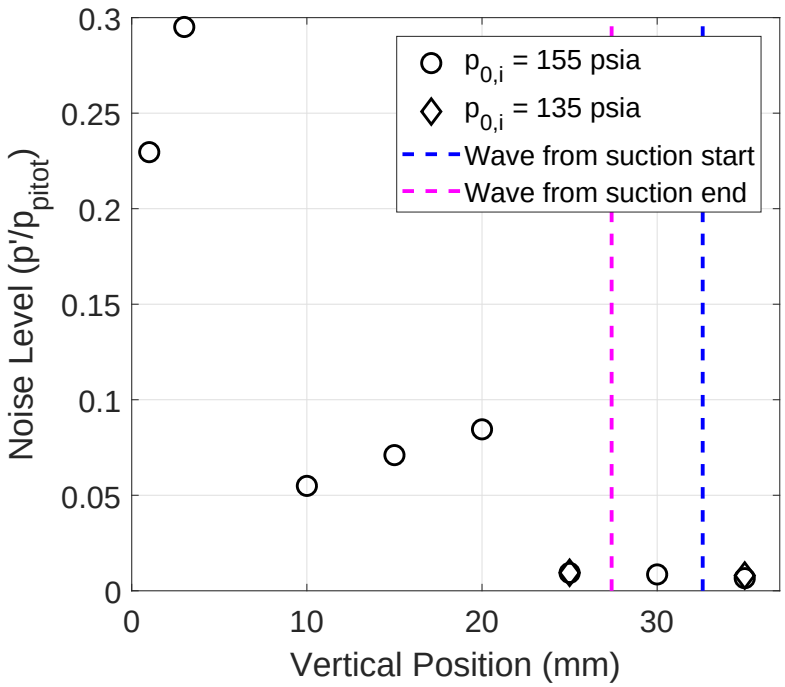

Figure 4.53. Noise levels measured above the model 34.8 cm from the model nosetip. Run SS1.16-21

Comparison to smooth plenum measurements

Table 4.7 lists the noise levels measured with both the smooth and suction measurements in each position with $p_0 = 155$ psia. Figures 4.54 to 4.56 present the noise levels graphically. The values from periods of nozzle-wall boundary-layer separation or fluctuating mean pitot pressure are labeled n/a. Most of the measurements made show comparable fluctuation levels with both the smooth and suction inserts, with magnitudes around 0.01%. This is comparable to the freestream noise levels measured in the BAM6QT by Steen [22].

The measurements made 26.9 cm from the nosetip, shown in Figure 4.54, do not show a significant difference in noise between suction and smooth measurements. The measurements made 28.9 cm from the nosetip, shown in Figure 4.55, measured slightly higher noise levels with suction only in the 35 mm position. The noise levels

measured with the smooth and suction inserts between 1 and 30 mm are comparable. The measurements made 34.8 cm from the nosetip are shown in Figure 4.56. The noise levels measured at $h = 1$ and 3 mm are significantly larger than the other heights for both smooth and suction inserts. This may be due to the normalizing the fluctuations by a lower pitot pressure in the expansion or due to an interaction between the probe and the model boundary layer. The noise levels measured 10 to 20 mm above the model are higher with suction due to the 57 kHz peak but is still small. The measurements from $h = 25$ to 35 mm are comparable.

Table 4.7. Comparison of the smooth and suction pitot noise levels for runs with $p_{0,i} = 155$ psia

Axial Position (cm)	**Vertical position (mm)**	**Smooth noise level (%)**	**Suction noise level (%)**
26.9	1	0.014	n/a
26.9	3	0.011	0.014
26.9	5	0.010	0.008
26.9	10	0.015	0.011
26.9	15	n/a	0.009
26.9	20	0.014	0.009
26.9	25	0.014	0.011
26.9	30	0.014	0.010
26.9	35	0.011	0.009
28.9	1	0.008	n/a
28.9	3	0.007	0.009
28.9	5	0.007	0.008
28.9	10	0.009	0.010
28.9	15	0.009	0.010
28.9	20	0.009	0.008
28.9	25	0.011	0.010
28.9	30	0.009	0.010
28.9	35	0.009	0.014
34.8	1	0.077	0.230
34.8	3	0.341	0.295
34.8	5	0.007	n/a
34.8	10	0.011	0.055
34.8	15	0.010	0.071
34.8	20	0.011	0.085
34.8	25	0.010	0.009
34.8	30	0.009	0.009
34.8	35	0.009	0.008

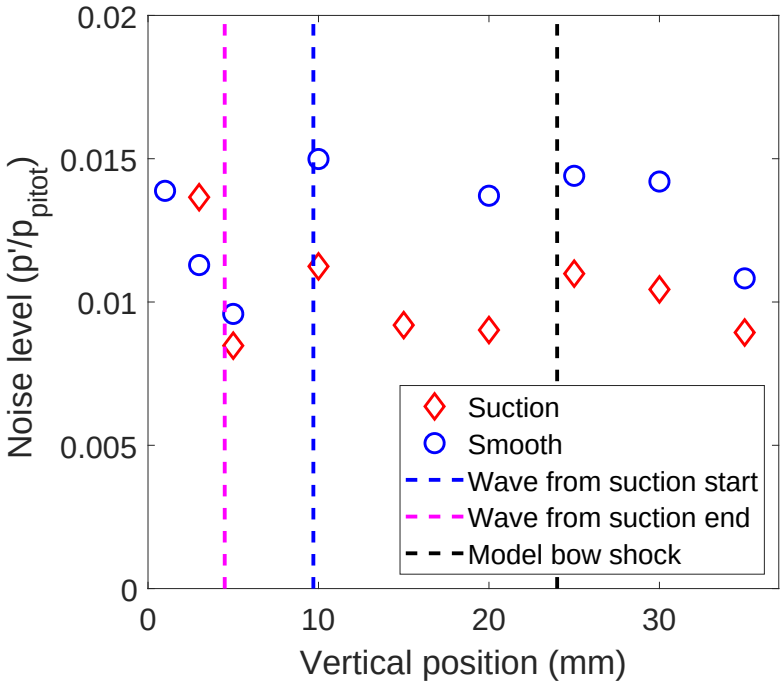

Figure 4.54. Comparison of suction and smooth noise levels above the model 26.9 cm from the model nosetip.

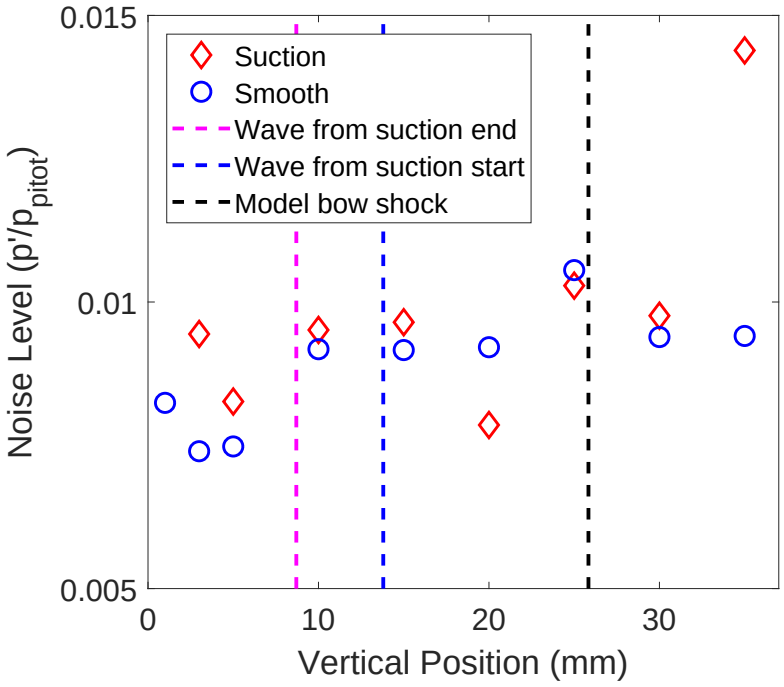

Figure 4.55. Comparison of suction and smooth noise levels above the model 28.9 cm from the model nosetip.

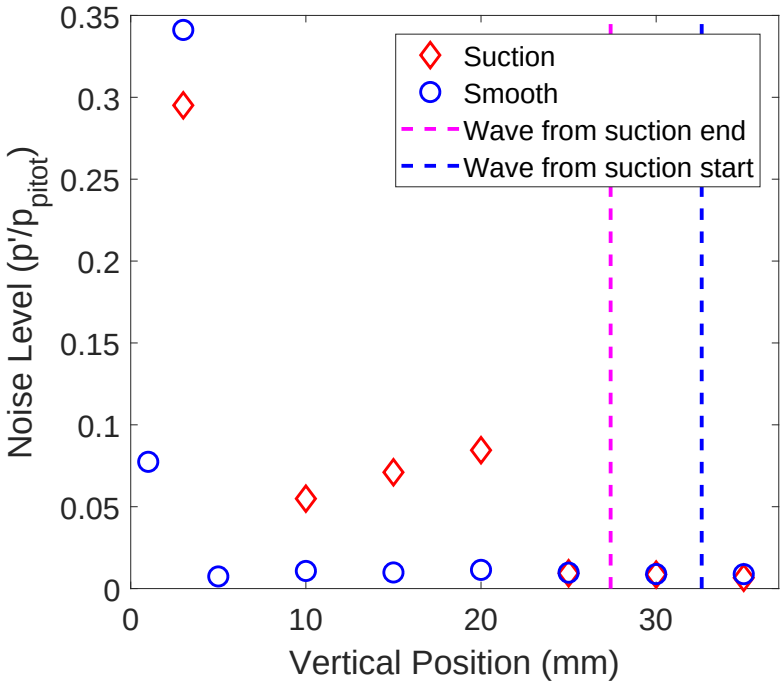

Figure 4.56. Comparison of suction and smooth noise levels above the model 34.8 cm from the model nosetip.

4.4 Suction Measurements II

The measurements from the second entry with suction using Suction Section 1 are presented here. The loose pitot probe was fixed, and additional surface sensors were installed in the model for this entry. The weld on the suction skin was rotated away from the viewing region. Additionally, suction-enabled runs were made with the pitot probe not in the flow. The runs presented use the reference format Suction Section Entry 2, abbreviated to SS2.N, and are logged in Appendix A.8.

4.4.1 Surface Pressure Fluctuations

Zeroing Angle of Attack

The PSD of the model after fine angle-of-attack adjustments is shown in Figure 4.57. A second-mode instability was measured with three PCBs at 0°, 90°, and 180° around the model azimuth, PCB1, PCB2, and PCB3, respectively. These sensors are located on the flare 45.1 cm from the nosetip. The wires for PCB4 broke during installation. The peak frequency measured by each sensor was 120 ± 3 kHz. This is higher than the 110 kHz peaks measured with the smooth insert. A harmonic of the instability was measured with PCB1 but not with PCB2 or PCB3.

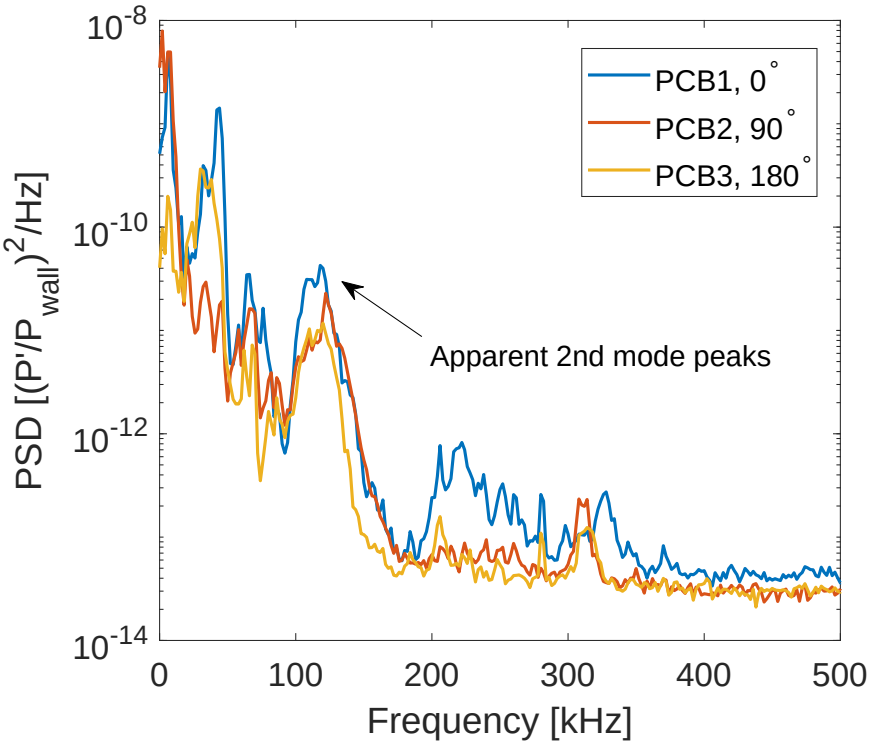

Figure 4.57. PSD of PCB1, PCB2, and PCB3. $Re_\infty = 10.3\times10^6$ m^{-1}. Run SS2.8

Second-mode Instability

Figure 4.58 shows the change in the peak frequency of the second-mode instability with respect to axial position on the flare. The PSDs were calculated at $Re_\infty = 10.3\times10^6$ m^{-1}. The peak frequency and RMS of the pressure fluctuations are provided in Table 4.8. The sensors at $x = 47.5$ and 52.6 cm had higher electronic noise which may be due to poorly isolating the sensor housing from the model. The peak frequency of the second mode appears to increase with downstream position. This may be attributed to the expected decrease in boundary-layer thickness due to the compression along the flare. The maximum RMS of the pressure fluctuations occurred at $x = 50.0$ cm with $f_{peak} = 122$ kHz.

Shown in Figure 4.59 are the PSDs measured at $x = 50.0$ cm from four suction-enabled runs at $Re_\infty = 11.0\times10^6$ m^{-1}. The run conditions for the four runs each are detailed alongside the peak, second-mode frequency and normalized, RMS pressure

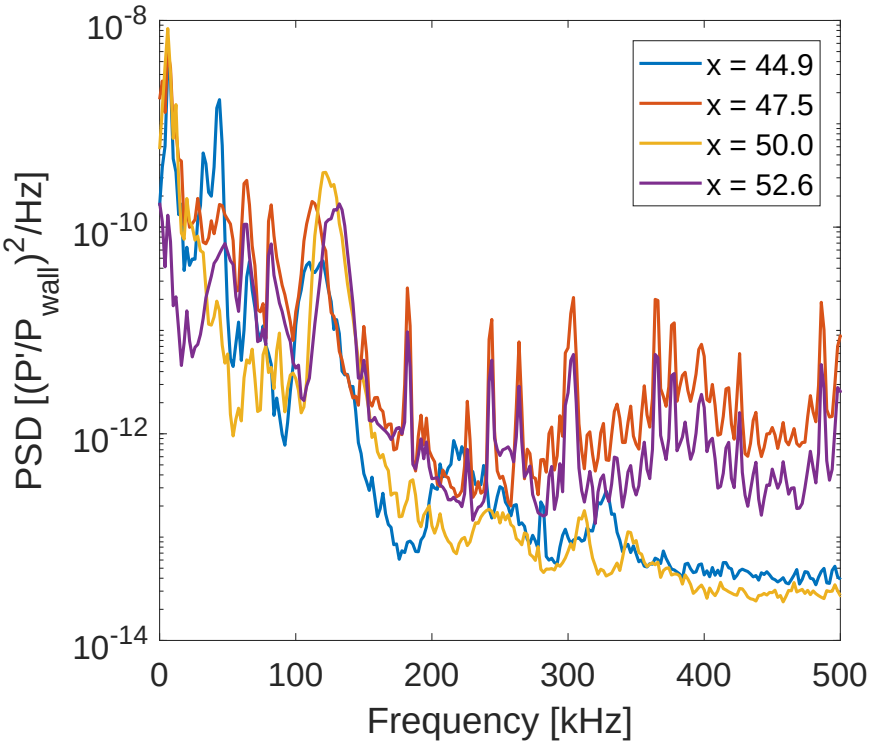

Figure 4.58. PSD of 4 sensors axially spaced by 2.54 cm at $Re_\infty = 10.3 \times 10^6$ m^{-1}. Run SS2.10

Table 4.8. Peak frequency and RMS pressure fluctuations at different axial locations, $Re_\infty = 10.3 \times 10^6$ m^{-1}

x **(cm)**	f_{peak} **(kHz)**	$\frac{p'_{RMS}}{p_{edge}} \times 100\%$
44.9	112	0.103%
47.5	112	0.159%
50.0	122	0.224%
52.6	134	0.166%

fluctuations in Table 4.9. The peak frequency of each is 132 kHz. Although Run SS2.8 measured a slightly higher power than the other three runs, the results appear repeatable.

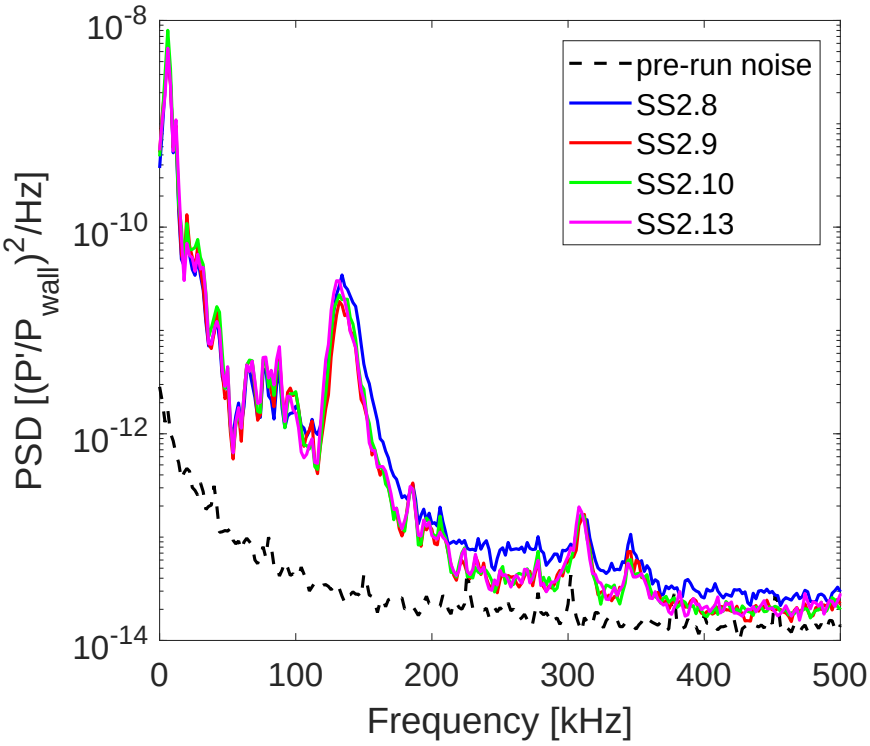

Figure 4.59. PSDs measured at $x = 50.0$ cm for four suction-enabled runs with $Re_\infty = 11.0 \times 10^6$. Run SS2.8-10, 13

Table 4.9. Peak frequency and RMS pressure fluctuations for the PSDs shown in Figure 4.59.

Run reference	f_{peak} **(kHz)**	$\frac{p'_{RMS}}{p_{edge}} \times 100\%$
SS2.8	132	0.079%
SS2.9	132	0.062%
SS2.10	132	0.069%
SS2.13	132	0.073%

Figure 4.60 shows the PSDs of the surface pressure fluctuations measured at $x = 45.1$ cm with decreasing Reynolds numbers in two runs. The peak frequency decreases from 122 kHz at $Re_\infty = 11.0 \times 10^6$ to 114 kHz at $Re_\infty = 9.4 \times 10^6$. However, the decrease in the RMS pressure fluctuations does not seem monotonic. At $Re_\infty =$

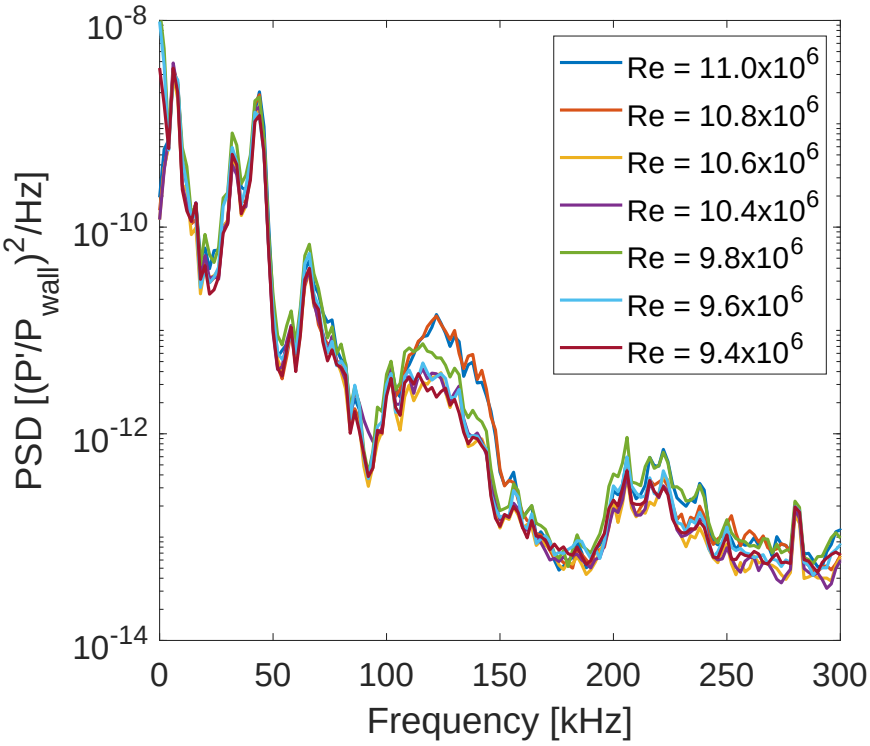

Figure 4.60. PSDs of surface pressure fluctuations measured at x = 45.1 cm at decreasing Reynolds number. Run SS2.10, 12

9.8×10^6 m^{-1} broke the trend of decreasing RMS pressure fluctuations and measured a higher power. The freestream conditions are detailed alongside peak frequency and RMS pressure fluctuations in Table 4.10.

Table 4.10. Peak frequency and RMS pressure fluctuations for the PSDs shown in Figure 4.60.

Re_∞ **(m^{-1})**	f_{peak} **(kHz)**	$\frac{p'_{RMS}}{p_{edge}} \times 100\%$
11.0×10^6	122	0.064%
10.8×10^6	122	0.063%
10.6×10^6	120	0.042%
10.4×10^6	120	0.046%
9.8×10^6	116	0.056%
9.6×10^6	116	0.046%
9.4×10^6	114	0.042%

Second-mode Instability With Suction Off

While the suction system is disabled, the pressure in the plenum is higher than the surface pressure of the model. The air inside the model should be blowing into the flow on the model. The plenum pressure was not measured as it exceeded 5 psia, the upper limit of the plenum sensor, for the entire run.

Figure 4.61 shows the PSD of the surface pressure fluctuations measured at 50.2 cm with the suction disabled. The Reynolds number was decreasing during a run starting at a $p_{0,i} = 155$ psia. The peak frequency increases from 60 kHz at $t = 0.5$ s to 164 kHz at $t = 2.5$ s. This may be due to the pressure in the plenum decreasing with time in a run creating less blowing and resulting in a thinner boundary layer, but this could not be verified. Table 4.11 details the peak frequencies and RMS pressure fluctuations for the Figure 4.61.

4.4.2 Surface Heat Transfer

As the heat transfer measured in Section 4.3.3 was influenced by the pitot-probe wake, the probe was not in the flow for the heat-transfer measurements presented in

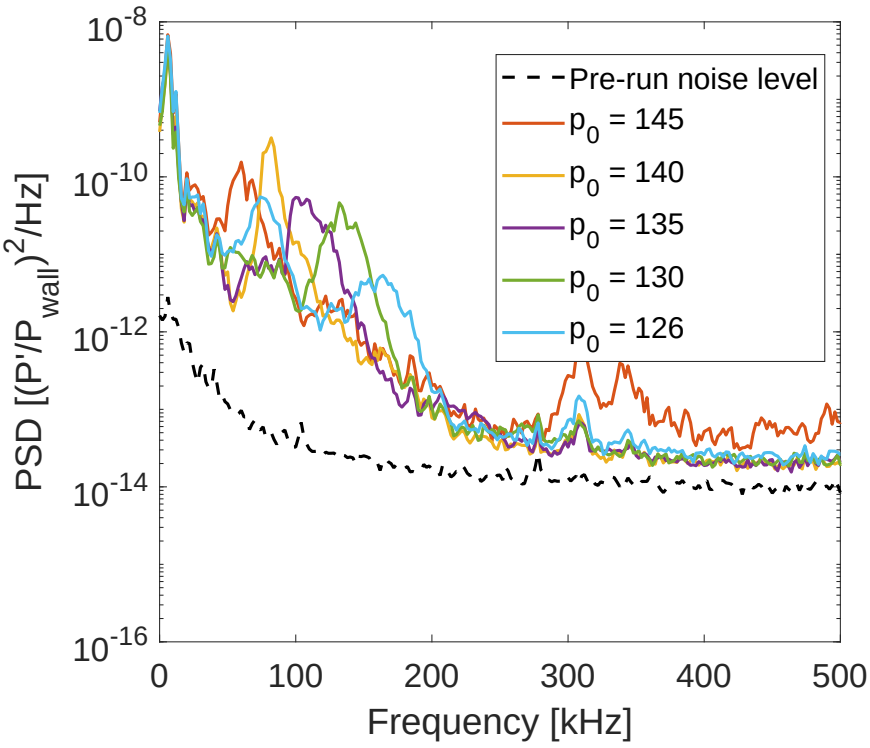

Figure 4.61. PSD of PCB13 while suction disabled. Run SS2.15

Table 4.11. Peak frequency and RMS pressure fluctuations for the PSDs shown in Figure 4.61

t **(s)**	Re_∞ **(m^{-1})**	p_0 **(psia)**	T_0 **(K)**	f_{peak} **(kHz)**	$\frac{p'_{RMS}}{p_{edge}} \times 100\%$
0.5	11.0×10^6	145	424	60	0.209%
1.0	10.8×10^6	140	420	82	0.218%
1.5	10.6×10^6	135	416	106	0.162%
2.0	10.4×10^6	130	412	132	0.151%
2.5	10.3×10^6	126	408	76, 164	0.171%

this section. The weld from the suction section is also not upstream of the imaged region.

Figure 4.62 shows the surface heat transfer on the suction model at $Re_\infty = 11.0 \times 10^6$ m^{-1}. The source of increased heating on the top and bottom of the model is unknown. The streak above the main sensor array is from a small spot of RTV accidentally applied to the model at $x = 44.9$ cm. Figure 4.63 shows the mean heat transfer along an axial slice at spanwise reference 0.01 m. The measured heating is near 2 kW/m^2 at $x = 0.35$ m. It decreases to near 0 kW/m^2 at $x = 0.40$ m. Downstream of $x = 0.45$ m the measured heat transfer increases up to 3 kW/m^2 by the end of the model. Similar measurements were made in each run during this entry. The measured results are vastly different from the mean-flow calculations at $Re_\infty = 12.1 \times 10^6$ m^{-1}. The cause of this is unclear. A depiction of the streamwise slice used to calculate the axial change in heat transfer is shown in Figure 4.64.

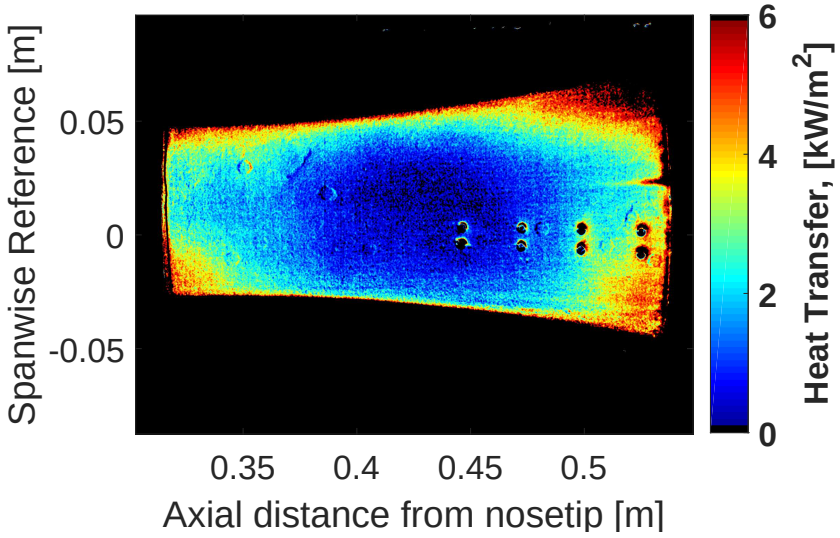

Figure 4.62. Heat transfer on the suction model at $Re_\infty = 11.0 \times 10^6$ m^{-1} with the probe not in the flow. Run SS2.10

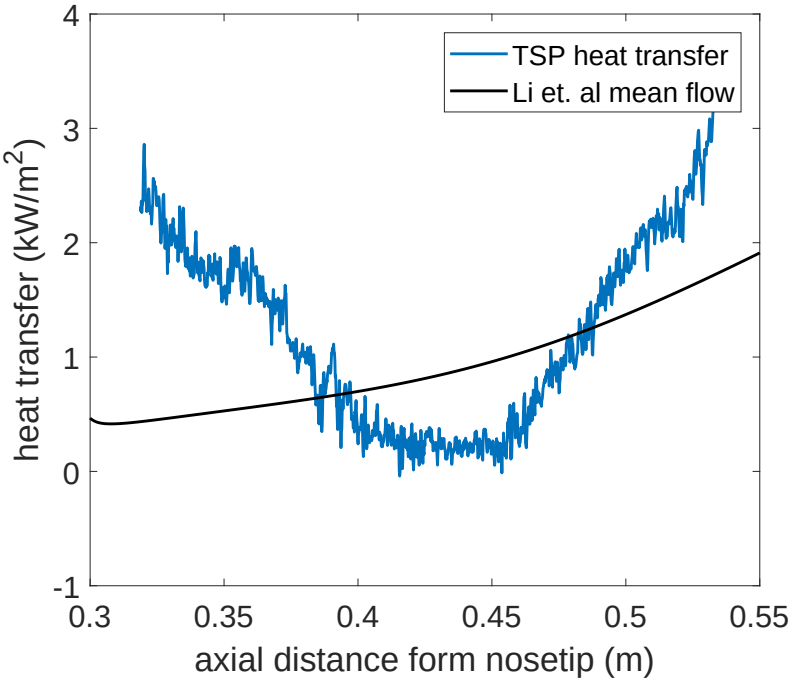

Figure 4.63. Axial change in mean heat transfer from a narrow slice at spanwise reference of 0.01 m, depicted in Figure 4.64. Also shown are Li et al.'s predicted heat transfer at $Re_\infty = 12.1 \times 10^6$ m $^{-1}$ [19] Run SS2.10

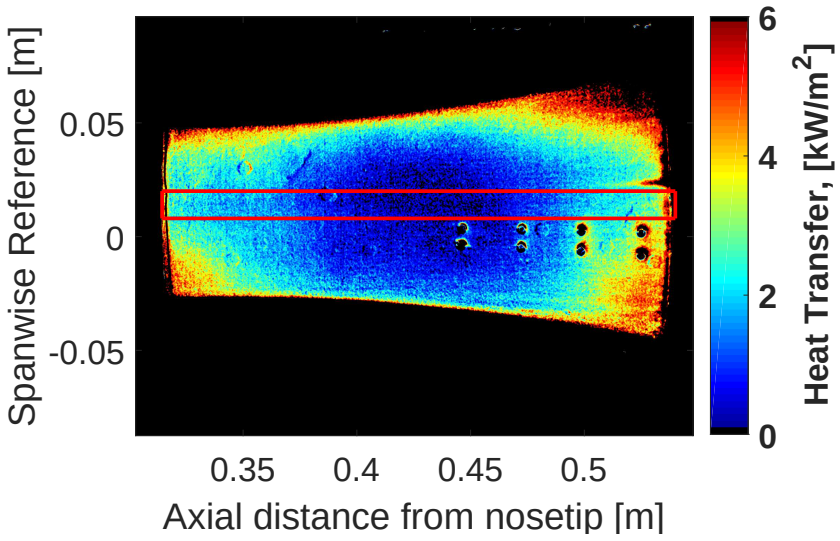

Figure 4.64. Depiction of the streamwise slice used to determine axial change in heat transfer in Figure 4.63. Run SS2.10

4.4.3 Pitot-Probe Measurements

The probe was traversed vertically at an axial location 31.5 cm from the nosetip to obtain an additional set of measurements in the expansion on the model with suction enabled. There is currently no set of smooth-wall measurements in this position without suction. The pitot probe was fixed and did not wiggle for this entry.

Mean Pitot Pressure

Figure 4.65 shows the normalized, mean pitot pressures for runs with $p_{0,i} = 155$ and 135 psia with respect to vertical position. The normalized mean pressures in each vertical position for runs with $p_{0,i} = 135$ psia are similar to the runs with $p_{0,i} = 155$ psia. This is as expected as shock position and normalized pitot pressure should not change significantly with the freestream pressure. This was less visible in the measurements in Section 4.3.4 as the loose pitot probe affected the probe height for those earlier measurements. Measurements at 1 mm above the model were influenced by a probe-boundary layer interaction and are not used. The drop in pitot pressure near 27 mm agrees reasonably well with theory. More experimental data points are needed to confirm this.

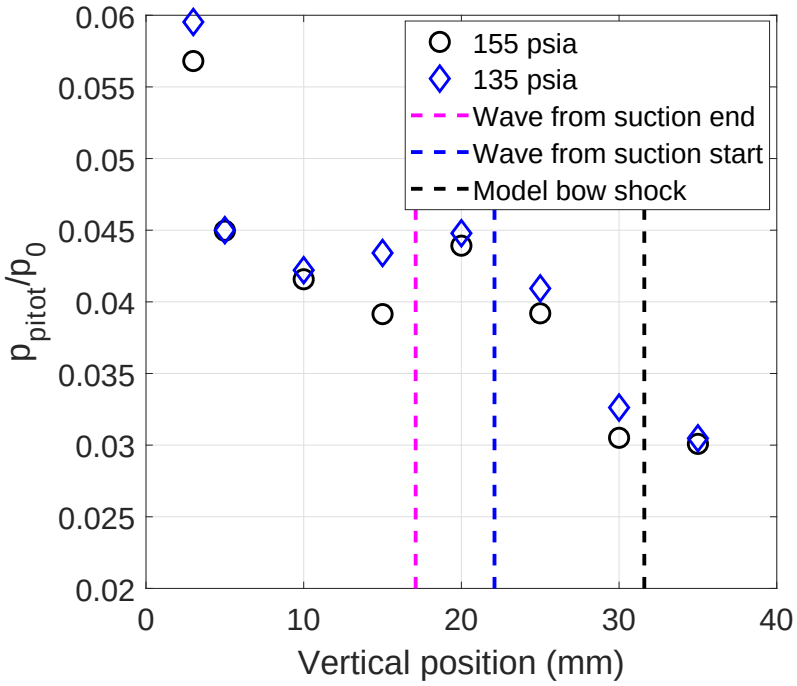

Figure 4.65. Mean pitot pressure with respect to vertical position measured at $x = 31.5$ cm with $p_{0,i} = 155$ and 135 psia. Run SS2.18-23

Frequency Content

Figure 4.66 shows the PSD for the pitot fluctuations normalized by the mean pitot pressure measured 31.5 cm axially from the nosetip for vertical positions 3, 10, and 25 mm. A very large peak is measured at 61 kHz in the 3 mm position, and an additional peak is measured at 92 kHz, presumably due to a shock boundary-layer interaction. The cause of these peaks are unclear, but a peak was similarly measured near 60 kHz at $x = 26.9$ and 34.8 cm near the model surface, shown in Section 4.3.4. The electronic noise floor was measured with no flow in the tunnel and the contraction pressure at 2.7 psia. Nothing of particular note is measured in the $p_{0,i} = 135$ psia measurements.

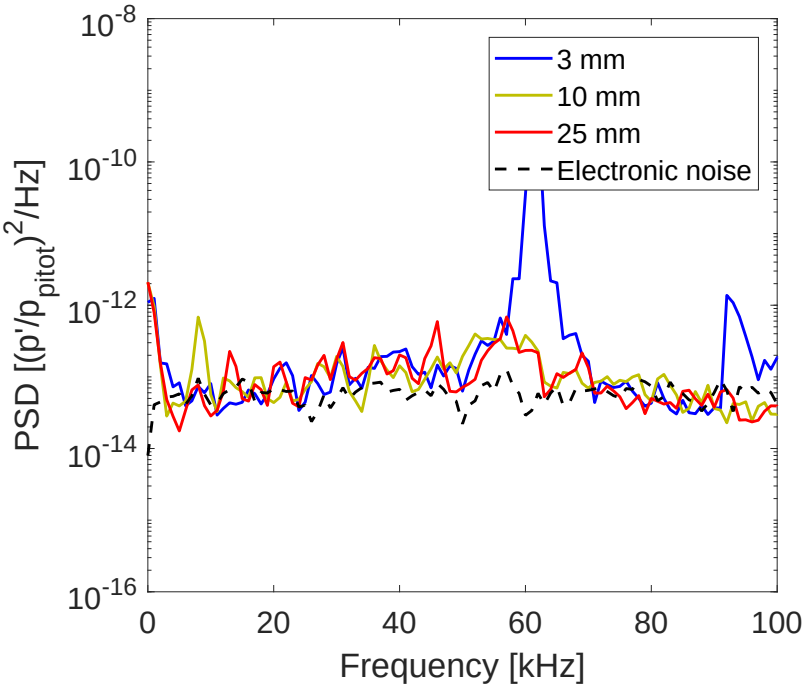

(a) $p_{0,i} = 155$ psia, Run SS2.18-20

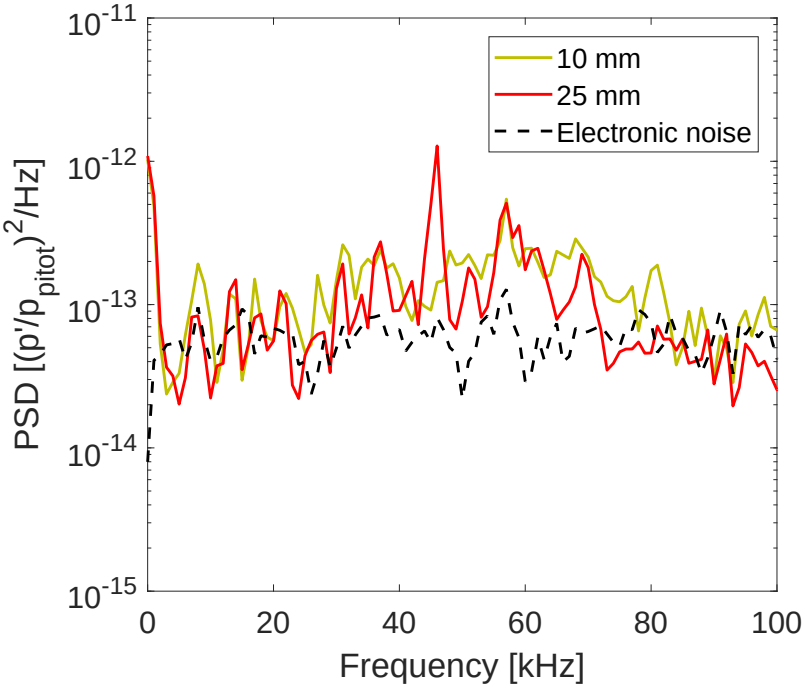

(b) $p_{0,i} = 135$ psia, Run SS2.22-23

Figure 4.66. PSDs of pitot probe measurements 31.5 cm from nosetip.

Noise Levels

Figure 4.67 shows the noise levels measured above the model 31.5 cm axially from the model nosetip. The noise level measured 3 mm above the model is an order of magnitude higher than the other measurements. This is from the 61 kHz disturbance, presumably due to a shock boundary-layer interaction as described by [46]. The remaining measured values range from 0.006% to just under 0.01%. These magnitudes are comparable to the freestream noise levels measured in the BAM6QT by Steen [22] and Gray [23]. There is no evidence of any higher noise radiated from the suction section.

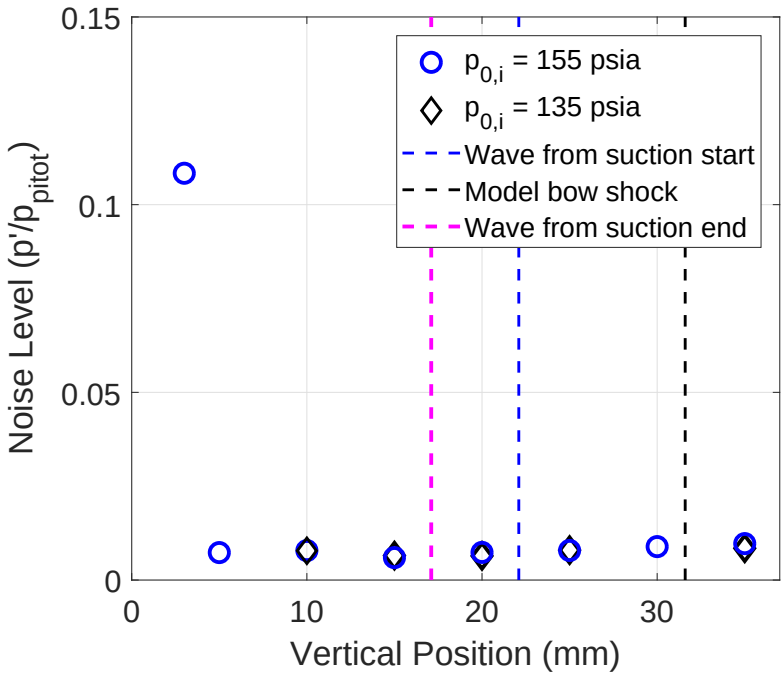

Figure 4.67. Noise levels measured above the model 31.5 cm from the model nosetip. Run SS2.18-23

4.4.4 FLDI Measurements

As the pitot probe interfered with the flow when placed near the wall, FLDI was also used to measure disturbances. The FLDI was traversed through the flow in two axial positions, x = 26.9 and 31.5 cm. Baseline FLDI measurements have not been made with the smooth insert. The phase shift and optical-path fluctuations were calculated via Equations 2.6 and 2.7 in Section 2.3.8.

Figure 4.68 shows the PSD of the FLDI measurements from 4 runs with suction enabled at x = 26.9 cm. At the time of the data shown, $Re_\infty = 10.8\times10^6$ m^{-1}. The peaks at 40, 60, 78, 87, 118, and 169 kHz are observed in the electrical noise. The cause of the peaks in the electrical noise is unknown. The cause of the ringing in the sub-40 kHz region in the h = 0.9 mm measurement is unclear. For all heights except h = 0.45 mm, a common peak is measured at 67 kHz. At h = 1.8 mm, a peaks are observed at 13 and 55 kHz. At h = 2.7 mm peak is measured at 135 kHz. Table 4.12 lists the RMS values for the optical-path fluctuations measured at x = 26.9 cm.

Table 4.12. RMS of optical-path fluctuations measured at x = 26.9 cm with FLDI

h **(mm)**	**RMS** $\times10^{-10}$ **(m)**
0.45	5.78
0.9	7.02
1.8	5.39
2.7	3.78

Figure 4.69 shows the PSD of the FLDI measurements from 6 runs at x = 31.5 cm with suction enabled. The freestream Reynolds number are 10.8×10^6 m^{-1} for the data shown. For all heights, a peak was measured between 61 and 68 kHz with peak power at h = 3.15 mm. This is similar to the 67 kHz peak measured at h = 3 mm with the pitot probe. A broad increase in fluctuations is measured around 130 kHz in the h = 0.45 and 0.9 mm measurements. Table 4.13 lists the RMS values of the

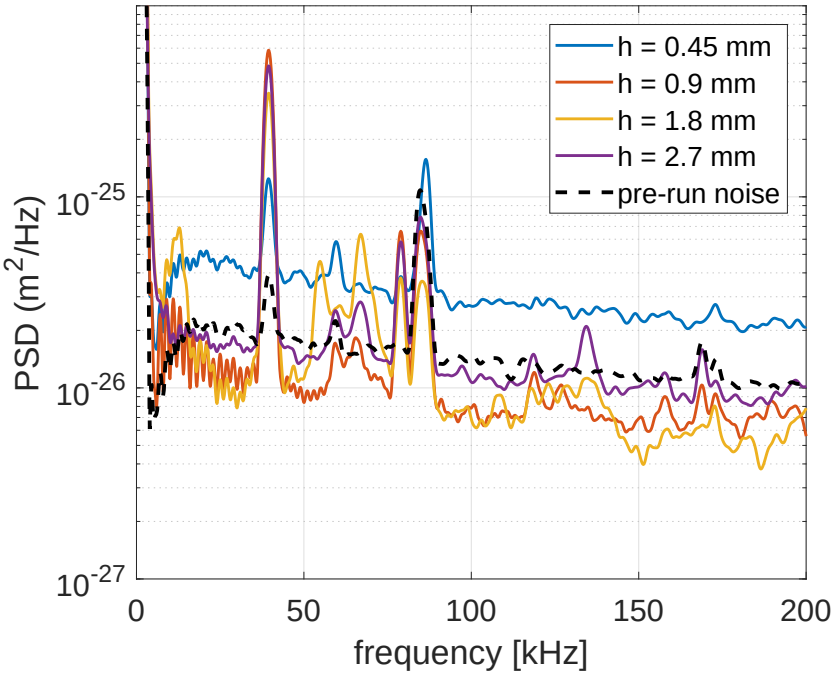

Figure 4.68. PSD from FLDI measurements at $x = 26.9$ cm. Run SS2.36-39

optical-path fluctuations measured at $x = 31.5$ cm. The RMS of the optical-path fluctuations measured at $x = 31.5$ cm are a little higher than the measurements at $x = 26.9$ cm. The cause of this is unclear.

Table 4.13. RMS of optical-path fluctuations measured at $x = 31.5$ cm with FLDI

h **(mm)**	**RMS** $\times 10^{-10}$ **(m))**
0.45	6.02
0.9	3.18
1.8	7.58
2.7	7.56
3.15	8.86
4.05	15.4

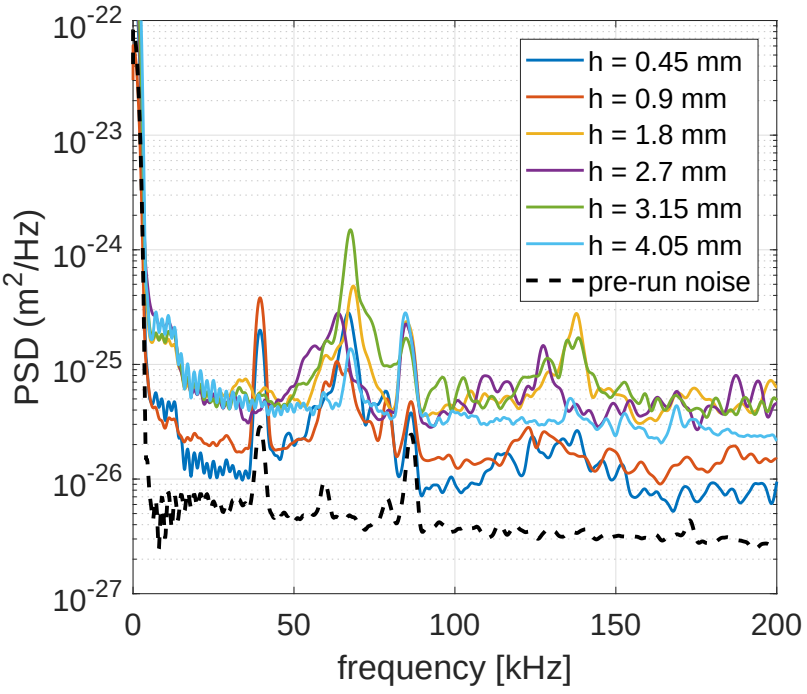

Figure 4.69. PSD from FLDI measurements at $x = 31.5$ cm with suction enabled. Run SS2.40-48

5. SUMMARY OF RESULTS

This research sought to reduce the risks of future designs that might use boundary-layer suction for quiet wind tunnels. A model was designed to enable boundary-layer suction, and experiments focused on measuring fluctuations radiated into the flow from the suction, and measuring Görtler-vortex development.

A suction system was designed and constructed to provide a sufficiently low pressure inside the model to choke flow through the porous skin during runs. The mean pressure inside the plenum was on average 3.5 Torr during tunnel runs at the maximum quiet pressure. This was less than the required 4.5 Torr pressure for choked suction. Thus, suction appeared successful.

Temperature-sensitive paint and oil flow were used in an attempt to visualize and measure Görtler-vortex development. The vortex strengths were apparently insufficient to overcome the low signal-to-noise ratio of the measurement techniques. As the vortices could not be measured, perhaps the suction did not introduce large streamwise vorticity into the flow.

Fluctuations were measured above the model in four axial locations for a smooth insert and a suction insert. The noise levels measured for both inserts were less than 0.05% above the 7°-cone portion of the model. There was no evidence of noise radiated from the suction surface. The flow expanding from the turn to the flare heavily influenced measurements in that region. Pitot measurements made 1 mm above the model with suction experienced broad fluctuations in mean pressure likely due to a probe-boundary-layer interaction.

Heat-transfer measurements with the smooth insert showed an increase from 1.0 kW/m^2 at 0.45 m from the nosetip to 2.25 kW/m^2 at 0.53 m for max-quiet conditions. With suction, an increase from 0.75 kW/m^2 at 0.43 m to 2.5 kW/m^2 at 0.53 m was

shown. A decrease in heat transfer was measured from 0.35 to 0.43 m in both cases, and the cause is unclear. The heat transfer showed fair agreement with computations.

Surface-pressure fluctuations were measured showing apparent second-mode instabilities. With the smooth insert, a peak frequency of 110 kHz was measured 47.5 cm from the nosetip with $Re_m = 10.9 \times 10^6$ m^{-1}. With suction enabled, a peak frequency of 122 kHz was measured at the same location and Reynolds number. The frequency increase may be attributed to the thinner boundary layer due to suction. As the RMS amplitude of the instability did appear to increase with suction, large unsteadiness was not introduced into the flow.

FLDI measurements near the model surface at 26.9 cm from the nosetip with suction enabled showed density fluctuations with a peak frequency of 67 kHz. Measurements 31.5 cm from the nosetip showed density fluctuations with peak frequencies between 62 and 67 kHz and possible harmonics. FLDI measurements were not made with the smooth insert for comparison.

5.1 Future Work

Although measurements to date appeared to show no fluctuations radiated from the suction surface, there is still much work to be done. The following suggestions for future work would both improve the suction system and further reduce the risk of developing a suction-based quiet-tunnel nozzle.

1. A no-cost extension on the project grant has been approved to continue this work beyond this master's degree into January 2020. The vertical position of the traverse measurements was unclear in the earlier parts of the present work due to the missing set screw allowing deflection of the sensor. Measurements will be repeated with a more accurate measurement of the vertical position of the probe. Additionally, Suction Sections 2, 3, and 5 could not be tested in the present work. Measurements of surface heat transfer, surface pressure fluctuations,

and noise radiation will be made with one test piece. Measurements with the remaining suction sections are to be left for future endeavors.

2. The code written to predict the plenum pressure has not been rigorously validated. Additionally, the results from the code did not align with experimental measurements. The code should be revisited to improve its prediction accuracy. Time permitting, this will be completed as part of the no-cost extension.

3. The current design of the suction system is difficult to install and seal, and it provides limited margin in plenum pressure. The most-limiting factor on the throughput of the system is currently the model baseplate. A schematic is available in Appendix B. Presently, the bore for airflow is 0.75 in. diameter and 7 in. long to allow angle-of-attack adjustments. The part should be redesigned to allow either a larger diameter hole or a shorter length.

4. The suction section designed to seed the Görtler instability, Suction Section 4, failed to be constructed. The skin should be redesigned and fabricated. Measurements with this skin should show strongly amplified Görtler vortices.

5. Limited repeatability measurements were made during this project. Repeated tests should be made to show the consistency of both surface and off-surface measurements. As only one entry was performed with the FLDI, limited near-surface measurements are available. Additional measurements in the model-surface boundary layer with FLDI would further improve understanding of near-surface fluctuations.

6. Attempts to measure Görtler vortices on the flare were unsuccessful with TSP. Infrared heat-transfer measurements (IR) on PolyEtherEtherKetone (PEEK) models have recently become possible in the BAM6QT. The signal-to-noise ratio of the IR measurements is higher than TSP measurements. A PEEK afterbody could be fabricated to quantitatively measure heat transfer and improve the chances of observing Görtler vortices.

REFERENCES

REFERENCES

[1] John J. Bertin, E. S. Idar, and Winston D. Goodrich. Effect of Surface Cooling and Roughness on Transition for the Shuttle Orbiter. *Journal of Spacecraft and Rockets*, 15(2):113–119, 1978.

[2] J. L. van Ingen. A suggested semi-empirical method for the calculation of the boundary layer transition region. Report VTH-74, Delft University of Technology, September 1956.

[3] Peter G. Baines, Sharan J. Majumdar, and Humio Mitsudera. The mechanics of the Tollmien-Schlicting wave. *Journal of Fluid Mechanics*, vol. 312:107–124, 1996.

[4] Anthony Demetriades. An Experimental Investigation of the Stability of the Hypersonic Laminar Boundary Layer. Technical Report Memorandum No. 43, Guggenheim Aeronautical Laboratory, California Institute of Technology, May 1958. Army Ordnance Contract No. DA-04-495-Ord19.

[5] W. B. Brown. Stability of Compressible Boundary Layers. *AIAA Journal*, Vol. 5, No. 10:1753–1759, 1967.

[6] Herman Schlichting. *Boundary-Layer Theory*. McGraw-Hill Book Company, Seventh edition, 1979. Translated by J. Kestin.

[7] H. Görtler. On the Three-Dimensional Instability of Laminar Boundary Layers on Concave Walls. Technical Report NACA TM 1375, National Advisory Committee for Aeronautics, 1954. Translation of Über eine dreidimensionale Instabilitat laminarer Grenzschichten an konkaven Wänden, Geselleshcaft der Wissenschaften zu Göttingen, Nachrichten, Mathmmatik, v.2, no.1, 1940.

[8] A. M. O. Smith. On the Growth of Taylor-Görtler Vortices Along Highly Concave Walls. *Quarterly of Applied Math*, Vol. 13:233–262, December 1955.

[9] Fei Li, Meelan Choudhari, Chau-Lyan Chang, Minwei Wu, and Patrick Greene. Development and Breakdown of Görtler Votices in High Speed Boundary Layers. *AIAA 2010-705*, January 2010.

[10] Ronald Joslin. Aircraft Laminar Flow Control. *Annual Review of Fluid Mechanics*, 30:1–29, 1998.

[11] Albert Braslow. *A History of Suction-Type Laminar-Flow Control with Emphasis on Flight Research*. NASA History Division, 1999. Monographs in Aerospace History Number 13.

[12] D. Bushnell and M. Tuttle. Survey and Bibliography on Attainment of Laminar Flow Control in Using Pressure Gradient and Suction. *NASA Reference Publication 1035*, September 1979.

[13] S. R. Pate. Investigation of Drag Reduction by Boundary-Layer Suction on a Body of Revolution at Mach Number 2.5, 3, and 3.5. Technical Report AEDC-TR-65-36, Von Kármán Gas Dynamics Facility, Arnold Engineering Development Center, February 1965.

[14] W. Pfenninger and J. Syberg. Reduction of Acoustic Disturbances in the Test Section of Supersonic Wind Tunnels by Laminarizing Their Nozzle and Test Section Wall Boundary Layers By Means of Suction. Contractor's Report CR-2436, NASA Langley Research Center, November 1974.

[15] Steve P. Schneider. Development of Hypersonic Quiet Tunnels. *Journal of Spacecraft and Rockets*, 45(4):641–664, July 2008.

[16] Ivan E. Beckwith and William O. Moore III. Mean Flow and Noise Measurements in a Mach 3.5 Pilot Quiet Tunnel. *12th Aerodynamic Testing Conference*, (0569):48–70, 1982.

[17] Ivan E. Beckwith and Barbara B. Holley. Görtler Vortices and Transition in Wall Boundary Laayers of Two Mach 5 Nozzles. Technical Paper NASA TP 1869, NASA Langley Research Center, August 1981.

[18] I. E. Beckwith, M. R. Malik, and F.-J. Chen. Design and Fabrication Requirements for Low-Noise Supersonic/Hypersonic Wind Tunnles. Technical Report AIAA 88-0143, NASA Langley Research Center, January 1988.

[19] Fei Li, Meelan Choudhari, Pedro Paredes, Steve Schneider, and Phillip Portoni. Görtler Instability and Its Control via Surface Suction Over an Axisymmetric Cone at Mach 6. *AIAA 2018-3069*, June 2018.

[20] Fei Li, Meelan M. Choudhari, and Pedro Paredes. Nonlinear Goertler Vortices and Their Secondary Instability in a Hypersonic Boundary Layer. *AIAA 2019-3216*, June 2019.

[21] Charles Hollender, Anubhav Dwivedi, and Graham V. Candler. Goertler instability analysis of Mach 6 flow on a flared axisymmetric cone with and without suction. *AIAA 2019-3219*, June 2019.

[22] Laura-cheri E. Steen. *Characerization and Development of Nozzles for a Hypersonic Quiet Wind Tunnel*. PhD thesis, Purdue University School of Aeronautics and Astronautics, December 2010.

[23] Kathryn Gray. Flowfield Characterization of the Boeing/AFOSR Mach-6 Quiet Tunnel. Master's thesis, Purdue University, December 2018.

[24] Drew Turbeville. Nozzle Wall Hot Film and Static Pressure Kulite Overview. Unpublished, February 2018. From an unpublished in-lab report.

[25] Matthew P. Borg, Roger L. Kimmel, and Scott Stanfield. Traveling Crossflow Instability for HIFiRE-5 in a Quiet Hypersonic Wind Tunnel. *AIAA 2013-2737*, June 2013.

[26] Varun Viswanathan and Mark Wason. Pressure Fluctuation and Temperatures Sensitive Paint Measurements on Inverse Flare Cone at Mach 6. Unpublished, April 2017. As part of Purdue AAE520 coursework.

[27] Mark Wason. Measurements of Low-pressure Shock Waves Towards a Calibration Method for High-frequency Pressure Sensors. Master's thesis, Purdue University, May 2019.

[28] Kulite, Leonia, New Jersey. *Miniature Ruggedized High Temperature Pressure Transducer XTEL-190 (M) Series*.

[29] Kulite, Leonia, New Jersey. *High Temperature Ultraminiature Pressure Transducer XCE-062 Series*.

[30] Kulite, Leonia, New Jersey. *Miniature Digitally Corrected Pressure Transducer ETL-79-HA-DC-190 Series*.

[31] Anthony D. Kurtz, Alexander A. Ned, Joseph VanDeWeert, and Steve Carter. High Accuracy Miniature Pressure Transducer. Technical report, Society of Flight Test Engineers, 2006.

[32] John P. Sullivan, Steven P. Schneider, Tianshu Liu, Justin Rubal, Chris Ward, Joseph Dussling, Cody Rice, Ryan Foley, Zeimin Cai, Bo Wang, and Sudesh Woodiga. Quantitative Global Heat Transfer in a Mach-6 Quiet Tunnel. Technical Report CR-2012-217331, NASA, February 2012.

[33] N. Parziale, J. Shepherd, and H. Hornung. Reflected shock tunnel noise measurement by focused differential interferometry. *AIAA Journal*, 2012. doi:10.2514/6.2012-3261.

[34] Elizabeth Benitez. Basic FLDI optical setup, illustration. Unpublished, April 2019. From an in-lab communication.

[35] Elizabeth Benitez. Quantifying FLDI signal. Unpublished, September 2019. From an in-lab communication.

[36] Saravanamutoo, H. I. H. and Rogers, G. F. C. and Cohen, H. and Straznicky, P. V. *Gas Turbine Theory*. Pearson Education Limited, Sixth edition, 2009.

[37] Zucrow and Hoffman. *Gasdynamics*, volume II. Krieger, Malabar, Florida, 1985.

[38] A. Roth. *Vacuum Sealing Techniques*. AIP Press, April 1994. Pages 5– 9, 750.

[39] Fox, McDonald, and Pritchard. *Fluid Mechanics*. Wiley, Eighth edition, 2011.

[40] Karl Yrjanainen. *Plumbing Engineering Design Handbook*, volume 2, chapter Vacuum Systems, pages 175–196. American Society of Plumbing Engineers, 8614 W. Catalpa Avenue, Suite 1007, Chicago, IL 60656-1116, 2006.

[41] R. Gordon Livesey. Flow of Gases Through Tubes and Orifices. In James M. Lafferty, editor, *Foundations of Vacuum Science and Technology*, pages 103–104. John Wiley and Sons, Inc., 1998.

[42] R. G. Cunningham. Orifice Meters With Supercritical Compressible Flow. *Transactions of the AMSE*, (50-A-45):625–638, July 1951.

[43] Oerlikon Leybold Vacuum, Cologne, Germany. *Soegevac SV630B-SV750B, Single-stage, oil-sealed rotary vane pump*.

[44] Franklin Turbeville. Parametric Study of a 7° Half-Angle Cone With Highly-Swept Fins at Mach 6. Master's thesis, Purdue University, May 2018.

[45] Brandon Chynoweth. *Measuremetns fo Transition Dominated by the Second-Mode Instability at Mach 6*. PhD thesis, Purdue University, May 2018.

[46] M. V. Morkovin. Probe Interference in Measurements in Supersonic Laminar Boundary Layers. *Journal of the Aeronautical Sciences*, Vol. 21(No. 11):785–787, 1954.

APPENDICES

A. LOG OF RUN CONDITIONS

This appendix contains a log of the BAM6QT runs made during tunnel entries over the course of this project.

A.1 Inverse Flare Entry

Dates of entry: 19 - 23 June 2017

Entry unsuccessfully repeated AAE 520 experiments trying to start the model in BAM6QT with varied pipe-insert positions.

Run Number	$p_{0,i}$	$T_{0,i}$	Vacc (torr)	Quiet	Thermocouple
INF.3	71.1	155.5	1.59	Y	0.995

A.2 Smooth Insert Entry I

Dates of entry: 29 January to 2 February 2018

First entry making measurements with the suction model. The entry was largely unsuccessful with issues such as poorly applied temperature-sensitive paint. Also, the traverse scratched the smooth insert surface, and a few of the PCB wires broke shortly after installing. As the cold-junction-compensator battery died on the last day with no spares available, the listed thermocouple value is 0 in the table.

Run number	$p_{0,i}$ **(psia)**	$T_{0,i}$ **(°C)**	**Vacc. (torr)**	**Quiet?**	**Thermocouple (mV)**
SJF.11	117.2	156.7	0.8410	Y	1.1896

A.3 Low Max-Quiet Entry

Dates of entry: 2 - 6 April 2018

Entry where the first iteration of the suction system was tested. The maximum quiet pressure in the tunnel was 28 psia.

Run number	$p_{0,i}$ **(psia)**	$T_{0,i}$ **(°C)**	**Vacc. (torr)**	**Quiet?**	**Thermocouple (mV)**
SAF.12	28.9	149	1.06	Y	0.952
SAF.13	28.9	149.3	1.37	Y	0.952

A.4 Oil-Flow Entry

Dates of entry: 7 - 11 May 2018

Entry where oil flow was attempted on the model.

Run number	$p_{0,i}$ **(psia)**	$T_{0,i}$ **(°C)**	**Vacc. (torr)**	**Quiet?**
OIF.3	133	152.7	1.63	Y
OIF.4	154.8	155.4	1.94	Y

A.5 Unsuccessful Suction System Entry

Dates of entry: 3 - 14 September 2018

The first week of the entry was tests with the smooth plenum insert, and the second week provided the first tests involving the updated suction system. The traverse Kulite was not functioning properly during the entry, and the suction system leaked during the second week.

Run number	$p_{0,i}$ **(psia)**	$T_{0,i}$ **(°C)**	**Vacc. (torr)**	**Quiet?**	**Thermocouple (mV)**	**Suction Vacc. (torr)**
SSF.1	93	153	5.59	N	1.077	n/a
SSF.8	159.4	159.2	1.36	Y	0.843	n/a

A.6 Smooth Insert Entry: Successful

Dates of entry: 7-23 November 2018

Entry in which the smooth insert data was successfully measured in a controlled manner. The first week and a half was used to test the smooth blank. The last week was intended for suction tests, but several issues arose and no data was measured with the suction setup.

Run number	$p_{0,i}$ **(psia)**	$T_{0,i}$ **(°C)**	**Vacc. (torr)**	**Quiet?**	**Thermocouple (mV)**
Smooth.1	155.3	159.8	2.19	Y	0.983
Smooth.2	155.1	158	1.41	Y	0.992
Smooth.3	155.6	158	1.56	Y	1.022
Smooth.4	135.2	157.7	2.14	Y	1.043
Smooth.5	115.6	158.4	1.43	Y	1.042
Smooth.6	155.8	158.5	3.71	Y	1.126
Smooth.7	155.6	157.8	1.55	Y	1.163
Smooth.8	156.2	158.4	3.01	Y	1.211
Smooth.9	136.2	157.9	3.54	Y	1.244
Smooth.10	136.7	157.4	1.43	Y	1.244
Smooth.11	136.2	157.4	3.52	Y	1.27
Smooth.12	156.7	156.4	1.57	Y	1.128
Smooth.13	156.2	157.2	2.05	Y	1.142
Smooth.14	155.5	157.2	3.48	Y	1.059
Smooth.15	135.6	158.3	3.23	Y	1.119
Smooth.16	136.2	157.8	1.6	Y	1.15
Smooth.17	136.7	157.6	1.69	Y	1.18
Smooth.18	153.8	158.4	2.01	Y	1.045
Smooth.19	155.6	159.2	2.86	Y	1.113
Smooth.20	154.6	159.6	2.12	Y	1.209
Smooth.21	134	157.9	1.52	Y	1.171
Smooth.22	136.4	158.1	1.81	Y	1.163
Smooth.23	133.6	158.9	2.1	Y	1.16

A.7 Suction Insert Entry I: Successful

Dates of entry: 14 - 25 January 2019

First successful tunnel entry with the suction system providing choked suction. The

first suction section was used during the tests. Measurements were made in positions to match those from the Smooth Insert Entry: Successful.

Run number	$p_{0,i}$ **(psia)**	$T_{0,i}$ **(°C)**	**Vacc. (torr)**	**Quiet?**	**Thermocouple (mV)**	**Suction Vacc. (torr)**
SS1.1	154	158.5	8.27	Y	1.1	0.191
SS1.2	151.3	158.1	1.39	Y	1.101	0.612
SS1.3	150.3	158.3	2.02	Y	1.197	0.941
SS1.4	152.6	160.1	10.7	Y	1.1	0.462
SS1.5	153.2	159.5	3.89	Y	1.321	0.425
SS1.6	153.2	159.5	5.58	Y	1.393	0.344
SS1.7	153.3	159.4	6.65	Y	1.468	0.316
SS1.8	153	158.2	1.39	Y	1.338	0.312
SS1.9	151.9	158.7	5.05	Y	1.434	0.244
SS1.10	152.7	154.4	2.62	Y	1.1	0.278
SS1.11	153.7	156	10.8	Y	1.571	0.244
SS1.12	135.2	156.3	5.56	Y	1.536	0.2
SS1.13	136.4	156.1	4.53	Y	1.531	0.206
SS1.14	136.1	156.5	6.14	Y	1.551	0.209
SS1.15	153.2	156.9	4.16	Y	1.539	0.219
SS1.16	153.8	159.2	7.72	Y	1.129	0.212
SS1.17	154	159.4	5.11	Y	1.324	0.212
SS1.18	152.2	158.5	5.61	Y	1.396	0.206
SS1.19	136.6	157.6	3.39	Y	1.538	0.194
SS1.20	136	158.3	5.58	Y	1.571	0.166
SS1.21	135.7	157.7	5.25	Y	1.507	0.172

A.8 Suction Insert Entry II: Successful

Dates of entry: 29 April - 17 May 2019

Second set of tests with the first suction section. Measurements included suction runs without the traverse probe, comparisons with the suction system disabled, an additional set of measurements downstream of the turn, and FLDI measurements. All measurements were made in quiet flow.

Run number	$p_{0,i}$ **(psia)**	$T_{0,i}$ **(°C)**	**Vacc. (torr)**	**Thermocouple (mV)**	**Suction Vacc. (torr)**

SS2.1	149.2	165.7	3.33	0.695	0.153
SS2.2	150.6	159.5	2.84	0.732	0.144
SS2.3	152.7	159.3	1.55	0.754	0.128
SS2.4	151.8	157.7	1.68	0.777	0.137
SS2.5	149.4	160.2	2.03	0.772	0.131
SS2.6	131.0	155.7	21.5	0.793	0.137
SS2.7	153.7	159.5	5.37	0.825	0.137
SS2.8	153.6	158.9	3.25	1.076	0.131
SS2.9	153.2	159.1	4.62	1.152	0.125
SS2.10	152.8	158.3	3.08	1.162	0.131
SS2.11	153.5	158.0	5.25	1.224	0.122
SS2.12	135.5	157.2	8.05	1.263	0.125
SS2.13	153.5	160.2	7.11	1.286	0.122
SS2.14	135.2	157.9	9.75	1.317	0.131
SS2.15	153.6	158.2	7.72	1.322	0.109
SS2.16	153.0	158.3	7.61	0.909	0.137
SS2.17	153.8	159.1	5.68	1.123	0.131
SS2.18	153.2	157.7	2.58	1.186	0.125
SS2.19	153.5	158.2	5.55	1.237	0.134
SS2.20	151.4	159.3	15.8	0.839	0.131
SS2.21	137.2	159.2	6.35	1.072	0.119
SS2.22	137.3	158.8	6.48	1.159	0.128
SS2.23	137.3	158.3	1.86	1.091	0.134
SS2.24	153.0	158.4	2.46	1.139	0.134
SS2.25	153.8	157.7	6.47	1.203	0.134
SS2.26	152.6	158.9	6.03	1.222	0.134
SS2.27	136.1	157.3	4.41	1.224	0.131
SS2.28	137.0	160.2	8.75	0.878	0.125
SS2.29	136.2	160.0	6.49	1.045	0.125
SS2.30	149.3	159.2	2.43	1.059	0.125
SS2.31	152.8	159.0	5.33	1.159	0.125
SS2.32	152.2	158.2	3.73	1.164	0.153
SS2.33	136.2	157.2	4.04	1.222	0.15

SS2.34	136.9	158.7	3.78	0.839	0.153
SS2.35	136.5	159.0	6.42	1.041	0.137
SS2.36	153.6	159.5	5.40	0.826	0.159
SS2.37	153.6	159.0	1.37	0.969	0.153
SS2.38	151.1	160.1	6.11	0.804	0.153
SS2.39	152.0	159.8	3.70	1.010	0.137
SS2.40	152.1	158.2	2.50	1.016	0.153
SS2.41	152.9	158.4	5.83	1.143	0.153
SS2.42	153.9	158.1	2.32	1.112	0.15
SS2.43	152.5	158.5	5.31	1.169	0.153
SS2.44	152.1	159.2	8.30	0.870	0.144
SS2.45	152.3	159.6	6.50	1.053	0.131
SS2.46	152.7	159.3	5.49	1.126	0.137
SS2.47	152.9	158.6	2.38	1.102	0.137
SS2.48	151.5	158.4	5.29	1.172	0.137
SS2.49	153.0	158.2	7.00	1.226	0.134
SS2.50	151.4	157.8	6.12	1.223	0.131
SS2.51	153.8	157.3	3.51	1.223	0.134
SS2.52	153.2	159.9	5.98	0.856	0.144
SS2.53	150.1	159.3	4.41	0.945	0.141
SS2.54	153.4	159.2	5.58	1.076	0.141
SS2.55	152.7	158.9	6.35	1.178	0.134
SS2.56	152.7	158.5	7.25	1.203	0.137

B. MODEL DRAWINGS

Provided are drawings of the model parts, suction section plenum, hollow angle-of-attack adapter, and hollow sting. Included are both the initially machined parts and later modifications.

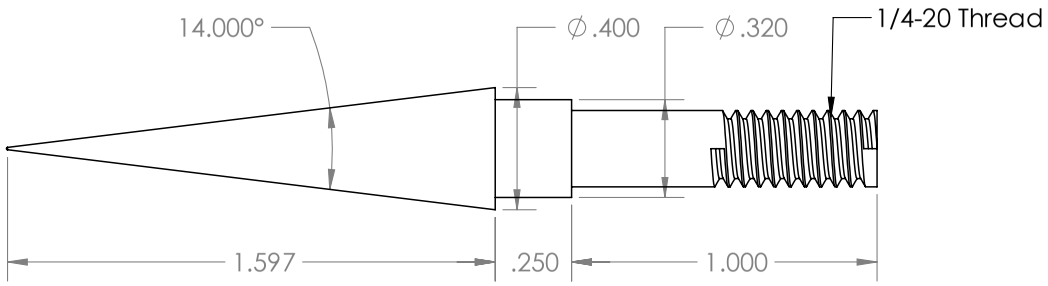

TITLE: Nosetip

UNLESS OTHERWISE SPECIFIED: - DIMENSIONS ARE IN INCHES - TOLERANCES 0.001 INCHES - DEBURR AND BREAK SHARP EDGES	DRAWN: PHILLIP PORTONI CONTACT: PPORTONI@PURDUE.EDU (501) 909 4290 ASL ROOM 5	MATERIAL: 17-4 steel	DATE: 1/19/2018
		SCALE: 2:1	SHEET 1 OF 1

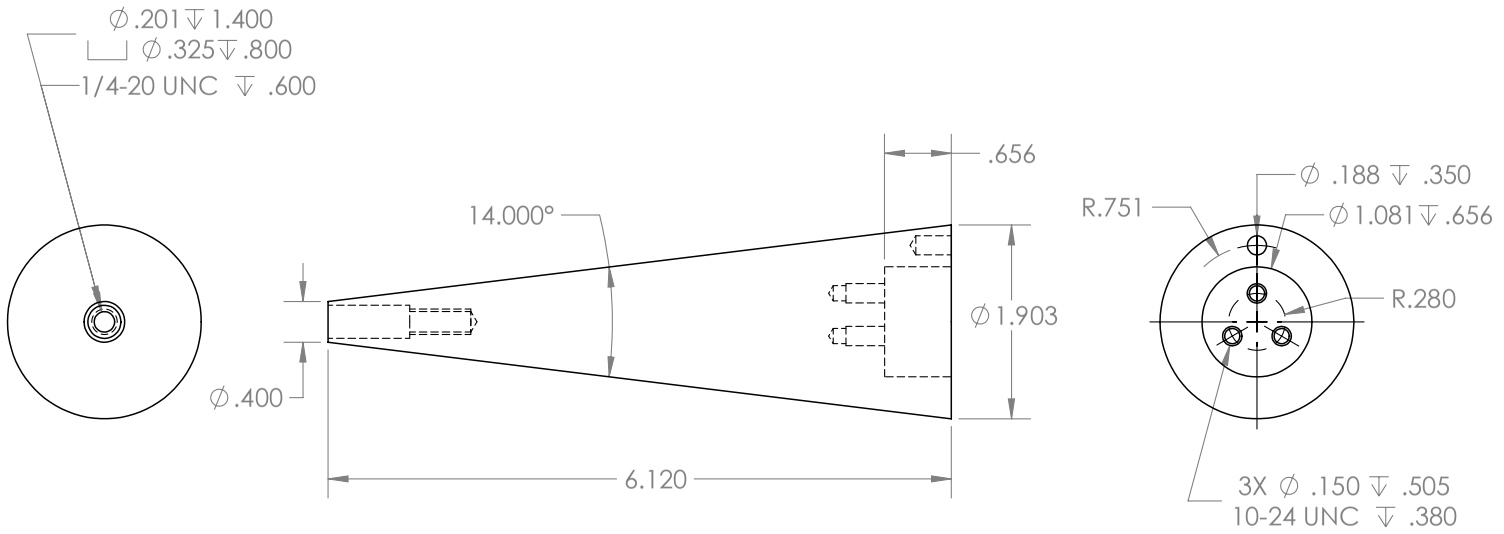

		TITLE: Forecone - As Machined	
UNLESS OTHERWISE SPECIFIED: - DIMENSIONS ARE IN INCHES - TOLERANCES 0.001 INCHES - DEBURR AND BREAK SHARP EDGES	DRAWN: PHILLIP PORTONI CONTACT: PPORTONI@PURDUE.EDU (501) 909 4290 ASL ROOM 5	MATERIAL: Al 6061	DATE: 1/19/2018
		SCALE: 2:3	SHEET 1 OF 1

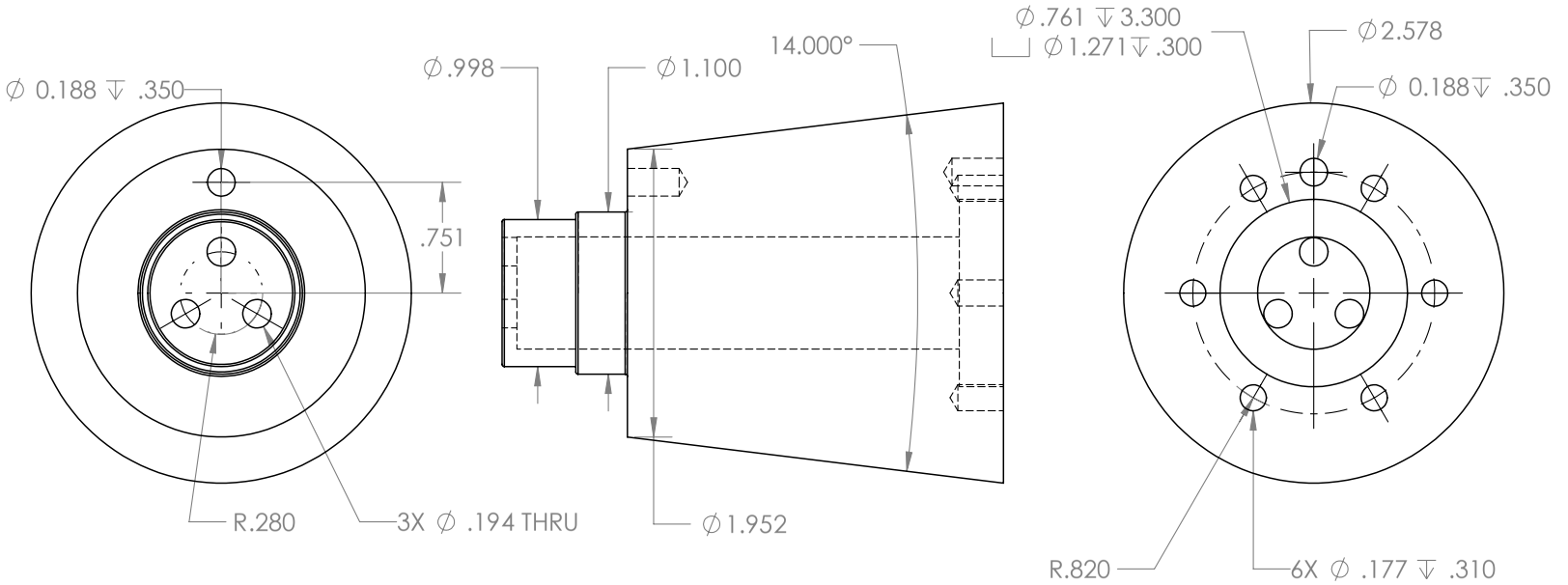

		TITLE: Plenum Blank - As Machined	
UNLESS OTHERWISE SPECIFIED: - DIMENSIONS ARE IN INCHES - TOLERANCES 0.001 INCHES - DEBURR AND BREAK SHARP EDGES	DRAWN: PHILLIP PORTONI CONTACT: PPORTONI@PURDUE.EDU (501) 909 4290 ASL ROOM 5	MATERIAL: Aluminum	DATE: 1/19/2018
		SCALE: 1:1	SHEET 1 OF 1

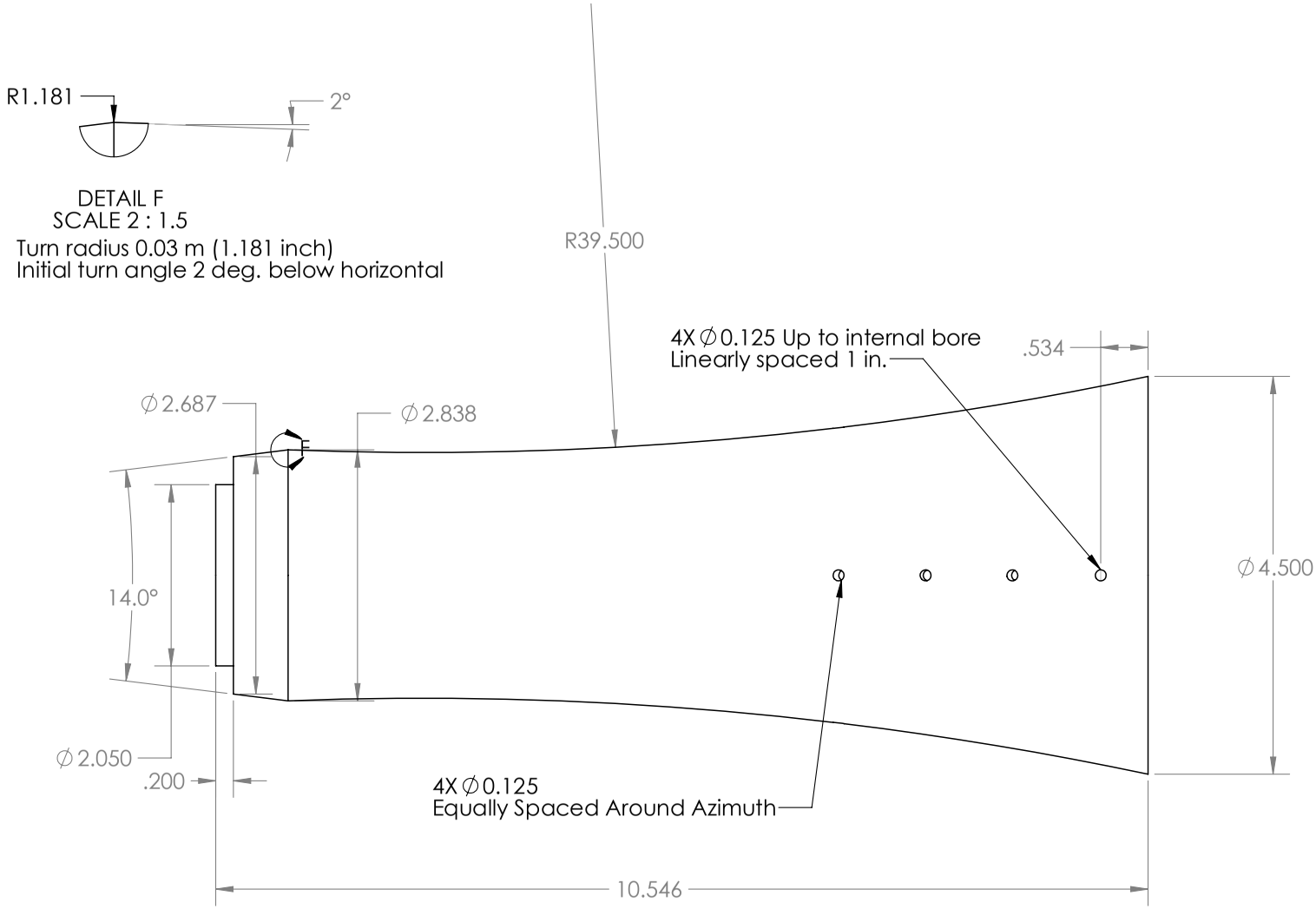

	TITLE: Afterbody - As Machined	
DRAWN: PHILLIP PORTONI CONTACT: PPORTONI@PURDUE.EDU (501) 909 4290 ASL ROOM 5	MATERIAL: Al 6061	DATE: 8/16/2018
	SCALE: 2:3	SHEET 1 OF 3

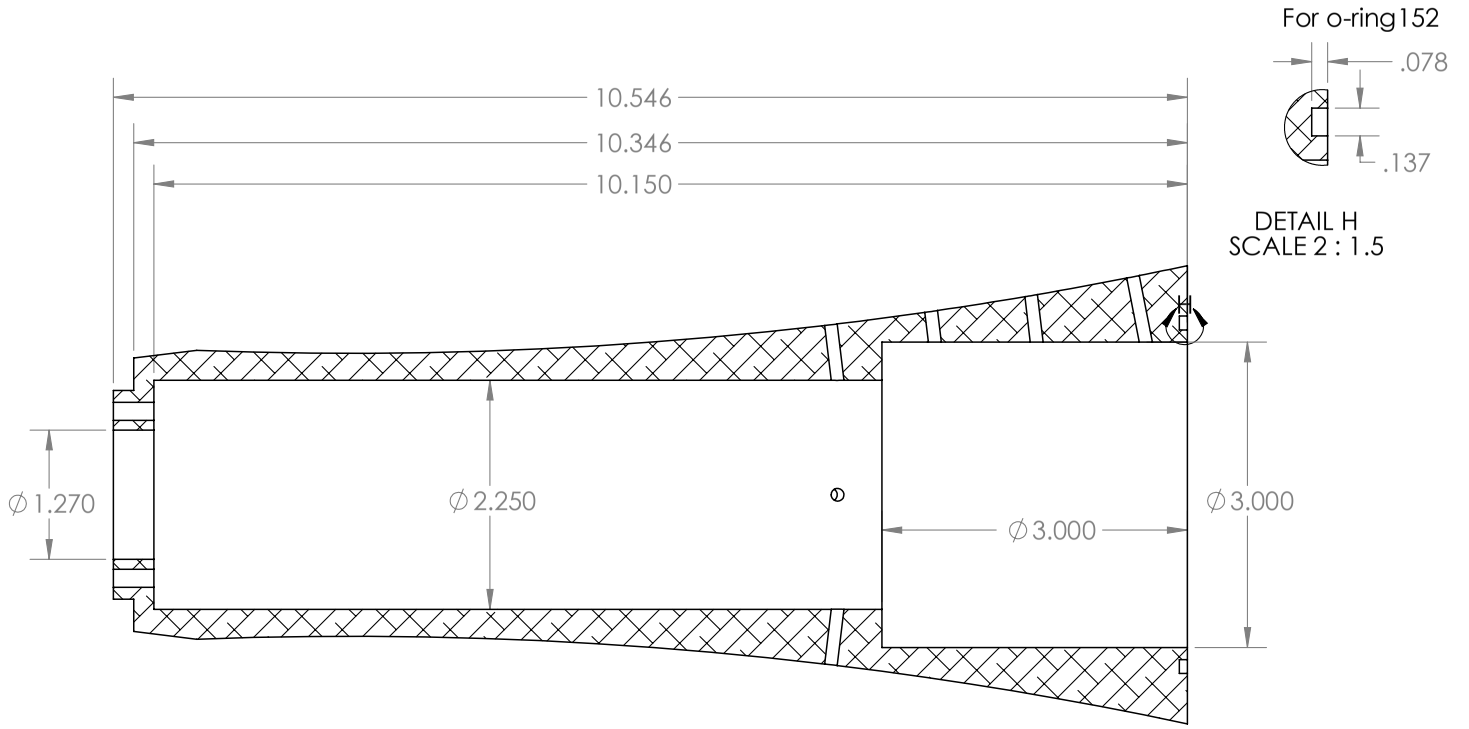

SECTION G-G
SCALE 1 : 1.5

	TITLE: Afterbody - Section and O-ring views	
DRAWN: PHILLIP PORTONI CONTACT: PPORTONI@PURDUE.EDU (501) 909 4290 ASL ROOM 5	MATERIAL: Al 6061	DATE: 8/16/2018
	SCALE: 2:3	SHEET 2 OF 3

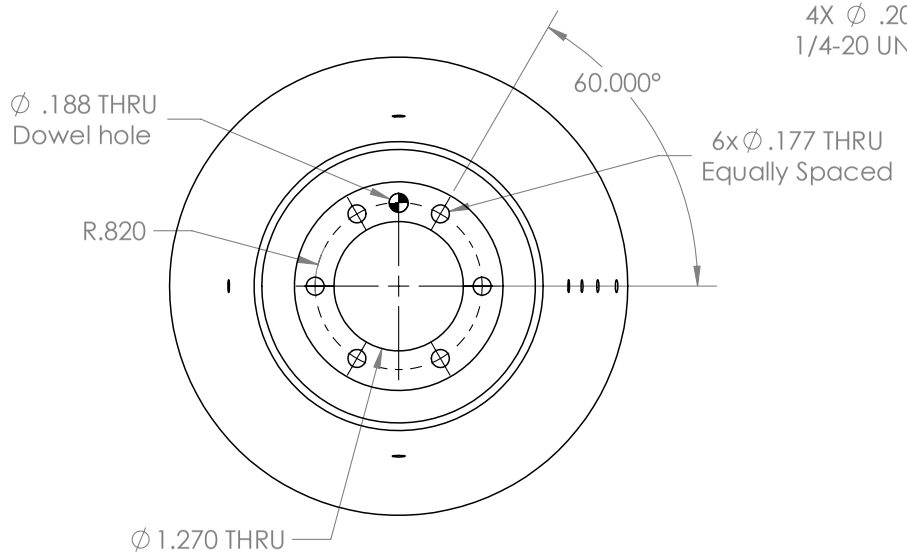

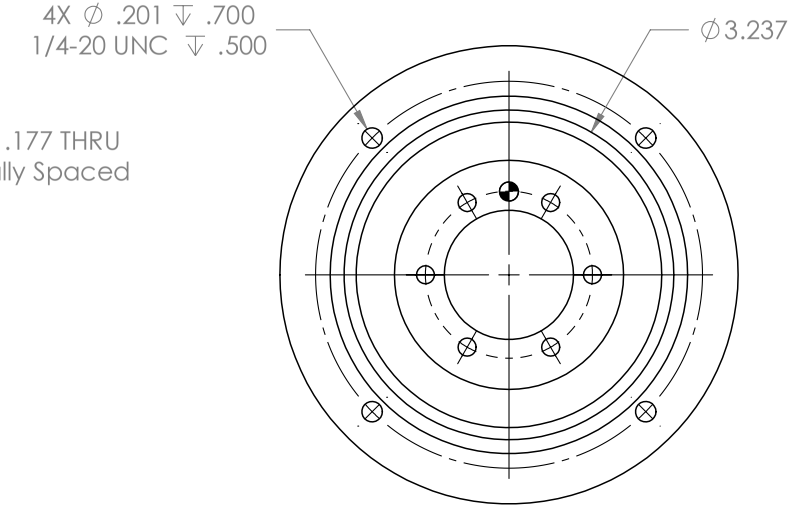

Note: holes match to Calspan fitrings

	TITLE: Afterbody - Front and Back view	
DRAWN: PHILLIP PORTONI CONTACT: PPORTONI@PURDUE.EDU (501) 909 4290 ASL ROOM 5	MATERIAL: Al 6061	DATE: 8/16/2018
	SCALE: 2:3	SHEET 3 OF 3

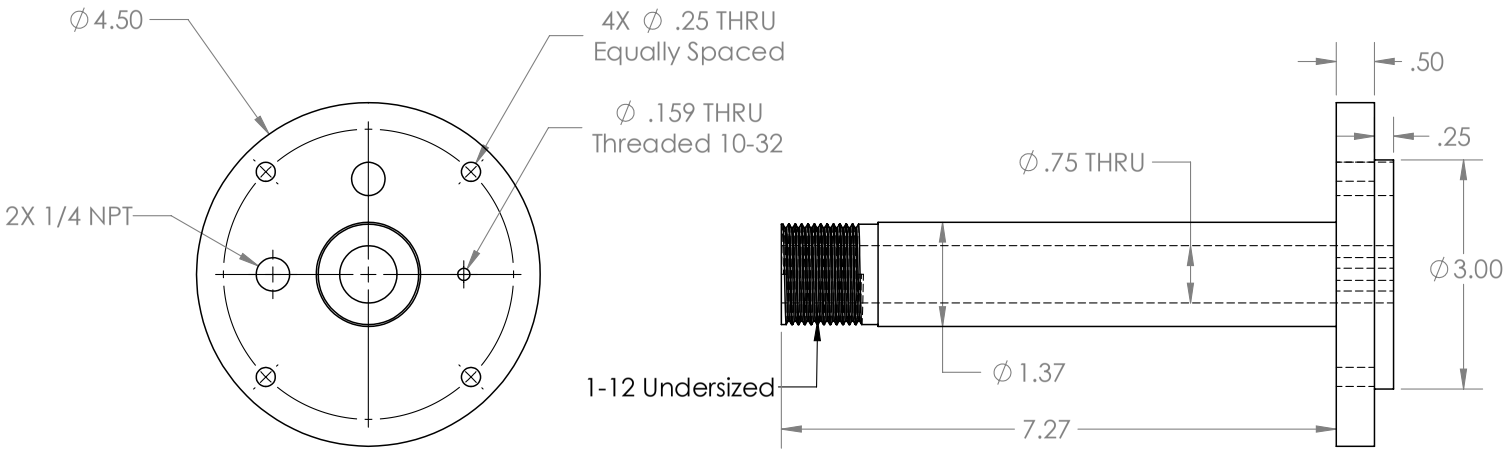

	TITLE: Baseplate - As Machined	
DRAWN: PHILLIP PORTONI CONTACT: PPORTONI@PURDUE.EDU (501) 909 4290 ASL ROOM 5	MATERIAL: Al 6061	DATE: 1/19/2018
	SCALE: 1:2	SHEET 1 OF 1

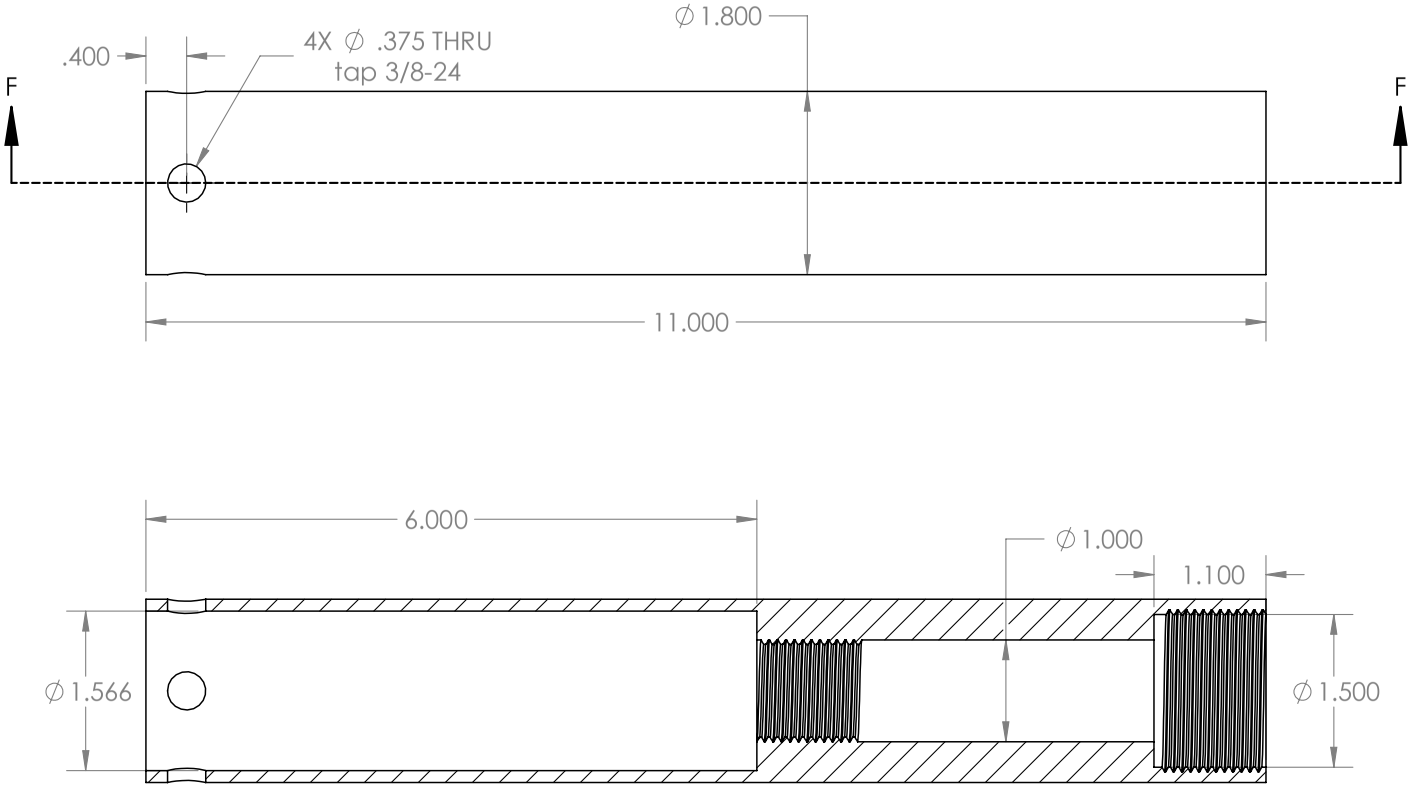

SECTION F-F
SCALE 1 : 1.5

	TITLE: AOA adapter - As Machined	
DRAWN: PHILLIP PORTONI CONTACT: PPORTONI@PURDUE.EDU (501) 909 4290 ASL ROOM 5	MATERIAL: Stainless steel	DATE: 1/19/2018
	SCALE: 2:3	SHEET 1 OF 2

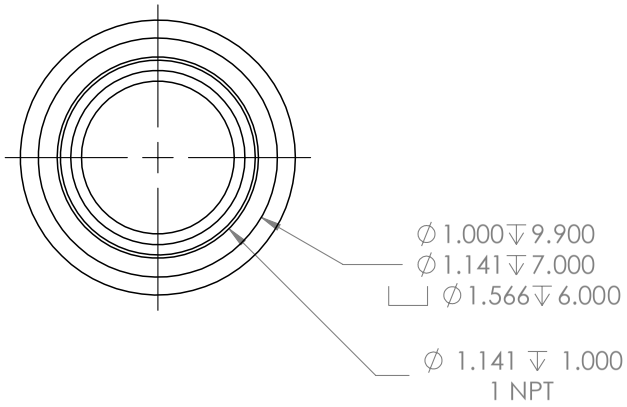

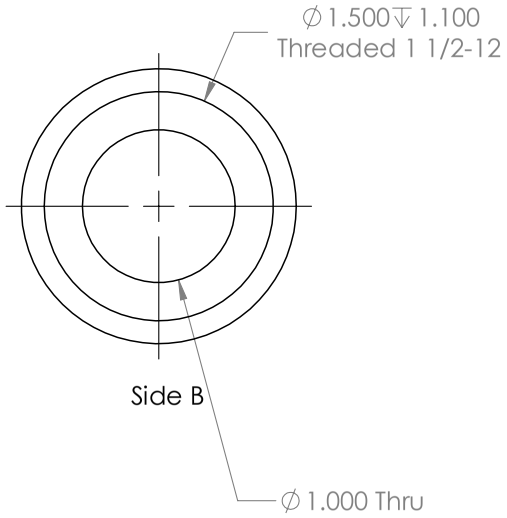

	TITLE: AOA adapter - As Machined	
DRAWN: PHILLIP PORTONI CONTACT: PPORTONI@PURDUE.EDU (501) 909 4290 ASL ROOM 5	MATERIAL: Stainless steel	DATE: 1/19/2018
	SCALE: 1:1	SHEET 2 OF 2

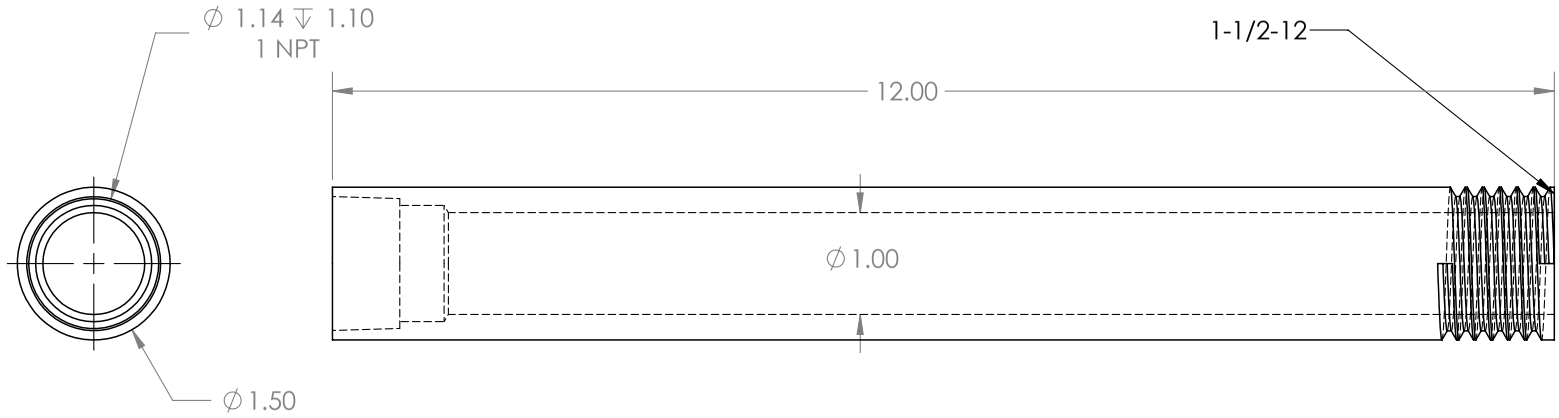

TITLE:
Sting - As Machined

DRAWN:
PHILLIP PORTONI
CONTACT:
PPORTONI@PURDUE.EDU
(501) 909 4290
ASL ROOM 5

MATERIAL:
17-4 Steel

DATE:
4/20/2018

SCALE: 1:2

SHEET 1 OF 1

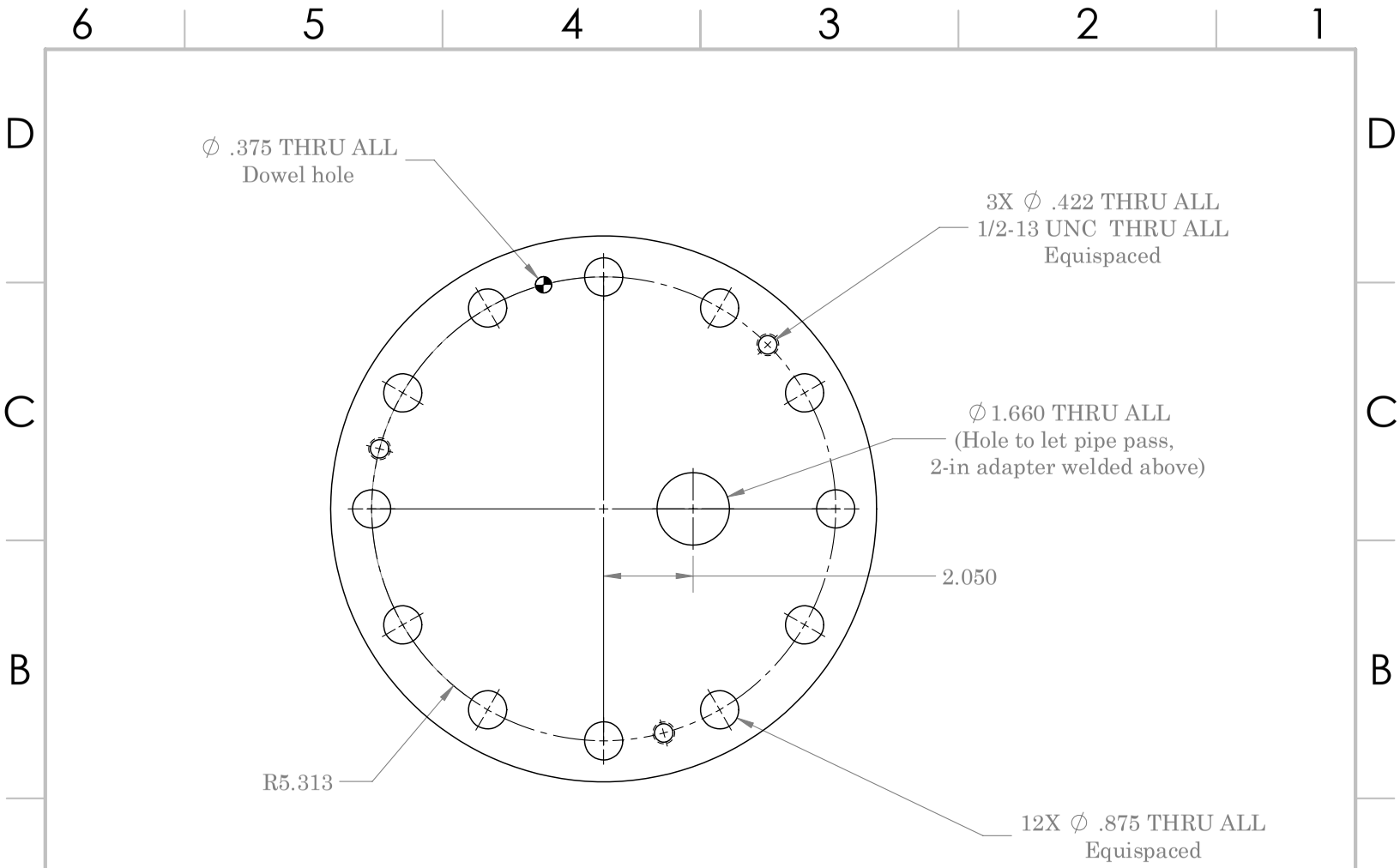

flange to let pipe pass through tunnel wall	Sheet: 1 Scale: 1:3
Material: 304L Stainless Steel Phillip Portoni 5/21/2018	

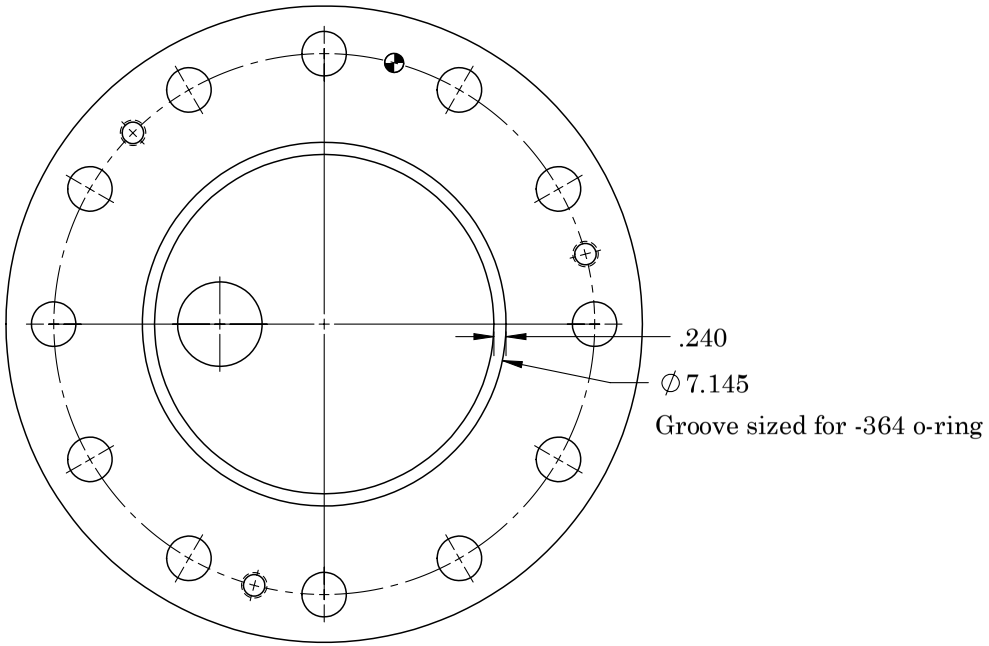

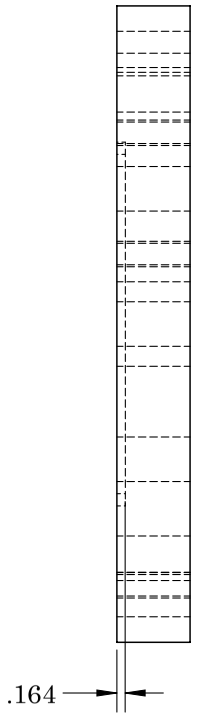

O-ring groove cut by mistake due to misreading tunnel schematic

o-ring groove detail	Sheet: 2 Scale: 1:3
Phillip Portoni	9/11/2019

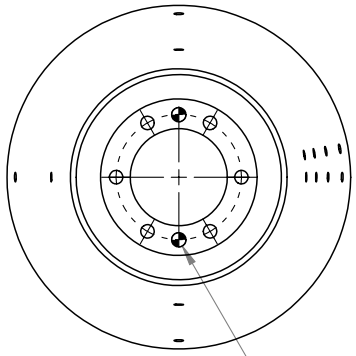

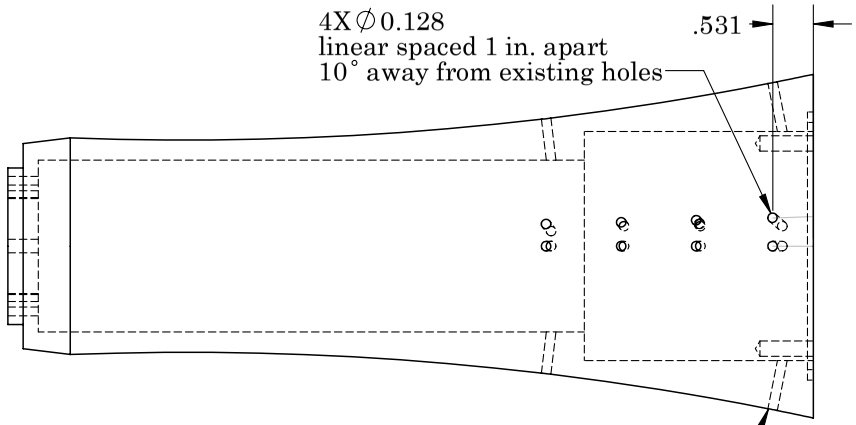

Clean up the 3 inch bore on the back side of the model

Modifications to existing Al6061-T6 afterbody

afterbody_modified	Sheet: 1 Scale: 1:2
Phillip Portoni	9/11/2019

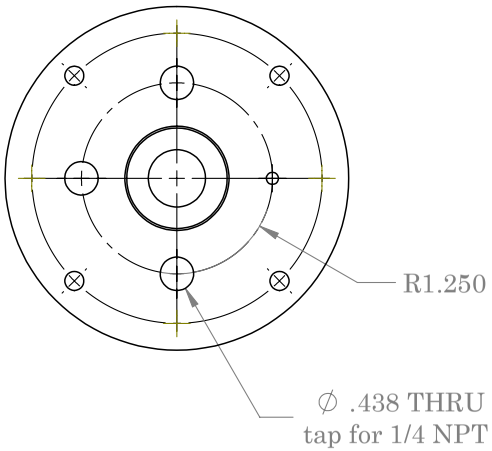

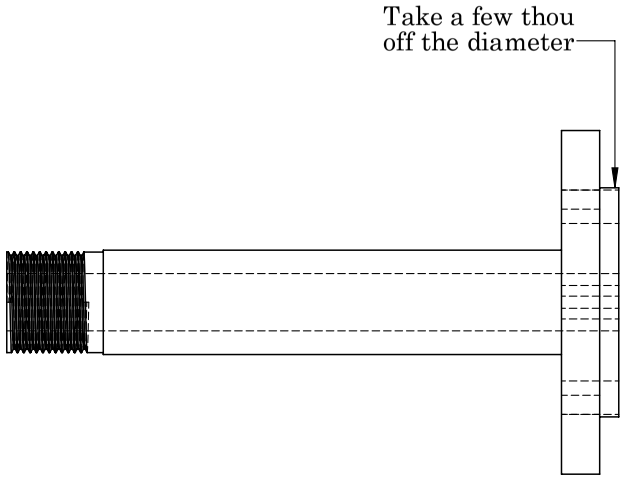

Modifications to existing Al 6061-T6 baseplate

baseplate_modified	Sheet: 1 Scale:1:2
Phillip Portoni	9/11/2019

C. PLENUM PRESSURE PREDICTION CODE

Provided below is the Matlab script used to predict the pressure in the plenum and determine whether or not the suction flow was sonic.

```
% Code to predict the pressure in the suction plenum during runs
% Iterative mass flow rate in the suction plenum over the course of a run.
% Start with an initial pressure in the plenum of 155 psia and assume a
% resevoir in the vacuum tank at 1 torr. Work it out from pressure change,
% to mass flow rate. Create an iterative process that updates every 0.01
% seconds or so. Create a nice fancy plots of plenum pressure vs. time
% in the end.

% Udpate:
% Now including subsonic mass addition from the
% suction section and mass removal from the vacuum pump.

% Update: 1/9/2019
% Reworked how starting high pressure flow removal is calculated

% Update: 4/10/2019
% Tried several methods to approach measured plenum pressures, nothing
% worked. Reapplied code to generate figures for thesis.

clear all; close all; clc;

tic
% Analysis
% Sizes and conduction of each section in suction assembly
```

```
% Diameters (cm)
ss1_diam = 2.25*2.54; % Narrow part of the afterbody
ss2_diam = 3*2.54; % Wide part of the afterbody
ss3_diam = 0.75*2.54; % Baseplate pass through
% (Increasing requires redesign of model end,
%  max is 1.38" (1-1/4 pipe)
ss4_diam = 1.0*2.54; % Angle-of-attack adapter and sting
% (Cannot be increased)
ss5_diam = 1.38*2.54; % 1-1/4" pipe
% (sting to 6"line, to solenoid in prop)
ss6_diam = 2.067*2.54; % proposed 2" hose (soleniod to 6" line)

% Lengths (cm)
ss1_l = 7.15*2.54; % Section is 7.15 in long
ss2_l = 3.0*2.54; % Section is 3 in long
ss3_l = 7.27*2.54; % Section is 7.27 in long (Ideal 6)
ss4_l = 11.5*2.54; % Sections are 11.5 in long
ss5_l = 144*2.54; % Section is 12 ft long
ss5b_l = 24*2.54; % Section is 2 ft long
ss6_l = 120*2.54; % Proposed section is 10 ft long
L_tot = ss1_l + ss2_l + ss3_l + ss4_l + ss5b_l + ss6_l;

% Volumes of sections under pressure (cm^3)
ss1_V = pi*(ss1_diam/2)^2*ss1_l;
ss2_V = pi*(ss2_diam/2)^2*ss2_l;
ss3_V = pi*(ss3_diam/2)^2*ss3_l;
ss4_V = pi*(ss4_diam/2)^2*ss4_l;
ss5_V = pi*(ss5_diam/2)^2*ss5b_l; % Section under pressure is 24 in.
V_tot = (ss1_V +ss2_V +ss3_V +ss4_V +ss5_V)*1*10^-6; % m^3

% Additional volumes
```

```
plenum_vol = 0.055*0.001; % m^3
tank_vol = 500*0.0283168; % m^3
plenV_rat = plenum_vol/V_tot;

% Conductance equation: C = kv*pbar*diam^4/length
% Diameter in cm, length in cm, C in liter/sec, pbar mean
% presssure in torr
% kv = pi/(128*mu), where mu is the dynamic viscosity
% Sutherland's approximation for air at 300 K:
S = 110.4; % K, Sutherland temperature
Tref = 273.15; % K, reference temp
muref =1.716*10^-5; % kg/ms, reference dynamic visc at ref. temp
mu = muref*(300/Tref)^1.5*((Tref+S)/(300+S)); % pa*s
kv = pi/(128*mu)*133/1000; % L/(cm^3*torr*s)
% includes conversion factors for pa to torr and cm3 to L

% C = pbar*kv*d^4/l for each of pipe section
% The pressure independent variables are defined here
C1_pbar = kv*(ss1_diam)^4/ss1_l;
C2_pbar = kv*(ss2_diam)^4/ss2_l;
C3_pbar = kv*(ss3_diam)^4/ss3_l;
C4_pbar = kv*(ss4_diam)^4/ss4_l;
C5_pbar = kv*(ss5_diam)^4/ss5_l;
% 90 deg. turn in 1-1/4 pipe has an equivalent length of 30*L/D
% So for 1-1/4 in elbow:
Cvirt_pbar = kv*(ss5_diam)^4/(30*1.38*2.54);

% Total conductance per mean pressure
C_pbar_tot = (1/C1_pbar + 1/C2_pbar + 1/C3_pbar + 1/C4_pbar...
+ 1/C5_pbar + 1/Cvirt_pbar)^-1; % L/s
```

```
% % Use the following if modeling 2 in hose
% C5_pbar = kv*(ss5_diam)^4/ss5b_l;
% C6_pbar = kv*(ss6_diam)^4/ss6_l;
% C_pbar_tot = (1/C1_pbar + 1/C2_pbar + 1/C3_pbar + 1/C4_pbar...
%     + 1/C5_pbar + 1/C6_pbar + 1/Cvirt_pbar)^-1; % L/s

% Equations from Roth, Vacuum Sealilng Techniques
% Throughput, Q
% Q = (p1 - p2)*C_tot
% rate of pressure change, dp/dt = Q/V,
% simple approximation, p = mRT/V with const. temperature
% yields RT/V*dm/dt = Q/V
% dm/dt = Q/RT = C_tot*(p_plenum-p_tank)/RT

T0_fs = 430; % K, typical freestream total temperature before a run
R  = 287.058; % J/(kg*K), gas constant for air
T_tank = 300; % K, assume tank temp. is constant around 27 deg C

% Mass addition from suction and removal from pump
% Approximating the freestream pressure in the tunnel as fixed
% at 155 psia for the duration of a run

% The vacuum pump manual lists a pump speed of around 400 cfm for tank
% pressures of 1 to 10 torr.
Vdot_out = 400/60*0.0283168; % m^3/s

% The mass flow rate in the boundary layer of a 7 deg cone in 170 psia
% quiet flow was calculated in STABL. The result is 0.0061 kg/s. The
% suction system was initially desgined to remove up to 10% of this.
mdot_20per = 0.00061; % kg/s
```

```
% Reality of course is different and the amount of flow being removed
% is a function of the surface pressure, plenum pressure and
% orifice size.

% The surface area of first suction section is about 6.94 in^2,
% and has 3.5% porosity. The later suction sections have a
% porosity of around 5%.
porosity = 0.05;
A_ori = porosity*6.94*0.00064516; % m^2

% Assuming a discharge coefficient of 0.995 per White,
% Fluid Mechanics
Cd = 0.995;
% For air, the specific heat ratio is around 1.4
gam = 1.4;
% Taylor-Maccoll approximation for a 7 deg half-angle cone in
% Mach 6 flow
p_edge_p_0fs = 1.97922954*0.00063336; % surface static pressure ratio
rho_edge_rho_fs = 1.62273142; % surface density, rho_fs is the
% freestream density
p_0fs = 155*6894.76; % pa, freestream total pressure

% Using isentropic relations for mach 6 flow
p_fs = p_0fs*0.00063336; % pa, freestream static pressure
T_fs = T0_fs*0.12195121; % K, freestream static temperature
rho_fs = p_fs/(R*T_fs); % kg/m^3, freestream density
% Edge conditions
rho_edge = rho_fs*rho_edge_rho_fs; % kg/m^3, edge denstity
T_edge = T_fs*1.21969015;% K, edge static temperature
p_edge = p_0fs*p_edge_p_0fs;% pa, edge pressure
% Surface conditions
```

```
p_surf = p_edge; % pa,
% pressure remains constant across the boundary layer
T_surf = 300; % K, typical model temperature at run start
rho_surf = rho_edge*T_edge/T_surf; % kg/m^3, temperature rises in
% boundary layer and the density decreases to copmensate

% For unchoked mass flow rate
% mdot_sub = Cd*A_ori*sqrt(2*p_surf*rho_surf*(gam/(gam-1))*...
% ((p(i)/p_surf)^(2/gam)-(p(i)/p_surf)^((gam+1)/gam)));
% where mdot is the mass flow rate, Cd is a discharge coefficient,
% A_ori is the diameter of the orifice,
% gam (gamma) is the ratio of specific heats,
% rho_surf is the density of the gas,
% p_surf is the pressure upstream of the orifice
% p(i) is the plenum pressure.

% For choked flow through an orifice, the equation simplifies to:
% mdot = Cd*A_ori*...
% sqrt(gam*rho_surf*p_surf*(2/(gam+1))^(gam+1)/(gam-1))
% which is only a function of the surface pressu

% Define the time vector
dt = 1e-6;
t = 0:dt:0.5;% seconds
tlen = length(t);

% preallocate variables
p = zeros(1,tlen);
p_tank = zeros(1,tlen);
m = zeros(1,tlen);
C_tot = zeros(1,tlen);
```

```
mdot_plen_out = zeros(1,tlen);
mdot_rec = zeros(1,tlen);
suck_check = zeros(1,tlen);
Q = zeros(1,tlen);

% Initial conditions
p(1) = 155*6894.76; % pa, initial plenum pressure of 155 psia
% p(1) = 36*133.322; % pa, the actual plenum pressure when solenoid opens
m(1) = p(:,1)*V_tot/(R*T_surf); % kg, initial mass of air in the system
p_tank(:) = 0.2*133.322; % pa, inital tank pressure of 0.2 torr

jj = 1; % counter
cup = 0;
for tt = t(1:(tlen-1))

% Calculate the mean and pressure difference
pbar = (p(jj)+ p_tank(1))/2; % pa
pdiff = p(jj)- p_tank(jj); % pa
pbar_torr = pbar*0.007500612102838; % torr
pdiff_torr = pdiff*0.007500612102838; % torr
%     pbar_torr = 3.14; % mean pressure from simple analysis

if isnan(pbar)||isinf(pbar) == 1
error('NaN or Inf issue');
end

% Update conduction
C_tot(jj) = C_pbar_tot*pbar_torr; % L/s
C_tot_m3 = C_tot(jj)*0.001; % m3/s

% Before the boundary-layer removal begins, the pipe-flow
```

```
% can be modelled as a pipe with uniform initial pressure, p(1,x)
% closed at x = 0 (since it is assumed the air does not blow
% out of the suction skin). The valve opens to a
% constant-pressure tank at t = 0, with the valve located at x = l.
% Per Livesey, the throughput from the pipe is calculated with
% the pressure
% gradient at the end of the pipe.
% Q = C*l(dP/dx) evaluated at x = l.
% The pressure in the pipe, p(t,x) can be calculated by the
% following:
% p(t,x)-p_tank = 4/pi*(p(1,x)-p_tank)*SUM(-1^n/(2*n+1)...
% *exp(-(2*n+1)^2*pi^2*C/(4*V))...
% *cos((2*n+1)*pi/2*x/l));
% for the SUM ranging  n = 0 to infinty
% Source: Foundations of Vacuum Sci. and Tech, Livesey

% The time constant for the first (slowest) term is given by:
% tau0 = 4*V_tot/(pi^2*C_tot(1)*0.001);
% this gives 3.32e-6.
% For t > 0.3*tau0, first term of the series is a good approximation

% Use this relation while plenum pressure exceeds model surface
if p(jj) > p_surf

% at plenum, x = 0, so cos(...*x/l) = cos(0) = 1
p(jj+1) = 4/pi*(p(1) - p_tank(jj))*exp(-pi^2/4*...
100*0.001/V_tot*(t(jj)+dt))- p_tank(jj);
delp = p(jj+1)-p(jj);
m(jj+1) = m(jj) - delp*R*T_surf/V_tot;
Q(jj) = C_tot(jj)*pdiff_torr; % torr*L/s
```

```
%         else
%
%             % Mass removal thin-plate orifice from White Fluid Mechanics.
%             % Expansion factor chosen based on best alignment with
%             % experiments
%             Y = 0.4; % expansion factor
%             bet = 0; % Thin-plate asumption
%             rho = p(jj)/R/T_surf; % kg/m^3, density in plenum
%             mdot_white = Cd*A_ori*Y*sqrt(2*rho*(p(jj)-p_tank(jj))/(1-bet^4));
%             delm_white = mdot_white*dt;
%             p(jj+1) = p(jj) - ( delm_white)*R*T_surf/V_tot;
%             Q(jj) = C_tot(jj)*pdiff_torr; % torr*L/s
%
%
%         end
% Other models used to try modeling plenum pressure

%         % Empirical fit of first 0.4 s from experiments
%         p(jj+1) = 565*exp(-16.46*tt)*133.322;

%          % Throughput and blowing
%         prat = p_surf/p(jj);
%         mdot_blow = Cd*A_ori*sqrt(p(jj)*rho_surf*gam...
%             *(2/(gam+1))^((gam+1)/(gam-1))); % kg/s
%         delm_blow = mdot_blow*dt;
%         mdot_plen_out(jj) = pbar*C_tot_m3/T_surf/R;
%         delm_plen_out = mdot_plen_out(jj)*dt;
%         p(jj+1) = p(jj) - (delm_plen_out + delm_blow)*R*T_surf/V_tot;
%         m(jj+1) = p(jj+1)*V_tot/T_surf/R;

%        %Vacuum pump removal
```

```
%                 mdot_tank_out = p_tank(jj)*Vdot_out/(R*T_tank);
%                 delm_tank_out = mdot_tank_out*dt;
%                  p_tank(jj+1) = pf_tank(jj)-(delm_Q-delm_tank_out)...
%                      *R*T_tank/tank_vol;

else
if cup == 0
cup = 1;
cup_iter = jj %index where suction begins
end

% mass flow rate out of plenum (into tank), kg/s
mdot_plen_out(jj) = C_tot_m3*pdiff/(R*T_surf);
%         Q(jj) = C_tot(jj)*pdiff_torr;%(p(jj+1)-p_tank(jj))*0.00750062; % torr*L/s
%         mdot_plen_out(jj) = Q(jj)*1.56*0.001; % kg/s, Conversion factor from Roth
% mass removed from the plenum, kg
delm_plen_out = mdot_plen_out(jj)*dt;

%         % Vacuum pump mass removal
%         mdot_tank_out = p_tank(jj)*Vdot_out/(R*T_tank); %
%         delm_tank_out = mdot_tank_out*dt;

%         % New tank pressure
%         p_tank(jj+1) = p_tank(jj) + (delm_plen_out-delm_tank_out)...
%             *R*T_tank/tank_vol;

% Is plenum pressure less than surface pressure?
check1 = p(jj)< p_surf; % 0 is false, 1 is true

switch check1
case 0 % Blowing, omit mass addition
```

```
% Update mass and pressure in the model and plenum
% (obsoloete, now using Livesey model).
% m(jj+1) = m(jj) - delm_plen_out; %kg
% p(jj+1) = p(jj) - delm_plen_out*R*T_surf/V_tot;% pa
error('Still blowing, fix that');
case 1 % Sucking
check2 = p(jj)/p_surf < 0.528;
prat = p(jj)/p_surf;
suck_check(jj) = 1;

switch check2
case 0 % Subsonic suction
mdot_sub = Cd*A_ori*sqrt(p_surf*rho_surf*2*...
((gam/(gam-1))*((prat).^(2/gam)-(prat)...
.^((gam+1)/gam))));% kg/s
delm_sub = mdot_sub*dt;
m(jj+1) = m(jj) - delm_plen_out + delm_sub; % kg
p(jj+1) = p(jj) - (delm_plen_out - delm_sub)...
*R*T_surf/V_tot;
mdot_rec(jj) = mdot_sub;
Q(jj) = C_tot(jj)*pdiff_torr; % torr*L/s
case 1 % Sonic suction
mdot_sonic = Cd*A_ori*sqrt(p_surf*rho_surf*gam...
*(2/(gam+1))^((gam+1)/(gam-1))); % kg/s
delm_theory = mdot_sonic*dt;
m(jj+1) = m(jj)- delm_plen_out +...
delm_theory; % kg
p(jj+1) = p(jj) - (delm_plen_out - delm_theory)...
*R*T_surf/V_tot;
mdot_rec(jj) = mdot_sonic;
Q(jj) = C_tot(jj)*pdiff_torr; % torr*L/s
```

```
end
end
end
jj = jj+1;
end

% Plot plenum and tank pressures
figure(1);
p_plot = p*0.00750062; % torr,
p_tankplot = p_tank*0.00750062; % torr
semilogy(t,p_plot,'linewidth',1.5);
hold on
grid on
semilogy(t,p_tankplot,'linewidth',1.5);
xlim([0.005,inf]);
leg1{1} = 'Plenum';
% leg{2} = 'Vacuum tank';
g = gca;
g.FontSize = 16;
xlabel('Time (sec)');
% legend(leg);
ylabel('Pressure (torr)')

% Plot surface pressure ratios
figure(2)
prat = p./p_surf;
semilogy(t,prat,'linewidth',1.5,'color','b');
hold on;
plot([t(1),t(end)],[0.528, 0.528],'linestyle','--','linewidth',1.5,'color','r')
xlim([0.005,inf]);
hold on;
```

```
grid on
g = gca;
g.FontSize = 16;
xlabel('Time (sec)');
ylabel('P_p_l_e_n_u_m/P_s_u_r_f');
legend({'Analysis pressure ratio','Sonic suction threshold'});

% Output mean Conductance and pressure ratio
starter = find(t >= 0.3);
c_mean = mean(C_tot(starter:end));
prat_mean = mean(p(starter:end)/p_surf);
fprintf('The mean conductance is %5.2f\n',c_mean);
fprintf('The mean pressure ratio is %5.3f\n',prat_mean);

% Plot mass flow rates in and out of plenum
% Edit to throughput - 4/11
figure(3)
% semilogy(t,mdot_rec*1000,'linewidth',2);
semilogy(t,Q,'linewidth',1.5,'color','b');
hold on
grid on
% semilogy(t,mdot_plen_out*1000,'linewidth',2,'linestyle','--');
xlim([0.005,inf]);
leg3{1} = 'Tunnel to plenum';
leg3{2} = 'Plenum to tank';
g = gca;
g.FontSize = 16;
xlabel('Time (sec)');
ylabel('Mass flow rate (g/s)')
ylabel('Throughput (torr L/s)')
% legend(leg3);
```

```
% Initial pressure drop in plenum as function of time
% compared to an "ideal" scenario
% Calculated pressure in plenum
begsuc = find(suck_check~=0,1);% up to suction beginning
% begsuc = 1000000;
pfit = p(2:begsuc)*0.00750062;% torr
pfit = pfit';
tfit = t(2:begsuc);
tfit = tfit';
fcalc = fit(tfit,pfit,'exp2');

% "Ideal" pressure drop in the plenum
% Modeled as a tank with an initial pressure of 155 psia
% blowing out of an choked 1-1/4 pipe hole to perfect vacuum
V_tot = 0.0016; %m^3, volume of pipes under pressure
A_out = ((1.83*0.0254)/2)^2*pi; %m2, area of hole

dt = 1e-6;% time step
idtime = 0:dt:0.3;%tfit(end); %s, time variable

% preallocate vectors
p_ideal = zeros(length(idtime),1);
mdot_ideal = zeros(length(idtime),1);
m_ideal = zeros(length(idtime),1);

% initial pressure
p_ideal(1) = 155*6894.76; % pa
m_ideal(1) = p_ideal(1)*V_tot/R/T_surf;

for ti = 1:length(idtime)
```

```
rho_ideal = p_ideal(ti)/(R*T_surf);

mdot_ideal(ti) = A_out*sqrt(gam*p_ideal(ti)*rho_ideal...
*(2/(gam+1))^((gam+1)/(gam-1)));
dm_ideal = mdot_ideal(ti)*dt;
% New pressure based on mass removed
p_ideal(ti+1) = p_ideal(ti) - (dm_ideal*R*T_surf/V_tot);

end
p_ideal = (p_ideal(1:end-1))*0.00750062;% torr
idtime = idtime';
fideal = fit(idtime,p_ideal,'exp1')

% Plot the calcluated and ideal lines
figure(4);
semilogy(tfit,pfit,'linewidth',2);
leg4{1} = 'Analysis';
hold on
grid on
semilogy(idtime,p_ideal,'linewidth',2);
leg4{2} = 'Sonic orifice';
plot([0,tfit(end)],[10,10],'linewidth',2,'linestyle','--');
leg4{3} = 'Surface pressure';

g = gca;
g.FontSize = 18;
ylabel('pressure (torr)');
xlabel('time (s)');
xlim([0,tfit(end)]);
ylim([1,inf]);
legend(leg4);
```

```
% Open figures in Plot Browser
figs = gcf;
for jj = 1:figs.Number
plotbrowser(jj,'on');
end

% Testing another Lafferty analysis
% friction factors
% f_d(1) = 0.03; % startup, From Moody diagram
% f_d(2) = 0.015; % once steady, "laminar" result
% Q_lam = kv * (p_u^2 -p_d^2)/2;
% Cz = A*sqrt(R*T);
% Q_turb = Cz * sqrt((diam/(f_d(1)*length))*(p_u^2-p_d^2));
% Q_comp = sqrt(gam)*Cz*p(x)*Ma*sqrt(1 + *(gam-1)/2*Ma^2);
```

D. TRAVERSE POSITIONING PROGRAM

This appendix consists of one of the codes used to move the traverse probe through the flow above the model. The code outputs a file of the position and time of the probe for each movement.

```
'Program written by Phillip Portoni, Mar 26, 2018
'Based off of Katie Gray's sample program from Jan 18
'Used for entry with suction model - Initial entry probe impacted model

'Revision 3a - Oct 24, 2018

'Probe starts 1 mm above model surface then shifts to 3 mm after
'a 0.8 second delay, repeat to 5 mm, then remains in this position
'til the end.

'Declare any variables used for post-processing
DVAR $htime  'file handle for exporting timer values
DVAR $hpos  'file handle for exporting position values
DVAR $var 'index for postion and time variable
DVAR $pos[200] 'define position array as 200x1
DVAR $time[200] 'define time array as 200x1
DVAR $varcount

ENABLE X
'turns on control for the X axis
'(vertical motion in the tunnel and only possible axis)
ABSOLUTE
'sets programming mode to incrmental. ie, all distances are
```

```
'defined relative to previous position.
'remains in effect until ABSOLUTE mode is specified
PRIMARY
'uses primary units, determined by parameter file.
'with parameter file parameter_file_with_stage.prma
'this means mm. Use Secondary to use secondary units,
'which are inches for this parameter file
SECONDS
'specifies that feedrates are in distance units per second.
WAIT( $AI[1].X > 1 ) -1
'the program pauses here until the scope is triggered
'controller waits until Analog Input #1 on the X axis is
'less than 1 volt. this condition may need to be changed
'depending on scope AUX out settings before and after trigger
'the -1 means to wait infinite time
DWELL 0.5
'probe is held in place here, to wait on tunnel startup

'initialize index
$var = 0

'Initialize timer used to measure time during run
TIMER 0 CLEAR

'Record initial position and time
$pos[$var]= AXISSTATUS(X, DATAITEM_PositionFeedback)
$time[$var] = TIMER (0,PERFORMANCE)
$var = $var+1

DWELL 0.8 'Wait in initial position for data gathering.
```

```
LINEAR X-3 F10 'Move to 3 mm above the model
'X-# moves up, X# moves down: up 10 mm
'F# dictates the velocity: 240 mm/s
'max velocity is 248.92 mm/s

$pos[$var]= AXISSTATUS(X, DATAITEM_PositionFeedback) 'record position
$time[$var] = TIMER (0,PERFORMANCE) 'record time at position
$var = $var+1 'increase the index



DWELL 0.8 'Wait for data collection

Linear x-5 F10 'Move to 5 mm above the model

$pos[$var]= AXISSTATUS(X, DATAITEM_PositionFeedback) 'record position
$time[$var] = TIMER (0,PERFORMANCE) 'record time at position
$var = $var+1 'increase the index

DWELL 5.0 'Wait for til end of run

$pos[$var]= AXISSTATUS(X, DATAITEM_PositionFeedback) 'record position
$time[$var] = TIMER (0,PERFORMANCE) 'record time at position
$var = $var+1 'increase the index

'Write timer and position results to files
$htime = FILEOPEN "C:\Users\Phil Portoni\Desktop\Sept 2018\Traverse files 8-20-2018\time
$hpos = FILEOPEN "C:\Users\Phil Portoni\Desktop\Sept 2018\Traverse files 8-20-2018\posit
$varcount = $var
$var=0
REPEAT $varcount+1
FILEWRITE $htime, $time[$var]  'Write the timer outputs to time.txt
```

```
FILEWRITE $hpos, $pos[$var]  'Write the position outputs to position.txt
$var = $var+1
ENDREPEAT

FILECLOSE $htime 'close timer.pgm
FILECLOSE $hpos 'close position.pgm
```

E. INSTALLING THE SUCTION SYSTEM

This appendix describes the install procedure for the suction system. Note that all NPT-pipe joints must be wrapped with pipe-tape to seal. Isolate the vacuum pumps so that one is connected to the 500 cubic-foot tank and one is connected to the BAM6QT vacuum tank.

E.1 Install Sequence

The most effective sequence in setting up the suction system is briefly described here. Each step is explained in the following sections. The 6-inch, class-150 flange on the aluminum pipe that is plumbed through the wall to Room 29A is referred to as 29A-flange. The 6-inch, class-300 flange with a 2-inch-NPT adapter that is installed in place of the steel plug in the side of the sting support section of the BAM6QT is referred to as tunnel-flange.

- Set up the 29A-flange on the pipe that is plumbed through the wall to 29A.
- Adjust the pipe insert
- Remove the steel plug from the wall of the BAM6QT.
- Install the sting
- Screw the 1-1/4-inch pipe into the sting.
- Using the dowel-pin, loosely install the tunnel-flange with the 1-1/4-inch pipe passing through the 2-inch-NPT adapter.
- Install the Conax to seal the pipe.
- Tighten the bolts around the tunnel-flange.
- Install the solenoid valve on the pipe.

- Connect the hose between the solenoid valve and the 29A-flange.
- Check for leaks.

E.2 29A-Flange

The 29A-flange is a 6-inch, class-150 flange mounted to a 6-inch aluminum pipe plumbed through the wall between 29A and 29B. The aluminum pipe connects to the 500 cubic foot vacuum tank outside. There are two flanges available. One is for using 1-1/4 hose, and the other is for the 2-inch hose. The flange for the 2-in hose is shown in Figure E.1. The flange is sealed with a gasket.

The Kulite ETL-79-HA-DC-5A calibrations currently must be completed with the 1-1/4 flange. Remember to install the corresponding on-off valve and the 1/4-NPT ISO-KF mount. The 1/4-NPT ISO-KF mount is to attach the Ceravac vacuum gage.

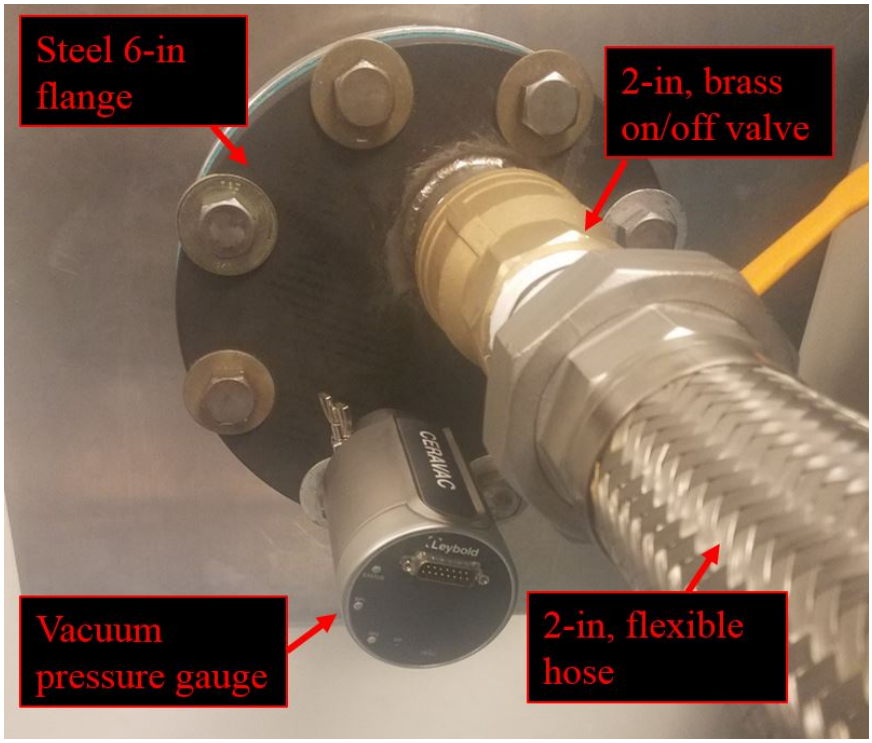

Figure E.1. 29A-flange connecting to 6-in aluminum pipe plumbed through the wall between 29A and 29B

E.3 Steel Plug and Tunnel-Flange

Typically installed in the side of the sting support section of the BAM6QT is a 6-inch, class-300 steel plug with four Conax-fitting ports tapped on it, see Figure E.2. This must be removed and replaced with the tunnel-flange which has a 2-NPT fitting welded to it, see Figure E.3.

The steel plug is removed via the three push-off screws. Once there is about 1-1/2-inch clearance between the back of the flange and the tunnel, the plug slides out of the tunnel with minimal effort. The eye-bolts and chain to attach the crane are typically stored next to the window-swap counterbalance in the east end of 29B. When reinstalling the plug after the entry, always use the chain to support the plug. Also, apply liberal amounts of silicon lubricant to the plug before inserting it into the tunnel.

When installing the tunnel-flange, use the dowel pin for alignment. The pipe should pass through the 2-inch-NPT adapter without issue. Due to a mis-design, there are 2 o-rings grooves, one on the tunnel and one on the flange, so be sure both have o-rings in position when attaching the flange. If only one o-ring is used, the flange will leak. I recommending having a partner assist with one person hold the flange in position, while a second attaches the bolts. Do not tighten the bolts fully until after the suction pipe is installed in the Conax. Keeping it loose allows some adjustment room when installing the rest of the piping.

Figure E.2. 6-inch, stainless steel plug typically installed in the side of the BAM6QT just downstream of the sting support.

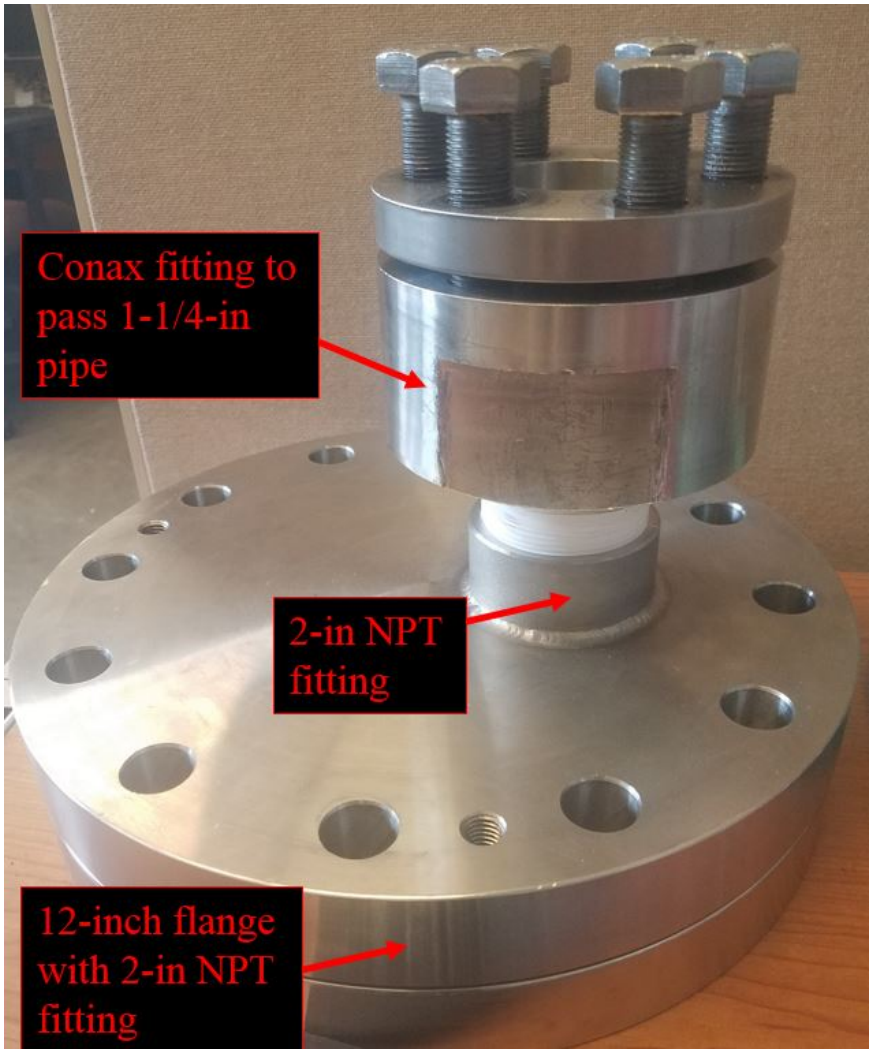

Figure E.3. Flange with 2-in. NPT adapter

E.4 Pipe Insert

A hole was drilled in the side of the pipe insert of the tunnel to allow a pipe to pass through the tunnel. The pipe insert has to be adjusted so that it uses the second hole, see Figure E.4. This position provides the best alignment between the hole in the pipe insert and the sting.

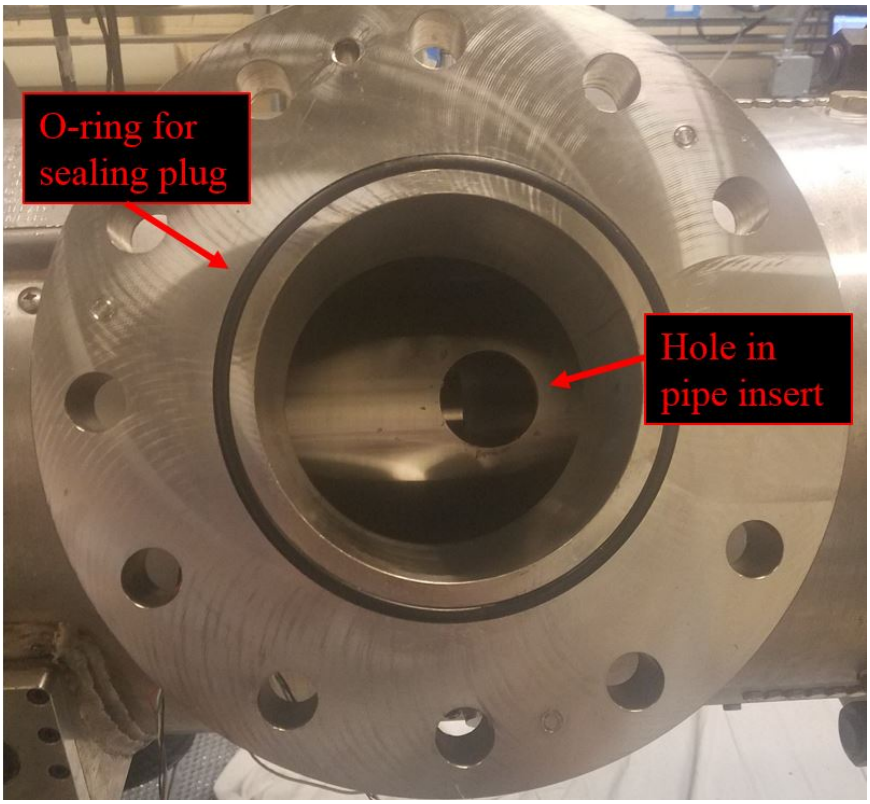

Figure E.4. The hole in the pipe insert observed thorough the hole created when the stainless steel plug is removed.

E.5 Sting

A custom sting was made to use with the suction system. The back side of the sting is a 1-NPT hole in which a 1-to-1-1/4 elbow adapter is mounted.

Attach the adapter to the sting before putting it in the tunnel and tighten it down fully. The sting has to be installed in the backside of the sting mount. Do not tighten the sting set screws until after the pipe is sealed in the Conax.

E.6 Pipe, Solenoid Valve, and Hose

A 2-ft, 1-1/4 pipe passes through the flange with the 2-NPT fitting as shown in Figure E.6. Tighten the pipe into the sting with an 14-inch pipe wrench before installing the 6-inch flange, shown in Figure E.5.

After installing the tunnel-flange, install 1-1/4 pipe Conax around the pipe. Use the 36-inch pipe wrench to torque the Conax into position. The alignment of the tunnel-flange and pipe is tricky, and requires careful adjustments to get the rubber sealant in the Conax around the pipe. After the Conax is assembled, the bolts in the tunnel-flange can be tightened.

The solenoid valve attaches to the end of the 1-1/4 pipe. Use a pipe union to install it. There is an arrow pointing in the direction of flow on the valve, and the valve will leak if installed backwards.

The hose connects the solenoid to the on/off valve on the 6-inch flange. The 2-inch hose requires an adapter as shown in Figure E.7.

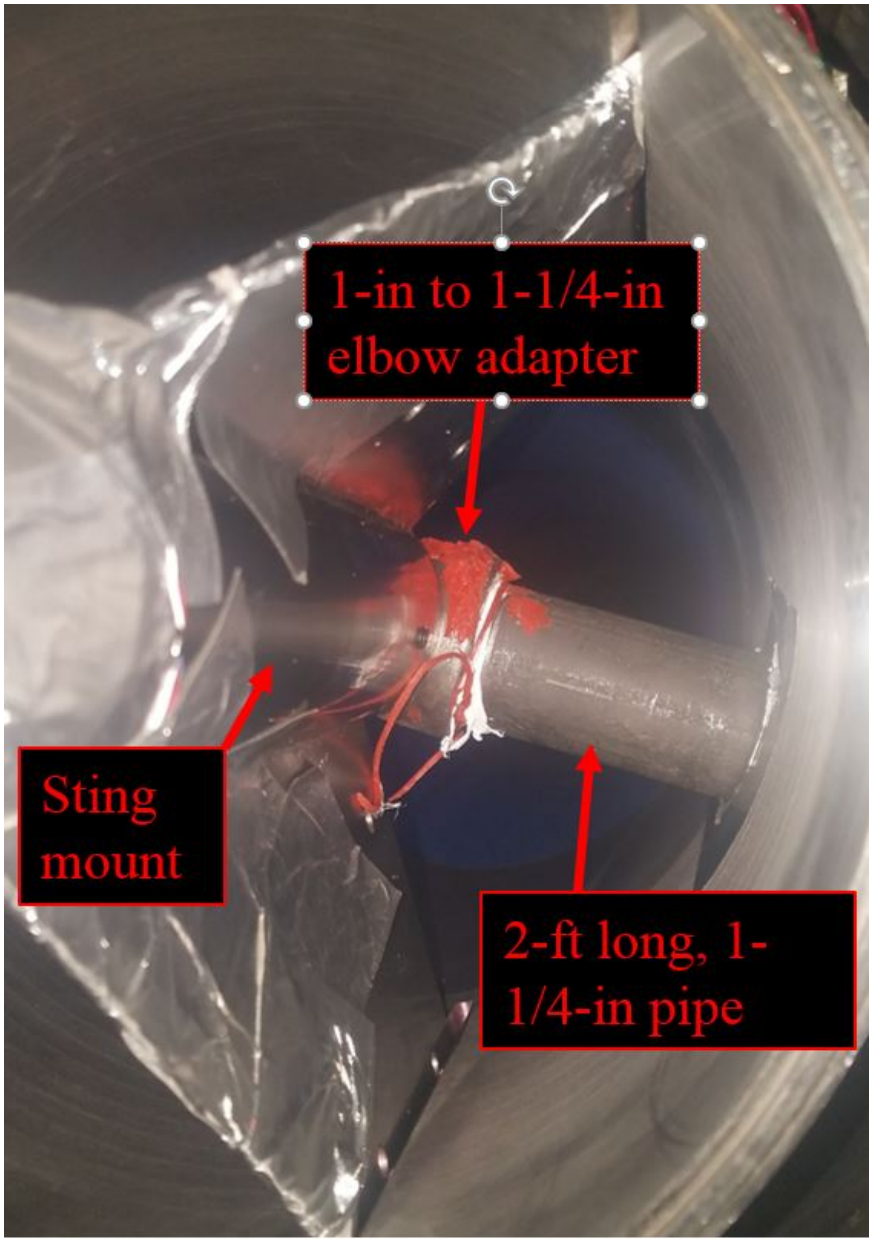

Figure E.5. 2-ft, 1-1/4-in. pipe mating with sting inside BAM6QT

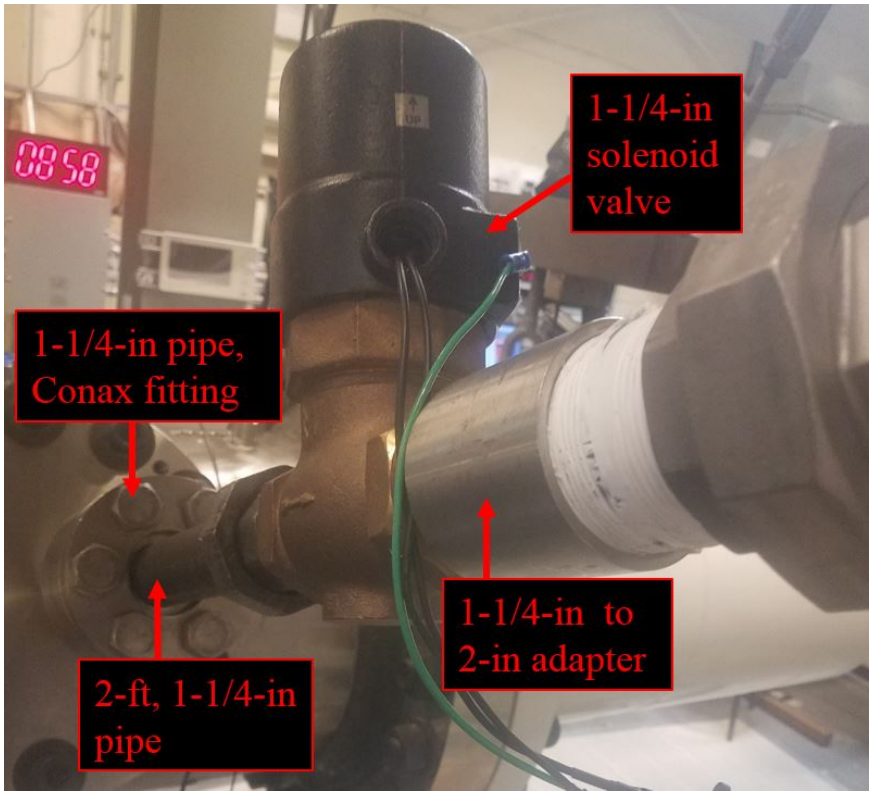

Figure E.6. 2-ft, 1-1/4-in. pipe passing through tunnel wall

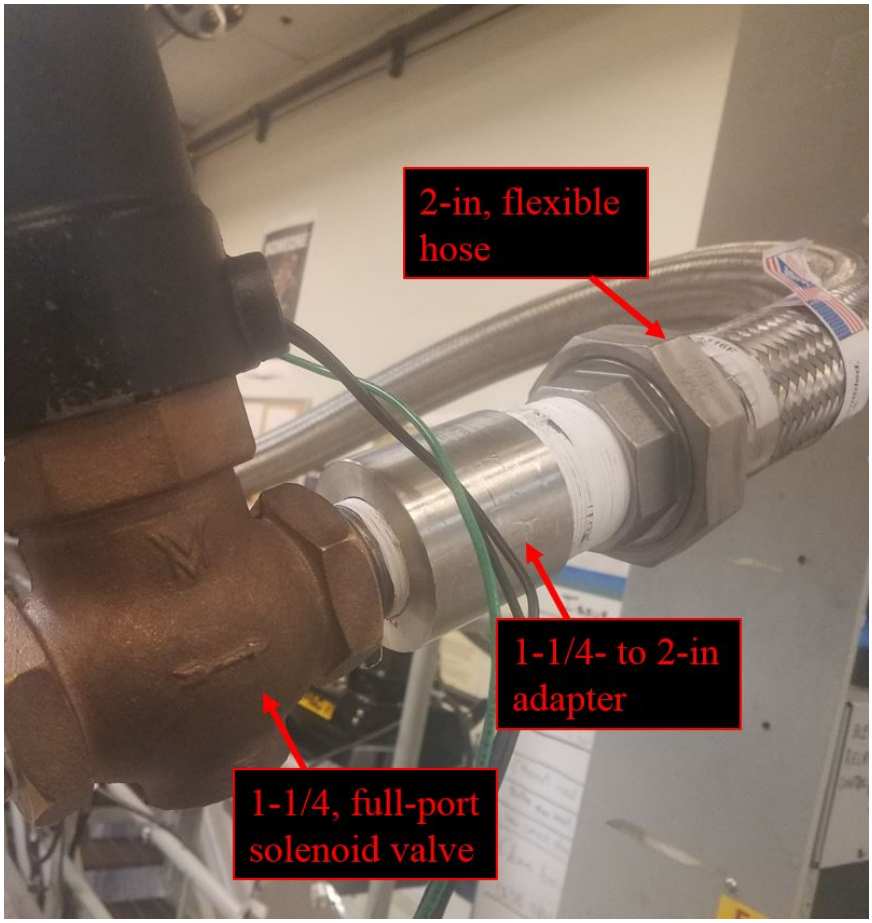

Figure E.7. 2-in hose connection to solenoid valve

E.7 Sealing and Leak Testing

Go through and check all of the joints to ensure nothing is loose. After installing the model, leak test the suction system. Open the on/off valve and solenoid, and have a partner bleed air into the supersonic tunnel. Keep the pressure around 5 psig. Apply soapy-water to each joint and if bubbles form on the joint, or you hear a hiss, either tighten the connection or use RTV to seal the joint.

After leak testing, close the 12-inch wafer valve in the supersonic tunnel and placard it off.

F. VACUUM SENSOR CALIBRATIONS

The tables below show the comparisons of the Ceravac 100 torr vacuum sensor used in this project against a Ceravac 1000 Torr and a Ceravac 1 Torr vacuum sensor. These comparisons were made in a shock tube by Mark Wason.

Table F.1. Comparison of Ceravac 100 torr vacuum sensor against a Ceravac 1000 torr vacuum sensor

Ceravac 100 (torr)	**1000 torr reference**
88.14	88.15
66	65.97
43.43	43.37
23.32	23.27
7.9	7.83
4.52	4.47
3.97	3.92
2.98	2.92
1.89	1.84
0.903	0.85
0.266	0.22

Table F.2. Comparison of Ceravac 100 torr vacuum sensor against a Ceravac 1 torr vacuum sensor

Ceravac 100 (torr)	**1 torr reference**
0.953	0.9165
0.609	0.5760
0.469	0.4365
0.328	0.2977
0.175	0.1447
0.1	0.0675

The ETL-79-HA-DC-190-5A Kulite pressure transducers were calibrated against the Ceravac 100 vacuum sensor before each suction entry. The Ceravac 100 vacuum sensor was mounted to the 29A-flange via a quick-clamp high-vacuum fitting. The ETL-79 pressure transducers were connected to the flange via small tubing and modified sensor mount designed by Mark Wason for use in the Purdue Shock Tube. These are shown in Figure F.1. Examples of the calibrations for two of the ETL-79 pressure transducers are shown in Tables F.3 and F.3.

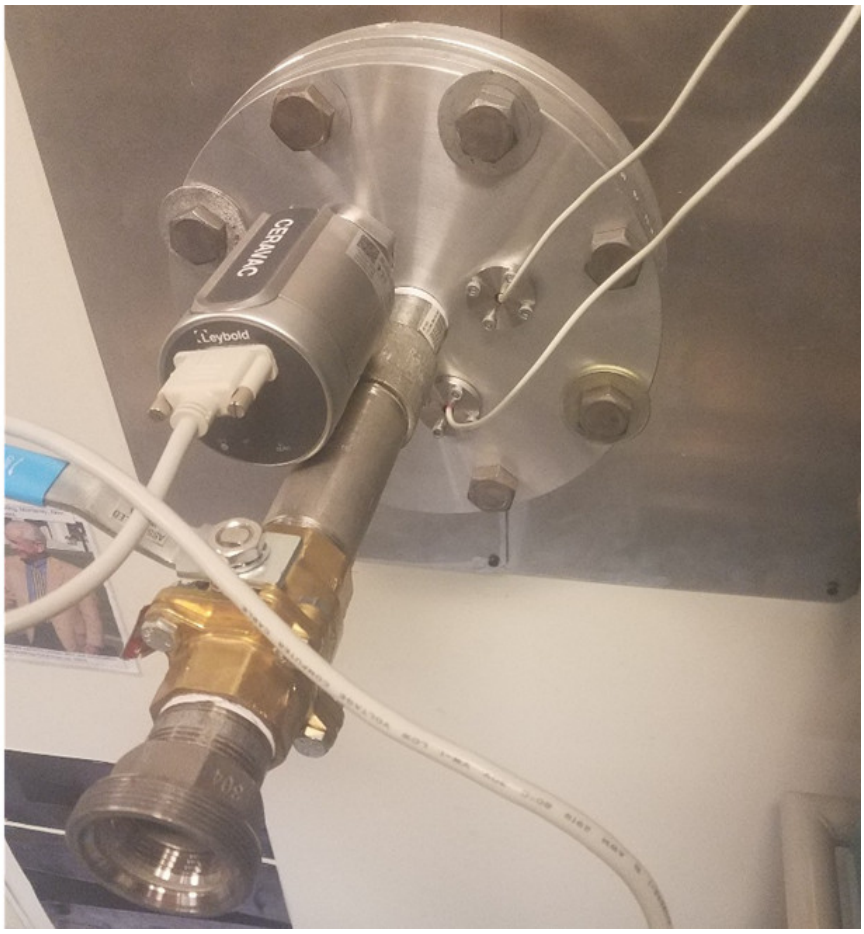

Figure F.1. Picture of 29A-flange set up to calibrate ETL-79-HA-DC-190-5A Kulite pressure transducers.

Table F.3. Calibration of low pressure sensor with serial number 51

SN: 51 voltage (V)	**100 torr reference**
0.634	7.65
0.596	5.48
0.605	6.01
0.618	6.75
0.526	0.82
0.529	1.51
0.539	2.26
0.553	3.00
0.565	3.75
0.578	4.50

Table F.4. Calibration of low pressure sensor with serial number 49

SN: 49 voltage (V)	**100 torr reference**
0.662	9.66
0.602	6.16
0.564	3.98
0.549	3.09
0.54	2.49
0.531	1.80
0.521	0.80
0.532	2.11
0.553	3.37
0.573	4.50